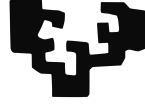


A Thesis submitted for the degree of Doctor of Philosophy

eman ta zabal zazu



Universidad del País Vasco Euskal Herriko Unibertsitatea

Theoretical characterization in the functionalization and design of low dimensional systems: carbon transition metal nanostructures and phosphorene isoelectronic compounds

Tomás Alonso Lanza

2017

Supervised by Andrés Ayuela Fernández

Centro de Física de Materiales, San Sebastián
Materials Physics Department, University of Basque Country

A mi padre

Contents

Resumen	vii
1 Introduction	1
1.1 Nanoscale: low dimensional materials	1
1.2 Zero-dimensional materials	4
1.2.1 Fullerenes	5
1.2.2 Quantum dots, graphene nanoflakes	6
1.2.3 Polycyclic aromatic hydrocarbons (PAHs)	6
1.3 Two-dimensional materials	11
1.3.1 Graphene	11
1.3.2 Phosphorene	18
1.3.3 Isoelectronic compounds to graphene and phosphorene	19
2 Methods	23
2.1 Many-body equation	23
2.2 Density functional theory	24
2.2.1 Kohn-Sham equations	25
2.2.2 Functionals	26
2.3 The SIESTA method	27
2.3.1 Pseudopotentials	28
2.4 Projector augmented waves - The VASP method	29
2.5 Full-potential linearized augmented-plane-wave method - the ELK method	32
3 Zero-dimensional systems	33
3.1 Introduction	33
3.2 Interaction of cobalt atoms and small clusters with circumcoronene $C_{54}H_{18}$	35
3.2.1 Free molecules and clusters	35
3.2.2 Co atom on circumcoronene	40
3.2.3 Co_2 molecule on circumcoronene	43
3.2.4 Co_4 molecule on circumcoronene	44
3.2.5 Charges and bonding	45
3.2.6 Magnetism	48
3.3 Non-collinear ground state for Co_3Bz_3	51
3.3.1 Collinear calculations	51
3.3.2 Non-collinear calculations	52
3.3.3 Anisotropic Heisenberg Spin Model	55

3.4	Ultrashort Mn-Mn bond for manganese benzene clusters	57
3.4.1	Rice-ball Mn-Bz clusters	58
3.4.2	Multiple-decker Mn-Bz clusters	62
3.4.3	A detailed analysis of Mn_2Bz_2	62
3.4.4	Ultrashort Mn-Mn bonding	64
3.4.5	Considerations related to possible synthesis of Mn_2Bz_2	66
3.5	Large magnetic anisotropy for Ni_3Bz_3	67
3.5.1	Non spin-orbit calculations	68
3.5.2	Spin-orbit calculations	68
3.5.3	Electronic structure	71
3.6	Conclusions	74
4	Graphene doping: cluster adsorption and substitutional atoms	77
4.1	Introduction	77
4.2	Adsorption of clusters over graphene	77
4.2.1	Stability of free Co_{13} clusters	77
4.2.2	Stability of Co_{13} isomers bonded to graphene	79
4.2.3	Charge transfer between Co_{13} cluster and graphene	84
4.2.4	Bonding mechanism	85
4.2.5	Magnetic moment	89
4.2.6	DFT+U study: on-site interaction	90
4.2.7	Bringing results into contact with experiments	90
4.3	Substitutional impurities in graphene	92
4.3.1	Adsorption energies and bond lengths	94
4.3.2	Magnetism	95
4.3.3	Manganese group magnetism	97
4.4	Conclusions	101
5	New two-dimensional materials design	105
5.1	Introduction	105
5.2	Silicon monosulfide monolayers	105
5.2.1	SiS monolayers: a new phase	106
5.2.2	Summary of structures: stability	111
5.3	Carbon monosulfide nanostructures	114
5.3.1	Monolayers	114
5.3.2	Chains	121
5.3.3	Thin films	124
5.3.4	Comments on stability	126
5.4	Conclusions	127
6	Summary and outline	129
6.1	Outline	132
7	List of publications	133

8 Bibliography

135

Resumen

Esta tesis se enmarca en el campo de las simulaciones computacionales de materiales de dimensiones nanométricas. El estudio de estos sistemas se conoce como nanociencia o nanotecnología. La nanociencia fue propuesta por Feynman en una charla en el Instituto Caltech a mediados del siglo pasado, prediciendo el control de los átomos y el diseño de nuevos materiales. Dichas predicciones fueron acertadas y hoy en día la nanotecnología es un campo de investigación en crecimiento, con múltiples aplicaciones con uso en la vida real. La importancia de la nanotecnología se debe a efectos cuánticos que aparecen debidos al confinamiento gracias al pequeño tamaño, al elevado ratio de superficie frente a volumen, y a otros fenómenos relacionados. Todo ello produce como resultado propiedades inimaginables en materiales macroscópicos.

Las simulaciones computacionales han resultado ser de gran utilidad para el avance de la ciencia, y complementan el trabajo experimental. Sin embargo, el camino para poder llevar a cabo simulaciones útiles y razonables desde el punto de vista de equipamiento, tiempo y presupuesto ha sido largo. Hoy en día es posible llevar a cabo simulaciones computacionales que permiten caracterizar materiales, la explicar fenómenos observados experimentalmente o predecir nuevos materiales. En esta tesis se llevan a cabo cálculos computacionales utilizando diferentes métodos incluyendo principalmente SIESTA, VASP y ELK. Estos métodos se basan en la teoría del funcional de la densidad, que expresa la energía electrónica como un funcional que se minimiza con respecto a la densidad electrónica. El problema de un sistema de muchas partículas como el átomo es cómo tratar la interacción de todos los electrones con todos los electrones de forma que el problema sea resoluble. A este respecto la propuesta de Kohn-Sham permite trabajar con un sistema de partículas independientes, simplificando enormemente los cálculos. Los términos de intercambio y correlación, más la parte de la energía cinética se incluyen en un funcional de intercambio y correlación. La expresión exacta de dicho funcional no es conocida, por lo que se aproxima de diferentes maneras. En esta tesis se usan la aproximación de densidad local, que depende de la densidad electrónica en cada punto y toma el valor de la energía de intercambio y correlación del gas homogéneo de electrones, y la aproximación de gradientes generalizados, que tiene en cuenta no sólo la densidad sino también su variación. Las ecuaciones de Kohn-Sham de partícula independiente se resuelven en un esquema autoconsistente. Se comienza con una densidad electrónica de entrada, para la que se calcula el potencial y se resuelven las ecuaciones. Como resultado se obtiene una densidad de salida, la cual se compara con la densidad electrónica de entrada. El cálculo termina cuando ambas densidades electrónicas son coincidentes o difieren por una cantidad pequeña llamada tolerancia.

La reducción del tamaño de los materiales en la nanotecnología lleva a la existencia de materiales de bajas dimensiones, cero, uno y dos dimensiones. Por ejemplo, se considera

bidimensional aquel material cuya longitud en una dirección es suficientemente pequeña para producir confinamiento cuántico. En esta tesis estudiamos nanomateriales de baja dimensión usando simulaciones computacionales. El material bidimensional por excelencia es el grafeno, aislado en 2004 por primera vez mediante el uso repetido de cinta adhesiva para separar las láminas de grafito. Las increíbles propiedades (electrónicas, mecánicas, etc.) del grafeno lo hicieron candidato para multitud de aplicaciones, y desataron un creciente interés por el estudio de este tipo de materiales. Sin embargo, el grafeno presenta la desventaja de no tener gap, lo que le inhabilita para dispositivos electrónicos que requieren encendido y apagado. Una forma de modificar las propiedades del grafeno es el dopado con otros elementos, como los metales de transición. Otro enfoque consiste en diseñar nuevos materiales bidimensionales que mejoren sus propiedades u ofrezcan nuevas alternativas.

En esta tesis hemos seguido los dos enfoques, estudiando la interacción de metales de transición con átomos de carbono en grafeno pero también en moléculas con estructura de grafeno, y diseñando nuevos materiales bidimensionales.

Las pequeñas moléculas conocidas como hidrocarburos aromáticos policíclicos son similares a fragmentos de grafeno o nanografenos, con la diferencia de tener sus bordes saturados con hidrógeno. En esta tesis estudiamos la interacción de átomos y agregados metálicos pequeños de cobalto con circumcoroneno $C_{54}H_{18}$. El circumcoroneno es una molécula hexagonal compuesta de 19 anillos bencénicos. Aunque en nanografenos similares se pueden observar momentos magnéticos locales en los átomos situados en los bordes, en el caso del circumcoroneno el momento local y total es cero debido a que el tamaño no es lo suficientemente grande. Cuando se depositan átomos y agregados pequeños de cobalto sobre circumcoroneno hay diferentes posibles posiciones. Por ejemplo, dentro de un mismo anillo bencénico destacan tres sitios: sobre el centro del hexágono, sobre un átomo de carbono y sobre un enlace carbono-carbono. En nuestros cálculos hemos encontrado que los átomos de cobalto prefieren situarse sobre el centro del anillo bencénico. Además, al ser un sistema finito, se puede distinguir entre anillos bencénicos centrales y periféricos. Desde el punto de vista energético, el cobalto prefiere depositarse sobre anillos situados en el borde de la molécula del circumcoroneno. En cuanto al dímero de cobalto, obtenemos que prefiere situarse perpendicularmente al circumcoroneno en lugar de estar horizontal con los dos átomos de cobalto interactuando directamente con la superficie. Al igual que para los átomos de cobalto, el centro de un anillo bencénico es el sitio más favorable energéticamente. Por último, el agregado de cuatro átomos de cobalto adopta una estructura tetrahedral y se sitúa con una cara paralela al circumcoroneno con tres átomos de cobalto sobre los centros de tres anillos bencénicos consecutivos, preferiblemente cercanos al borde. La diferencia de energía entre los posibles zonas en las que se deposita el agregado de cuatro átomos de cobalto es pequeña, lo que sugiere que el agregado de cuatro átomos de cobalto podría deslizarse sobre la superficie del circumcoroneno, a falta de calcular las posibles barreras. Tanto para el dímero de cobalto como para el agregado de cuatro átomos de cobalto, los átomos de cobalto prefieren estar enlazados entre sí a separarse sobre la superficie de circumcoroneno. Este resultado muestra la fortaleza del enlace cobalto-cobalto, prior-

izado sobre el enlace cobalto-carbono. Se pueden extraer dos tendencias generales sobre la adsorción de cobalto sobre circumcoroneno: la preferencia por el centro de los anillos bencénicos y la preferencia por los bordes. El análisis de la energía de enlace muestra que los átomos de cobalto ganan energía al enlazarse entre sí y al circumcoroneno, lo que implica que los agregados de cobalto se adherirán al circumcoroneno. Desde el punto de vista del magnetismo, el enlace con circumcoroneno conlleva una reducción del momento magnético de los átomos y agregados de cobalto, y la inducción de un pequeño momento negativo en los átomos de carbono más cercanos. Hemos investigado la estructura hiperfina del circumcoroneno con y sin cobalto, encontrando variaciones en la densidad de carga cercana a los núcleos de los átomos de carbono en función de la posición y los átomos vecinos. Esta densidad de carga se relaciona con el desplazamiento isomérico, detectable en los experimentos, lo que permitiría conocer si hay cobalto sobre la superficie de circumcoroneno, pudiéndose aplicar a moléculas similares.

La unidad más pequeña con la estructura hexagonal del grafeno es el benceno, con su anillo hexagonal aromático. La interacción de metales de transición con anillos bencénicos conduce a fenómenos magnéticos relevantes. En concreto, en esta tesis estudiamos la interacción de átomos de manganeso, cobalto y níquel con varias unidades bencénicas. La interacción metal-metal es dominante respecto a metal-carbono para estos elementos, lo que determina la estructura de estos compuestos. Los átomos metálicos se sitúan en el centro formando pequeños agregados metálicos y quedan cubiertos por los bencenos que se sitúan alrededor, normalmente con el centro del anillo sobre un átomo metálico. Este tipo de estructura da lugar a efectos muy variados dependiendo del metal de transición. Para el agregado Co_3Bz_3 , la presencia de benceno estabiliza un acoplamiento antiferromagnético entre los átomos de cobalto, cuando en Co_3 y para agregados libres de cobalto el acoplamiento es ferromagnético. Si en el cálculo se permiten soluciones magnéticas no colineales, es decir con los momentos magnéticos locales apuntando en direcciones no paralelas entre sí, el agregado Co_3Bz_3 se estabiliza aún más respecto al estado antiferromagnético. Se encuentra una familia de soluciones no colineales con los momentos magnéticos en cada átomo de cobalto bien paralelos al correspondiente anillo bencénico o bien perpendiculares. En resumen, encontramos un estado fundamental con momentos no colineales en los átomos de cobalto, lo que se debe al efecto de los bencenos sobre la estructura triangular de cobalto, que ya de por sí promueve la frustración magnética. Hemos modelado el espectro energético de este sistema con un hamiltoniano que incluye anisotropías locales sobre cada unidad cobalto-benceno y dos términos de interacciones de intercambio para tener en cuenta asimetrías en la interacción. El triángulo formado por los átomos de cobalto no es totalmente equilátero, lo que da lugar a dichas asimetrías. De hecho, el ajuste de los parámetros del hamiltoniano da como solución dos interacciones de intercambio diferentes, una fuerte y otra débil.

Por otro lado, cambiando el metal de transición situado en el centro de los bencenos los resultados son drásticamente diferentes. Para el caso de manganeso, encontramos para el agregado Mn_3Bz_3 una superdimerización con una distancia manganeso-manganeso ultracorta de tan sólo 1.8 Å, acompañada de una reducción del magnetismo. Es importante remarcar que las distancias para el enlace manganeso-manganeso en diferentes

formas alotrópicas del bulk y en otros compuestos se encuentran en el intervalo 2.3-2.9 Å. El fenómeno genuino es observado para Mn_2Bz_2 , con momentos locales cero y distancia ultracorta. El estudio de los orbitales moleculares y de la función de localización electrónica permite afirmar que entre los átomos de manganeso se produce un enlace triple, de tipos σ , π y δ . Es importante recordar que el dímero de manganeso tiene una enlace de tipo van der Waals con distancia de enlace superior a los 3 Å, lo que da idea del gran cambio inducido por la presencia de los bencenos. La reducción del magnetismo permite acortar distancias debido a que se reduce la repulsión al tener los electrones espines opuestos, de acuerdo con el principio de Pauli. Este enlace manganeso-manganeso con distancias ultracortas supone un notable aumento de la estabilidad, ganando el sistema dos electronvoltios. Por ello es posible encontrarlo en otros agregados de mayor tamaño, como es el caso del agregado Mn_4Bz_4 , el cual se puede interpretar como la composición de dos agregados de Mn_2Bz_2 , uno de ellos rotado un ángulo recto.

Finalmente, para el tercer metal de transición que hemos estudiado, el níquel, el efecto de añadir bencenos es cambiar el eje fácil de magnetización, quedando fuera del plano de los tres átomos de níquel para el agregado Ni_3Bz_3 , cuando para el agregado Ni_3 los estados magnéticos en el plano son más estables. La explicación al cambio de estabilidad viene dada por la presencia de dos niveles electrónicos en la energía de Fermi compartiendo un electrón; el campo magnético perpendicular estabiliza el sistema llenando uno de los niveles, mientras que los casos con campos magnéticos en el plano de los tres átomos de níquel no son capaces de romper la degeneración. En el caso del níquel las soluciones magnéticas que hemos encontrado son colineales, a diferencia del caso del cobalto. Los estados magnéticos en el plano son prácticamente degenerados tanto para Ni_3 como para Ni_3Bz_3 . Hemos estudiado también los momentos magnéticos orbitales locales en los átomos de níquel. Mientras que para el agregado de Ni_3 los momentos orbitales locales no siguen la misma dirección que los momentos magnéticos de espín, al añadir las moléculas de benceno se crea un campo cristalino que recuerda al caso del sólido y que provoca la reducción de los momentos magnéticos orbitales locales y un mayor alineamiento con los momentos magnéticos de espín locales. Asimismo, los mayores valores de los momentos magnéticos orbitales locales para cada sistema se encuentran para los estados magnéticos más estables: los estados en el plano para Ni_3 y el estado fuera del plano para Ni_3Bz_3 .

A continuación comentamos los resultados del estudio de la interacción de los metales de transición con el grafeno. Para estudiar esta interacción hemos elegido dos enfoques, el estudio de agregados metálicos, en nuestro caso agregados de 13 átomos de cobalto, Co_{13} , y el estudio de impurezas sustitucionales de diferentes metales de transición. El estudio de agregados de Co_{13} sobre grafeno tiene puntos en común con la investigación ya comentada de átomos y pequeños agregados de cobalto sobre el circumcoroneno. En ambos sistemas hemos encontrado la fortaleza del enlace cobalto-cobalto sobre el enlace cobalto-carbono y la ganancia de energía cuando el agregado se deposita sobre la superficie de carbono. Aunque en esta tesis no lo estudiamos, un átomo de cobalto prefiere situarse sobre el centro de un hexágono en grafeno, de forma similar a nuestros resultados de cobalto y circumcoroneno. Todos estos puntos en común refuerzan el uso

del circumcoroneno como sistema para modelar grafeno. No obstante, aunque puede ser útil para comparar resultados como sitios de adsorción energéticamente favorables, se trata de sistemas diferentes debido a la existencia de bordes y al tamaño finito, que provocan un gap distinto de cero y niveles discretos, a diferencia del grafeno que tiene gap cero y una estructura de bandas bien conocida.

Para el agregado Co_{13} existen diferentes isómeros con diferentes estructuras geométricas. Hemos estudiado cinco estructuras o isómeros diferentes para este cluster, encontrando que la estructura más estable en el estado libre es un isómero bidimensional. Sin embargo, al depositar los agregados de Co_{13} sobre grafeno se produce una inversión en el orden de estabilidad, siendo el isómero de geometría icosaedra la estructura más estable. El estudio de los agregados de Co_{13} sobre grafeno arroja conclusiones sobre el tipo de enlace, cuya naturaleza no es aún bien conocida. Nuestros resultados muestran que no se trata de un enlace iónico en base a la transferencia de carga. Encontramos que se establecen una serie de enlaces cobalto-carbono, que varían en número y longitud. La cuantía y longitud de los enlaces no guardan una relación unívoca con la estabilidad como se había dicho previamente, aunque esta idea funciona para explicar algunos casos particulares. Por otro lado, demostramos la existencia de un criterio que permite entender el orden de estabilidad entre las distintas disposiciones de un isómero del agregado de cobalto sobre la superficie de grafeno. La mayor estabilidad se consigue cuando el agregado se une al grafeno por los átomos de cobalto con exceso de electrones en el estado libre del cluster. Este criterio prevalece sobre el número de enlaces. Por ello es importante caracterizar el estado de carga del agregado libre. Los agregados de cobalto sobre grafeno inducen momentos magnéticos en el grafeno del orden de $-0.3 \mu_B$. Asimismo, el momento magnético del agregado de cobalto se ve reducido. Este comportamiento es similar al de cobalto sobre circumcoroneno. Para ampliar la validez de nuestras conclusiones sobre la interacción de agregados de cobalto con grafeno hemos simulado el dopado de grafeno con cargas positiva y negativa, así como incluido términos para tener en cuenta que los sistemas con metales de transición como es el cobalto están fuertemente correlacionados. El resultado es que las principales conclusiones se mantienen.

Un enfoque diferente consiste en el estudio de impurezas sustitucionales en grafeno usando metales de transición $3d$, $4d$ y $5d$. La red hexagonal de grafeno puede sufrir imperfecciones que se conocen con el nombre de defectos. Los defectos en grafeno se clasifican en intrínsecos y extrínsecos. Los defectos intrínsecos incluyen vacantes, dobles vacantes, defectos de Stone-Wales, etc. Una vacante en grafeno se refiere a un punto de la red donde se ha perdido el átomo de carbono, lo cual puede conseguirse irradiando la superficie. Después esta vacante se puede reconstruir geoméricamente, o puede acoger un átomo diferente al de carbono. En esta tesis estudiamos una vacante en la que se sustituye el átomo de carbono por un átomo de un metal de transición, que se conoce como impureza. Los átomos de los metales de transición son más grandes que los de carbono, por lo que se quedan enlazados a determinada altura sobre la red hexagonal. La vacante sin reconstruirse tiene una simetría D_{3h} que puede mantenerse al incorporar la impureza, quedando ésta a igual distancia de los tres átomos de carbono, o perderse al haber diferentes distancias impureza-carbono. En nuestro caso hemos estudiado impurezas sustitucionales en grafeno para metales de transición $3d$, $4d$ y $5d$ de los grupos

del cromo al níquel. Para todos los casos hemos encontrado que la simetría de la vacante es C_{3h} , reducida respecto a la D_{3h} por la altura de la impureza sobre la red. Las impurezas $4d$ y $5d$ tienen mayores energías y distancias de enlace debido a su mayor tamaño respecto a las $3d$. Las impurezas $4d$ y $5d$ se comportan de forma similar entre sí debido a su similar tamaño, que se debe al fenómeno conocido como contracción de los lantánidos. Para los elementos $5d$ la carga nuclear efectiva es mayor, porque los electrones de la capa $4f$ que se añaden entre los $4d$ y los $5d$ son muy externos y producen un apantallamiento menor. Como consecuencia, los elementos $4d$ y $5d$ tienen tamaños y características similares como átomos sustitucionales en vacantes en grafeno. Para los grupos de cromo y manganeso el momento magnético en la impureza es elevado, con momentos magnéticos inducidos opuestos en los tres primeros vecinos de carbono. Para los siguientes grupos de hierro, cobalto y níquel se reduce el momento magnético en la impureza, alternando valores totales de 0 y $1 \mu_B$ según el grupo. Además, el momento magnético inducido en los tres primeros vecinos de carbono es del mismo signo que en la impureza. Aunque el comportamiento desde el punto de vista magnético es similar para las impurezas $3d$, $4d$ y $5d$, hay una diferencia notable entre el momento total de la celda de cálculo al pasar de las impurezas $3d$ a las $4d$ en el grupo del manganeso; el momento se reduce de $3 \mu_B$ para el caso del manganeso a $1 \mu_B$ para el caso del tecnecio. Esta reducción se debe a una alteración en el orden de llenado de los niveles cerca de la energía de Fermi, producida por la reducción de la separación entre los niveles de diferente espín. La causa de ello es la pérdida de carácter atómico de la impureza por una mayor hibridación con los átomos de carbono en el caso de las impurezas $4d$ y $5d$ respecto a las $3d$. La validez de nuestros resultados ha sido ampliada incluyendo términos para sistemas fuertemente correlacionados como son los metales de transición.

Finalmente, hemos trabajado en el diseño teórico de nuevas estructuras bidimensionales que puedan ser una alternativa al grafeno, realizando cálculos sobre dos compuestos isoelectrónicos al fósforo negro: silicio azufre y carbono azufre. Hemos seguido la aproximación isoelectrónica, que consiste en replicar un compuesto conocido usando elementos diferentes, bien de grupos adyacentes en la tabla periódica o bien del mismo grupo, de forma que se tenga el mismo número de electrones de valencia. En el caso de silicio azufre presentamos una nueva fase de carácter semiconductor, la cual mejora la estabilidad respecto a otras predichas anteriormente gracias a un enlace extra silicio-silicio. Dicho enlace es particular porque recuerda a un enlace doble (σ y π), lo que estaría en contra de la regla del doble enlace que afirma que los elementos con número cuántico principal n mayor que dos no forman enlaces múltiples. Se encuentra una hibridación de tipo spd en el silicio, con el concurso no despreciable de parte de los orbitales d . La estabilidad de la nueva fase se ha comprobado mediante el cálculo de la dispersión de los fonones y mediante una dinámica molecular a temperatura ambiente. Asimismo, analizamos el orden de estabilidad entre todas las fases de silicio azufre, incluyendo otras estructuras más gruesas halladas recientemente. La estabilidad aumenta cuando el silicio y el azufre establecen cuatro y dos enlaces respectivamente.

Por otra parte, estudiamos por primera vez nanoestructuras de carbono azufre, incluyendo cadenas, monocapas y películas delgadas. En las monocapas destaca como

más estable una fase semiconductor con estructura similar al fósforo negro, así como una fase cuadrada de carácter metálico. Ambas fases son estables a temperatura ambiente, y no presentan frecuencias negativas en la dispersión de fonones. Dichas fases tienen geometrías que podrían intercambiarse mediante la aplicación de tensión en la estructura, obteniéndose así un control mecánico sobre la conductividad. De hecho, hemos encontrado una monocapa metaestable que parece ser un estado intermedio entre ambas fases. En cuanto a las películas delgadas, no tienen gap y demostramos que son inestables a temperatura ambiente mediante dinámicas moleculares. Las estructuras más estables, las cadenas, forman una monocapa interaccionando entre sí mediante fuerzas de dispersión y son estables a temperatura ambiente. El orden de estabilidad de las nanoestructuras permite obtener conclusiones sobre las hibridaciones preferidas por los átomos de carbono y de azufre. El azufre, al igual que en silicio azufre, prefiere formar dos enlaces. En el caso del carbono, prefiere tener hibridación sp^2 con dos enlaces sencillos y un enlace doble a tener hibridación sp^3 con los cuatro enlaces saturados.

En esta tesis hemos caracterizado la interacción de carbono con metales de transición tanto en hidrocarburos aromáticos policíclicos como en grafeno; esta interacción es muy común en el dopaje requerido para moldear las propiedades de las nanoestructuras de carbono de cara a su implantación en aplicaciones y dispositivos. Asimismo, hemos ampliado el conocimiento de los materiales bidimensionales, proponiendo dos nuevos compuestos isoelectrónicos al fósforo negro.

1 Introduction

1.1 Nanoscale: low dimensional materials

Nanoscience and nanotechnology study small materials within the size scale of 1-100 nm and their associated quantum phenomena. At the nanoscale, the sizes are small enough to enable quantum properties not found at larger scales; this is called the quantum realm. The first reference to nanoscience comes from the renowned talk There's Plenty of Room at the Bottom of Richard Feynman at the California Institute of Technology in 1959 [1]. Feynman suggested that in the future it would be possible to control atoms individually. A breakthrough came with the Scanning Tunneling Microscopy, which allowed to "see" atoms in 1981 [2] and later the control of individual atoms was achieved as shown by IBM [3]. Researchers manipulated xenon atoms to reproduce the IBM logo as shown in Fig. 1.1(a). Another nanoscience milestone was the discovery of fullerene by Kroto and Smalley in 1985 [4].

Nanotechnology has experienced a huge boost lately because of the new experimental techniques and the large variety of novel materials presenting impressive properties, and previously inconceivable phenomena. Nanotechnology shows promising results for the future, but it also has many applications in the present for a large variety of fields, including medicine, electronics, solar cells, batteries, chemical sensors, etc. In medicine, applications have been proposed for drug delivery [5, 6], therapy techniques or diagnostic [7]. Flexible electronics could be achieved using graphene [8], and carbon nanotubes [9]. Chemical sensors based on nanotechnology could detect much smaller amounts of a gas because of the small size of the detectors, needing few molecules. For instance, carbon nanotubes based sensors [10] are promising because of the great change of their electronic properties when exposed to the target gas. Miniaturizing devices is also a hallmark of nanotechnology, as achieved for gears with the rotation control of a molecule deposited over a surface [11]. There is a large list of breakthroughs related to nanoscience. Nanotubes have been even proposed as tunnels through cell membranes[6] as shown in Fig. 1.1(c). In this thesis we¹ will focus on the electronic and magnetic properties of nanomaterials, e.g. finding peculiar magnetic behaviors, and on the design of novel materials.

Lower-dimensional materials appear as one of the novelties of nanoscience, with the possibility of dealing with single layer materials purely two-dimensional, or even with tubes formed by rolling the layers, which are considered one-dimensional objects. Indeed, fullerenes, such as Buckminsterfullerene C_{60} and similar complexes, are zero-dimensional. Examples of low dimensional systems based on carbon are shown in Fig

¹"we" is used throughout this thesis as being part of team. However, the work describes author main contribution.

1 Introduction

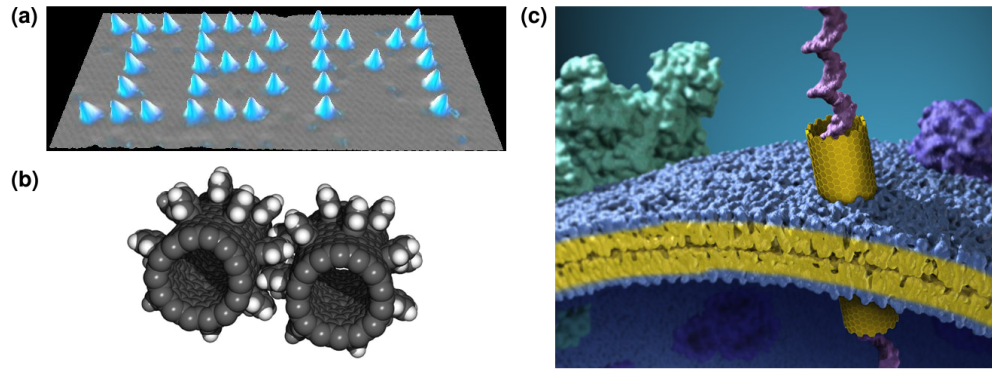


Figure 1.1: Nanotechnology applications: (a) IBM researchers could reproduce the logo of their company manipulating xenon atoms. Figure reproduced from <https://www-03.ibm.com/press/us/en/photo/28500.wss>. (b) Model of a possible nanogear based on tubes with molecules adsorbed on their surface. Figure reproduced from NASA Ames Research Center. (c) Artist view of a carbon nanotube inserted in a plasma membrane of a cell reproduced from <http://newscenter.lbl.gov/2014/10/31/nanotubes-that-insert-themselves-into-cell-membranes/>. The nanotube forms a nanoscale tunnel in the membrane and a single long strand of Deoxyribonucleic acid (DNA) is passing through that tunnel.

1.2. Low dimensional materials have nm scale and display confinement of the wave function in at least one dimension, which produce unexpected quantum effects. Besides, low dimensional materials offer an increased surface area to volume ratio, which means that surface states become dominant. So low dimensional materials present unexpected electronic, optical, mechanical and chemical properties, which make them promising and exciting for the discovery of novel physics phenomena involved in applications.

The graphene isolation in 2004 revealed incredibly promising properties proposing it as the best material ever. Graphene is the thinnest and strongest material, and the best electricity and heat conductor, among other characteristics. Although ten years later there is still some distance to find it implemented in industry as largely expected, graphene undoubtedly started a new era in condensed matter physics. Work has been done on graphene but also in similar systems because of the large opportunities offered by the low dimensional materials. In this thesis we follow this approach and we focus on the theoretical characterization of graphene and new low dimensional materials.

However, graphene has drawbacks. The most important is the absence of a band gap, relevant for switching on-off devices. Graphene was tuned and decorated with atoms, molecules and clusters. Doping graphene has several objectives: opening a band gap, inducing magnetism, etc. Many times, graphene doping was carried out using transition metal atoms, which suggest to study the carbon transition metal interaction.

Graphene being unable to satisfy all the expectations leads to the two objectives of this thesis: (i) to study interacting carbon nanostructures with transition metals atoms

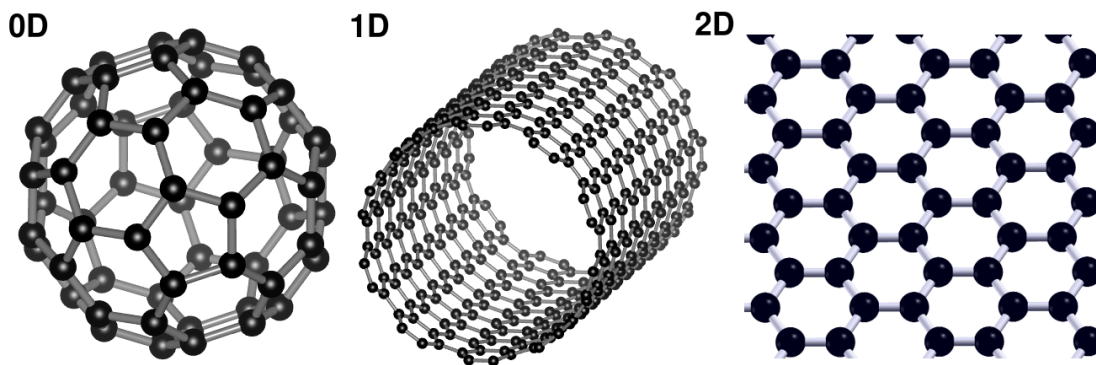


Figure 1.2: Carbon based nanomaterials examples of zero, one and two-dimensional objects. Buckminsterfullerene C_{60} is an example of zero-dimensional object. The armchair carbon nanotube (10,10) is a one-dimensional system. A single layer of graphite is a two-dimensional object. Coordinates of C_{60} obtained from <http://www.nanotube.msu.edu/fullerene/fullerene-isomers.html>. Coordinates of carbon nanotube (10,10) obtained from <http://www.nanotube.msu.edu/tubeASP/>.

(ii) to design theoretically new layers that could be used as an alternative to graphene.

Focusing on the first objective, we are interested in the interaction of transition metal atoms or clusters with carbon atoms from graphene but also from other graphene-like nanostructures. Not only the magnetic effects are key to our research, but also the structural and electronic properties. To this aim, we follow a double approach. On one hand, keeping the hexagonal pattern of carbon atoms characteristic of graphene, we reduce the size of the carbon nanostructure, studying zero-dimensional polycyclic aromatic hydrocarbons (PAHs) interacting with transition metals. Indeed, we also study the simplest unit of the carbon hexagonal pattern, benzene, interacting with transition metal atoms, within the broad field of organometallics [12].

On the other hand, we study graphene doping with transition metals in the form of atoms or clusters. While this second approach remains two-dimensional, the first approach is zero-dimensional because of the size of the molecules involved, even though they are graphene-like. Therefore, the first objective of this thesis leads us to two different chapters: zero-dimensional and two-dimensional graphene-nanostructures interacting with transition metals systems.

A radically different approach to overcome the drawbacks of graphene consists on finding other two-dimensional materials that either outperform graphene or offer different and broader opportunities. During last years a wide variety of new two-dimensional materials have been proposed theoretically and sometimes synthesized experimentally. Thus, the second objective of the thesis was to design theoretically other two-dimensional counterparts to graphene as an alternative for the applications in the growing fauna of the two-dimensional materials. We dedicated the last chapter of this thesis to present some new low dimensional materials.

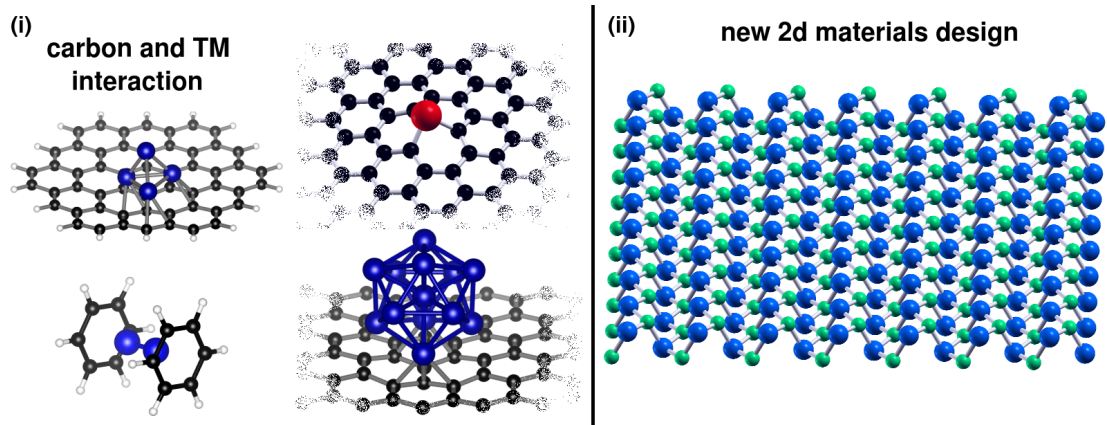


Figure 1.3: Objectives of the Thesis: (i) to study carbon-based nanostructures interacting with transition metals, (ii) to design new two-dimensional materials.

Next we present the introduction to this thesis, where we cover the previous work and the state-of-the-art for some of the topics we study later. We have decided to divide the introduction in two different parts, zero-dimensional and two-dimensional nanostructures. The first part, on the zero-dimensional materials, prepares the ground for the first chapter of this thesis. We comment on fullerenes, quantum dots, graphene flakes, PAHs, and benzene, and their combination with transition metals. The second part deals with two-dimensional systems, starting with graphene. We comment about the basic graphene properties and discuss the doping as a way to tune its properties, setting the basis for the second chapter of this thesis. Furthermore, we will also cover recent two-dimensional materials such as phosphorene. The design of isoelectronic materials opens the door for other nanostructures. This part prepares the reader for the last chapter of this thesis, where we present new two-dimensional materials isoelectronic to phosphorene.

1.2 Zero-dimensional materials

Nanoscience offers the opportunity to work with zero-dimensional systems. These systems show particular properties because of their nanoscale size. First we comment briefly on some well-known zero-dimensional materials, such as fullerenes, quantum dots and nanographene flakes. Fullerenes are the prototype of zero-dimensional systems. We pass commenting briefly on fullerenes to quantum dots, highlighted as promising zero-dimensional systems. Among them, we find graphene quantum dots, which are graphene-like molecules. Graphene flakes of nanometric size are interesting because of their edges. Note that saturating graphene nanoflakes edges with hydrogen atoms leads to the polycyclic aromatic hydrocarbons (PAHs).

1.2.1 Fullerenes

The term fullerene names the different carbon molecules, including different shapes such as spheres, ellipsoids or even nanotubes. Buckminsterfullerene refers to C_{60} molecule, discovered in 1985 [4]. C_{60} is formed of 20 hexagons and 12 pentagons, and recalls a football ball. The pentagons are needed adding curvature to the surface in order to close the sphere. Other fullerene molecules are C_{30} , C_{80} , C_{720} , as shown in Fig. 1.4(a).

The C_{60} molecule is not aromatic because of the combination of hexagons and pentagons. There is a rule for curved surfaces equivalent to Huckel's rule for flat surfaces, which is to have $2(n+1)^2$ delocalized electrons [13] being n an integer for being aromatic. For C_{60} fullerene the rule is not fulfilled for an integer. Fullerenes do not show superaromaticity because π electrons are localized on the double bonds between hexagons, which are slightly shorter. The C_{60} molecule is stable, preserving its shape at high pressures and temperatures [14]. Fullerenes have been proposed for several applications, such as for hydrogen storage [15], or many applications in the fields of medicine [16], and biology [17]. Doping fullerenes includes the possibility to anchor atoms or molecules inside the spherical surface. These structures are called endohedral fullerenes [18–22], and the inner atom can be a metal or a non-metal, or even small molecules. Exohedral fullerenes [23–25] present atoms or ligands bonded on the outer fullerene surface.

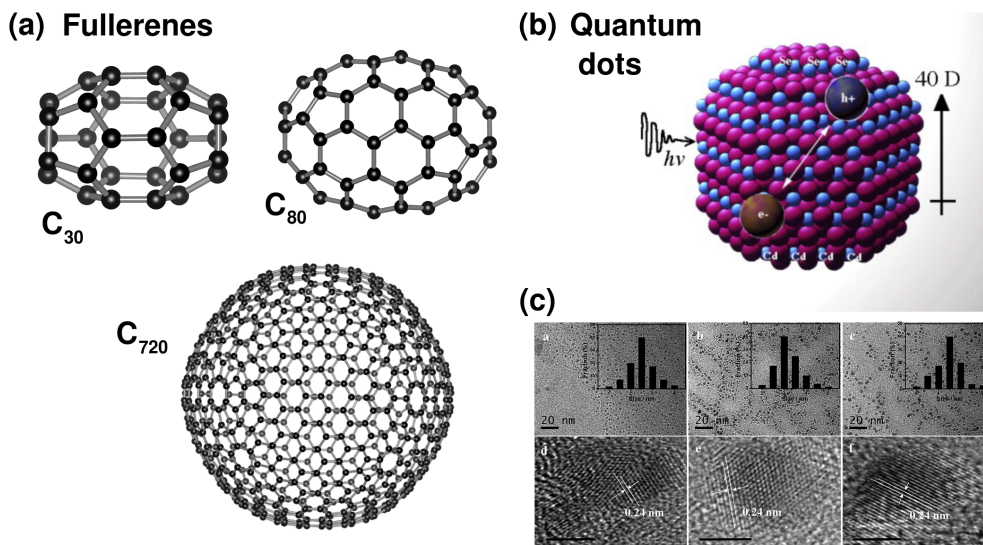


Figure 1.4: (a) Examples of fullerenes molecules. Coordinates of C_{30} , C_{80} and C_{720} obtained from <http://www.nanotube.msu.edu/fullerene/fullerene-isomers.html>. (b) Cadmium selenide quantum dot. Image reproduced from Ref. [26]. (c) Transmission electron microscopy (TEM) images of graphene quantum dots purple-blue, blue and green. Image reproduced from Ref. [27].

1.2.2 Quantum dots, graphene nanoflakes

Quantum dots are semiconductor nanoparticles with interesting electronic and optical properties. The small size of quantum dots forces the electrons and holes to be confined in bound states. So quantum dots are referred to as artificial atoms. Controlling shape and size of quantum dots is possible to modify the electronic and optical properties, such as the color of emitted light. Inorganic quantum dots are formed by an inorganic core surrounded by ligands which protect the optically active core from the external environment [28]. Different compositions have been proposed for inorganic quantum dots, including cadmium selenide [29], cadmium sulfide [30], lead sulfide [31], lead selenide [32], indium arsenide [33] and indium phosphide [34].

Graphene quantum dots usually have diameters below 20 nm, and are particularly interesting because of the confinement properties of graphene [35]. Differently from graphene, the graphene quantum dots have a non-zero band gap which depends on size [36, 37] and shape [38], allowing to control photoluminescence. One advantage of graphene quantum dots with respect to inorganic quantum dots is their low toxicity [39]. Other advantages of graphene quantum dots are the abundance of carbon, the easiness to add functional groups, and the solubility depending on these functional groups. Fabricating graphene quantum dots follows two different approaches: bottom-up and top-down. The bottom-up approach consists on the synthesis of large graphene-like molecules with well-defined structures [40, 41]. The top-down approach is based on fragmentation or cutting graphene sheets. First, a graphite material is oxidized so that graphene oxide layers are produced. Then there are different methods to cut them into quantum dots, such as hydrothermal cutting [42]. Graphene quantum dots have been proposed for a wide variety of applications [43], including optoelectronic devices such as light-emitting diodes or solar cells [44]. Graphene nanoflakes or nanosheets are graphene nanostructures with dimensions between 1 and 100 nanometers. The finite dimensions open a band gap, which enables their use for multiple applications.

1.2.3 Polycyclic aromatic hydrocarbons (PAHs)

Hydrogenation of the edges of the graphene nanoflakes leads to polycyclic aromatic hydrocarbons (PAHs). Some PAHs examples are shown in Fig. 1.5(a). The differences in cohesive energy and band gap have been thoroughly studied [45]. We have seen that PAHs are useful as models for graphene nanosheets or graphene nanoflakes. Polycyclic aromatic hydrocarbons (PAHs) are molecules formed by benzene rings, reaching different shapes and sizes. PAHs are found as by-products in combustion processes [46] as well as in the interstellar medium [47] accounting for the IR spectra. The IR spectra have been computed for some PAHs [48–50]. Because of the carbon hexagonal pattern, these molecules are like graphene flakes. In flat hexagonal configurations, carbon atoms adopt the sp^2 hybridization and show three σ covalent bonds with the three carbon neighbors. For PAHs, the carbon atoms found at the edge have two σ covalent bonds with other carbon atoms, and saturate the third σ bond with hydrogen atoms.

For the inner carbon atoms, three of the four carbon valence electrons form σ bonds

and the extra electron rests in the remaining p_z orbital. The interaction between p_z electrons makes the difference between graphene and PAHs. For graphene, π -type delocalized bonds are formed over all the surface yielding outstanding electronic properties such as the linear dispersion known as Dirac cone. The PAHs present some aromaticity but not over the whole surface, only over certain rings [51]. The Huckel's rule predicts that a molecule will be aromatic if the number of π electrons is equal to $4n + 2$, being n zero or a positive integer. The Clar structure for these molecules maximizes the number of disjoint aromatic rings, as shown in Fig. 1.5(b). As a result, the electronic structure of graphene and PAHs must present noticeable differences. For instance, the zero band gap of graphene contrasts with the large gaps of the PAHs. Indeed, the PAHs have discrete levels as a molecule, while graphene shows bands. Because of PAHs simplicity, they have been used as basic models for graphene [52–57]. In this thesis we discuss the relevance of such models.

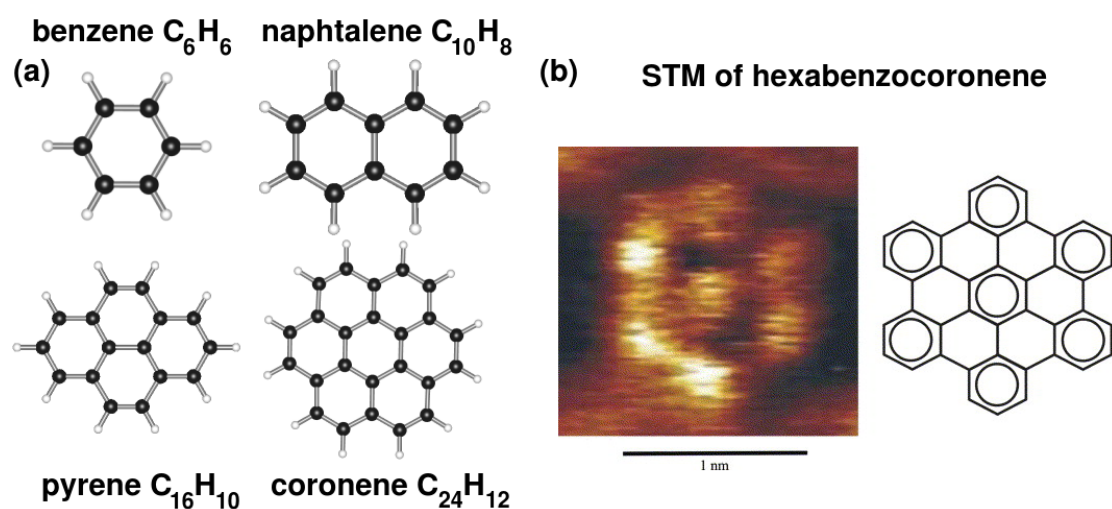


Figure 1.5: (a) Examples of polycyclic aromatic hydrocarbons. (b) Scanning tunneling microscope (STM) current-image of hexabenzocoronene and the Clar aromatic sextet formula. Image from Ref. [58].

There is a large variety of PAHs, a few examples are given in Fig. 1.5(a). In fact, the simplest case of PAH is the benzene molecule, with a single hexagon of carbon atoms saturated with hydrogen atoms. Benzene is the smallest aromatic molecule. By combining and adding benzene molecules it is possible to build larger PAHs.

Organometallics

Because PAHs are organic molecules, the study of the interaction of hydrocarbons and transition metals falls into the broad field of organometallics [12]. Organometallic compounds have been synthesized for their use in different applications [59–63]. Doping of PAHs has been largely studied [64–66]. For instance, PAHs doped with late transition

1 Introduction

metals have been proposed as ultimate memories in spintronics [67]. The interaction of iron atoms and clusters deposited on coronene has been studied theoretically [68], and experimentally by photoelectron spectroscopy [68] and mass selected laser photodissociation [69]. For the larger circumcoronene, theoretical calculations predict adsorption of iron atoms over hollow sites at the edges [70, 71]. Similarly, cobalt interacting with coronene has been studied using density functional theory (DFT) and photoelectron spectroscopy [72].

When going to the smallest PAH, like benzene, the interaction with transition metals should be examined using a different approach. Because of the small size of benzene, a small cluster of two or three transition metal atoms is comparable in size to benzene. It is possible to study theoretically a single benzene molecule with a transition metal atom over it. The interest is to determine whether hollow, top or bridge sites are preferred, apart from studying how benzene changes the magnetism of transition metal clusters. These particular results are useful for comparison with graphene doping. Normally, the same adsorption site is found over benzene and graphene, such as the hollow site for cobalt [64]. Nevertheless, it is more common to study several benzene units interacting with several transition metal (TM) atoms, TM_nBz_m with $n=1, \dots, n$ and $m=1, \dots, m$.

This particular field within organometallics experienced a great boost in the fifties of the past century because of the synthesis [73, 74] and characterization [75] of ferrocenes [76]. Ferrocene is a molecule with an iron atom sandwiched by two cyclopentadienes as shown in Fig. 1.6(a). Similar compounds with different transition metal atom were synthesized, such as cobaltocene, nickelocene [77], rhodocene [78], and manganocene [79]. The metallocene name includes all the compounds with a transition metal atom between cyclopentadienes C_5H_5 following the pattern of ferrocene. Compounds of C_5H_5 and different transition metals are still under study [80–82]. Metallocenes have been proposed for applications such as spintronics [83–85], biomedical products [86, 87], and solar cells improvement [88–90]. Although these compounds have C_5H_5 , similar results can be expected for benzene substituting cyclopentadiene. Benzene complexes with first row transition metals have been indeed studied [91–96].

A recent breakthrough in this field came with the synthesis of the first binuclear metallocene, the so-called dimetallocene (decamethyldizincocene $\text{Zn}_2(\eta^5\text{C}_5\text{Me}_5)_2$) in 2004 [98]. This complex has two zinc atoms sandwiched between two organic molecules as shown in Fig. 1.6(b). This finding opened the door to simulations with several metal atoms sandwiches by different organic molecules such as benzene or even fullerenes [99]. Calculations have been carried out for alkaline-earth dimetallocenes [100–103], transition metal dimetallocenes [51, 104, 105], heterodinuclear compounds [106, 107], and zinc isoelectronic elements such as cadmium and mercury [108]. Therefore, it has been shown experimentally that two organic molecules similar to benzene react with one or two metal atoms inside forming a stable complex.

An example of these complexes shows the metal atom covered by the two benzene-like molecules, forming a structure that recalls a sandwich. Furthermore, several structural patterns can be proposed to arrange a larger number of benzene rings and transition metal atoms. Two main structural patterns arise: sandwich-like or multiple-decker, and rice-ball or bowl-like.

(a) ferrocene (b) decamethylzincocene

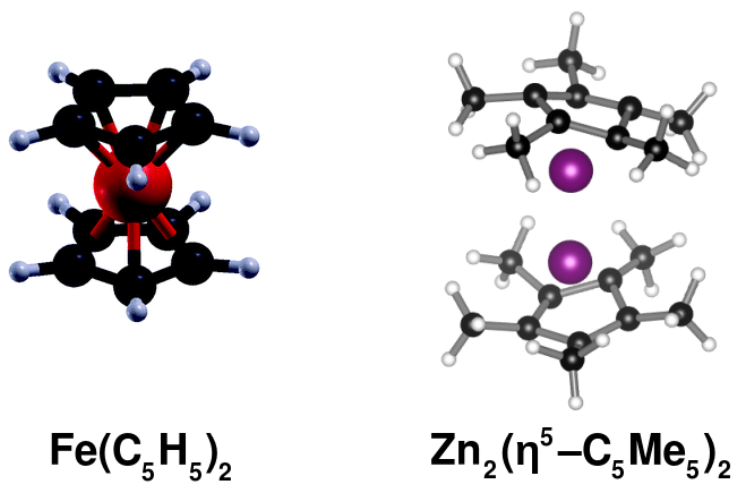


Figure 1.6: (a) Schematic representation of ferrocene. Image adapted from Ref. [97]. (b) Schematic representation of decamethylzincocene reproduced from <http://expchem3.com/mols/773895-85-5.htm>.

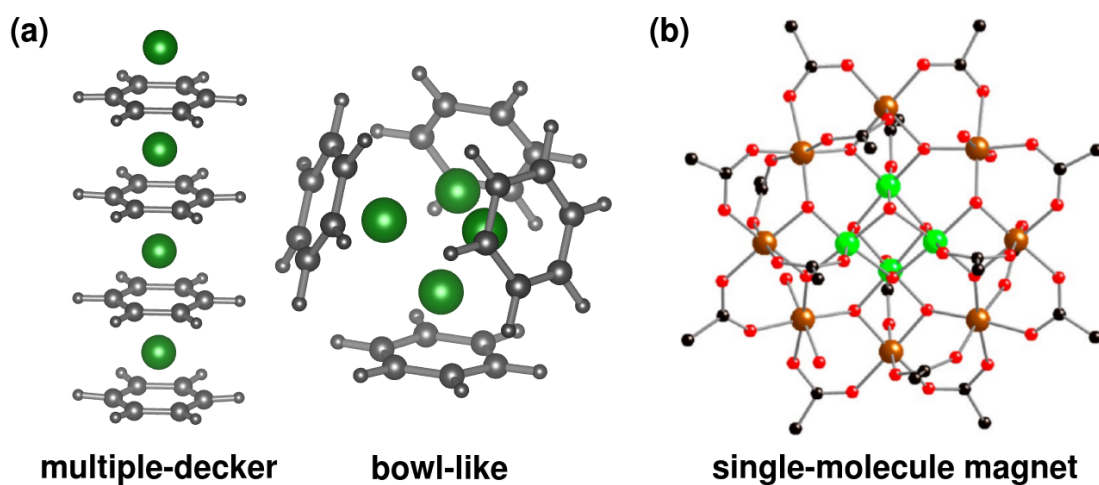


Figure 1.7: (a) Two main structural patterns for transition metals and benzene complexes. (b) Molecular structure of $[\text{Mn}_{12}\text{O}_{12}(\text{OAc})_{16}(\text{H}_2\text{O})_4]$. Color scheme: Mn(IV), green; Mn(III), brown; O, red; C, black. Image reproduced from [109].

1 Introduction

The multiple-decker structure alternates metal atoms and benzene molecules, forming a wire when the system becomes large. The bowl-like structure groups the metal atoms in the center and cover them with benzene molecules. Figure 1.7(a) includes schematic representations of these structures. Experimental works [110] have shown that early transition metals (Sc, Ti, V) prefer the multiple-decker structure, and the late transition metals (Fe, Co, Ni) prefer the bowl-like structures. The multiple-decker structures favor the benzene-transition metal interactions, and the bowl-like structures maximizes the metal-metal interactions. The relative strength between the metal-metal and metal-benzene interactions is a decisive factor in choosing the corresponding structural pattern [111].

Magnetism

The applications of organometallic compounds also consider magnetism, such as the single-molecule magnet (SMM) shown in Figure 1.7(b). The single-molecule magnets show superparamagnetic behavior below the blocking temperature. The spin relaxation time is comparable to the timescale in experiments and SMMs display magnetic hysteresis. Much is known on single-molecule magnets [112, 113], promising for fields such as spintronics [114, 115], molecular electronics [113], and quantum computing [116–118]. However, little is known on the magnetism of organometallic multimetalloenes. We comment on the two possible structures for metallocenes. For multiple-decker structures the metal atoms are normally isolated from one another and only interact with benzene molecules. There could be metal magnetic interactions induced by superexchange mechanism. When interacting with benzene, early transition metal atoms such as Sc, V and Ti enhance their magnetic moments. Other metals such as Mn, Fe and Co reduce the magnetic moments. For the nickel case, the magnetic moment is totally quenched [93]. Furthermore, transition metals yield spin injection in the carbon atoms of benzene [94].

For the bowl-like structures, three, four or more metal atoms are interacting directly between themselves. This is in contrast to SMMs in which transition metal centers are surrounded by organic compounds protecting their magnetic moment [109, 119, 120]. Thus, metallocenes have small transition metal clusters with strong exchange interactions covered by benzene molecules. These structures seem interesting for magnetism. It is known that magnetism is enhanced for small transition metal clusters [121–123]. Indeed, magnetism arises for small clusters of transition metals which are not magnetic in the bulk [124, 125]. The electronic and magnetic properties of small transition metals clusters have been largely studied in the past both theoretically [126–132] and experimentally [133, 134]. When covering these small transition metals clusters with organic molecules, such as benzene, changes in the magnetism are expected that requires further studies. In this thesis we cover this gap for some multimetalloenes considering PAHs, manganese, cobalt and nickel.

1.3 Two-dimensional materials

Nanoscience deals today with two-dimensional materials. It was believed that two-dimensional materials would be unstable because of thermal fluctuations displacing atoms far from their equilibrium positions as postulated by R. E. Peierls [135] and L. D. Landau [136]. However, isolating graphene paves the way to the two-dimensional realm. Many other two-dimensional materials have been later proposed. The growing wide variety of two-dimensional materials is expanded by stacking different monolayers mediated by van der Waals interactions as shown in Fig. 1.8. They are known as heterostructures, opening a world of possibilities to design and build materials with specific properties [137, 138].

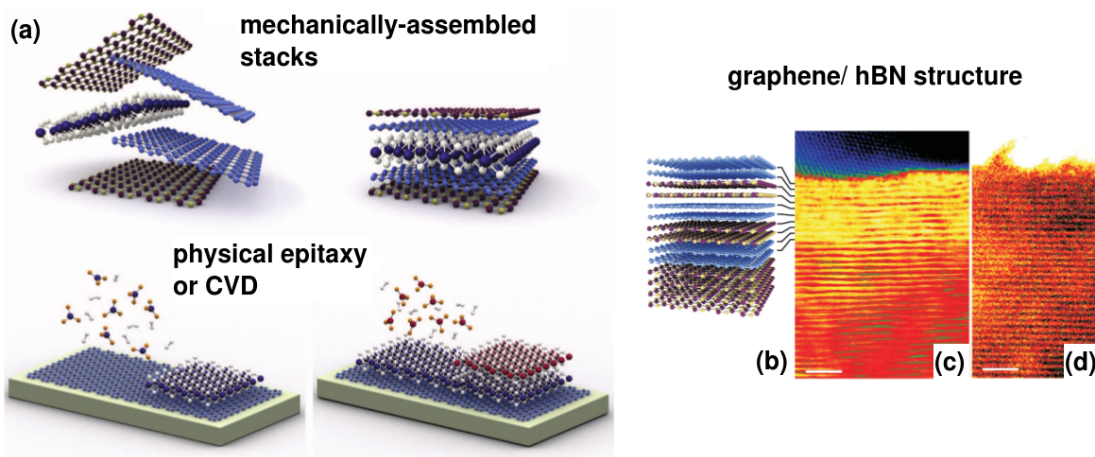


Figure 1.8: (a) Synthesis methods of van der Waals heterostructures. (b) Graphene/hBN heterostructure scheme, (c) scanning transmission electron microscopy (STEM) image, and (d) high-angle annular dark-field image. Scale bars are 2 nm. Images reproduced from Ref. [137].

1.3.1 Graphene

Graphite is formed by stacking single layers separated by more than 3.35 \AA and mediated by van der Waals forces, as shown in Fig. 1.9(a). A single layer of graphite [139] received the name of graphene. Graphene opened a novel field in the condensed matter area. Realization of two-dimensional materials was shown possible. Graphene properties were measured and shown to be promising to develop novel electronic devices, that could preserve Moore's law.

Graphene has a wide range of properties which largely outperform the best counterparts and are key for a wide variety of applications [139]. Graphene properties include high electron mobility, ballistic transport, and the quantum Hall effect [140–146]. Graphene has been proposed for electronic applications because of the high electron mobility. In graphene charge carriers behave like Dirac fermions, travelling microns at

1 Introduction

room temperature without suffering scattering. Furthermore, graphene can be easily functionalized [147, 148], interesting for electronic applications such as graphene-based transistors [149, 150].

Graphene has been proposed for spin valves [151, 152] and spintronics [153] because a single layer of graphene exhibits spin transport over micrometre-scale distances [154]. This is a consequence of the low spin-orbit interaction of carbon and the long spin coherence length of graphene [155]. Spin injection in graphene could be achieved via ferromagnetic cobalt and nickel contacts [156, 157]. Furthermore, doped graphene nanoribbons have been reported to show perfect spin filter effects [158].

A graphene drawback is the magnetism absence. However, it is possible to generate magnetism by growing nanoislands [159], nanoribbons [160] or doping it with structural defects [161]. Note that some carbon materials have been proposed to show intrinsic magnetism [162–164]. A magnetic signal has been indeed reported for graphite nodules [165], rhombohedral C_{60} [166], and schwarzite-like structures [167].

Graphene synthesis

Several methods are synthesizing graphene, each of them with advantages that propose it for some applications and drawbacks that limit its use. Graphene was first achieved by mechanical exfoliation [139]. This method is based on overcoming the weak van der Waals interactions between layers in graphite, which can be achieved applying normal or shear forces [168]. For instance, an example of normal forces methods is the Scotch tape method [139]. An alternative is the sonication method, which consists on the liquid phase exfoliation of graphite [169]. Graphene samples produced by mechanical exfoliation are appropriated for research purposes but are too small for industrial applications. Secondly, chemical vapor deposition is other widely used alternative method to synthesize graphene. Carbon precursors dissociate at high temperatures with the help of catalytic metals and are deposited over a metal substrate forming graphene. Copper [170, 171] and nickel [172, 173] are the most used substrates to synthesize graphene [174]. The role of substrates is important because it controls the growing mechanism and act as catalyst for graphene synthesis. Thirdly, other alternative is thermal decomposition of silicon carbide [175–177]. Silicon carbide wafers are heated and silicon desorbs yielding graphene samples. This technique allows to produce graphene over ribbons and other shapes using lithographic techniques. Finally, other alternative is the reduction of graphene oxide [178]. The process start with graphite, which is converted to graphite oxide using the Hummer’s method [179]. Graphite oxide is hydrophilic and the separation between layers is larger because of ligands, which favor its dispersion in water using sonication, obtaining graphene oxide. Graphene oxide is an electrical insulator because the sp^2 bonding network is disrupted [180]. Then, graphene oxide is electrochemically reduced in order to remove the organic ligands. Graphene samples produced with this technique shows lower quality concerning properties such as electron mobility.

Electronic structure of graphene

The electronic structure of graphene is key to understand its outstanding properties. Graphene is formed by a hexagonal pattern of carbon atoms, with a distance of 1.42 Å between neighbors. Each carbon atom has four valence electrons, three of them forming σ bonds with the three carbon neighbors and the other in the remaining p_z orbital. The p_z electrons form a π band delocalized over the surface. There is no strong coupling between in-plane electrons (σ bonds) and out-of-plane electrons (π bonds), which means it is reasonable to study graphene using a tight binding model with the p_z electrons [140]. The band theory of graphite can be analyzed near the Fermi energy using a tight binding model [181]. Figure 1.9(b) shows the unit cell of graphene, which has two carbon atoms. The lattice vectors are $\vec{a}_1 = \frac{a}{2}(3, \sqrt{3})$ and $\vec{a}_2 = \frac{a}{2}(3, -\sqrt{3})$. The reciprocal lattice vectors shown in Fig. 1.9(c) are $\vec{b}_1 = \frac{2\pi}{3a}(1, \sqrt{3})$ and $\vec{b}_2 = \frac{2\pi}{3a}(1, -\sqrt{3})$.

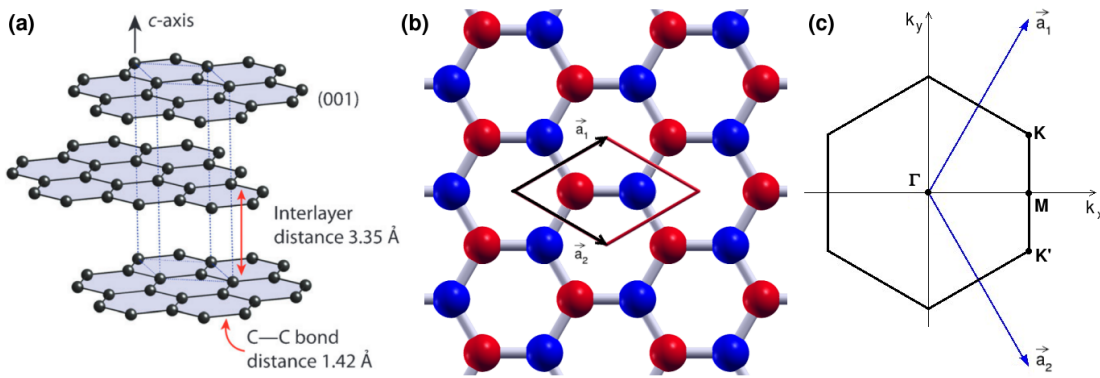


Figure 1.9: (a) Graphite including geometrical parameters. Image reproduced from Ref. [182]. (b) Hexagonal lattice, using red and blue colors for the two different sublattices. (c) Brillouin zone of graphene, with the reciprocal vectors and the high symmetry points.

The tight binding Hamiltonian considering first neighbors interactions is

$$H = -t \sum_{\langle i,j \rangle, \sigma} (a_{\sigma,i}^\dagger b_{\sigma,i}^\dagger + h.c.) \quad (1.1)$$

where $a_{\sigma,i}$ and $a_{\sigma,i}^\dagger$ annihilates and creates an electron with spin σ on site \mathbf{R}_i on sublattice A. The same definition is used for sublattice B. The hopping parameter between nearest neighbors (different sublattices) is about 2.8 eV.

The energy bands of this Hamiltonian are obtained as

$$E_{\pm}(\mathbf{k}) = \pm t \sqrt{3 + 2\cos(\sqrt{3}k_y a) + 4\cos\left(\sqrt{\frac{3}{2}}k_y a\right)\cos\left(\frac{3}{2}k_x a\right)} \quad (1.2)$$

There are positive and negative signs applying to the bonding and antibonding π bands. These bands are symmetric at this level of approximation. Figure 1.10 shows the bands

1 Introduction

obtained in this tight binding model. It is interesting to look in detail at the bands close to the K and K' points in the Brillouin zone. If we expand the bands dispersion around the K point using $\mathbf{k} = \mathbf{K} + \mathbf{q}$ with $\mathbf{q} \ll \mathbf{K}$ we obtain

$$E_{\pm}(\mathbf{q}) \approx \pm v_F |q| \quad (1.3)$$

where v_F is the Fermi velocity $v_F = 3ta/2$ which is approximately 10^6 m/s. For metals the dispersion is quadratic in q , which means that the velocity depends on the energy and momentum. However, the carrier velocity for graphene is constant. There are two opposed cones on the K and K' points, which are called the Dirac cones and points. This behavior had been previously reported for relativistic massless particles. Graphene is a zero band gap semiconductor because the Dirac cones just touch at the Fermi energy.

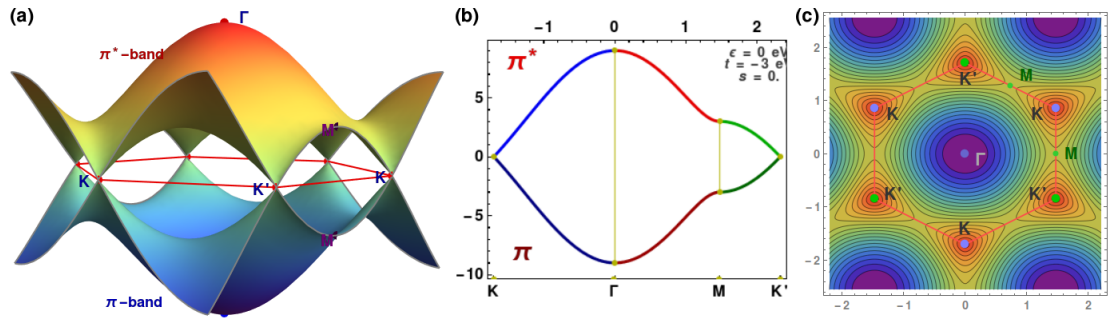


Figure 1.10: (a) 3D view, (b) 2D view and (c) contour plots of graphene bands. The three images were obtained within the tight-binding model implemented in Mathematica [183].

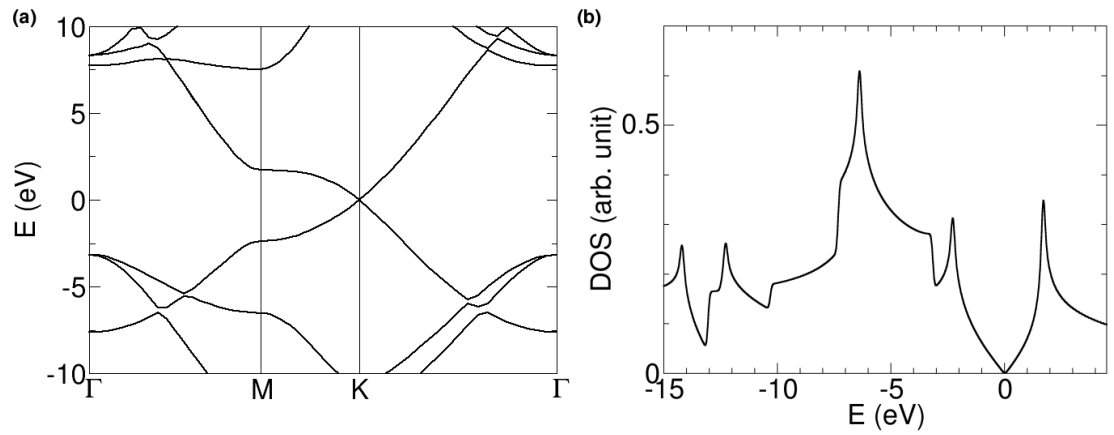


Figure 1.11: (a) Band structure of graphene and (b) density of states of graphene obtained using the SIESTA method.

Although the tight-binding model describes important features of graphene, more accurate results are obtained using density functional theory (DFT) calculations. We

have carried out DFT calculations of graphene using the SIESTA method. Figure 1.11 shows the band structure and the density of states of graphene. The band structure presents the Dirac cone, as the tight-binding model. However, the π and π^* bands symmetry is lost because valence bands are occupied. The density of states for graphene has Van Hove singularities agreeing with Ref. [184].

Graphene defects and doping

Research about doping and functionalizing graphene to improve its properties is done overcoming some drawbacks such as the absence of a band gap, or to tune the properties for applications. For instance, adsorption of transition metal atoms [185] and clusters [186, 187] is suggested for graphene magnetism because of their localized magnetic moments. It is important to remark that the electronic properties commented above correspond to a single layer graphene. When carrying out theoretical calculations it is straightforward to calculate pristine graphene. However, experiments deal with defective graphene. Defects can be classified into intrinsic and extrinsic character.

Intrinsic defects imply changes in the hexagonal lattice and include vacancies, divacancies, dislocations, Stone-wales defects, and domain defects. Figure 1.12 shows examples of some intrinsic defects. Defects are related to magnetism as revealed by STM experiments with the presence of states close to the Fermi energy [188, 189]. The magnetism induced by a vacancy could vary because of an applied strain [190]. Vacancies in graphene lead to magnetism.

There could be coupling between the defects leading to long-range ferromagnetic or antiferromagnetic magnetic order depending on the sublattice defect. Graphene samples from graphene oxide have been reported to produce a weak ferromagnetic signal at room temperature [191]. There is no consensus about the coupling of defects. On one hand, an experiment has shown that there is no ferromagnetic interaction between defects, agreeing with reported calculations [192]. On the other hand, nanographenes exhibit local magnetic states [164] because of their zigzag edges [159, 193–195] for straight edges of more than three zigzag units [196].

Intrinsic defects are present in graphene samples because of the imperfect process of synthesis, changing the electronic properties. The presence of undesired defects drastically reduces the sample quality, spoiling their properties. Because these defects arise spontaneously and must be avoided to obtain high quality graphene samples, large computational efforts have been dedicated to study them [197–206]. They are usually studied using graphene supercells, that consider each defect separately or combined with others at different concentrations. Depending on the synthesis method, there can be also extrinsic defects on graphene. For instance, organic compounds remain bonded to graphene when following the synthesis route of graphite oxide.

Previously we have commented on non-desired defects, which spoil the quality of the samples. However, it is possible to add defects to graphene with the aim of adjusting certain graphene properties. This is achieved by intrinsic and extrinsic defects. Extrinsic defects include chemical functionalization with different organic molecules, adsorption of carbon or metal atoms as shown in Fig. 1.13(a), and transition metal clusters and

1 Introduction

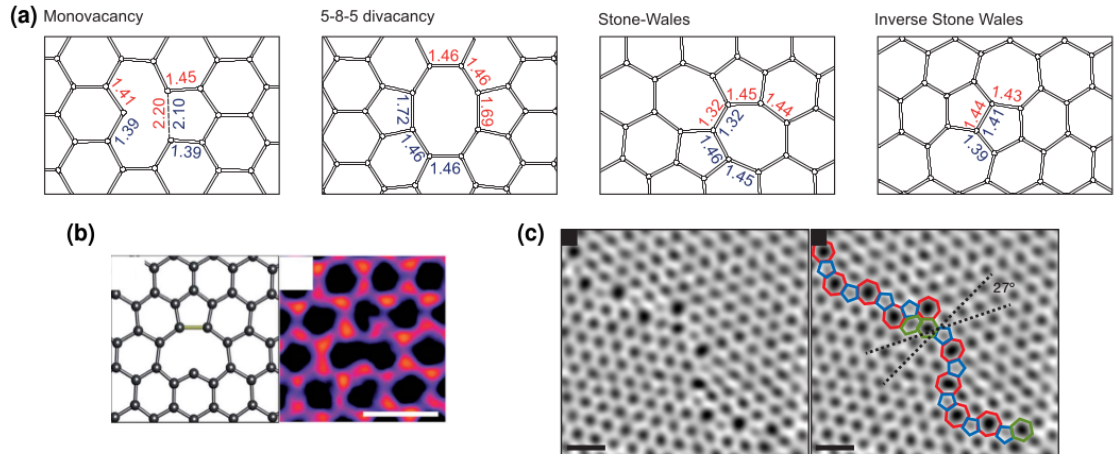


Figure 1.12: (a) Some intrinsic defects, including the distances between carbon atoms. Image reproduced from Ref. [197]. (b) Atomic resolution aberration-corrected transmission electron microscopy (AC-TEM) image of a reconstructed monovacancy. AC-TEM image scale bar is 0.5 nm. Image reproduced from Ref. [198]. (c) Atomic-resolution annular dark-field scanning transmission electron microscope (ADF-STEM) image of two grain boundaries (bottom left, top right) intersect with a 27° relative rotation. An aperiodic line of defects stitches the two grains together, with pentagons (blue), heptagons (red), and distorted hexagons (green), forming the outlined grain boundary. Scale bar is 5 Å. Image reproduced from Ref. [199].

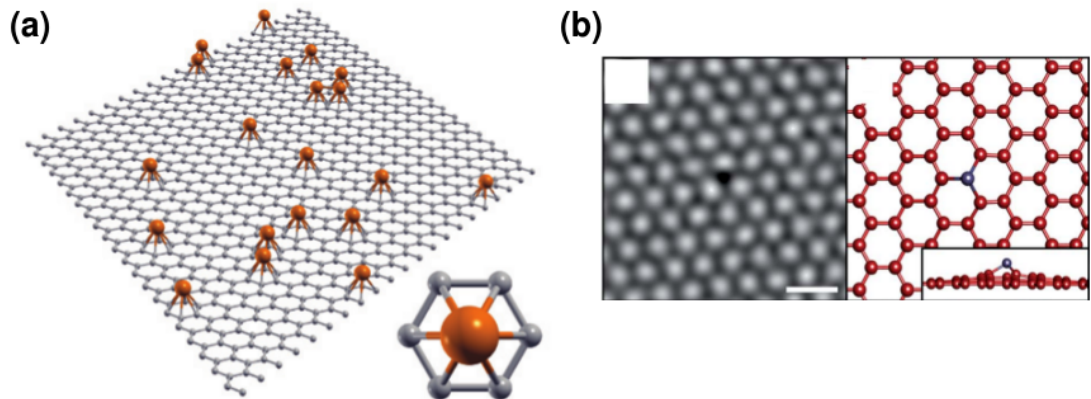


Figure 1.13: (a) Adatoms scattered over graphene. Image reproduced from Ref. [207]. (b) aberration-corrected transmission electron microscopy (AC-TEM) image of an iron atom dopant substitution in graphene and theoretical geometry of the substitutional defect. Inset shows a side view. Image reproduced from Ref. [198].

substitutional impurities among others. The adatoms and substitutional impurities can be placed on vacancies and divacancies [208]. The carbon adatoms have been reported to produce localized magnetic moment [209]. Research works have been done on the interaction of transition metal atoms with graphene [210, 211] and graphene nanoribbons [212, 213]. Adatoms adsorption includes osmium and iridium to open a giant insulator topological gap in graphene [214], or gold to enhance spin-orbit splitting of π bands [215]. Nevertheless, graphene doping with adatoms is not restricted to transition metals, as shown by the study of hydrogen atoms [161, 216–218] and second period atoms [219, 220] interacting with graphene.

$3d$, $4d$ and $5d$ adatoms on graphene have been studied experimentally [221, 222]. The experimental procedure to create an extrinsic defect such as a substitutional impurity, requires to create vacancies by irradiation as trapping centers for foreign atoms [223, 224]. Irradiation of nanostructures is a helpful tool to create vacancies that tailor electronic properties [225]. Defective graphene is characterized using Raman spectroscopy, a useful tool to determine the presence of defects [226]. An alternative is the use of x-ray absorption fine structure (XAFS), reported to study nickel atoms trapped in graphene [227].

Transition metals are used in different ways doping graphene. A reason for using transition metals is their inherent magnetism, which is useful to induce magnetism on graphene for spintronics applications.

Substitutional impurities

Extrinsic defects are substitutional impurities that occur when a carbon atom is removed from the hexagonal lattice, and its place is occupied by another atom different from carbon as shown in Fig. 1.13(b). Single vacancies suffer structural distortions reconstructing the surface to a lower energy geometry.

$3d$ transition metals are candidates as substitutionals in single vacancies. Because of their larger size compared with carbon, substitutional atoms are located at certain height over the surface, sometimes preserving the C_{3h} symmetry of the non-relaxed vacancy. $3d$ transition metal substitutionals have also been thoroughly studied proposing a simple model to explain bonding and magnetism [228, 229]. However, a study of $4d$ and $5d$ substitutional impurities lacks behind, and in this thesis we cover this gap.

Cluster adsorption

Transition metal clusters deposited over graphene have also been studied as a way to tailor its properties [186, 187]. Specifically, clusters of $3d$ transition metals are candidates for magnetic applications. For instance, magnetic nanoparticles have been proposed as magnetic bits [230], and a cobalt dimer over benzene was proposed as a basic unit for magnetic data storage [67]. The interest on transition metals clusters comes from their unexpected electronic and magnetic properties, which are a consequence of the quantum phenomena arising because of the small size. Thus, it is interesting to study the bonding between itinerant d electrons and delocalized p electrons.

1 Introduction

Many computational works have been done on the adsorption of transition metal atoms [231–233] and clusters [234–236] on graphene and nanoribbons [212]. Atom adsorption occurs over pristine graphene at three different sites: hollow, top and bridge. However, defects on graphene also arises as potentially preferred adsorption sites to anchor atoms. Defective graphene interacting with metal clusters has been studied, such as for platinum [237, 238], iron or aluminium [239], ruthenium [240], and gold [241]. There has also been an intense study of transition metals cluster and alloys, including platinum and palladium, deposited over pristine and defective graphene [242–250]. Similarly, experimental works have been reported on the interaction of transition metals with graphene [185, 251–258]. Furthermore, two-dimensional cobalt structures grown between graphene layers have been reported [259]. Although many works have been done, the bonding between graphene and transition metal clusters still lacks understanding. In this thesis we study thoroughly how Co_{13} clusters bind graphene.

1.3.2 Phosphorene

Graphene is a novel material with outstanding properties that suggests its use for many applications. However, graphene has drawbacks difficult to overcome: although a band gap can be opened in graphene by doping, some of its desired properties are lost. The impressive electronic, optical and mechanical properties of graphene [140, 141, 145, 146, 260, 261] developed experimental techniques to produce, analyze and deal with two-dimensional materials, searching for other two-dimensional materials. Research today is focused not only on other carbon nanostructured materials but on other two-dimensional materials [262]. The need for novel materials that solve the drawbacks of graphene, the existence of advanced experimental techniques [263–265] and the excitement for the novel unexplored realm explain the ongoing search for new two-dimensional materials. In addition, efficient and fast electronic structure codes explain the proliferation of theoretically predicted novel two-dimensional materials, some of them already synthesized experimentally.

Phosphorus is found in several different allotropic structures: mainly white and red, but also black, violet and blue phosphorus [268–271]. Black phosphorus is formed by single layers mediated by van der Waals interaction. Analogously to graphene, few layers have been isolated to form phosphorene [266, 272]. Phosphorene is noticeably different from graphene, displaying a puckered structure with two different heights of phosphorus atoms. Each phosphorus atom is bonded to three phosphorus atoms as the carbon atoms in graphene. However, there are two equal bonds and one different, while graphene has three equal bonds. Phosphorene unit cell is rectangular as shown in Fig. 1.14(c). Because of its structure, phosphorene presents improved mechanical flexibility [273]. While graphene is isotropic, phosphorene presents anisotropy as revealed by electronic transport properties in Fig.1.15(d). Each phosphorus atom has five valence electrons and three of them form covalent bonds with phosphorus neighbors. The other two electrons form a dangling bond in a sp^3 hybridized phosphorus atom [274].

Phosphorene shows high carrier mobility, anisotropic electronic properties because of its structure, and a direct band gap that depends on thickness [275], which reveals a

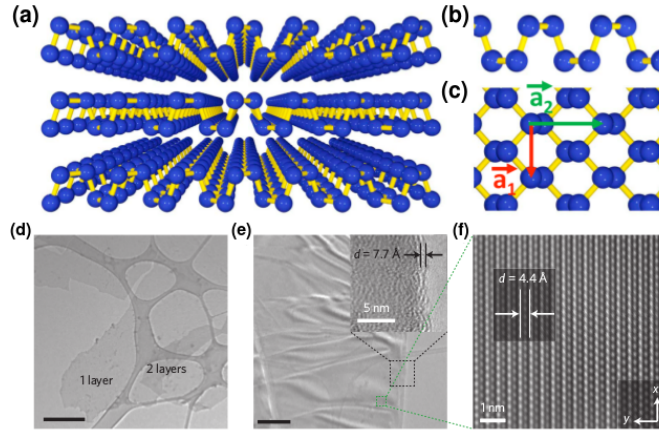


Figure 1.14: (a)-(c) Phosphorene structure reproduced from Ref. [266]. (d) Transmission electron microscopy (TEM) image of monolayer phosphorene, with a scale bar of $2 \mu\text{m}$. (e) TEM image of trilayer phosphorene nanobelt showing the long side. Scale bar is 200 nm . Inset: HRTEM image of the edge. (f) High-resolution transmission electron microscopy (HRTEM) image of selected area of (e) with measured lattice spacing. Images (d), (e) and (f) reproduced from Ref. [267].

promising material for novel electronic devices such as field-effect transistors [276, 277]. The band gap is an advantage comparing with graphene, and phosphorene can be used for switching on/off devices. Besides, the band gap size can be controlled by the number of black phosphorus layers [275] or by the stacking as reported for phosphorene bilayers [278] without spoiling the electronic properties as it happens for graphene.

Nevertheless, phosphorene suffers fast degradation in contact with air [279, 280]. Phosphorene has a dangling bond on each phosphorus atom which reacts with oxygen in air spoiling phosphorene properties [281], so it is required to passivate the surface against ambient degradation [279]. The dangling bonds allow phosphorene to show strong bonds with metal adatoms without suffering large structural distortions [282]. Similarly, molecules are adsorbed on phosphorene by charge transfer, producing changes in the electronic transport, which enables it to be used as a gas sensor [283]. Following graphene family, other low dimensional phosphorene nanostructures have been reported such as nanoribbons and nanotubes [284–286].

1.3.3 Isoelectronic compounds to graphene and phosphorene

A solid and fruitful way to design novel two-dimensional materials consists on using well-known structures, such as graphene and phosphorene, as models and try to replicate them. Replication implies starting structural relaxations from the model system geometry and having the same number of valence electrons. This process is called transmutation. We next comment on the successful application of these ideas to graphene

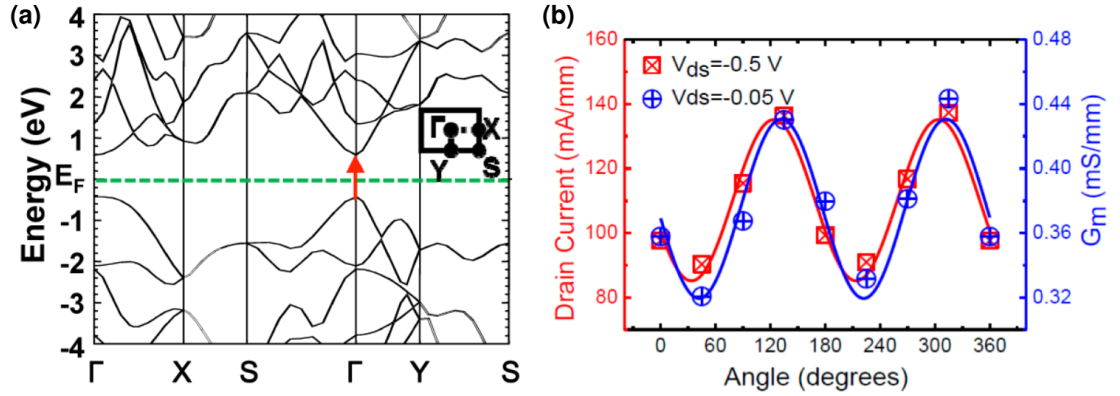


Figure 1.15: (a) Theoretical band structure of a single layer of black phosphorus or phosphorene. (b) Transport properties of phosphorene: angular dependence of the drain current and the conductance of a device with a film thickness of 10 nm. Figures reproduced from Ref. [266].

and phosphorene.

Different approaches can be followed to obtain isoelectronic compounds. The first approach substitutes an element by other within the same periodic table group. The second approach is similar but it combines two elements of the same group. Finally, the third approach combines one element from the previous group and other from the next group. The three approaches ensure the same number of valence electrons. We here cover the isoelectronics design for graphene and phosphorene. Figure 1.16 summarizes the three approaches, using colors green, orange and blue for the first, second and third approaches, respectively.

Graphene isoelectronics

Following the first approach to get isoelectronic compounds, materials such as silicene, germanene and stanene have been synthesized [287–290]. Differently to graphene, silicene has a buckled structure [291, 292]. Consequently, silicene shows higher reactivity and a more easily tunable gap by surface adsorption [293, 294]. These differences arise because silicon, germanium and tin prefer the sp^3 hybridization, in agreement with the double bond rule [295–297], which state that double bonds are not found for elements in the third period such as silicon.

The second approach yields compounds such as silicon carbide [298]. Structures similar to graphene and graphane [299] composed of the group IV elements have been studied [300]. The third approach combining the II-IV group elements leads to boron nitride. Boron nitride nanotubes were proposed and synthesized [301] and hexagonal boron nitride single layers were exfoliated from a bulk phase [302]. An advantage of boron nitride with respect to graphene is that the different potential of boron and nitride opens a band gap of more than 5 eV [303, 304], being a promising dielectric with the adsorption peak

in the ultraviolet [305].

graphene isoelectronics

5 B Boron 11	6 C Carbon 12	7 N Nitrogen 14
13 Al Aluminum 27	14 Si Silicon 28	15 P Phosphorus 31
31 Ga Gallium 70	32 Ge Germanium 73	33 As Arsenic 75
48 In Indium 115	50 Sn Tin 119	51 Sb Antimony 122
81 Tl Thallium 204	82 Pb Lead 207	83 Bi Bismuth 209

**silicene,
germanene,
stanene**
SiC, GeC, ...
BN, ...

phosphorene isoelectronics

6 C Carbon 12	7 N Nitrogen 14	8 O Oxygen 16
14 Si Silicon 28	15 P Phosphorus 31	16 S Sulfur 32
32 Ge Germanium 73	33 As Arsenic 75	34 Se Selenium 79
50 Sn Tin 119	51 Sb Antimony 122	52 Te Tellurium 128
82 Pb Lead 207	83 Bi Bismuth 209	84 Po Polonium 210

**arsenene,
antimonene**
AsP, ...
SiS, GeSe, ...

Figure 1.16: Groups of the periodic table shown to illustrate the three approaches to obtain isoelectronic compounds to graphene and phosphorene. Side names collect some isoelectronic compounds taken as examples.

Phosphorene isoelectronics

Phosphorene has a large variety of isoelectronic compounds. First, using elements of phosphorus group such as nitrogen, arsenic and antimony, monolayers known as nitrogene, arsenene and antimonene has been reported [306–308]. Then, combining elements of phosphorus group it is possible to build binary compounds materials as AsP and SbP [309]. Those materials are being characterized by the study of doping [310], point defects [310, 311], and oxygen contamination [312]. Finally, the last approach to obtain more phosphorene isoelectronic compounds consists on using elements from carbon and oxygen groups, groups IV-VI, such as GeSn, SnSe among many others. This approach follows the path opened by boron nitride with respect to graphene. Compounds of the IV-VI groups, also called Group IV monochalcogenides [313–316], are reported to be semiconductors with band gaps larger than those in the bulk phase [317]. Combinations of light elements have been reported such as silicon monosulfide monolayers and thin films [318, 319], but also heavy (Ge,Sn) and light (O,S) elements [320]. A strain tunable indirect band gap has been reported for silicon telluride [321] and germanium monosulfide [322] monolayers.

The common approach when designing phosphorene isoelectronic compounds consists on keeping the same structure as phosphorene. However, other phases with different geometries are competing in stability. These phases with different geometries widen

1 Introduction

even more the two-dimensional materials alternative or complementary to graphene. Each element has its preferences about hybridization or coordination, which explain the stability order between phosphorene-like and other possible geometries. In this thesis we study two different isoelectronic compounds to phosphorene, silicon monosulfide and carbon monosulfide monolayers. We study the stability and electronic properties for several phases of these compounds.

2 Methods

2.1 Many-body equation

Materials electronic structure requires understanding the interactions that are present and including them in system model. Matter is composed of atoms, which have protons and neutrons in the nuclei and electrons around them. There exists four different interactions in the universe: gravitational, electromagnetic, strong nuclear and weak nuclear. To study the electronic structure the electromagnetic interaction is the leading term. As neutrons have no net electric charge, we limit the interactions to electron and protons. The hamiltonian that accounts for the interactions between electrons and nuclei is given as

$$\hat{H} = -\frac{\hbar^2}{2m_e} \sum_i \nabla_i^2 + \sum_{i,I} \frac{Z_I e^2}{|\mathbf{r}_i - \mathbf{R}_I|} + \frac{1}{2} \sum_{i \neq j} \frac{e^2}{|\mathbf{r}_i - \mathbf{r}_j|} - \sum_I \frac{\hbar^2}{2M_I} \nabla_I^2 + \frac{1}{2} \sum_{I \neq J} \frac{Z_I Z_J e^2}{|\mathbf{R}_I - \mathbf{R}_J|}, \quad (2.1)$$

where the first and the fourth terms represent the kinetic energies of the electrons and nuclei, respectively, and the rest of the terms represent the Coulomb interaction between electron-nuclei, electron-electron and nuclei-nuclei. The time-dependent Schrödinger equation is

$$i\hbar \frac{d\Psi(\{\mathbf{r}_i\}; t)}{dt} = \hat{H}\Psi(\{\mathbf{r}_i\}; t), \quad (2.2)$$

and the time-independent Schrödinger equation is

$$\hat{H} |\Psi\rangle = E |\Psi\rangle. \quad (2.3)$$

Solving the time-independent Schrödinger equation including the nuclei and electron coordinates requires too many variables. However, the Born-Oppenheimer approximation allows to simplify the equations by decoupling the electron and nuclei movement. The Born-Oppenheimer approximation consists on two steps. In the first step, the kinetic energy of the nuclei, $\sum_I \frac{\hbar^2}{2M_I} \nabla_I^2$, is neglected. This term is much smaller than others due to the large mass of the nuclei compared with the electron mass. The interaction of the electrons with the nuclei is not removed, the electrons move in the fixed external potential created by the nuclei and the other electrons. The hamiltonian can be rewritten as

$$\hat{H} = \hat{T} + \hat{V}_{ext} + \hat{V}_{int} + E_{II}, \quad (2.4)$$

where \hat{T} is the kinetic energy of electrons, \hat{V}_{ext} is the nuclei-electron interaction, \hat{V}_{int} is the electron-electron interaction and E_{II} is the nuclei-nuclei interaction, which is fixed once the nuclei positions are specified. The Hamiltonian is solved yielding the energy

2 Methods

eigenvalues, which depends on the nuclei coordinates. The nuclei coordinates could be considered as parameters. The potential energy surface of the system is obtained by computing the electronic energy eigenvalue E_e for different nuclei coordinates. In the second step of the Born-Oppenheimer approximation the nuclear motion $\phi(\mathbf{R})$ is solved. The Schrödinger equation for the nuclear motion, which includes the kinetic energy of the nuclei T_{nuclei} and the electronic eigenvalues $E_e(\mathbf{R})$ as a potential, is

$$(T_{nuclei} + E_e(\mathbf{R}))\phi(\mathbf{R}) = E\phi(\mathbf{R}) , \quad (2.5)$$

where E is the total energy. Nuclei are in equilibrium when the forces are zero.

The interaction between electrons is the most difficult part to solve. Another step towards solution of the equations is the independent-electron approximation, which consider electrons as non-interacting. The electrons move under an effective potential that accounts for all the effects. The difficulty is to design the effective potential. The interaction between electrons yield two terms called exchange and correlation. The exchange interaction is the result of the Pauli exclusion principle and the correlation accounts for the rest of the many-body electron interaction not included in the Coulomb and exchange terms. The correlation energy can also be defined as the difference between exact solution of non-relativistic Schrödinger equation and the Hartree-Fock limit. Hartree-Fock approximation includes exchange but not correlation. For Density Functional Theory (DFT) calculations using the Kohn-Sham ansatz, apart from the exchange and correlation, the exchange correlation energy term also incorporates part of the kinetic energy not included in the independent particle kinetic energy.

2.2 Density functional theory

The density functional theory [323] was designed for large correlated many-body systems. It works with the density instead of the many-body wave functions. The main assumption is that any property of many interacting particles can be represented as a functional of the ground state density. The proofs for that idea are the Hohenberg and Kohn theorems reported in 1964. The hamiltonian representing the system of interacting particles in an external potential would be

$$\hat{H} = -\frac{\hbar^2}{2m_e} \sum_i \nabla_i^2 + \sum_i V_{ext}(\mathbf{r}_i) + \frac{1}{2} \sum_{i \neq j} \frac{e^2}{|\mathbf{r}_i - \mathbf{r}_j|} . \quad (2.6)$$

The first theorem states that for any system of interacting particles in an external potential V_{ext} , the potential V_{ext} is determined uniquely, except for a constant, by the ground state density $n_0(\mathbf{r})$. As V_{ext} defines the hamiltonian and the hamiltonian sets the many-body wave functions, all the properties are determined if the ground state density is given. The second theorem states that there is a universal functional $E[n]$ for the energy in terms of the density $n(\mathbf{r})$, valid for any V_{ext} . For any external potential V_{ext} , the exact ground state energy of the system is the global minimum value of this functional, and the density $n(\mathbf{r})$ that minimizes the functional is the exact ground state

density $n_0(\mathbf{r})$. Therefore, the functional alone is enough to determine the exact ground state energy and density.

Nevertheless, the functional expression remained unknown. Previously Thomas and Fermi proposed an equation with the kinetic energy approximated as a density functional. A practical way to advance searching for a solution is the Kohn-Sham ansatz. The ansatz consists in substituting the many-body problem with an independent-particle problem that eases the numerical solution. The independent-particle auxiliary system has the same density as that of the ground state density of the original interacting system. The advantage is that the auxiliary system allows to include all the difficult many-body terms in the exchange-correlation functional. The results would be exact when the exact functional expression was known. The calculation accuracy depends on the exchange-correlation functional. The auxiliary hamiltonian includes a kinetic operator and an effective local potential $V_{eff}^\sigma(\mathbf{r})$ acting on an electron of spin σ at point \mathbf{r} . In atomic units ($\hbar = m_e = e = 4\pi/\epsilon_0 = 1$) the auxiliary hamiltonian is expressed as

$$\hat{H}_{aux}^\sigma = -\frac{1}{2}\nabla^2 + V^\sigma(\mathbf{r}) . \quad (2.7)$$

The density of the auxiliary system is computed as the sum of squares of the orbitals for each spin

$$n(\mathbf{r}) = \sum_{\sigma} n(\mathbf{r}, \sigma) = \sum_{\sigma} \sum_{i=1}^{N^\sigma} |\phi_i^\sigma(\mathbf{r})|^2 . \quad (2.8)$$

The ground state energy functional within the Kohn-Sham approach can be written as

$$E_{KS} = T_s[n] + \int d\mathbf{r} V_{ext}(\mathbf{r})n(\mathbf{r}) + E_{Hartree}[n] + E_{I,I} + E_{XC}[n] , \quad (2.9)$$

where the first term is the independent-particle kinetic energy. The Hartree energy represents the classical Coulomb interaction

$$E_{Hartree} = \frac{1}{2} \int d^3r \int d^3r' \frac{n(\mathbf{r})n(\mathbf{r}')}{|\mathbf{r} - \mathbf{r}'|} . \quad (2.10)$$

The kinetic energy part related to the many-body interactions is included in the E_{XC} term.

2.2.1 Kohn-Sham equations

Kohn-Sham equations can be written as a Schrödinger-like equation as

$$(\hat{H}_{KS}^\sigma - \epsilon_i^\sigma)\phi_i^\sigma(\mathbf{r}) = 0 , \quad (2.11)$$

where ϵ are the eigenvalues and H_{KS} is the effective hamiltonian, which expression is

$$\hat{H}_{KS}^\sigma(\mathbf{r}) = -\frac{1}{2}\nabla^2 + V_{KS}^\sigma\mathbf{r} , \quad (2.12)$$

2 Methods

with

$$V_{KS}^\sigma(\mathbf{r}) = V_{ext}(\mathbf{r}) + V_{Hartree}(\mathbf{r}) + V_{XC}^\sigma(\mathbf{r}) . \quad (2.13)$$

The solution of the Kohn-Sham equations is a problem of minimization with respect to the density or the effective potential. The self-consistent process to solve the Kohn-Sham equations starts with an initial guess density. The density determines the effective potential and then the Kohn-Sham equations are solved. The output density is computed and compared with the initial density. The process is finished when the input and output densities differ by less than a specified value given as tolerance. If the difference is larger than the tolerance the output density is used as the input density to build a new effective potential and solve the Kohn-Sham equations again. The process is repeated iteratively until convergence.

The input density on each iteration is not chosen directly from the output density of the previous iteration. The reason is that convergence to the minimum requires softer variations of the input density. For instance, the linear mixing approach has the input density for step $i + 1$ is computed as $n_{i+1}^{in} = \alpha n_i^{out} + (1 - \alpha)n_i^{in}$, where α is the key parameter to achieve convergence. There are other approaches such as Broyden or Pulay mixings. In the SIESTA calculations for this thesis we use the Pulay mixing [324, 325], which has memory from previous iterations. In the SIESTA method using the Pulay mixing the input density is computed as $n_{i+1}^{in} = \alpha n_{-i}^{out} + (1 - \alpha)n_{-i}^{in}$, where n_{-i}^{out} and n_{-i}^{in} are constructed from previous cycles. We use values of around 0.05-0.1 for the mixing weight α , although smaller values are also required at times to help convergence for some magnetic systems.

2.2.2 Functionals

The exact exchange-correlation functional of the Kohn-Sham equations is not known. However, there are several approximations to functionals, either local or non-local. By subtracting the independent particle kinetic energy and the long-range Hartree terms, the rest of the exchange-correlation can be reasonably approximated by local functionals.

The local spin density approximation (LSDA) approximates the exchange correlation energy as an integral over all space with the exchange correlation density at each point assumed to be the same as for a homogeneous electron gas with that density

$$E_{XC}^{LSDA}[n^\uparrow, n^\downarrow] = \int d^3r n(\mathbf{r}) \epsilon_{XC}^{hom}(n^\uparrow(\mathbf{r}), n^\downarrow(\mathbf{r})) , \quad (2.14)$$

where ϵ_{XC} is the exchange-correlation energy density of the homogeneous electron gas, and n^\uparrow and n^\downarrow are the spin densities $\sigma = \uparrow, \downarrow$. This approximation usually works correctly for most solids because they can be considered close to the limit of the homogeneous gas electron, where all the exchange and correlation effects have local character. Calculations using LDA functionals yields systematic errors, underestimating the bond lengths and overestimating the bonding energies [326, 327].

The generalized gradient approximation (GGA) is an extension of the local density approximation that improves results reaching chemical accuracy. GGA considers the

variation of the density at each point by including its gradient ∇n^σ , apart from the density itself

$$E_{XC}^{GGA}[n^\uparrow, n^\downarrow] = \int d^3r n(\mathbf{r}) \epsilon_{XC}(n^\uparrow, n^\downarrow, \nabla n^\uparrow, \nabla n^\downarrow), \quad (2.15)$$

where ∇n^\uparrow and ∇n^\downarrow are the spin densities gradients. Both the LDA and the GGA functionals underestimate the band gaps [328, 329]. We mainly use both LDA and GGA for our DFT calculations in this thesis.

2.3 The SIESTA method

Based on the Density Functional Theory (DFT), plenty of computational methods let the user study the electronic properties of a wide variety of condensed matter systems. Methods at the level of DFT yield accurate results for all the properties related to ground states. However, electron excitations require different approaches that go beyond DFT. DFT methods based on single determinant approach do not account for configuration interactions.

In this thesis we mainly use the SIESTA (Spanish Initiative for Electronic Simulations with Thousands of Atoms) method [330, 331], which is a self-consistent DFT method that solves the Kohn-Sham equations iteratively using the pseudopotentials approach. Differently from all-electron methods, the use of pseudopotentials imply that valence electrons, and sometimes semi-core electrons, are directly included in the Kohn-Sham equations. This approximation works correctly when calculating electronic properties such as the ground state, bond lengths and phonons. In next section we comment further on the pseudopotential method.

Two different approaches are used for the basis functions to expand the solutions of the Kohn-Sham equations in the DFT ground state methods: atom-centered and atom-independent basis. A representative example of the atom-independent method is the use of plane waves. The SIESTA method uses atom-centered basis, specifically a linear combination of atomic orbitals. The use of the atom-centered approach for the basis functions implies that the computational cost scales with the number of atoms and the number of orbitals per atom. Thus, the free space in the unit cell does not increase largely the computational cost. It is noteworthy that the SIESTA basis functions have finite size, which means that for certain distance between two atoms there is no interaction. The atomic basis orbitals within the radius of confinement for an atom I found at R_I are given by the product of the radial function $\phi_{In}(r_l)$ and the spherical harmonic $Y_{lm}(\hat{r}_I)$. The angular momentum is labeled by (l, m) , and n labels the radial functions for the same angular momentum. The expression for the atomic basis orbitals is

$$\phi_{Imn}(r) = \phi_{In}(r_l)Y_{lm}(\hat{r}_I), \quad (2.16)$$

where $r_l = r - R_I$. SIESTA method computes geometries without any symmetry. So even for symmetric molecules or solids there could be small differences in distances and angles. For the exchange and correlation the method uses local density density (LDA)

2 Methods

or generalized gradient approximations (GGA). We mainly use the generalized gradient approximation with the PBE functional flavor [332].

2.3.1 Pseudopotentials

The SIESTA method uses the pseudopotential approach. The basic idea behind pseudopotentials is to replace a problem with another easier or more convenient to be solved. The strong Coulomb potential of the nucleus and the effects of core electrons are replaced with an effective and smooth ionic potential that acts on the valence electrons. Figure 2.1 includes a representation of the pseudopotential and the pseudo-wave function. The pseudopotential approach works nicely because the core electrons remain approximately unchanged in complexes or in the bulk. Pseudopotentials are generated in atomic calculations.

In our calculations with the SIESTA method we use norm-conserving pseudopotentials, which must follow a series of requirements. First, all-electron and pseudo-valence eigenvalues must agree for the atomic reference configuration. Second, all-electron and pseudo wave functions and their logarithmic derivatives must agree beyond a chosen core radius R_C . The norm-conservation condition means that the integrated charge within the core radius R_C for each wave function agrees.

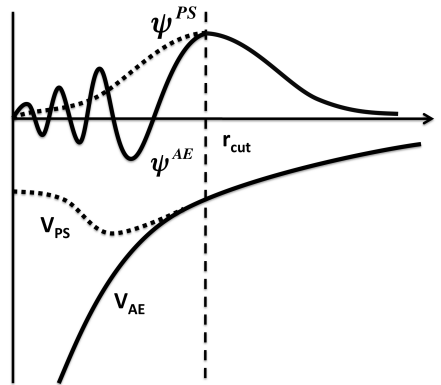


Figure 2.1: Pseudopotential and the pseudo-wave function. Figure reproduced from Ref. [333].

Generating pseudopotentials is a magic black art, although some guidelines can be outlined. The program ATOM within the SIESTA software package appears as a useful and basic tool to generate them. First, one must choose an exchange correlation functional and the pseudopotential flavor. We consider generalized gradient approximation (GGA) and Troullier-Martins [334] pseudopotentials, respectively. Then, we choose an electronic configuration to generate the pseudopotential, which could be the free atom configuration for example. Finally, the cutoff radii for each l channel must be set. The radii fix the distance from which the pseudopotential and the all-electron potential and the pseudo-wave function and the all-electron wave function must agree.

It is important to test carefully the pseudopotentials after the generation process. First, there is good agreement between the eigenvalues of the all-electron and pseudopotential calculations for the atom. Secondly, the agreement must be tested also for other electronic configurations. Atom cross-excitations are the energy differences between the different electronic configurations. The cross-excitations must be similar for the all-electron and pseudopotential calculations. These conditions are fulfilled related to the transferability of pseudopotentials. Further testing of the pseudopotential is advisable by computing for example bulk phases, trying to reproduce well-known properties.

Pseudopotentials would also often include relativistic effects. Although these effects originate in the atom close to the nucleus, they could affect valence electrons. These pseudopotentials are called scalar relativistic pseudopotentials when including shifts due to relativistic effects.

Core corrections are important when core and valence electron densities overlap. Then, core corrections are needed in the pseudopotential because the exchange-correlation potential is not a linear function of density. The core correction is expressed as the difference

$$V_{xc}([n^{PS}] + n^{core}, \mathbf{r}) - V_{xc}([n^{PS}], \mathbf{r}) . \quad (2.17)$$

We show the computational details of the pseudopotentials and basis set for many atoms used in our study in Tables 2.1 and 2.2. Length units are expressed in Bohr because these are the standard inputs.

2.4 Projector augmented waves - The VASP method

The Viena ab-initio Simulation Package (VASP) method [335–338] allows to carry out quantum mechanical calculations to solve the Kohn-Sham equations using pseudopotentials or the projector-augmented wave (PAW) method. For the first approach it uses ultrasoft Vanderbilt pseudopotentials, which are smooth although they do not fulfill the norm-conserving condition. Here we focus on the projector-augmented wave (PAW) method [339] when performing the VASP calculations. The PAW method build basis functions for the valence states orthogonal to the functions localized around each nucleus. The basis function for valence states $\chi_q(\mathbf{r})$ is given as

$$\chi_q(\mathbf{r}) = \frac{1}{\Omega} \{ e^{i\mathbf{q}\mathbf{r}} - \sum_j \langle u_j | \mathbf{q} \rangle u_j(\mathbf{r}) \} , \quad (2.18)$$

where u_j are localized functions around the nucleus.

In the electronic structure calculations the valence wave functions must be orthogonal to the core states, which have many nodes that complicate calculations. For example, depending on the method, the presence of nodes imply more Fourier components or a very fine grid for integration. Therefore, some methods to ease the calculations have been developed. These methods yield smooth valence wave functions orthogonal to core states. The PAW method introduces projectors and auxiliary functions that allow to obtain smooth valence wave functions.

2 Methods

Table 2.1: SIESTA: Radii for the pseudopotentials of the computed elements (in Bohr units).

element	r_s	r_p	r_d	r_f
H	1.19	1.19	1.19	1.19
C	1.19	1.19	1.19	1.19
Si	1.89	1.89	1.89	1.89
S	1.61	1.76	1.92	1.92
Cr	1.49	1.50	2.19	2.19
Mn	1.98	2.16	1.88	1.88
Fe	2.00	2.00	2.00	2.00
Co	2.00	2.00	2.00	2.00
Ni	2.05	2.05	2.05	2.05
Mo	2.28	2.46	1.67	1.99
Tc	2.69	2.76	2.76	2.76
Ru	2.38	2.38	1.70	2.38
Rh	2.18	2.30	1.68	2.18
Pd	2.27	2.45	1.66	1.98
W	2.00	3.03	2.24	2.24
Re	2.67	2.74	2.51	2.51
Os	2.67	2.81	2.57	2.57
Ir	2.60	2.77	2.60	2.60
Pt	2.24	2.77	1.79	2.24

Table 2.2: SIESTA: Cutoff radii of the employed basis for the computed elements (in Bohr units).

element	1s	2s	
H	6.047, 4.053		
	2s	2p	
C	4.994, 3.475	6.254, 3.746	
	3s	3p	3d
Si	7.106, 4.588	9.355, 5.465	
S	7.984, 3.587	7.984	7.984, 7.407
	4s	4p	3d
Cr	8.141, 7.185	8.141	8.141, 3.071
Mn	8.013, 6.399	8.013	8.013, 2.384
Fe	8.100, 6.632	8.100	8.100, 2.533
Co	7.998, 6.467	7.998	7.998, 2.349
Ni	8.107, 6.314	8.107	8.107, 2.209
	5s	5p	4d
Mo	8.063, 7.205	8.063	8.063, 3.715
Tc	8.075, 7.216	8.075	8.075, 3.324
Ru	8.091, 6.878	8.091	8.091, 3.129
Rh	8.112, 6.725	8.112	8.112, 2.947
Pd	8.136, 6.662	8.136	8.136, 2.742
	6s	6p	5d
W	8.133, 6.414	8.133	8.133, 3.794
Re	8.025, 6.821	8.025	8.025, 3.345
Os	8.119, 6.731	8.119	8.119, 3.140
Ir	8.014, 6.984	8.014	8.014, 3.138
Pt	8.112, 6.009	8.112	8.112, 3.060

The PAW method maintains the all-electron wave function. The all-electron wave function $|\Psi\rangle = \sum_m c_m |\Psi_m\rangle$ is related to the smooth pseudized valence function $|\tilde{\Psi}\rangle = \sum_m c_m |\tilde{\Psi}_m\rangle$ by a linear transformation $\Psi = \mathcal{T}|\tilde{\Psi}\rangle$. The linear transformation is unity except for a sphere centered on the nucleus, and is expressed using projection operators in the sphere $\langle \tilde{p}_m |$ as

$$\tau = \mathbf{1} + \sum_m \{|\Psi\rangle - |\tilde{\Psi}\rangle\} \langle \tilde{p}_m | . \quad (2.19)$$

This method evaluates the integrals as sums of the integrals of smooth wave functions over all the space and the integrals of the localized functions computed inside spheres. Outside the spheres, plane waves are used for the basis set. The PAW potentials used in this thesis are included on the VASP package [339, 340].

2.5 Full-potential linearized augmented-plane-wave method - the ELK method

The main problem in the electronic structure calculations is to deal with the different character of wave functions close to the nuclei and in the interstitial region. The augmentation method combines smooth functions for the interstitial region and radial functions times spherical harmonics for the tricky regions inside spheres around nuclei. A basis function for the augmented plane wave (APW) method is defined as:

$$\chi_{\mathbf{k}+\mathbf{G}}^{APW}(\mathbf{r}) = \begin{cases} \exp(i(\mathbf{k} + \mathbf{G})\mathbf{r}) & r > S \\ \sum_{Ls} C_{Ls}(\mathbf{k} + \mathbf{G})\psi_{Ls}(\epsilon, \mathbf{r}) & r < S \end{cases} \quad (2.20)$$

with plane waves for the region out the sphere boundary S and a wave function product of radial functions and spherical harmonics for the region inside the sphere. This method matches two different expansions at spheres boundaries. The matching yields non-linear equations due to the dependence of the basis functions with the energy for the APW method. Then, the linearization of the equations in energy was achieved by expanding the augmentation functions as linear combinations of a radial function and its energy derivative. The augmented methods are full potential by computing the matrix elements of the full non-spherical potential in the sphere and the full spatially varying potential in the interstitial. We use the ELK method, an all-electron full-potential linearized augmented-plane-wave (FP-LAPW) method to carry out density functional theory calculations [341, 342].

Some magnetic calculations require high energy precision as given by the ELK method. We used the ELK method for Ni_3Bz_3 and Co_3Bz_3 calculations. We choose a wave-vector cut-off of $K_{max}R_{Ni} = 12$, where $R_{Ni} \approx 1.16 \text{ \AA}$ is the nickel and cobalt muffin-tin radius. The carbon and hydrogen muffin-tin radius are 0.60 and 0.47 respectively. To initialize ferromagnetic configurations we applied external magnetic fields, which were reduced every self-consistent loop [341]. Local spin density approximation [343] was used for the exchange correlation functional. More details regarding calculations in this thesis can be found in the results sections.

3 Zero-dimensional systems

3.1 Introduction

In this chapter we study transition metals interacting with benzene and polycyclic aromatic hydrocarbons (PAH). Among PAHs, we specially consider benzene because it is the smallest "graphene-like" molecule. Furthermore, benzene enters as a basic building block in larger aromatic complexes.

First, we have studied cobalt atoms and small clusters interacting with PAHs. Polycyclic aromatic hydrocarbons are formed by several carbon hexagons with the edges saturated with hydrogen atoms. There is a large variety of complexes attending to shape and size. Some examples of PAHs are shown in Fig. 3.1. Here we have chosen circumcoronene $C_{54}H_{18}$ as a representative PAH and cobalt as transition metal. Note the likeness between some PAHs and graphene. People have two different views: PAHs as useful models for graphene, and PAHs with important differences with graphene and interesting by themselves. We believe that the circumcoronene is not an accurate model for graphene because there are edges, non-zero band gap, different electronic structure, among many others features. Therefore, although PAHs have been used as graphene models to reduce the computational cost it is important to keep in mind that graphene and PAHs present notable differences. On the other hand, some results obtained from PAHs could be useful to compare with when calculating graphene, such as the position of an adatom (hollow, top or bridge) or its height over the surface. For these purposes PAHs central ring would be the most accurate area to mimic graphene. The central region is a graphene-like area where carbon-carbon bond lengths are uniform. When the size of the hexagonal PAH increases, the size of this graphene-like central region grows [344]. We shall also comment below on using circumcoronene as a model for graphene.

Benzene is the lower limit of polycyclic aromatic hydrocarbons. It is common to compare some results of the adsorption of adatoms on both graphene and benzene. For example, as for graphene, the metal interaction with benzene has been largely studied. There are both theoretical and experimental results of systems containing benzene molecules and transition metal atoms. Here we are interested not only in the interaction of benzene and the transition metal atom but also in complexes of larger sizes, where few benzene molecules and transition metal atoms interact together. Experimental and theoretical works about these organometallic systems have discovered that structurally they are divided in two different groups. For the early transition metals (Sc, Ti, V) the complexes with benzene form sandwich-like structures, and for the late transition metals (Fe, Co, Ni) they form bowl-like structures, called rice-ball. The sandwich-like structures are formed alternating transition metal atoms and benzene molecules. The rice-ball structures consist of a transition metal nucleus covered with benzene molecules. Exam-

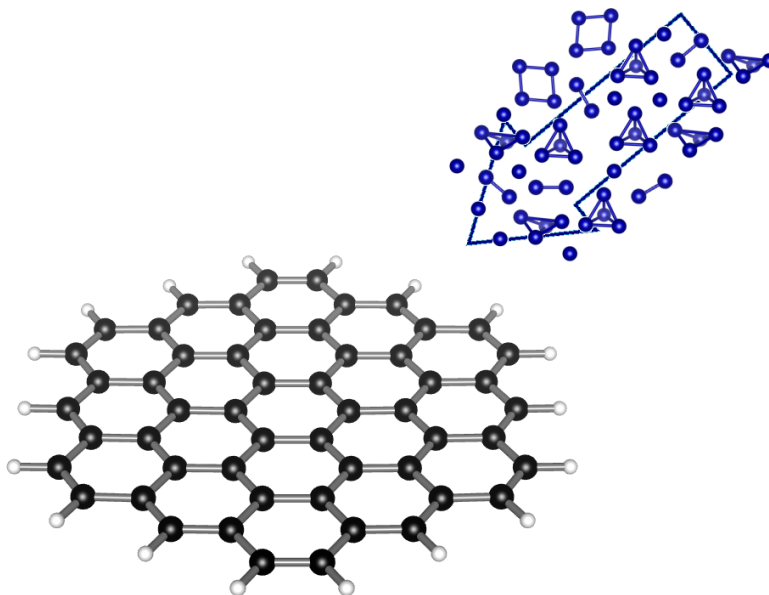


Figure 3.1: Scheme representing the experiment associated to our calculations of cobalt atoms and small clusters deposited on circumcoronene.

ples of rice-ball and sandwich structures are shown in Fig. 3.2 and 3.16, respectively. The reason for the different behavior is the relative strength of the benzene-metal and metal-metal interactions [111]. For stronger metal-metal interaction rice-ball structures are preferred, while for stronger metal-benzene interaction sandwich-like geometries are favored. For the sandwich-like structures, different applications have been proposed such as half-metallicity suggested for spin transport[345]. However, we are interested in the rice-ball structures for two reasons. On one hand, these are the preferred structures wrapping traditional ferromagnets (Fe,Co,Ni). On the other hand, the interaction between the transition metal atoms is preserved within the "cage" and we find exciting to study the influence of benzene on these organometallic systems. Below we will see that there are relevant changes in the interaction of transition metal atoms because of benzene addition, yielding several striking effects.

Specifically, we have chosen to study transition metal (TM) benzene compounds of the size TM_3Bz_3 with $\text{TM} = \text{Mn}, \text{Co}, \text{Ni}$ for several reasons. The interaction of three transition metals atoms forming an inner trimer is complex because of the competition between isosceles and equilateral structures for the TM core structure. This delicate balance could induce unexpected effects. Furthermore, this small size allows to form a compact cluster where each transition metal atom interacts with its benzene, so that the interactions between benzene molecules are small. We have chosen to study cobalt, nickel and manganese as show in Fig. 3.2.

Among traditional ferromagnets cobalt is the reference element for experiments, being ferromagnetic. We consider cobalt for the interactions with benzene in detail. We

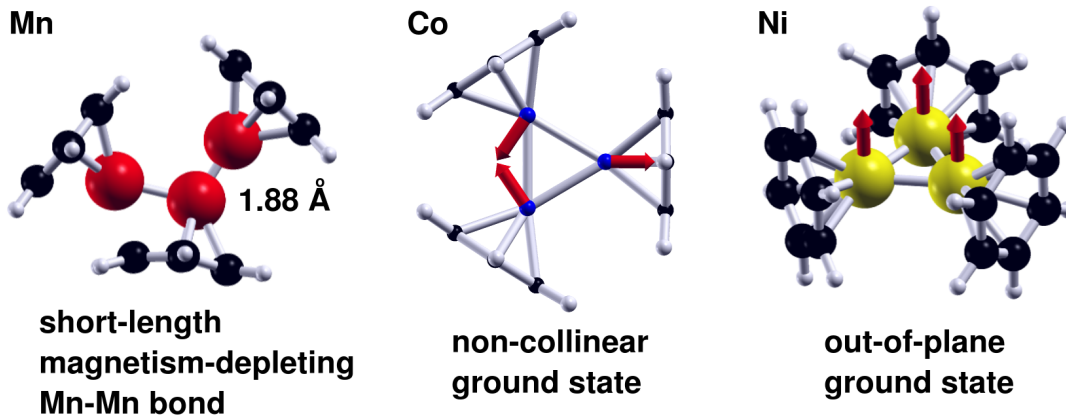


Figure 3.2: TM_3Bz_3 clusters with $TM = Mn, Co,$ and Ni , including their main characteristics.

also study nickel, also ferromagnetic, because Ni_3Bz_3 compound lacks understanding. Last, manganese presents half-filled $3d$ band and was not reported as rice-ball or as sandwich, being in the border between two type of structures. Furthermore, molecular beam experiments do not show a large peak for this size and the argument for that was the existence of spin restrictions. Here we want to shed more light on the evidence of manganese benzene compounds.

3.2 Interaction of cobalt atoms and small clusters with circumcoronene $C_{54}H_{18}$

3.2.1 Free molecules and clusters

First we show our results for the isolated circumcoronene and cobalt atoms and clusters, before studying the interacting cases.

Circumcoronene

The circumcoronene cluster ($C_{54}H_{18}$) is composed of 54 carbon atoms and 18 hydrogen atoms saturating the carbon dangling bonds on the edges. Circumcoronene is a polycyclic aromatic hydrocarbon (PAH) with lateral dimensions no larger than 1.5 nm. Circumcoronene is obtained adding an external layer to coronene ($C_{24}H_{12}$), preserving the hexagonal symmetry of benzene and coronene. In particular, circumcoronene has D_{6h} symmetry. Circumcoronene presents large stability attending to its large gap and to the binding energy per atom. The binding energy of circumcoronene can be computed as $E_b = (54E_C + 18E_H - E_{C_{54}H_{18}})$, where E_C is the total energy of a single C atom, E_H is the total energy of a single Co atom, and $E_{C_{54}H_{18}}$ is the energy of circumcoronene. The total binding energy is 464.98 eV, which is shared by the 54 carbon atoms and the 18

3 Zero-dimensional systems

hydrogen atoms. If we average over the 72 atoms of the cluster we obtain a value of 6.45 eV per atom, which indicates high stability for circumcoronene. Concerning the gap, the generalized gradient approximation (GGA) calculations yields a value of 1.84 eV. Considering the well-known underestimation of the gap when using the GGA functional [329, 346], the stability of circumcoronene is reassured.

To gain insight on the electronic structure of circumcoronene we plot in Fig. 3.3(a) the density of states projected on the different orbitals of carbon and hydrogen. From lower to higher energy we find carbon $2s$, $2p_x$ and $2p_y$, and $2p_z$ states. Carbon in-plane orbitals ($2s$ and $2p_x$ and $2p_y$) are hybridized among them and with $1s$ state from hydrogen. The combination of p states lying on the xy plane and $2s$ yields the so-called sp^2 hybridization. Note that close to the Fermi energy there are occupied and empty carbon $2p_z$ contributions, responsible for the interaction with other systems.

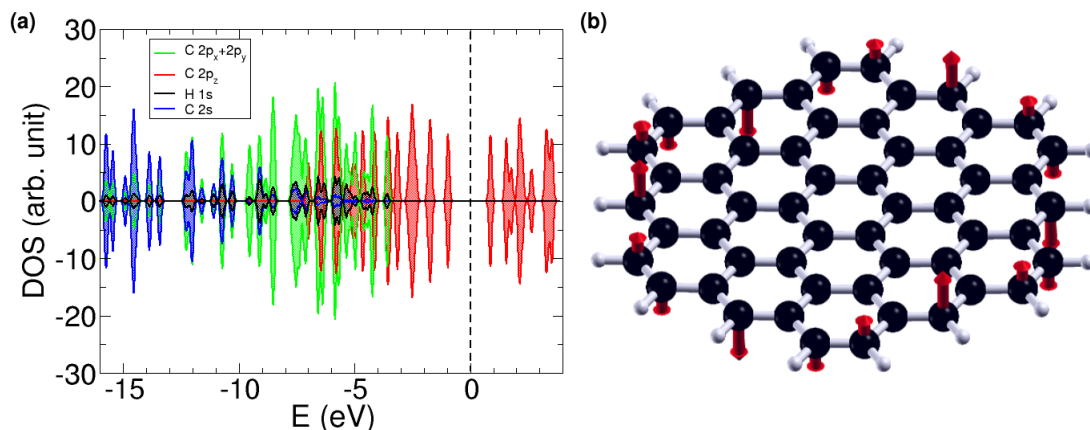


Figure 3.3: (a) Projected density of states for $C_{54}H_{18}$ circumcoronene. (b) Input disposition of the local magnetic moments, which go to zero after convergence.

As circumcoronene is a polycyclic aromatic hydrocarbon, we comment now on its aromaticity attending to the Huckel's rule. This molecule has 54 carbon atoms, each contributing with a p_z electron. The number of delocalized electrons, 54 for circumcoronene, is equal to $4n+2$ with $n=13$. Therefore the molecule should show aromaticity. To locate the aromatic rings over the structure we follow the Clar's rule, so that the structure has the largest number of disjoint aromatic π sextets with double bonds in the edges. The Clar's structure of circumcoronene is shown in Fig. 3.7(b). As we will comment in next sections, the Clar's structure seems not faithfully reproduced in our calculations, because charge is accumulated in the edge region, not only on the double bonds.

Circumcoronene is formed by adding benzene rings forming a hexagonal structure, with distances similar to those of benzene. However, the carbon-carbon bond length varies with the distance to circumcoronene. The largest bonds are found for the central ring (1.43-1.44 Å), slightly larger than those of pristine graphene (1.42 Å [140]) and benzene (1.39 Å [93, 347]). Moving towards the edge larger and shorter bond lengths

alternate, finding the shortest values for the six double bonds in the six corners (1.37 Å). On the carbon-hydrogen bonds, the distances are about 1.11 Å for the eighteen bonds. This value is similar to that reported for graphane [299] and benzene (1.09 Å [93]).

Finally we comment on the magnetism of the circumcoronene molecule when considering it as a nanographene plate. We obtained zero total magnetic moment for circumcoronene, in agreement with Lieb’s theorem which predicts zero spin polarization for circumcoronene because it has the same number of atoms on each sublattice. The projected density of states shown in Fig. 3.3(a) reveals that the electronic structure is spin compensated, so there is no local magnetic moments at edges. Nevertheless, it is possible to have a globally unpolarized structure with non-zero local magnetic moments on the edges [159]. Indeed, the spatial distribution of the edge spin states can be obtained using the electron spin resonance (ESR) technique at temperatures lower than 20 K [348]. When having local magnetic moment on the edges, they are ferromagnetic coupled on the same sublattice and antiferromagnetic coupled on different sublattice. The atoms for zigzag edges in circumcoronene belong to the same sublattice. The structure of circumcoronene yields six zigzag edges with three atoms on each side. Therefore, one could expect a locally polarized state for circumcoronene with ferromagnetic coupling between the atoms on the same side and antiferromagnetic coupling between close sides. We set an input configuration similar to that shown in Fig. 3.3(b) with two different codes (SIESTA and VASP). After fully relaxation of the structure no local magnetic moment is found. This result is agreeing with previous prediction [159], proposing that a minimum of eight atoms per side is required to find locally polarized states.

Circumcoronene as a model for graphene

We next comment briefly on our approach to study circumcoronene. It is tempting to use circumcoronene as a model for graphene because of its relatively large size when compared to benzene. Indeed, it has been used to model graphene for different purposes, to study the interaction with transition metals [52], Raman spectrum [53], NMR [54], adsorption on metal surfaces such as copper or gold [55], and hydrophilic and hydrophobic interactions [56, 57, 349, 350]. Even bended circumcoronene has been proposed as a model for carbon nanotubes to study its functionalization [351].

The use of circumcoronene as a model for graphene can be justified when the computational cost is high. For instance, when performing calculations using the CASSCF method [52]. Nevertheless, accurate results should use graphene instead of modeling it with polycyclic aromatic hydrocarbons like circumcoronene. The role of the edges, which is far from negligible in the electronic structure calculations, and the non-zero gap for PAHs represent large differences with graphene. The difference between coronene and graphene concerning the gap is well documented for the study of lithium adsorption [352].

Calculations with PAHs as model for graphene can give insight into the problem or show trends [353] that could be extrapolated to the case of pristine graphene. For example, a cobalt atom over benzene prefers the hollow site, a trend which is also found for pristine graphene. In particular, the central ring of circumcoronene would be the

3 Zero-dimensional systems

most suitable place to model a graphene hollow because the edge effects are reduced because of distance and symmetry. Note that the larger PAHs size, the more accurate is to use the PAH center as a graphene model.

Free cobalt clusters

Co atom

We find a total magnetic moment of $3 \mu_B$ for the cobalt atom. We also calculated the cobalt atom using the Amsterdam Density Functional (ADF) code and we obtained minimum energy when there are 1.6 electrons in the $4s$ orbitals and 7.4 electrons in the $3d$ orbitals. So we used this electronic configuration to generate the pseudopotential that we use with the SIESTA code.

Co dimer

We computed the cobalt dimer using the pseudopotential generated for the cobalt atom. Relaxation of the dimer yields a bond length of 2.04 \AA , a binding energy per atom of 1.139 eV and a magnetic moment of about $5 \mu_B$. Ultrasoft pseudopotential calculations of cobalt dimer have been reported with a distance of 1.94 \AA and a magnetic moment of $4 \mu_B$ [353]. Seifert et al [67] obtained a total magnetic moment of $4 \mu_B$ for cobalt dimer using an all-electron full-potential local-orbital (FLPO) code. A value of $5 \mu_B$ has been reported using the BLYP functional [65]. We calculated the cobalt dimer using the ADF code getting a value of $4 \mu_B$.

We tried to find explain these results by varying the pseudopotential we generated. We checked a large variety of pseudopotential radii and the cobalt dimer magnetic moment stayed about the value of $5 \mu_B$. Decreasing radii makes the pseudopotentials transferable although hard, and improves the result for the cobalt dimer but spoils the results for larger systems as Co_4 or even cobalt bulk. We also analyzed what is the role of the pseudopotentials being or not relativistic. We found that the non-relativistic case shows correct filling of levels is correct and yields a magnetic moment of $4 \mu_B$ when using small broadening.

Following a different approach to the problem, we include the $3p$ electrons as valence electrons in the pseudopotential. The calculations of the cobalt dimer using this pseudopotential result in a magnetic moment of $5 \mu_B$. Nevertheless, including the $3s$ as valence electrons produces a pseudopotential that reproduces the value of $4 \mu_B$ for Co_2 [67]. A different way to obtain a value closer to $4 \mu_B$ is to change the electronic configuration of the cobalt atom from $4s^{1.6} 3d^{7.4}$ to $4s^1 3d^8$.

All these calculations show that reproducing the magnetic moment of $4 \mu_B$ obtained with all-electron calculations for the cobalt dimer is not easy to achieve when generating pseudopotentials for cobalt. The cobalt dimer stands as a critical test for cobalt pseudopotentials. Note that we obtained a magnetic moment of $4 \mu_B$ when including inner electrons, which are considered in all-electron calculations using ADF or FLPO methods [67]. Nevertheless, for larger systems the cobalt pseudopotential is not so critical as similar results are obtained using different pseudopotentials for larger cobalt clusters.

Therefore, we use the pseudopotential that yields the smallest energy differences between different electronic configurations during the test we carried out. We checked that the pseudopotential reproduces the main bulk features. Although including the $3s$ and $3p$ electrons would slightly improve the results, it does not compensate the computational cost. Note that we chose SIESTA to test many different adsorption sites of cobalt clusters on circumcoronene and get general trends rather than to study in detail a specific configuration. Overall, studying Co_2 let us know the limits of our pseudopotential and it rises as a benchmark for cobalt pseudopotentials.

Co₄ cluster

We computed different geometries for the free Co_4 cluster, such as tetrahedra, square and line. Results are summarized in Fig. 3.4. The most stable structure is a non-regular tetrahedron, called butterfly wings (BW) attending to its shape, with a binding energy per atom of 2.078 eV. It has two bond lengths of 2.84 Å and four of 2.19 Å, which allow high interaction of the $3d$ electrons. Next, at 13 meV higher in energy, we find a flat rhombus geometry of 2.19 Å, after relaxing an input square of 2.1 Å. Third we find a more regular tetrahedron with a binding energy per atom of 1.980 eV. This tetrahedron has bond lengths of 2.25 and 2.37 Å. Note that tetrahedra have cobalt-cobalt bonds with short and long distances [354], which looks like a Jahn-Teller effect. Finally the linear structure is the least stable geometry with a binding energy per atom of 1.499 eV. It has three bond lengths: two short of 2.07 Å and one in the center of 2.38 Å.

Concerning magnetism, the four geometries have total magnetic moments about $10 \mu_B$. The magnetic moment is shared similarly by the four cobalt atoms with values per atom close to $2.5 \mu_B$. However the values are slightly different for each cobalt atom because there are different distances between cobalt atoms. For example, for the rhombus structure the atoms opposed in the large diagonal D have local values of $2.43 \mu_B$, and those in the short diagonal d have values of $2.58 \mu_B$. For the linear structure the cobalt atoms have local magnetic moments of $2.626 \mu_B$ at the ends, and $2.374 \mu_B$ in the center.

Next we compare our results with those reported for the Co_4 cluster. Although the tetrahedron is the most stable geometry [354–358], there are discrepancies about shape and distances. A regular tetrahedron with an average magnetic moment per atom of $3 \mu_B$ and an average bond length of 2.34 Å has been reported [356]. Larger distances within the interval 2.61–2.80 Å and a local magnetic moment of 2.50 Å has also been commented [358]. The same order of stability we obtained here, i.e. a tetrahedron followed closely by a rhombus and both far more stable than a linear structure, was also found previously [354]. About the BW ground state, a similar structure was reported by Johll et al [357] with two different bond lengths of 2.14 and 2.74 Å, slightly smaller than our results, and a total magnetic moment of $10 \mu_B$.

3 Zero-dimensional systems

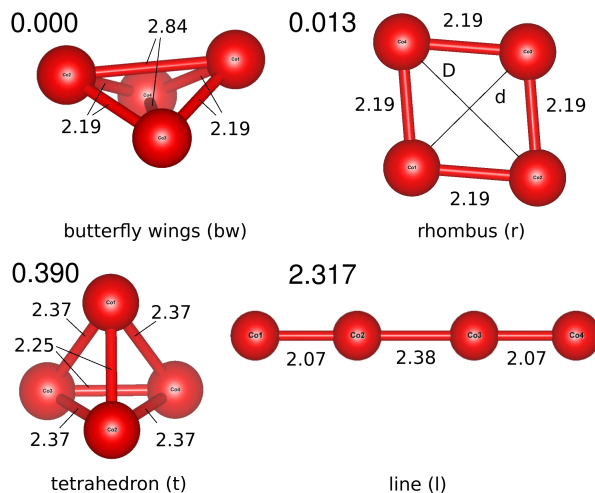


Figure 3.4: Stability order for free Co_4 isomers. The values of the relative energy respect to the ground state are shown for each isomer. For the rhombus, diagonal values are $D=3.34 \text{ \AA}$ and $d=2.85 \text{ \AA}$.

3.2.2 Co atom on circumcoronene

We study cobalt atoms adsorption on all the possible positions over the circumcoronene. Circumcoronene has D_{6h} symmetry, so the number of possible adsorption sites lessen. On one hand, the large number of sites are divided in four regions: central, intermediate, edges, and peripheral. On the other hand, the cobalt atom can be over three characteristic sites with respect to carbon atoms: hollow, bridge and top sites. These two factors are combined in a nomenclature as explained in Fig. 3.5.

We consider input position for the cobalt atom on circumcoronene and then we fully relax the geometry. Figure 3.6 shows all the input and final geometries in the upper left panel, with colors according to their stability. Notice that some geometries distort much during relaxations. Stability is related to the bonding energy, estimated as $E_b = (E_{C_{54}H_{18}} + n * E_{Co} - E_{C_{54}H_{18} + Co_n}) / n$ in eV, where n is the number of cobalt atoms $n=1, 2,$ and 4 . The most stable adsorption site suits to a hollow site in the edge zone, the EH1 configuration, with an adsorption energy of 1.43 eV.

Several conclusions are shown in Fig. 3.6. First, the hollow sites are more stable than the top and bridge sites. Some input geometries such as the CB, IB1, IB3 or IT2 structures relax the cobalt atom to the closest hollow site, which are other studied structures. The relaxation path for these geometries in Fig. 3.6 is denoted by the black thin lines joining the input and the relaxed sites. Second, the stability has a trend on the different hollow sites. The farther from the center the more stable the hollow sites are, as shown by the sequence $CH < IH < EH2 < EH1$. Besides, we studied two configurations, P1 and P2, with the cobalt atom initially set at zero high between two hydrogen atoms in the outer zone. After relaxations, the cobalt atom replaces the hydrogen atom bonding the carbon atom in the edge. These geometries evoke the role of cobalt as catalyst. Note

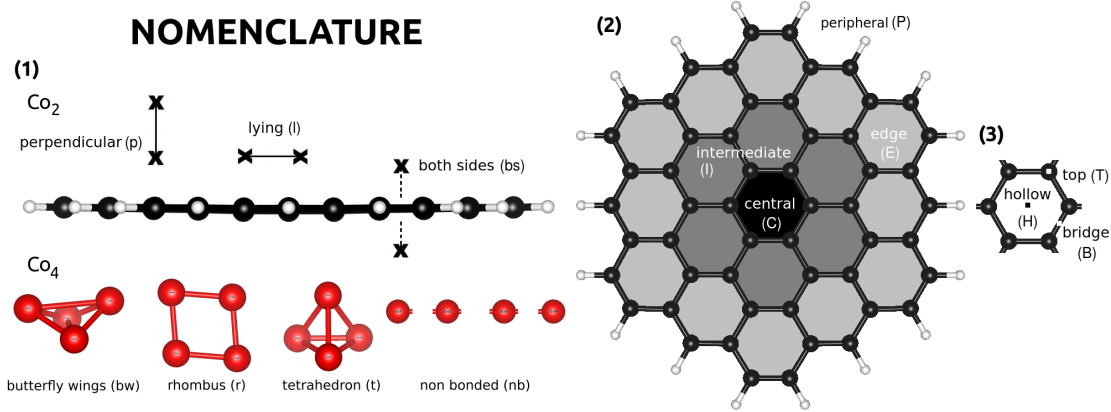


Figure 3.5: Different configurations of Co atoms, Co dimers, and Co_4 clusters on circumcoronene. Cobalt atom sites are labeled taking (1) the first character of the name describing the input disposition of Co_2 or Co_4 such as (p,l,bs) or (bw,r,t,nb), (2) the second from the circumcoronene region such as (C,I,E,P), and (3) the third from the hexagonal site. Note that for Co atom there is no option (1) to choose the disposition. When several configurations deserve an equal name they are distinguished by the order number as commented in text.

that they are the least stable sites for cobalt atoms on circumcoronene.

Next we study in more detail some geometric parameters, such as the cobalt atoms height over circumcoronene or the carbon-cobalt bond lengths. For the hollow geometries the cobalt atom height is about 1.45 Å, and for the bridge and top sites it expands to 2 Å, like for the EB1 and the IB2 cases. However, the carbon-cobalt bond lengths stay similar for all configurations, around 2 Å. Catalysts-like structures, such as the P1 and P2 configurations, are exceptions with shorter values of 1.8 Å for the carbon-cobalt bond, and 1.5 Å for the hydrogen-cobalt bond.

Finally we compare our results with previous works. For benzene, the cobalt atom prefers the hollow site with a carbon-cobalt distance of 2.02 Å [64]. For graphene or graphene nanoribbons [212], other DFT calculations using the generalized gradient approximation find that the cobalt atom prefers to adsorb on hollow sites [231, 232, 353, 359]. On graphene and graphene nanoribbons, the calculations predict heights of 1.64 and 1.5 Å, and adsorption energies within the intervals 0.97-1.34 eV and 0.97-2.08 eV, respectively. Cobalt atoms preference for hollow sites on graphene is also predicted by Quantum Monte Carlo, with a height of 1.49 Å [360]. A multi-configurational method, such as CASSCF, yields a cobalt atom height of 1.6 Å over hollow site [52] for the adsorption on coronene. Cobalt atoms prefer non-central hollow sites when deposited on coronene [72], as for the EH1 and EH2 configurations for circumcoronene. All these previous works support our results on the adsorption of cobalt atoms on circumcoronene.

3 Zero-dimensional systems

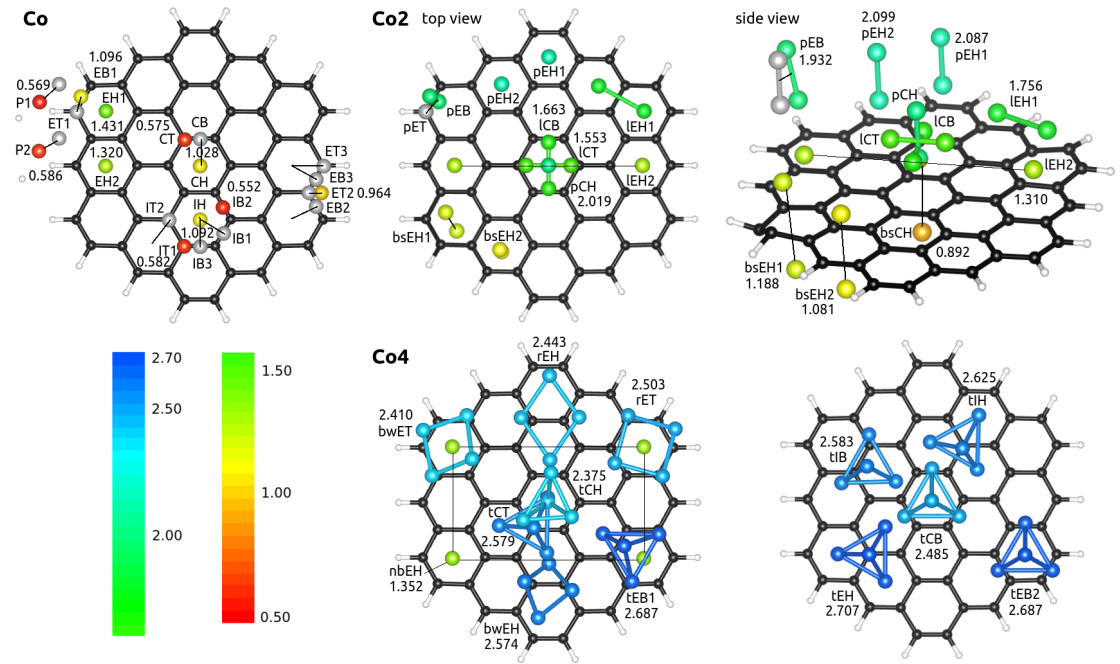


Figure 3.6: Geometries calculated for Co atom, Co₂ and Co₄ over circumcoronene. Cobalt atoms are colored according to their binding energy E_b in eV, as shown in the scale bars. Input arrangements are shown in gray for atoms and the pEB dimer, which relaxed to positions linked with a straight line. For the Co₂ and Co₄ cases, lines bond Co atoms calculated in the same geometry.

3.2.3 Co_2 molecule on circumcoronene

A cobalt dimer bonded perpendicularly to benzene has been reported as the ultimate magnetic storage device [67]. In this section we study the adsorption of a cobalt dimer on a larger PAH such as circumcoronene. We set first the cobalt dimer on different relative positions to circumcoronene, such as lying or upright, and over different zones. The relative position on circumcoronene and the zone are labeled according to rules explained in Fig. 3.5. Figure 3.6 shows the computed configurations that we have computed colored attending to their stability. Black lines join cobalt atoms computed together but with no direct cobalt-cobalt bonds between them. The pEB case suffers a large reconstruction during relaxation, and the black line joins the input positions with the relaxed configuration of the cobalt dimer.

We find that the perpendicular cobalt dimer over edge hollows are the most stable configurations, corner site pEH1 and middle side site pEH2. The pEH2 structure is slightly more stable than the pEH1 structure, an opposed behavior when compared with EH1 and EH2 configurations for the cobalt atom. The cobalt dimer has a perpendicular arrangement to circumcoronene, which is key to the stability, as shown for the four most stable configurations. Three of them place the cobalt dimer over hollow sites, in the pEH1, pEH2 and pCH configurations, and one over the bridge site (pEB). The three hollow cases are more stable than the bridge configuration. Among the hollow cases, the edge configurations are more stable. These two ideas agree with the trends previously commented for the cobalt atom adsorption. The bridge configuration pEB is tilted forming an angle of 13° with respect to the normal to circumcoronene. The geometric parameters of the perpendicular dimers are the cobalt atoms height to circumcoronene surface, the cobalt-cobalt distance, and the distance from the lower cobalt atom to the closest carbon atom. The height of the cobalt atom is 1.6 \AA and 3.7 \AA for the pEH1 and pEH2 configurations. The distances from cobalt atom to the first carbon neighbors are within the interval $2\text{-}2.2 \text{ \AA}$. The cobalt-cobalt bond lengths are around $2\text{-}2.1 \text{ \AA}$, slightly larger than 2 \AA found for the isolated cobalt dimer, signaling strong bonds.

Cobalt dimer lying parallel to circumcoronene leads to another group of configurations noticeably less stable than the perpendicular cases commented above. Specifically, there are three configurations that test the different sites. They are in order of decreasing stability: hollow (lEH1), bridge (lCB), and top (lCT). For the lEH1 configuration there are two cobalt atoms lying over neighbor edge hollows. The distance between cobalt atoms is 2.42 \AA , which is enlarged 0.3 \AA respect to perpendicular cases because of commensurability with the hollow sites. Other parallel configurations have the cobalt dimer over two bridge sites (lCB) and two carbon atoms (lCT). The cobalt-cobalt distances for these cases are 2.1 \AA . We compare these two central configurations with the perpendicular dimer over the central hollow (pCH). We find that the stability order hollow, bridge and top is still fulfilled.

Then we have the lEH2 configuration, with cobalt atoms far from each other in opposed edge hollows, separated by more than 8 \AA . This configuration is much less stable, showing that the cobalt atoms prefer to be bonded between them rather than to be spread separately over the surface of circumcoronene. Finally, the least stable configurations

3 Zero-dimensional systems

(bsEH1, bsEH2, bsCH) have the cobalt atom on both sides of the same hollow site of circumcoronene. For the edge case bsEH1 circumcoronene is deformed. The interaction between cobalt atoms becomes reduced, with cobalt-cobalt distances of 3.2 Å, supporting the idea of strong cobalt-cobalt interaction related to high stability.

A cobalt dimer adsorbed on graphene has been reported to display a perpendicular arrangement, with a height of 1.72 Å for the closest cobalt atom to circumcoronene and the other cobalt atom nearly 2 Å higher [232, 353]. A cobalt dimer over coronene is reported to bond perpendicularly to a bridge located on the edge of the molecule [72]. The findings seems analogous to the pEB configuration we report here, which is almost degenerated with the ground state. The carbon-cobalt bond length for coronene is 2.1 Å [72], close to 2.06 Å found for the pEB case.

3.2.4 Co₄ molecule on circumcoronene

Next we study Co₄ clusters interacting with circumcoronene. A difference of Co₄ clusters with atoms and dimers is that there are other possible isomers for the free clusters. Therefore, we tested the three most stable configurations for the free Co₄ cluster (tetrahedron, bw and rhombus) on the edges of circumcoronene (bwET, rET, tEB1), which are the most stable zone attending to above results for cobalt atoms on circumcoronene. We try to commensurate the isomers bw and rhombus over top and hollow sites. Our results show that the tetrahedron (tEB1) is becoming the most stable structure over circumcoronene.

Then we compute the tetrahedron structure on different positions to study the trends obtained for the cobalt atoms and dimers. We find that the most stable configuration is the tEH case, with three cobalt atoms over neighbor hollow close to the edge and a cobalt atom on top of them. When Co₄ clusters are adsorbed on edge zone circumcoronene is bended because Co₄ clusters are larger than atoms and dimers.

Some general ideas are obtained from the stability of tetrahedron configurations. First, edge sites are more stable than the center ones. Second, the hollow sites are preferred over bridge and top sites, which in a case shift towards closest hollows (tCT). Third, the nbEH geometry shows that the cobalt atoms prefer to be bonded together instead of being adsorbed as individual atoms. All these ideas are agreeing with our previous results for cobalt atoms and cobalt dimers.

Nevertheless, there is a particular case that deserve further comment. The tCH configuration inverts the tetrahedron, places one cobalt atom over the central hollow and leaves the other three cobalt atoms far from the surface, reducing carbon-cobalt interaction. The results for the cobalt dimer suggests that leaving a cobalt atom far from the carbon atoms as for perpendicular configurations increases stability. Then, we could expect that three cobalt atoms far from circumcoronene yields a more stable configuration. However, the tCH configuration is the least stable tetrahedron over circumcoronene. The tEH configuration, which maximizes carbon-cobalt interaction, is the most stable configuration. The different behaviors of Co₂ and Co₄ can be explained by two factors needed to understand stability. First, the cobalt atom adsorbed on a hollow site as for the EH1 case is highly stable. Therefore, the more cobalt atoms over hollow sites the larger the

stability. Second, commensurating cobalt atoms to be on neighbor hollow sites imply larger cobalt-cobalt distances, that weak the cobalt-cobalt bonds and reducing stability.

With these two ideas in mind we comment first on the Co_2 case. For the lEH1 configuration, with two cobalt atoms on neighbor hollows, the cobalt-cobalt bonds is 2.42 Å, a 21 % enlargement than to the free cobalt dimer distance of 2 Å. The extra cobalt atom over a hollow site does not compensate the weakening of the cobalt-cobalt bond. Thus, perpendicular configurations are more stable. For the Co_4 case, the tEH configuration places three cobalt atoms on neighbor hollows, and the cobalt-cobalt bond length is 2.5 Å. For the free Co_4 the bond length is around 2.3 Å, so there is a 9 % enlargement. The distortions are much lower and there are two extra cobalt atoms instead of an extra cobalt atom over hollow sites. Therefore, the configuration with more cobalt atoms interacting directly with carbon atoms is preferred.

Also many tetrahedron configurations are within a relatively small energy interval of 0.4 eV. Once the cluster is adsorbed on circumcoronene, it could slide easily with the plane formed by three cobalt atoms parallel to the surface, although barriers calculations are beyond the scope of this work. Previous calculations of Co_4 clusters interacting with graphene yield a similar geometry such as the tEH ground state obtained here [357].

3.2.5 Charges and bonding

Charge transfer

In this section we study the charge transfer using the Mulliken scheme for all the configurations of Co, Co_2 and Co_4 adsorbed on circumcoronene. We look carefully at the amount of charge and at the transfer direction. Attending to the Pauling scale of electronegativity, carbon and cobalt have values of 2.55 and 1.88, respectively. So it is expected that electrons move from cobalt to carbon atoms, as reported for the case of cobalt clusters deposited over graphene [361]. Figure 3.7(a) shows the charge transfer from cobalt towards circumcoronene. Positive values mean that electrons are gained by circumcoronene. Such is the case for most configurations.

First we comment on the configurations of a single cobalt atom adsorbed on circumcoronene. For the most stable configuration EH1, we find that 0.16 electrons pass from cobalt to carbon atoms. Similar values are obtained for other configurations except for the top sites (IT1, CT), where the charge value is about ten times smaller, and for the bridge configuration EB1, where the atom is over a double bond.

Next we focus on the cobalt dimer, which present a behavior that depends strongly on the relative arrangement of the cluster on the surface of circumcoronene. Nearly 0.15 electrons pass to cobalt atoms for the most stable configurations, which are the perpendicular arrangements pEH2, pEH1 and pCH. A detailed study of the charge distribution shows that the charge gained goes to the cobalt atom farther from the surface. For the bridge perpendicular pEB configuration, electrons passing from cobalt to carbon are largely reduced, following the EB1 behavior for the cobalt atom. The configurations with the cobalt dimer lying parallel to circumcoronene (lEH1, lCB, lCT) transfer electrons towards carbon atoms. The lEH2 configuration, where the cobalt

3 Zero-dimensional systems

atoms are too far to interact between them, presents a large value of 0.26 electrons, which is explained as the sum of two EH2 configurations for the Co atom.

Finally, we comment on the charge transfer for the Co_4 clusters. The values of the charge transfer are considerably smaller than for Co and Co_2 . There are charge transfer in the two directions depending on the configurations. For the tetrahedra, the trend we find is that when cobalt atoms are over hollow sites (tEH, tIH, tCT relaxed to hollows, tCH) they gain electrons, and over bridge sites (tEB2, tEB1, tIB, tCB) circumcoronene gains electrons. The tCH configuration presents the largest value among tetrahedra with more than 0.11 electrons gained by cobalt atoms. The tCH configuration bonds to circumcoronene by a cobalt atom, leaving the other three cobalt atom far from carbon atoms, similar to the perpendicular bonding for the cobalt dimer. Indeed, the charge behavior is similar. For Co_4 clusters, the nbEH configuration is explained as the sum of four EH1 configurations, as 1EH2 was explained as the sum of two EH1 configurations. The charge transfer is approximately the sum of four different EH1 cases. Figure 3.7(a) shows the lack of correlation between the amount and direction in the charge transfer and the stability of the different configurations of Co atoms, dimers and tetramers on circumcoronene.

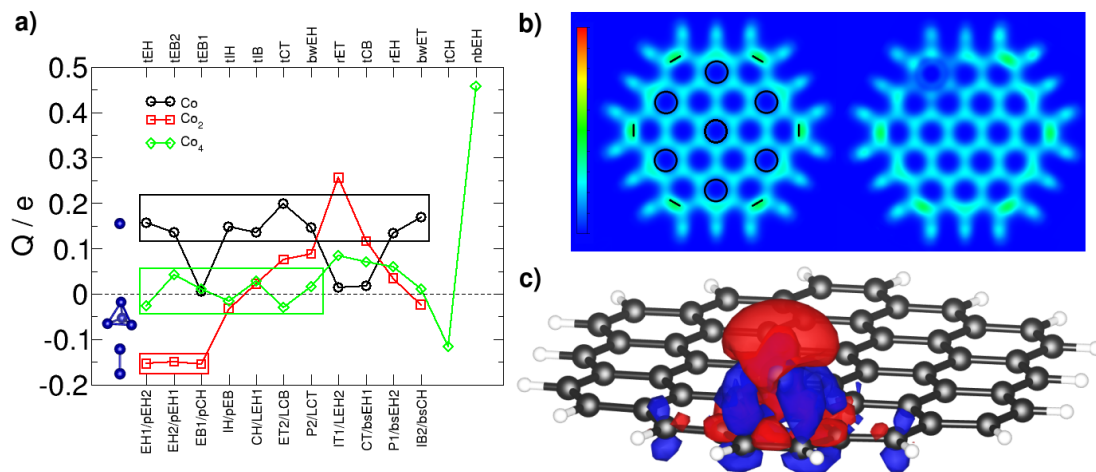


Figure 3.7: (a) Charge transfer Q for cobalt towards circumcoronene in all the computed geometries for Co, Co_2 showed in the lower part of the abscissas axis, and for Co_4 in the upper part of the abscissas axis. Positive charge values imply that electrons are gained by circumcoronene. Binding energies decrease from left to right. (b) Electron localization function (ELF) of circumcoronene without (left) and with Co in the EH1 configuration (right) shown in a plane nearly 1.2 \AA over circumcoronene. For circumcoronene, sextets and double bonds of the Clar structure are also shown. (c) Charge difference after the bonding process of the cobalt atom for the EH1 configuration. Blue (red) zones stand for zones gaining (losing) charge.

Bonding

We next analyze the stability of the different configurations of cobalt clusters adsorbed on circumcoronene. We find some trends about the preferred zones and positions for cobalt adsorption. We explain the bonding of cobalt on circumcoronene and the trends that rule it.

We focus on the preference for the edges rather than the center as the adsorption site. We consider the p_z electrons of carbon atoms, responsible for the bonding with cobalt atoms. Circumcoronene is a polycyclic aromatic hydrocarbon with aromaticity. Huckel's rule establishes that the molecule is aromatic when the number of π electrons is equal to $4n + 2$, being n an integer. Huckel's rule shows that the circumcoronene is aromatic because it has 54 π electrons yielding $n = 13$. Clar's rule states that the most representative Kekulé resonance structure for the PAH is the one with the largest number of disjoint aromatic -sextets. The resonant structure for the circumcoronene molecule is shown in Fig. 3.7(b) (left part), with seven circles representing aromatic bonds and six lines in the edges denoting double bonds. Nevertheless, the electron localization function included in the same figure does not follow exactly this pattern. The aromatic bonds are not visible. There is also charge collection at edge atoms not participating in double bond. Therefore, Clar structure seems not well reproduced. We propose the charge accumulation on circumcoronene edges as the main reason for increasing stability when moving closer to the edges.

Another argument for the edge preference is the lost of symmetry. When the cobalt atom is over the central hollow (CH), an analysis of the density of states shows that the couple of $3d$ levels ($3d_{xz}$ and $3d_{yz}$) are degenerated for the minority spin at the Fermi energy. The degeneration is broken for edge hollow configurations (EH1 and EH2) and these levels shift away from Fermi energy stabilizing the system.

Then, we comment why hollow sites are preferred instead of top sites. When a cobalt atom is over a hollow site, there is large hybridization between cobalt $3d$ orbitals and p_z carbon orbitals, so that the total magnetic moment decreases to $1 \mu_B$. Besides, cobalt atoms over top sites retain more the atomic character with a total magnetic moment of $3 \mu_B$, being much similar to that of the free atom. For cobalt atoms on top sites, the $4s$ levels are filled, and for the cobalt atom over hollow sites they are empty. The larger change suffered when adsorbed on hollow sites stabilizes them in comparison to top sites. Similar arguments explain why cobalt dimer prefers to be perpendicular instead of lying parallel. For the perpendicular cobalt dimer, the upper cobalt atom suffers large charge changes. However, the cobalt dimer lying parallel to circumcoronene has both cobalt atoms similar to the free state. The extra energy needed to recover the free state configuration explain the larger stability of hollow sites and perpendicular arrangements.

Finally, we focus on the most stable EH1 configuration for a cobalt atom over circumcoronene, which is a hollow site in the edge of circumcoronene. We analyze the charge reorganization when the cobalt atom is deposited. Figure 3.7(b) (right part) includes the electron localization function (ELF) for this configuration, which shows that the charge is removed from the carbon-carbon bonds. Figure 3.7(c) shows the charge redistribution after bonding. The red lobes shows a weakening of the bonds between carbon atoms,

3 Zero-dimensional systems

agreeing with ELF. Also, there are blue lobes representing the six carbon-cobalt bonds. In the cobalt atom, the big red lobe marks that charge moves from the upper part to the bonds established with carbon atoms.

3.2.6 Magnetism

We study the magnetic moments for the different configurations of the cobalt atom, dimer and tetramer over circumcoronene. We compute the local magnetic moment as the Mulliken charge difference between the up and down states. Figure 3.8 shows the magnetic moments of cobalt atoms and circumcoronene for all the computed configurations. In general the total magnetic moment is $1 \mu_B$ when cobalt atom bonds to circumcoronene, $4 \mu_B$ when it is the cobalt dimer, and $6 \mu_B$ for Co_4 . We test these values for the most stable configurations for each cobalt cluster by adding the Hubbard U term to cobalt atoms, and obtain the same results. For the cobalt dimer, Figure 3.8(b) shows the local magnetic moments for each cobalt atom. Similar values are reported for both cobalt atoms in parallel configurations. In the cases of perpendicular arrangements we find larger magnetic moments ($2.5 \mu_B$) in the cobalt atoms farther from circumcoronene. The explanation is that the lower cobalt atom shields somehow the effect of carbon atoms.

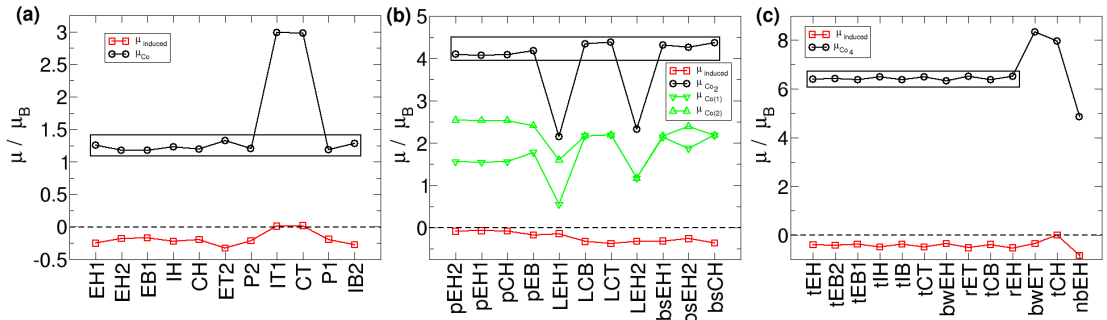


Figure 3.8: Magnetic moments of cobalt (positive) and induced magnetic moments in circumcoronene (negative) for all the computed configurations for (a) Co, (b) Co_2 and (c) Co_4 on circumcoronene. For the Co_2 configurations, Co(1) [Co(2)] refers to the cobalt atom closer [farther] to circumcoronene. Stability decreases from the left to the right configurations.

Figure 3.8 also shows that for most of the configurations there are negative induced magnetic moments in carbon atoms. For the most stable configuration of the cobalt atom (EH1), the total induced magnetic moment is $-0.25 \mu_B$, for the perpendicular cobalt dimer it is almost zero, and for the Co_4 cluster (tEH site) it is $-0.4 \mu_B$.

Next we compare our results with those reported before for similar systems. Previous calculations for a cobalt atom over a graphene hollow report $1.15 \mu_B$ for the local μ_{Co} [231, 232, 353, 359]. Quantum Monte Carlo method [360] yields a total magnetic moment of $1 \mu_B$. This value seems independent of the substrate because apart from our results

for circumcoronene, a total magnetic moment of $1 \mu_B$ has also been reported for a cobalt atom on a coronene hollow site using CASSCF method [52, 72]. For the cobalt dimer in a perpendicular arrangement over both graphene [232, 353] and coronene [72] the total magnetic moment is reported to be $4 \mu_B$. The local magnetic moment is smaller for the cobalt atom bonding to carbon atoms, with $1.66 \mu_B$ for the case of graphene and $1.58 \mu_B$ for coronene. For the Co_4 tetrahedron bonding graphene, the total magnetic moment is reported to be $6 \mu_B$ [357]. All these values found in literature are in good agreement with our results.

Finally we comment at some particular cases that deviated from the above trends. For the single cobalt atom case, the top site IT1 and CT configurations present values of $3 \mu_B$, with nearly zero induced magnetic moment. As already explained, the cobalt atoms in circumcoronene in these configurations keep part the atomic character. For Co_2 , the IEH1 and IEH2 configurations show a magnetic moment close to $2 \mu_B$, half the value for the other cases. The explanation is that the cobalt atoms are far from each other as to be considered as two separated atoms with $1 \mu_B$ each. The same applies for nbEH with $4 \mu_B$, explained as the sum of four individual cases. Other two exceptions for Co_4 are bwET and tCH, which present magnetic moments of $8 \mu_B$. These configurations leave more cobalt atoms far from the surface of circumcoronene, and these cobalt atoms have large magnetic moments because of the reduced carbon-cobalt interaction.

Hyperfine interactions

In this section we compute some hyperfine parameters that could be measured in experiments to determine the presence of cobalt atoms over circumcoronene molecules. Hyperfine structure is a consequence of the electrons interactions with nuclei, specially s electrons, which have non-zero probability of being in the nuclei. The isomer shifts are related to the average charge density within the nuclear volume [362]. Here we study this shift looking at the average charge density in nuclei by computing the hyperfine parameters using the ELK code [363]. We focus on the average contact charge density, computed as the charge averaged over a sphere around the nuclei in atomic units. We study the hyperfine structure for the carbon atoms in three different cases: the ground state circumcoronene, and the most stable configurations of $CoC_{54}H_{18}$ and $Co_2C_{54}H_{18}$.

We fit with a Lorentzian function for each case in Fig. 3.9. Figure 3.9(a) shows the spectra of the three different cases. It also includes a representation of the circumcoronene with colored atoms to differentiate each zone. Orange color is used to mark edge carbon atoms, blue for interior carbon atoms, and brown for those of the central ring. Cobalt atoms are shown in red and green for the $CoC_{54}H_{18}$ and $Co_2C_{54}H_{18}$ cases, respectively. The six carbon atoms closest to cobalt are colored in purple. We detailed the spectra for clean circumcoronene, as shown in Fig. 3.9(b). The blue and orange peaks corresponding to the internal and edge atoms are separated. There are several blue peaks, which represent the different distances to the center and therefore different environments. The same applies for the edge carbon atoms colored in orange. The brown peaks for the carbon atoms in the central ring are shifted towards the values of edge atoms. The spectra for Co and Co_2 deposited on circumcoronene are shown in

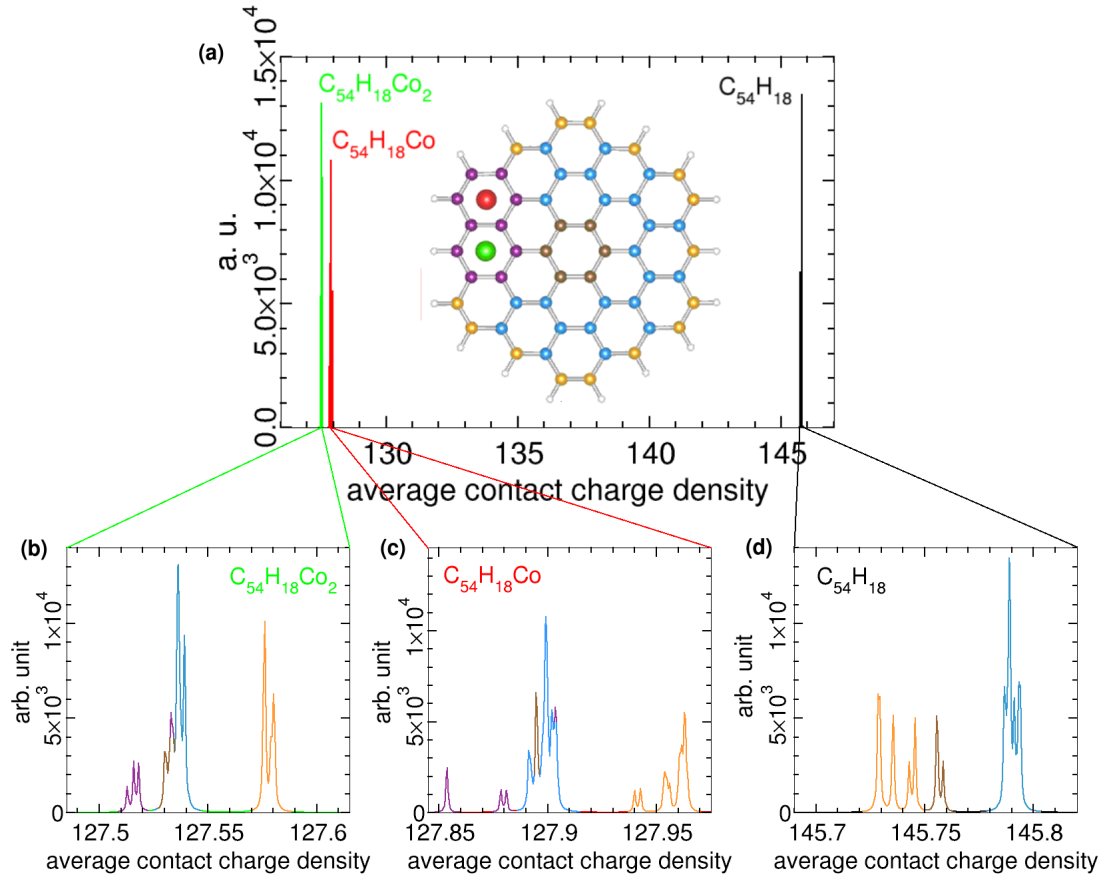


Figure 3.9: Relative intensity of the average charge contact density expressed in atomic units for C₅₄H₁₈, CoC₅₄H₁₈ and Co₂C₅₄H₁₈. Panel (a) includes the three calculated spectra, which are zoomed in panels (b), (c) and (d). Panel (a) displays colored atoms attending to the zones edge, inner, central, and ring where Co atom is bonded.

Fig. 3.9 (c) and (d), respectively. On one hand, the average contact charge density has considerable shift to smaller values, as shown in Fig. 3.9(a). The shifts are larger for the cases with more cobalt atoms. On the other hand, there is an inversion of the two main peaks, the orange and the blue peaks already seen in the spectrum for clean circumcoronene. The inversion is due to the larger shift experienced for the peaks of the inner carbon atoms. The carbon atoms bonded to cobalt, marked in purple, suffer the larger shifts for both cases. The different environments of these carbon atoms explain the splitting into different purple peaks.

3.3 Non-collinear ground state for Co_3Bz_3

We study in this section the magnetic order of the Co_3Bz_3 cluster shown in Fig. 3.10. We have carried out collinear and non-collinear calculations.

3.3.1 Collinear calculations

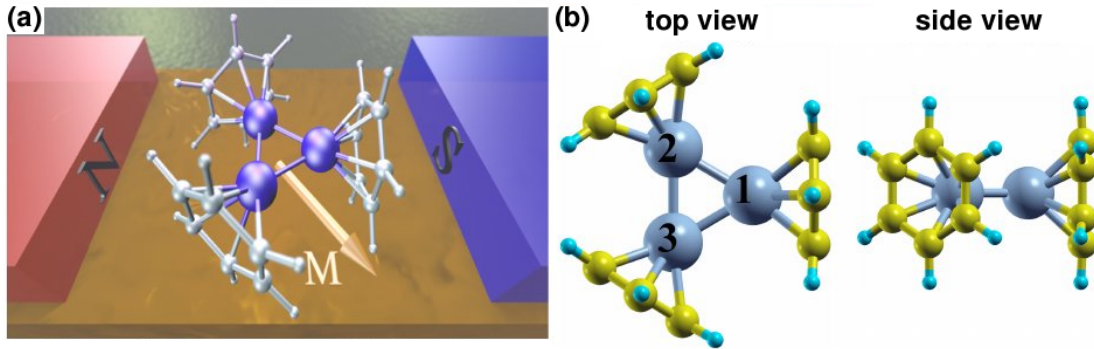


Figure 3.10: (a) Co_3Bz_3 cluster deposited on a substrate. (b) Ground state geometry. Cobalt atoms (blue spheres) form a triangle in the center, and are capped by benzene molecules. Carbon and hydrogen atoms are shown in yellow and cyan spheres.

Collinear calculations of the Co_3Bz_3 cluster have been carried out with the SIESTA method, which uses linear combinations of atomic orbitals. The results have been cross-checked using plane waves methods such as VASP and QUANTUM ESPRESSO. The ground state was found to be antiferromagnetic (AFM) with a total magnetic moment of $1 \mu_B$. The local magnetic moments on each atom were about $\pm 1 \mu_B$. The three cobalt atoms form a slightly distorted equilateral triangle, with two distances of $d_{1,2} = d_{1,3} = 2.34 \text{ \AA}$ and one of $d_{2,3} = 2.38 \text{ \AA}$. As for most rice-ball structures, the cobalt atom is placed over the center of the benzene at a distance of 1.61 \AA to its plane. Ferromagnetic states with total magnetic moments of 5 and $3 \mu_B$ have been also found for the Co_3Bz_3 cluster; however they lie 0.189 and 0.286 eV higher in energy, respectively. Previous calculations reported these ferromagnetic configurations as the ground state [65]. Con-

cerning stability, the antiferromagnetic Co_3Bz_3 has a gap of 1.26 eV. The real gap is expected to be even larger because generalized gradient approximation (GGA) calculations are reported to underestimate gaps [329, 346]. Therefore, the Co_3Bz_3 molecule can be considered stable as to be synthesized in experiments [110].

In order to clarify the role of benzene molecules in the preference for AFM states, we have considered the bare Co_3 cluster. The ground state was found to be a ferromagnetic isosceles triangle with two distances of 2.32 Å and one of 2.14 Å. The Co_3 distortion can be explained as a Jahn-Teller effect [364]. The total magnetic moment was $7 \mu_B$, with 2.61, 2.21 and 2.21 μ_B on each atom because of the isosceles configuration. The AFM configuration lies 0.6 eV higher in energy. There is a swap between the ferromagnetic and antiferromagnetic configurations for Co_3Bz_3 compared with Co_3 , which results from the attachment of benzene molecules. Concerning the geometry, adding benzene molecules symmetrizes the cobalt triangle through the transfer of 0.5 electrons to cobalt atoms. We have indeed checked that charging Co_3 cluster yields a more equilateral structure.

3.3.2 Non-collinear calculations

The AFM ground state of Co_3Bz_3 could be seen as a hint to search for the existence of non-collinear magnetic configurations because of geometric frustration as it happens for spin glasses [365]. To verify these ideas we have carried out non-collinear calculations using a full-potential linearized augmented plane wave method. We have found lower energy non-collinear configurations, as we show in Fig. 3.11. A set of three almost degenerated non-collinear configurations are found as the new ground state for Co_3Bz_3 , being 174.8 meV lower in energy than the AFM configuration. For the three cases the local magnetic moments on each cobalt atom are in-plane and lie parallel or perpendicular to the corresponding benzene ring.

About 22 meV higher in energy, we find two almost degenerated non-collinear configurations. The local magnetic moments are now perpendicular to the corresponding benzene rings, pointing either towards or away from the cobalt triangle center. For these five non-collinear configurations the local magnetic moment on each atom is within the range 0.83-0.97 μ_B . We have also found collinear configurations, which present magnetic moments oriented perpendicularly to the plane formed by the three cobalt atoms. Among them we have the AFM configuration, 174.8 meV higher than the ground state, and a ferromagnetic configuration with magnetic moment of $5 \mu_B$ at 948.5 meV. Note that to obtain these collinear configurations it was necessary to fix the directions of the local magnetic moments; otherwise, they relax to non-collinear arrangements because of strong spin-orbit coupling of cobalt atoms [366].

For the ground state configuration we analyze the magnetization density in Fig. 3.12. First, notice that magnetic moments are highly localized around the cobalt atoms. Second, the presence of vortex-like patterns between the cobalt atoms because of the rotation of magnetization density.

For strongly correlated systems, such as transition metals, it is advisable to include the on-site interactions in the calculations. As we are dealing here with clusters where the cobalt-cobalt interaction is crucial, it seems logical to add the Hubbard U and J_1

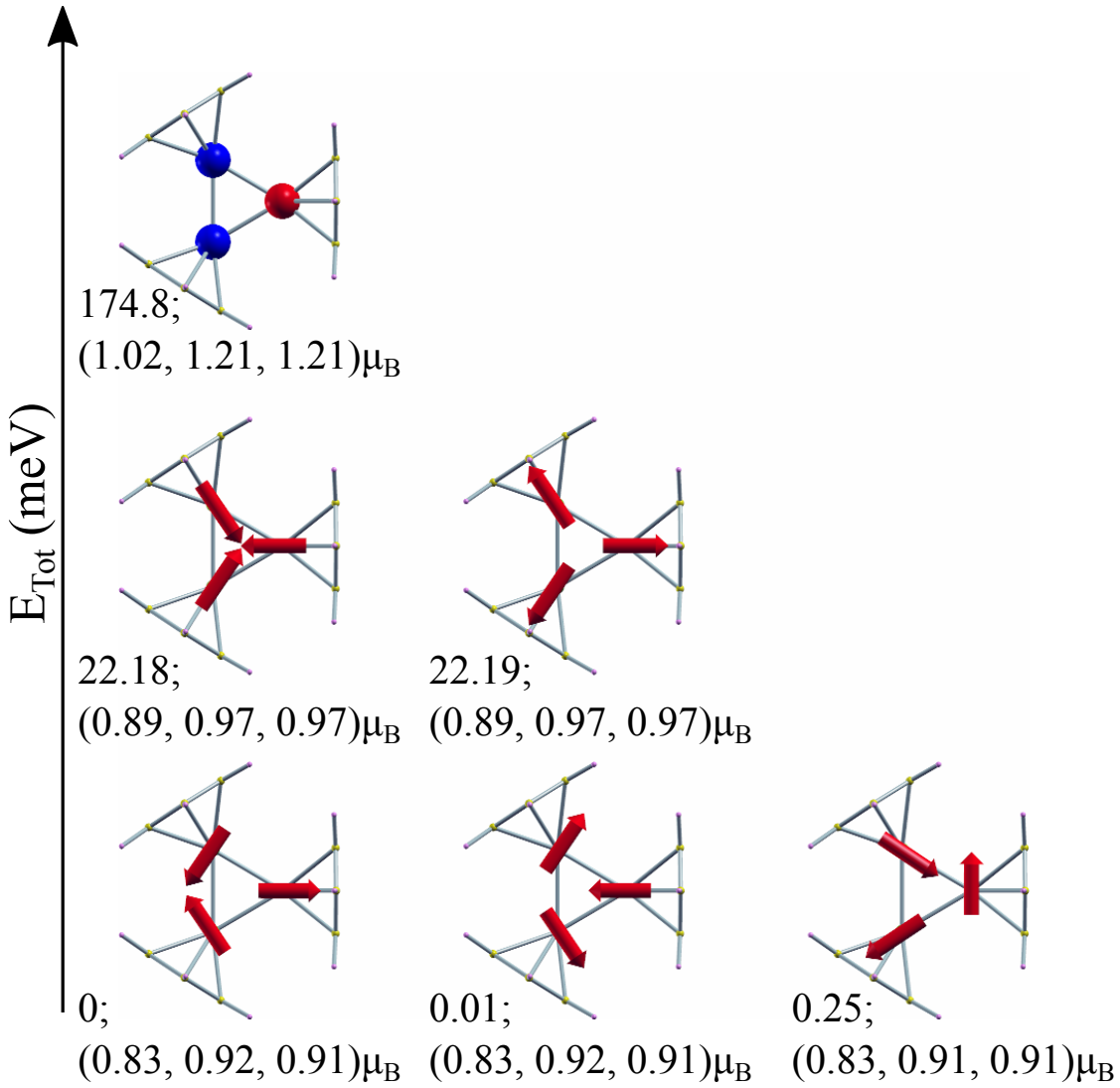


Figure 3.11: Low energy magnetic configurations of Co_3Bz_3 . The red arrows point the directions of the local magnetic moments of the cobalt atoms. Each label shows the energy difference (in meV) between the configuration shown and the ground state. In parentheses, the magnitude of the local magnetic moment at each cobalt atom (in units of μ_B) is given in the atom order shown in Fig. 3.10. Note that the non-collinear configurations become the ground state.

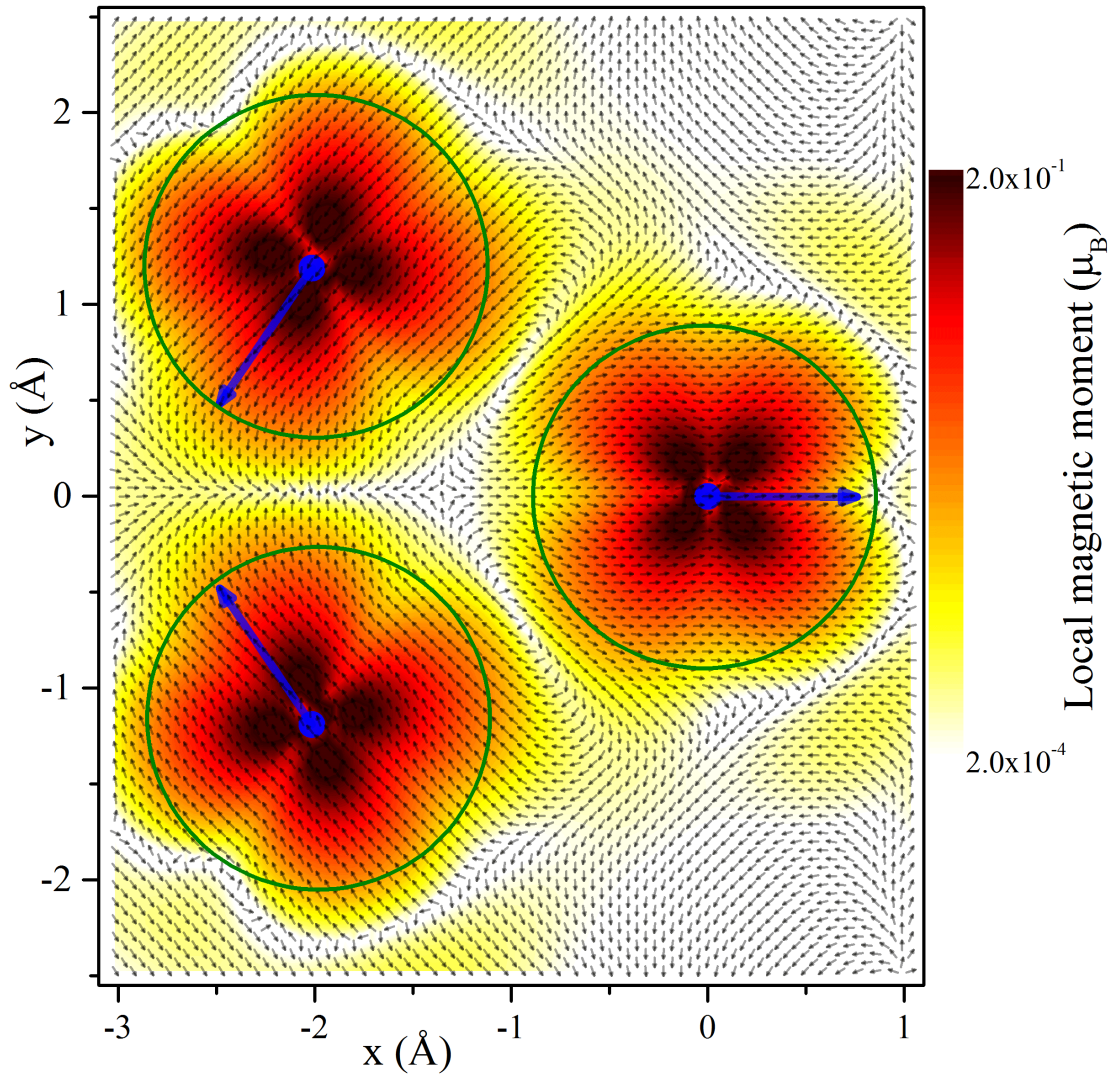


Figure 3.12: Vector field of the magnetization density of the ground state in the cobalt atom plane for the Co_3Bz_3 ground state. The small arrows point in the direction of the local density magnetic moments, and colors show the magnitudes of the vectors. Each green circle is around the muffin-tin radius of a cobalt atom, and the large blue arrows are the total magnetic moment assigned to the enclosed cobalt atom.

terms. We have carried out calculations using $U = 3$ eV for on-site interaction and $J_1 = 0.9$ eV for the exchange [367]. As expected the local magnetic moments are slightly increased because of localization of d-states. Nevertheless, the results are similar with the AFM configuration now at 332.5 meV, and the ferromagnetic configuration at 799.4 meV.

3.3.3 Anisotropic Heisenberg Spin Model

We propose a quantum spin model to describe the magnetic properties considering the previous results of ground and excited states. The Hamiltonian for the system is

$$H = J \left(\vec{S}_1 \cdot \vec{S}_2 + \vec{S}_1 \cdot \vec{S}_3 \right) + J' \vec{S}_2 \cdot \vec{S}_3 + \sum_{i=1}^3 H_i, \quad (3.1)$$

where J and J' are exchange constants, \vec{S}_i is the spin operator related to the i -cobalt atom as numbered in Fig. 3.10, and H_i is the local magnetic anisotropy of this atom induced by the neighbor benzene ring.

The chosen Hamiltonian implies two basic assumptions: (i) localized magnetic moments on the cobalt atoms as shown in Fig. 3.12, and (ii) quantized spins for each cobalt atom with the \vec{S}_i^2 magnitude conserved. The presence of two different exchange constants J and J' is related to the cluster geometry, with two different distances between cobalt atoms in a slightly distorted isosceles triangle. About the values for \vec{S}_i , the ground state configuration requires local magnetic anisotropy on each cobalt benzene unit, which indicates $\vec{S}_i > 1/2$ [364].

We choose a value of $\vec{S}_i = 3/2$ for each cobalt atom and we also tested other values such as $\vec{S}_i = 2$. The results are qualitatively similar. The density functional theory calculations for the CoBz system show that there is a splitting of the $3d$ levels in two groups of three and two levels. The triplet is lower in energy and almost fully occupied while the doublet is half occupied. The filling of the levels following the Hund's rule suggests a value of $3/2$. For the case of Co_3Bz_3 the degeneracy of the triplet is slightly broken but the electron filling is qualitatively kept.

The last term of the Hamiltonian, which represents the local magnetic anisotropy, is expressed as $H_i \approx D(S_i^{z_i})^2 + \dots$ [364], where D is a parameter representing the uniaxial anisotropy along the local high symmetry axis z_i . We use the lowest order terms compatible with C_{6v} symmetry agreeing with our density functional theory (DFT) results for the CoBz cluster. The Hamiltonian, with the operators expressed in a common numerical frame, was solved by numerical diagonalization of a 64×64 matrix. The eigenvalues and eigenvectors of the hamiltonian are ϵ_N and $|N\rangle$, respectively.

For the CoBz molecule our ELK calculations yield a magnetic anisotropy of 8.2 meV, being the easy axis out of the plane of benzene in a perpendicular disposition. The D value is -4.1 meV for $\vec{S}_i = 3/2$. The geometry of benzene molecules does not suffer large changes when computing Co_3Bz_3 , so we could think to use the local magnetic anisotropy of CoBz for the Hamiltonian. There are some facts strongly advising against doing so. First, the distances between the cobalt atoms (2.34 Å) are of the same order

3 Zero-dimensional systems

as the cobalt-carbon distances (2 Å). Second, there is charge transfer to cobalt atoms for Co_3Bz_3 , where they gain more than half electron. Third, there is a change of around 9 % in the cobalt-benzene distance. All these perturbations suggest that the D parameter should be fitted from Co_3Bz_3 results.

Therefore, we searched the values for the parameters J , J' and D that best fit the DFT total energy results. Remember that the features to be reproduced were: (i) a ground state with in-plane magnetization, (ii) two in-plane excitations at $\Delta_1 = 0.2$ meV and at $\Delta_2 = 22.2$ meV, and (iii) a first out-of-plane excitation at $\Delta_3 = 174$ meV with antiferromagnetic order.

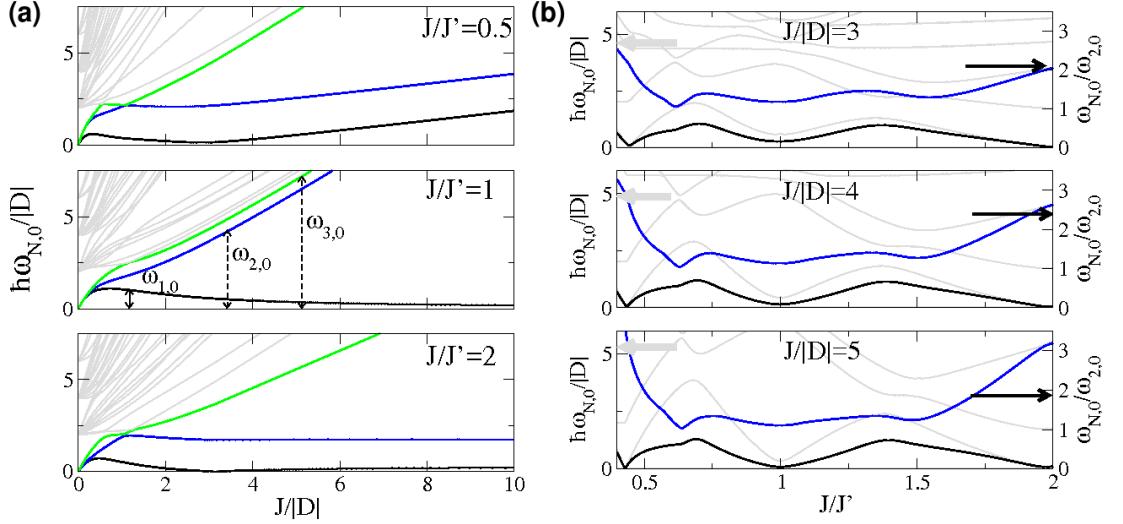


Figure 3.13: (a) Excitation energies from the ground state vs. $J/|D|$ for three different J/J' ratios. $\hbar\omega_{1,0}$ (black line) is identified with the 0.25 meV non-collinear excitation in Fig. (2), $\hbar\omega_{2,0}$ (blue line) with the 22 meV excitation, and $\hbar\omega_{3,0}$ (green line) with the antiferromagnetic configuration at 72 meV. (b) Excitation energies (gray lines, left axis) from the ground state vs. the ratio J/J' for three different ratios $J/|D|$. The ratios $\omega_{1,0}/\omega_{2,0}$ and $\omega_{3,0}/\omega_{2,0}$ (right axis) are plotted as thick blue and black lines, respectively. These ratios approach the DFT results of Fig. 2 when $J/J' = 2$ for $J/|D| = 5$.

We set three different ways choosing $J/J' = 0.5, 1$, and 2 . For each case we studied the energy spectrum for values of $J/|D|$ ranging from 0, which represents three isolated CoBz cases, to large values $J \gg |D|$, representing the isotropic cluster. We show the energy spectra in Fig. 3.13(a), including the excitation energies $\hbar\omega_{N,0}$ from the ground state. As the first excitation energy is associated to 0.2 meV and the second to 22.2 meV, we should choose parameters fulfilling that $\omega_{1,0}/\omega_{2,0} \approx 0.01$. The third excitation correspond to the AFM configuration out of plane found at 72 meV. The first two conditions are fulfilled for two cases: $J/|D| \approx 2.5$ in the asymmetric case with $J/J' \approx 0.5$, and $J/|D| \in [2.5, 6]$ with $J/J' = 2$. The fully symmetric case $J/J' = 1$ did

not provide good agreement for any value of $J/|D|$.

To fit the parameters we next study the excitation energies versus J/J' for three different ratios of $J/|D| = 3, 4, \text{ and } 5$. The $\omega_{1,0}/\omega_{2,0}$ and $\omega_{3,0}/\omega_{2,0}$ ratios versus J/J' are shown in Fig. 3.13(b) for three different values of $J/|D|$. The ideal ratios are close to 0 for $\omega_{1,0}/\omega_{2,0}$ and to 3.3 for $\omega_{3,0}/\omega_{2,0}$. Figure 3.13(b) also includes the energy spectra in gray. A value of $J/J' \approx 2$ yields the best agreement. The symmetric case is far from the searched values of the ratios in the range studied. In conclusion, the fitting parameters provide two different sets that present good agreement with DFT results: $(D, J, J') = (-12.64, 63.2, 31.6)$ meV and $(D, J, J') = (-12.64, 63.2, 134)$ meV.

There were two possible framework with asymmetric interactions: $J/J' \approx 0.5$ and $J/J' \approx 2$. The last option yielded the best agreement with DFT features, with $J \approx 5|D|$. However, the $J/J' \approx 0.5$ scenario could be also relevant under certain conditions. Although it could seem peculiar that the system features can be explained with so different scenarios, this duality has also been reported for magnetic clusters containing triangular Mn_3 clusters [368].

3.4 Ultrashort Mn-Mn bond for manganese benzene clusters

Experimental results showed that early $3d$ transition metals (Sc, Ti, V) prefer to form sandwich-like structures when they combine with benzenes [110]. Late transition metals (Fe, Co, Ni) with benzene prefer to form rice-ball structures. Manganese, in the middle of these to well-defined zones, is peculiar mainly because only the MnBz_2 molecule was reported [110]. The structures of larger manganese benzene clusters remain still unveiled.

We start by computing the rice-ball structure of Mn_3Bz_3 cluster, as shown in Fig. 3.2. We find that the relaxed geometry displays a striking short bond length of 1.88 Å between two manganese atoms. The ultrashort distance suggest that this phenomenon should be also present if we remove a manganese atom with its corresponding benzene ring. Indeed, when we computed Mn_2Bz_2 with two manganese atoms covered by two benzenes we obtained a ultrashort bond length of 1.8 Å. Besides, no magnetism was found for Mn_2Bz_2 , neither local or total. It appears that we have found a strong manganese-manganese bonding that yields ultrashort Mn-Mn distance and depletes magnetism as summarized in Fig. 3.14. Notice the key role of benzenes in this bonding scheme; manganese dimer is reported to be a van der Waals system with a distance of around 3.3 Å [369].

Motivated by the discovery of the ultrashort Mn-Mn bond, we studied other sizes of Mn-Bz clusters to check when this manganese-manganese bonding is present with more manganese atoms. Although we found that the basic unit is Mn_2Bz_2 , we know that it is also found for Mn_3Bz_3 . We computed other larger clusters such as Mn_4Bz_3 and Mn_4Bz_4 . We next comment the features of the manganese-manganese bonding within the rice-ball structures of Mn-Bz clusters.

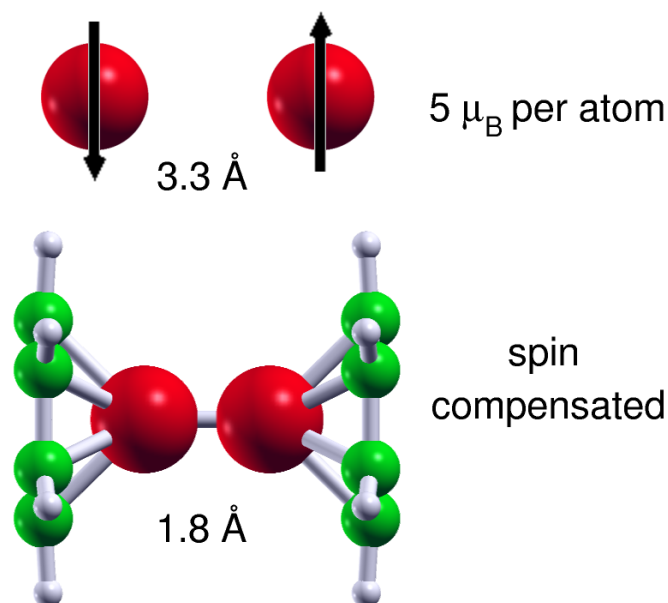


Figure 3.14: Scheme of the ultrashort bond on manganese dimer covered with benzenes. Note the large decrease in manganese-manganese distance and the total quenching of magnetic moments.

3.4.1 Rice-ball Mn-Bz clusters

Figure 3.15 collects the four different relaxed rice-ball structures of Mn-Bz clusters. We computed different geometries for each cluster size, obtained the lowest energy geometries reported here. Higher energy isomers are the sandwich-like structures.

The four ground state Mn-Bz clusters we present here display ultrashort manganese distances or related distortions because of this phenomenon. The simplest system is Mn_2Bz_2 , where the manganese-manganese bond length is only 1.8 Å. Notice that this bond length is strikingly short when compared with reported distances between manganese atoms in other environments, being 3.29 Å for manganese dimer [369], 2.93 Å for dimanganese decacarbonyl [370, 371], 2.4-2.6 Å for manganese carbides [372, 373], and 2.25-2.95 Å for manganese bulk [374]. We next comment separately on each Mn-Bz cluster.

The smallest cluster, Mn_2Bz_2 , can be seen as the building block for larger clusters displaying such ultrashort Mn-Mn distances. This idea is supported by the Mn_4Bz_4 cluster, which is nothing but two units of Mn_2Bz_2 conveniently arranged. We already commented on the Mn_2Bz_2 geometry; however the second hallmark of this phenomenon is magnetism depletion. The cluster has no spin polarization, with zero local magnetic moments on each manganese atom. The magnetism depletion is related to the short bond length of 1.8 Å, supporting the idea of close relationship between magnetism and distances [375, 376]. For larger sizes, total magnetism depletion requires perfect Mn_2Bz_2 building blocks. A reduction of magnetic moment from 5 to 3 μ_B has been reported

3.4 Ultrashort Mn-Mn bond for manganese benzene clusters

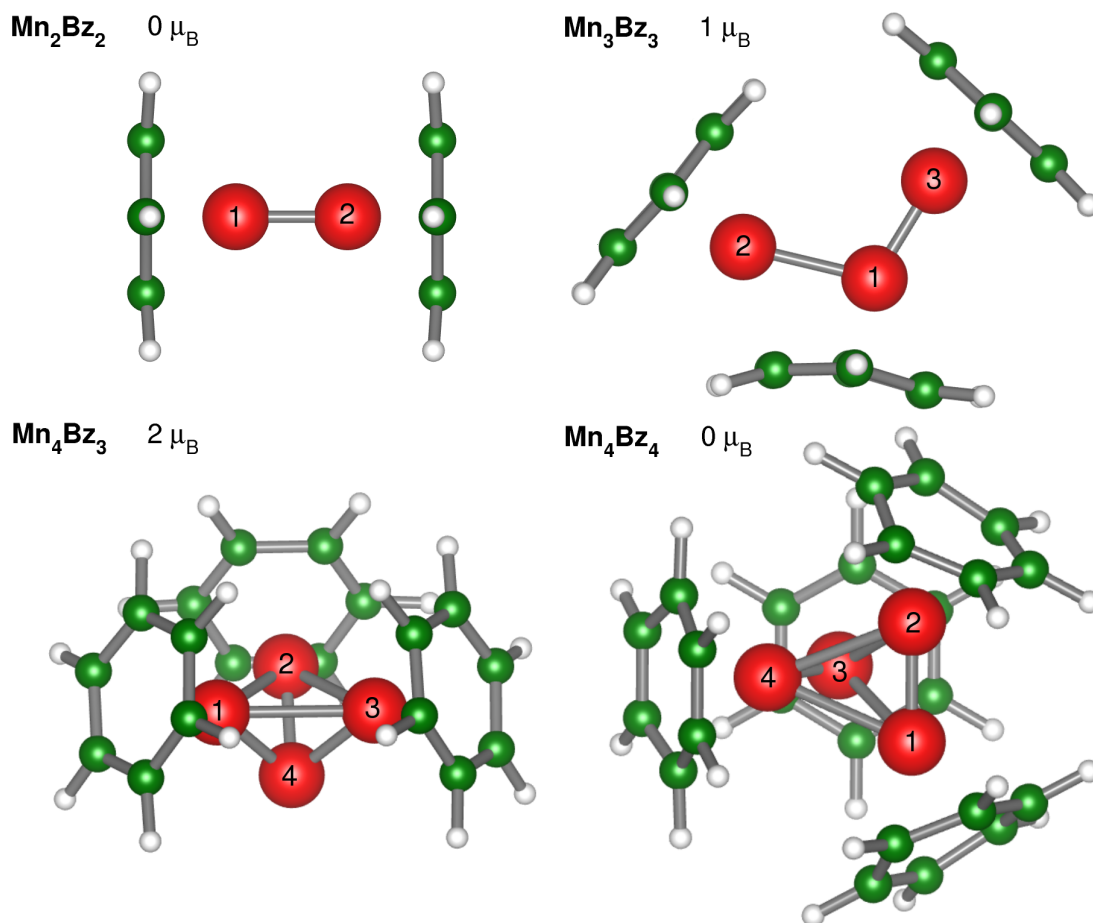


Figure 3.15: Geometries of the studied Mn_nBz_m molecules. Manganese, carbon and hydrogen atoms are displayed as red, green and white spheres, respectively. Total spin magnetic moment is shown for each case.

3 Zero-dimensional systems

for manganese atoms deposited on benzene rings [93]. Nevertheless, a total extinction of magnetism was totally unexpected. Notice that local magnetic moments were locally zero for manganese and for carbon atoms, and no induced magnetic moment was found.

We comment now on the Mn_4Bz_4 cluster, which can be obtained easily with two basic units of Mn_2Bz_2 rotating 90° one of them. Figure 3.15 shows benzenes tilting because of the Bz-Bz interaction in order to arrange the two building blocks in the final structure as a tetrahedron. Concerning the manganese atoms, there are two short bond lengths of 1.94 \AA between pairs of atoms labeled 1, 2 and 3, 4. This implies a slight increase with respect to the Mn_2Bz_2 cluster, because the neighbors number is increased. There are also four manganese-manganese bond lengths of 2.56 \AA , which agree with previously reported manganese-manganese bond lengths in clusters. Although the geometry is slightly distorted, the Mn_4Bz_4 cluster can be understood as the sum of two Mn_2Bz_2 clusters. This idea is reinforced because Mn_4Bz_4 has also magnetism depletion with all local magnetic moments being zero.

The same phenomenon of ultrashort Mn-Mn bonds was found for the two clusters Mn_2Bz_2 and Mn_4Bz_4 . However, other sizes of Mn-Bz clusters studied here, such as Mn_3Bz_3 and Mn_4Bz_3 , show distortions or deviations from the pristine case of Mn_2Bz_2 .

First we comment on Mn_3Bz_3 , which is the cluster where we found this behavior for the first time. An ultrashort bond is present between manganese atoms labeled as 1, 3 with a bond length of 1.88 \AA . The manganese atom (2) moves away from the manganese atom (3), separated by 3.32 \AA , so the interaction between them is largely reduced. The distance to the other manganese atom (1) is 2.22 \AA . Thus, a benzene molecule is bended. The modification introduced by the extra manganese atom (2) with respect to Mn_2Bz_2 avoids total magnetism depletion on manganese atoms 1, 3. The total magnetic moment is $1 \mu_B$ and the local magnetic moments are -0.57 , 1.53 and $0.28 \mu_B$ for manganese atoms 1, 2 and 3, respectively. Thus, small induced magnetic moments of opposed sign to that of the closest manganese atom and no larger than $0.06 \mu_B$ are found on carbon atoms. Note that the relaxed structure we present here looks unlike to be stable because of the way manganese atom (2) is left out and the interaction with manganese (3) totally reduced. Nevertheless, we find it to be the ground state because the ultrashort bond of two manganese atoms gives large stability.

Finally we consider the Mn_4Bz_3 cluster, which also deviates from standard ultrashort Mn-Mn bond found in Mn_2Bz_2 and Mn_4Bz_4 . It is a good idea to analyze the Mn_4Bz_3 cluster as a test to measure the importance of benzenes in ultrashort Mn-Mn bond. To obtain this cluster, we remove a benzene from the Mn_4Bz_4 cluster and we fully relax the geometry. The final structure, where the two short bond lengths disappear, shows that the role of benzenes is pivotal to achieve ultrashort Mn-Mn bond. Now we have an equilateral triangle of manganese atoms (1, 2, 3) with distances of 2.62 \AA , each atom with its neighbor benzene. The manganese atom (4) that lost its benzene is placed in the center of the triangle bonding the three manganese atoms at 2.05 \AA . Although the bond length is short and similar to ultrashort Mn-Mn bond, a brief comment on the magnetism of the cluster clarify the differences. The total magnetic moment of the cluster is $2 \mu_B$, being the local moments $1.07 \mu_B$ for manganese atoms (1, 2, 3) and $-0.86 \mu_B$ for manganese atom (4). Therefore, there is antiferromagnetic coupling between the

3.4 Ultrashort Mn-Mn bond for manganese benzene clusters

manganese atoms and the bonding is slightly different from ultrashort Mn-Mn bond previously reported. There is small negative induced magnetic moment of 0.02-0.03 μ_B on carbon atoms.

To give quantitative arguments on the stability of these four Mn_nBz_m clusters, we computed the formation energy per manganese atom as $E_f = (n * E_{Mn} + m * E_{Bz} - E_{total})/n$, obtaining the values of 1.76, 1.99, 1.98 and 2.18 eV for Mn_2Bz_2 , Mn_3Bz_3 , Mn_4Bz_3 and Mn_4Bz_4 , respectively. We also find that the gaps of the clusters are 1.17, 0.86, 0.50 and 0.72 eV for Mn_2Bz_2 , Mn_3Bz_3 , Mn_4Bz_3 and Mn_4Bz_4 , respectively. Note that as the cluster gets larger the stability is reduced, specially for Mn_4Bz_3 . However, considering that generalized gradient approximation calculations underestimates the gap notoriously [329, 346], the Mn-Bz clusters proposed here seem to be stable.

The distances between the manganese and the carbon atoms for the four Mn-Bz cluster agree with those reported previously. We measured the manganese-carbon distances for the four Mn-Bz cluster, finding 2.06 Å for Mn_2Bz_2 , and 2.10-2.15 Å for Mn_3Bz_3 and Mn_4Bz_3 , with the manganese atoms not exactly equidistant to the six carbon atoms on the near benzene rings. For each manganese in Mn_4Bz_4 there are four carbon-manganese distances of 2.15 and two of 2.37 Å because benzene rings are slightly tilted because of nearest benzenes. The manganese-carbon distances are agreeing to previously reported values. Manganese-carbon distances are 2.08 and 2.12 Å for some organomanganese compounds [377]. Averaged distances are between 2.09 and 2.17 Å for manganese carbides [372, 373]. Manganese adatom over graphene hollow yields a distance of 2.47 Å [231, 378].

For all studied Mn-Bz clusters, the carbon-carbon distances are mostly within the interval 1.43-1.44 Å. However, the distorted benzene as that of Mn(1) in Mn_3Bz_3 presents values slightly varying within 1.40-1.45 Å. These values are comparable to 1.40 Å reported for the free benzene molecule [379]; there is a slight enlargement to be explained by the presence of manganese atoms.

We next analyze the charge transfer under the Mulliken scheme. For the Mn_2Bz_2 cluster there is small transfer of 0.18 electrons from each manganese atom to the carbon atoms. For case of Mn_3Bz_3 the manganese atom numbered as (3) lost 0.11 electrons, while the other manganese atoms remain almost neutral. For Mn_4Bz_3 , the manganese atoms (1), (2) and (3) lost 0.07 electrons, and the manganese atom numbered as (4) gains 0.42 electrons. In total, manganese atoms receive 0.21 electrons from benzenes. For Mn_4Bz_4 there are 0.15 electrons moving from benzene to manganese atoms, being 0.04 in each atom. No special trends or large charge transfers are explaining the ultrashort Mn-Mn distance.

The ultrashort Mn-Mn distances reported here should be present for larger manganese-benzene compounds such as Mn_5Bz_5 or Mn_6Bz_6 . However, we do not continue studying larger rice-ball compounds because the arrangement of the benzenes is really complicated because of lack of space and their own interactions. Furthermore, it is difficult to place more manganese atoms inside the cluster in a way to obtain ultrashort Mn-Mn distances. For larger structures, this effect could be similar to that of Mn_3Bz_3 , distorting the structure, because of the large energy gain associated to the ultrashort Mn-Mn distances.

3.4.2 Multiple-decker Mn-Bz clusters

The ultrashort Mn-Mn bond implies an energy fall of 2 eV and the large dimerization induced for Mn_3Bz_3 cluster suggests a large stability. Nevertheless, we have also computed the sandwich-like structures, also known as multiple-decker, to ensure we are focusing on the ground state Mn-Bz clusters structures. Figure 3.16 shows the multiple-decker structures for the four Mn-Bz clusters studied here. The difference in total energy with respect to the counterpart structure is shown for each case, suggesting the preference for rice-ball structures. Besides, high total magnetic moments are found for multiple-decker structures, as shown in Fig. 3.16, in contrast to the previously reported values for rice-ball structures.

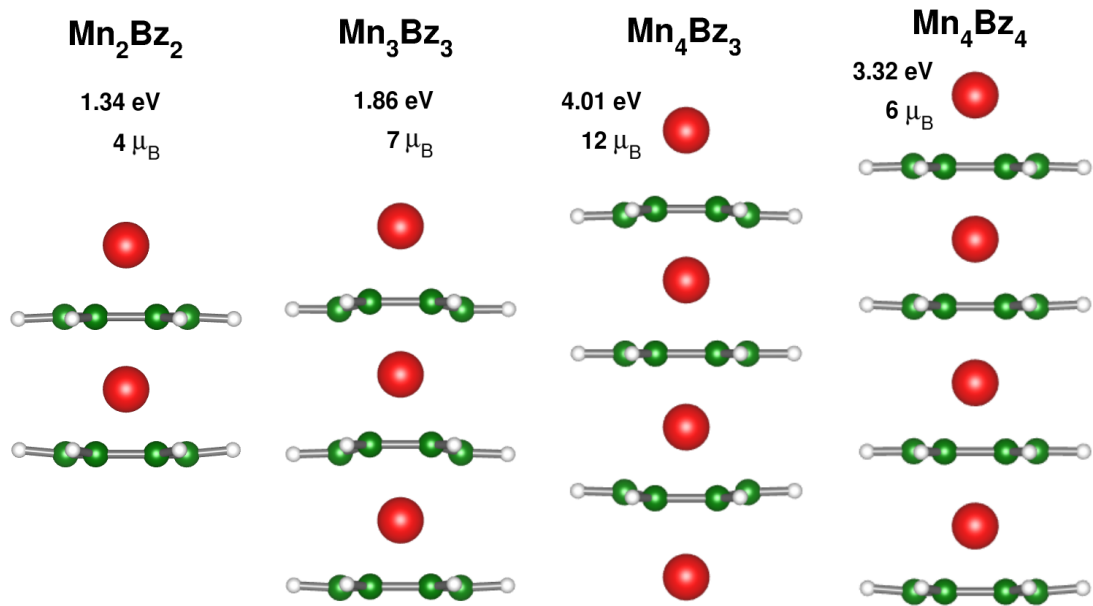


Figure 3.16: Sandwich-like isomers of the four different manganese benzene clusters studied. For each cluster the energy difference with rice-ball structures and the total magnetic moments are included.

3.4.3 A detailed analysis of Mn_2Bz_2

Stability

Ultrashort Mn-Mn distances are found in the Mn-Bz clusters studied here. Mn_3Bz_3 is distorted because of adding another MnBz unit to Mn_2Bz_2 , and Mn_4Bz_4 is similar to two units of Mn_2Bz_2 . Therefore, we focus on Mn_2Bz_2 to understand the bonding mechanism and the causes for such ultrashort Mn-Mn distances. As commented previously, the relaxed geometry of Mn_2Bz_2 cluster yields a manganese-manganese distance of 1.825 Å, which is almost half the distance reported for the bare manganese dimer [369] and still

considerably smaller than the values reported for the bulk, which varies between 2.2 Å and 2.95 Å depending on the allotropic structure [374]. The ultrashort Mn-Mn bond length when caging the dimer with benzenes imply changing the character of the bonding. The Mn-Mn short distance is not the only surprising hallmark of this phenomenon; also magnetism is totally depleted, with zero local magnetic moments on each atom. This is in contrast with the high-spin solutions reported for generalized gradient approximation (GGA) [380–383].

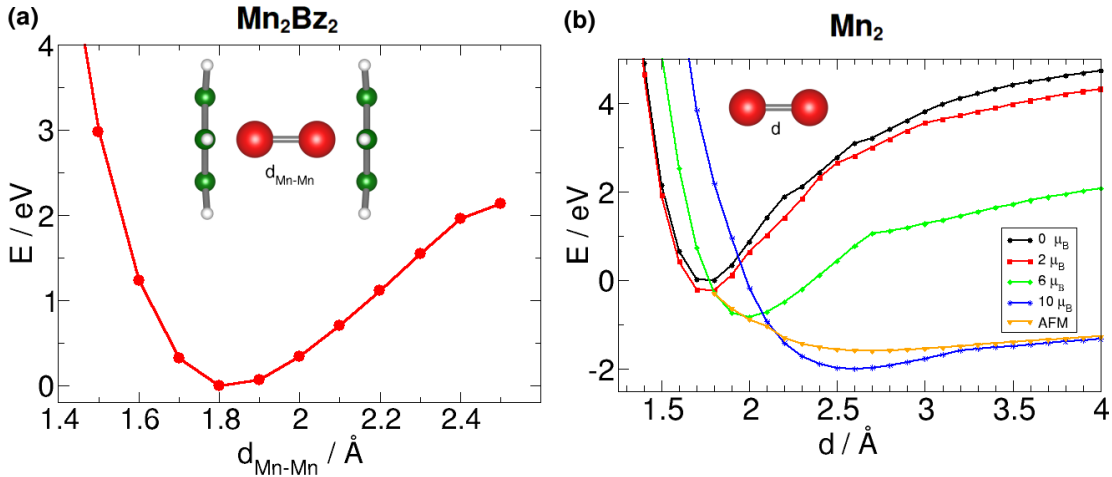


Figure 3.17: (a) Total energy versus distance for Mn_2Bz_2 . (b) Total energy for different spin fixed configurations and total magnetic moment for free spin calculations versus distance for Mn_2 .

To verify the stability of the Mn_2Bz_2 cluster we carried out single point calculations enlarging the manganese-manganese distance in steps of 0.1 Å, keeping the benzenes at the same relative position with the nearest manganese atom. We plot the energy versus the manganese-manganese distance in Fig. 3.17(a). The curve suggests a clear minimum around the distance of 1.8 Å with a depth of more than 2 eV. The distance corresponding to the minimum shows the manganese-manganese bond length. Apart from the deep minimum shown by the calculations, the relaxed ground state geometry was obtained with two different codes, which ensures that it is a true minimum and not a saddle point. This can be brought into contact with previously commented gap of 1.17 eV and formation energy per manganese atom of 1.76 eV. It is important to comment that no magnetic moment was found for these single point calculations until the manganese-manganese distance was 2.4 Å. Then, the ultrashort Mn-Mn bond length and magnetism depletion are related phenomena [375, 376].

Spin compensation

Now we try to explain the non-magnetic solution found for Mn_2Bz_2 by studying the bare manganese dimer. We have carried out single point calculations of the Mn_2 molecule for

3 Zero-dimensional systems

distances between from 1 Å to 4 Å with a step of 0.1 Å. The total magnetic moment of Mn₂ changed largely depending on the distance. For example, we found 2 μ_B for distances shorter than 1.7 Å and 10 μ_B for distances larger than 2.4 Å. This is evidence of the existence of difference curves of energy versus distance for different spin solutions. Then, we fixed the total magnetic moment of the Mn₂ to 0, 2, 6 and 10 μ_B and compute the corresponding curves as shown in Fig. 3.17(b).

The global minimum was obtained for a high spin solution of 10 μ_B at a distance between manganese atoms of about 2.5 Å, agreeing with previous calculations of this level of approximation (LDA/GGA) [380–383]. Close in energy we find the antiferromagnetic solution, specially for manganese-manganese distances larger than 3.2 Å, as reported previously [384]. Nevertheless, we are interested in the ultrashort Mn-Mn distances that explain the bonding for Mn₂Bz₂. We obtain two minimum close in energy for distances around 1.7-1.8 Å, corresponding to low spin solutions of 0 and 2 μ_B . Note that the distance between manganese atoms is the same as for Mn₂Bz₂ ground state. This local minimum with low spin and short distances has already been reported for manganese dimer [385, 386]. We show here that the attachment of benzenes stabilizes the minimum of 0 μ_B .

The explanation for the reduction of the magnetic moment comes from the 3*d* shells of manganese atoms. There is a delicate balance between exchange and spin splitting, and even small changes in distances can modify the magnetic character of Mn₂ [387]. When the two atoms are largely separated the spin splitting is large as for the free atom and the total magnetic moment is high. However, when the manganese atoms come closer the spin splitting is reduced. Thus, spin minority bonding orbitals can be occupied previously to spin majority antibonding orbitals. For short distances the result can be even total depletion of magnetism.

The bare manganese dimer is an example where the choice of the exchange correlation functional is pivotal within density functional theory calculations. The reason is that this molecule is bonded by van der Waals interaction with distance larger than 3 Å [374, 388, 389], which require the use of hybrid functionals [390] or even the CASSCF method [369]. By these methods it is possible to understand the antiferromagnetic coupling and the bond length larger than 3 Å reported in experimental works [391–395].

Here these functionals are not used because there is a strong ultrashort Mn-Mn bond for Mn₂Bz₂, which can be calculated accurately with GGA. Concerning the Mn₂ calculations, we are aware that we do not obtain the real van der Waals minimum, but for the short distances we are interested in strong interaction and GGA functionals work correctly.

3.4.4 Ultrashort Mn-Mn bonding

Molecular orbitals

In this section we study the molecular orbitals of the Mn₂Bz₂ cluster. They are the result of combining the 3*d* and 4*s* atomic shells of manganese with the well-known molecular orbitals of benzene. Carbon has four valence electrons, three of them are used

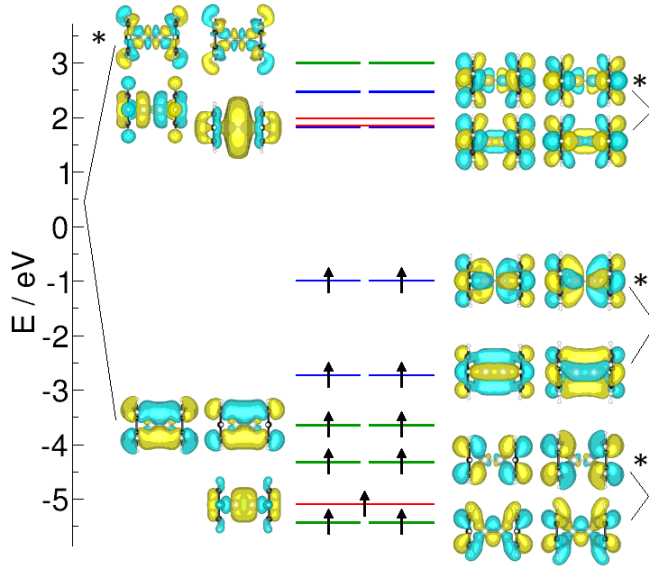


Figure 3.18: Energy levels and wave functions near the Fermi energy using the SIESTA method. The lines color denotes the molecular orbitals types: red for σ , green for π , and blue for δ . Antibonding orbitals are marked up with asterisks.

to build strong σ bonds with two carbon and one hydrogen neighboring atoms. The fourth electron remains as a p_z electron, forming delocalized π bonds with other five p_z electrons. These six p_z electrons combine to produce six molecular orbitals, which split into four energies attending to their symmetry: σ (π_1), π (π_2, π_3), δ (π_4^*, π_5^*) and ϕ (π_6^*). The π and δ degenerated levels would split for the Mn_2Bz_2 cluster.

We now comment on the $3d$ orbitals of manganese, degenerated for the atom. The presence of the crystal field of benzene split the $3d$ levels attending to their symmetry. If we set the xy plane containing benzene, being the z axis perpendicular to benzene, the $3d$ levels split into three energies: $d\sigma$ ($3d_{z^2}$), $d\pi$ ($3d_{xz}, 3d_{yz}$), and $d\delta$ ($3d_{xy}, 3d_{x^2-y^2}$). As the $3d_{z^2}$ orbital points to the center of benzene ring, it is not expected to suffer large hybridization. The $4s$ orbitals would hybridize with π_1 levels from benzene because of the same symmetry.

The molecular orbitals of Mn_2Bz_2 cluster are obtained by the hybridization of d levels and benzene molecular orbitals with the same symmetry. Figure 3.18 shows the molecular orbitals near the Fermi energy for a spin of Mn_2Bz_2 cluster, the other spin is equal because of spin compensation. The σ , π and δ molecular orbitals can be identified by the number of nodal planes (0, 1 and 2, respectively). For example, a filled σ orbital is shown in red in the lower part of Figure 3.18. The π molecular orbitals are lower in energy than the δ orbitals and they are filled with four more electrons. Figure 3.18 shows bonding and antibonding molecular orbitals. The number of π molecular orbitals is equal to eight, found as the sum of the four π orbitals of benzenes (two from each)

3 Zero-dimensional systems

and the four d levels from manganese atoms ($3d_{xz}$, $3d_{yz}$ from each) that hybridize. The same applies to the δ molecular orbitals.

In summary, we have found spin compensated electronic structure with σ , π and δ molecular orbitals built by hybridization of $3d$ orbitals of manganese and p_z orbitals of carbon following certain symmetry rules.

Electron localization function

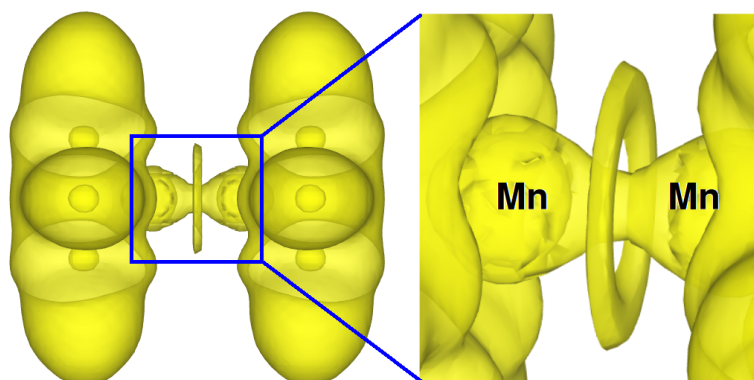


Figure 3.19: (Left) Electron localization function (ELF) of the Mn_2Bz_2 cluster at the cut off value of 0.125. (Right) The highlighted part of the left figure is zoomed in.

To complete the analysis of the bonding between manganese atoms for Mn_2Bz_2 cluster, we have calculated the electron localization function (ELF). The ELF informs about the bond electron localization. Figure 3.19 shows the ELF for Mn_2Bz_2 , including a zoom on the interatomic region. Two main features are observed related to the manganese bonding. First, there is a clear lobe linking the two manganese atoms, which represents the $3d_{z^2}$ orbitals. Second, there is a circular disk in the center of the two atoms which represents the π and δ molecular orbitals. These results agree with the molecular orbitals described previously. The presence of two different lobes evokes a triple bond between manganese atoms. Furthermore, the ELF value at which the basins for these bonds appear for the first time indicates the bonding type. In this case the basins are found for values of 0.125 for the ELF, which means they have delocalized metallic-like character.

3.4.5 Considerations related to possible synthesis of Mn_2Bz_2

We next bring into contact our calculations with experiments. Spectroscopic experiments on organometallic clusters report that only MnBz_2 is synthesized [110]. They suggested that the absence of larger manganese benzene compounds is due to the existence of spin limits on the growth process [396]. In order to shed more light on the possible existence of a barrier preventing formation of larger compounds, we have carried out calculations of Mn_2Bz_2 varying the distance between benzenes and fixing total spin moments to 0,

6, 8 and 10 μ_B . For each spin we computed the cluster for $d_{\text{Bz}-\text{Bz}}$ varying between 4.8 and 10 Å with a step of 0.2 Å. Figure 3.20(a) shows a scheme explaining the parameters varied in calculations. Carbon and hydrogen atoms are allowed to relax x - and y -coordinates, having $d_{\text{Bz}-\text{Bz}}$ frozen. Manganese atoms are in the center with a distance of 2 Å between them. Manganese atoms are allowed to relax on z -coordinate, but not on x - and y -coordinates.

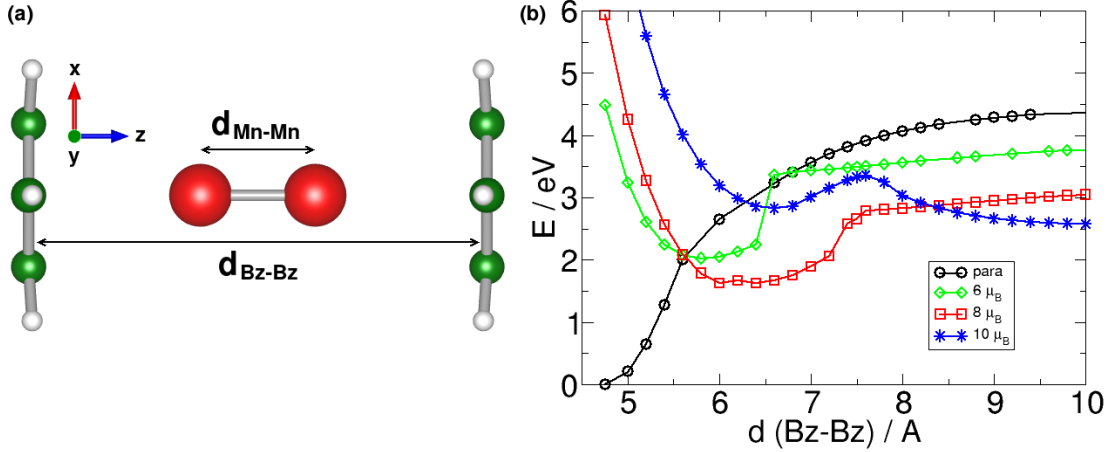


Figure 3.20: (a) Scheme of the barrier calculations. (b) Mn_2Bz_2 total energies for different distances between the benzene molecules. The total magnetic moment is fixed.

Figure 3.20(b) show the curves of energy versus distance between benzenes for different total spin values. Note that for short distances low spin clusters are more stable. However, for large distances high spin clusters are preferred. The spin curves order is inverted. Thus, there must be large change of the magnetic moment versus distance, which can be an obstacle to the formation of the Mn_2Bz_2 cluster. Nevertheless, it could be possible to overcome this barrier. A thermal excitation of high spin cluster with benzenes notably separated could get the molecule to an excited state, from which the route to the non-magnetic global minimum would be easier.

Fig. 3.20(b) shows two abrupt steps for curves of 6 μ_B at 6.4 Å and of 8 μ_B at 7.2 Å. For large $d_{\text{Bz}-\text{Bz}}$ values, manganese atoms have two options: stay bonded together in the middle or separate themselves and bond their corresponding benzene. These specific distances also correspond to inflection points in the potential curves with maximum manganese-manganese forces. For larger distances the manganese atoms prefer to bond together and separate from benzene molecules.

3.5 Large magnetic anisotropy for Ni_3Bz_3

Nickel clusters have been studied both theoretically and experimentally [121, 133, 397–400]. However, the size Ni_3Bz_3 of nickel-benzene clusters lacks understanding. Here we

study the structure and the electronic and magnetic properties of the Ni_3Bz_3 cluster.

3.5.1 Non spin-orbit calculations

Nickel benzene clusters have been reported to prefer rice-ball structures rather than sandwich-like [110]. Here we relax Ni_3Bz_3 rice-ball structures, obtaining that nickel atoms form an equilateral triangle with distances of 2.34 Å. There are small differences in the distances about mÅ, producing an isosceles triangle. Following numbers on nickel atoms in Fig. 3.21, the Ni(2)-Ni(3) distance is 2 mÅ shorter than Ni(1)-Ni(2) and Ni(1)-Ni(3), which are equal. The nickel-nickel distances obtained here are similar to those reported previously; 2.40 Å for Ni_2Bz_2 , 2.45 Å for Ni_3Bz_2 [401], and 2.34 Å for Ni_2Bz_2 [51]. The nickel atoms are placed over the center of the corresponding benzene, and the distances to the carbon atoms are within the interval 2.21-2.22 Å. Similar distances have been reported previously such as 2.04-2.21 Å for Ni_2Bz_2 and 2.08 Å for Ni_3Bz_2 [401] and 2.14-2.34 Å for Ni_2Bz_2 [51]. The larger range of distances is caused because the nickel atom is not η^6 -bonded. The distances between carbon atoms are 1.41 Å, slightly larger than the 1.40 Å reported experimentally for benzene [379].

To compare we also computed the bare Ni_3 cluster, obtaining an equilateral triangle with distances of 2.20 Å. Again there are small differences about mÅ. Benzenes covering the nickel trimer produces larger nickel-nickel bond lengths by 0.14 Å. This 6 % increase is explained because the nickel electrons are now shared by the Ni-Ni and Ni-C bonds, weakening the Ni-Ni bonds.

We comment on the charge transfer under the Mulliken scheme. For Ni_3Bz_3 the three nickel atoms gain more than 0.65 electrons from benzenes, around 0.2 electrons per nickel atom.

The total spin magnetic moment of Ni_3Bz_3 ground state cluster is $2 \mu_B$ with equal contribution from the three nickel atoms. A spin compensated excited state of Ni_3Bz_3 is found 0.2 eV higher in energy. Note that NiBz and Ni_2Bz_2 clusters are fully spin compensated. The results for the Ni_3 cluster show a total total magnetic moment of $2 \mu_B$ agreeing with literature [399, 400, 402–408].

3.5.2 Spin-orbit calculations

Energy and spin magnetic moments

We have already analyzed the ground state geometry of the Ni_3Bz_3 cluster. Next we carry out spin-orbit calculations using the relaxed geometry of Ni_3Bz_3 . First, we seek for non-collinear configurations of the local magnetic moments on nickel atoms. We tried many different input arrangements, however they relax to collinear configurations. Then we study magnetic configurations with the local magnetic moments within the plane of nickel atoms, such as M_x and M_y , and oriented perpendicularly to this plane. Figure 3.21(a) shows the magnetic configurations for Ni_3Bz_3 with their relative energy. The out-of-plane configuration, M_z , is found to be 8 meV more stable than the in-plane configurations, which are almost degenerated with a difference smaller than 0.1 meV. We find that the easy axis of magnetization for Ni_3Bz_3 is out-of-plane and the magnetic

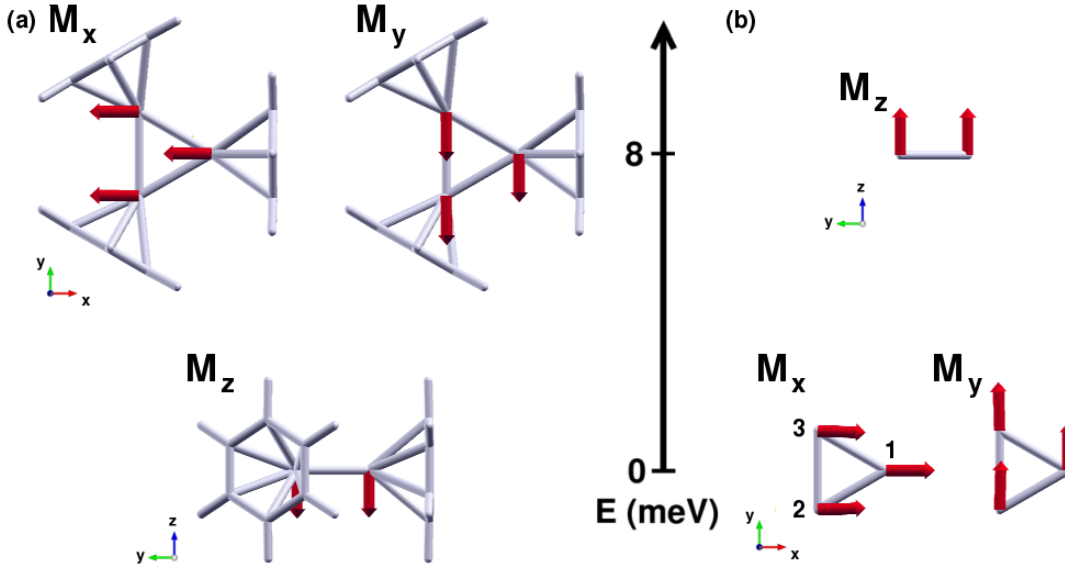


Figure 3.21: Energy of the different magnetic dispositions of the local spin magnetic moments represented by red arrows for (a) Ni_3Bz_3 and (b) Ni_3 . Number on nickel atoms are included.

anisotropy energy is around 8 meV. Note that for Fe, Co, and Ni bulk ferromagnets the intrinsic magnetic anisotropy is in the order of μeV per atom [409–411].

To compare we carried out spin-orbit calculations for the Ni_3 cluster, and we follow the same procedure as for Ni_3Bz_3 . First we searched for non-collinear states without success, and then we computed similar magnetic configurations as those for Ni_3Bz_3 . Figure 3.21(b) includes the orientation of the local magnetic moments for the different configurations and their relative energy. The in-plane configurations, M_x and M_y , are almost degenerated with energies differences lower than 0.2 meV. Notice that there is an inversion with respect to Ni_3Bz_3 results, being the in-plane configurations preferred by 8 meV over the out-of-plane configuration M_z . We conclude that the attachment of benzenes changes the easy axis of magnetization from in-plane to out-of-plane.

Orbital magnetic moments

The magnetic moment has two different contributions, the spin and the orbital magnetic moments. We study the orbital magnetic moments in the different magnetic configurations reported on the previous section. Tables 3.1 and 3.2 include the magnitudes of the atomic averaged operators $|L|$, $|S|$ and $|J|$ for Ni_3 and Ni_3Bz_3 . The $|L|$ value was similar in magnitude to $|S|$ for in-plane configurations of the Ni_3 cluster. However the attachment of benzenes reduces the $|L|$ value drastically. The largest $|L|$ values for Ni_3Bz_3 are found for the M_z configuration.

Apart from the magnitude of the orbital magnetic moments, the directions are also

3 Zero-dimensional systems

Table 3.1: Atomic averaged operators $|L|$, $|S|$ and $|J|$ for each atom for the four magnetic states of Ni_3 cluster.

	M_x			M_y			M_z		
	1	2	3	1	2	3	1	2	3
$ L $	0.44	0.23	0.23	0.01	0.39	0.39	0.06	0.06	0.06
$ S $	0.34	0.34	0.34	0.33	0.34	0.34	0.33	0.33	0.33
$ J $	0.78	0.51	0.51	0.34	0.71	0.71	0.39	0.39	0.39

Table 3.2: Atomic averaged operators $|L|$, $|S|$ and $|J|$ for each atom for the three magnetic states of Ni_3Bz_3 cluster.

	M_x			M_y			M_z		
	1	2	3	1	2	3	1	2	3
$ L $	0.05	0.07	0.07	0.07	0.05	0.05	0.12	0.12	0.12
$ S $	0.34	0.35	0.35	0.34	0.35	0.35	0.34	0.35	0.35
$ J $	0.39	0.42	0.42	0.41	0.40	0.40	0.46	0.47	0.47

important. Figure 3.22 shows the arrangement of the local orbital magnetic moments for the studied magnetic configurations. Note that the values of the local orbital magnetic moments are multiplied by a factor ten (five for the averaged values $|L|$ and $|S|$) with respect to local spin magnetic moments to ease their picture. For the Ni_3Bz_3 configurations shown in Fig. 3.22(a) the local orbital magnetic moments follow local spin magnetic moments shown in Fig. 3.21, with a little tilting on nickel atoms (2) and (3) for in-plane configurations. The configurations for Ni_3 in Fig. 3.22(b) show larger values as already comment but also larger discrepancy on the direction of the local orbital magnetic moment for in-plane configurations. The local magnetic moment is almost zero for nickel atom (1) in the M_y configuration. The finding can be explained because orbital magnetic moment is averaged over the sphere associated to each atom. Thus, the different directions of the orbital magnetic moment around the atom compensate and average to zero. Note that the local orbital magnetic moments are aligned with the local spin magnetic moments for the out-of-plane configurations of Ni_3Bz_3 and Ni_3 .

Finally we comment on some trends and we compare with previous results. When benzenes are added to the bare Ni_3 cluster covering the trimer, the orbital magnetic moments are notably reduced. Furthermore, benzenes force orbital magnetic moments to follow spin orbital magnetic moments. Therefore, benzenes addition makes the cluster behave more bulk-like. X-ray magnetic circular dichroism (XMCD) spectroscopy of isolated nickel clusters cations of 7-17 atoms in the gas phase yielded orbital magnetic moments within the interval of 0.25-0.43 μ_B [412], agreeing with our results. Much smaller values of 0.06 μ_B /atom have been reported for the bulk [413, 414], a large decrease as we found when adding benzenes.

The reason for the larger orbital magnetic moments in small clusters is that the crystal field interaction created by the neighbors is small compared with that of the bulks. Applied to our system, the benzenes induce a crystal field that quenches the orbital

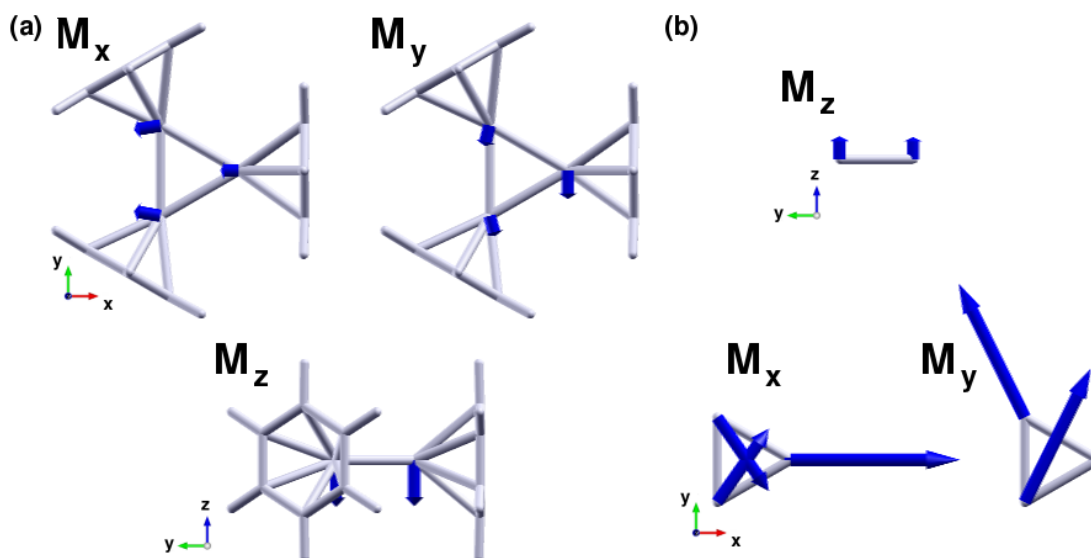


Figure 3.22: Local orbital magnetic moments represented by the blue arrows for the configurations of (a) Ni_3Bz_3 and (b) Ni_3 . There is a factor ten (five for the quantum numbers S and L) to local spin magnetic moments shown in Fig. 3.21.

magnetic moments of nickel atoms. Nevertheless, even for small clusters, the orbital magnetic moments are largely quenched to the 5-25 % of the atomic value of $3 \mu_B$ [415]. Note that in our calculations the largest values of the local and total orbital magnetic moments are found for the most stable configurations. For Ni_3 these are the in-plane configurations, and for Ni_3Bz_3 it is the out-of-plane configuration. This agrees with the predicted involvement of orbital magnetic moments in the magnetic anisotropy energy [416–418].

In summary, bare small nickel clusters such as Ni_3 have the orbital magnetic moments enhanced with respect to the bulk. However, covering cluster with benzenes quenches the orbital magnetic moments because of the crystal field they introduce.

3.5.3 Electronic structure

Ni_3Bz_3

In this section we study in detail the electronic structure of the Ni_3Bz_3 cluster to explain the stability order commented in previous section. We analyze the filling of the levels close to the Fermi energy. Figure 3.23 shows the levels close to the Fermi energy for non-spin-orbit (a) and spin-orbit (b) calculations. First we comment on non-spin-orbit levels. The highest occupied molecular orbital (HOMO) is a doubly degenerated level. There are two degenerated minority spin levels at the Fermi energy which share one electron. We plot in Fig. 3.23(a) the wave functions associated to these levels. The

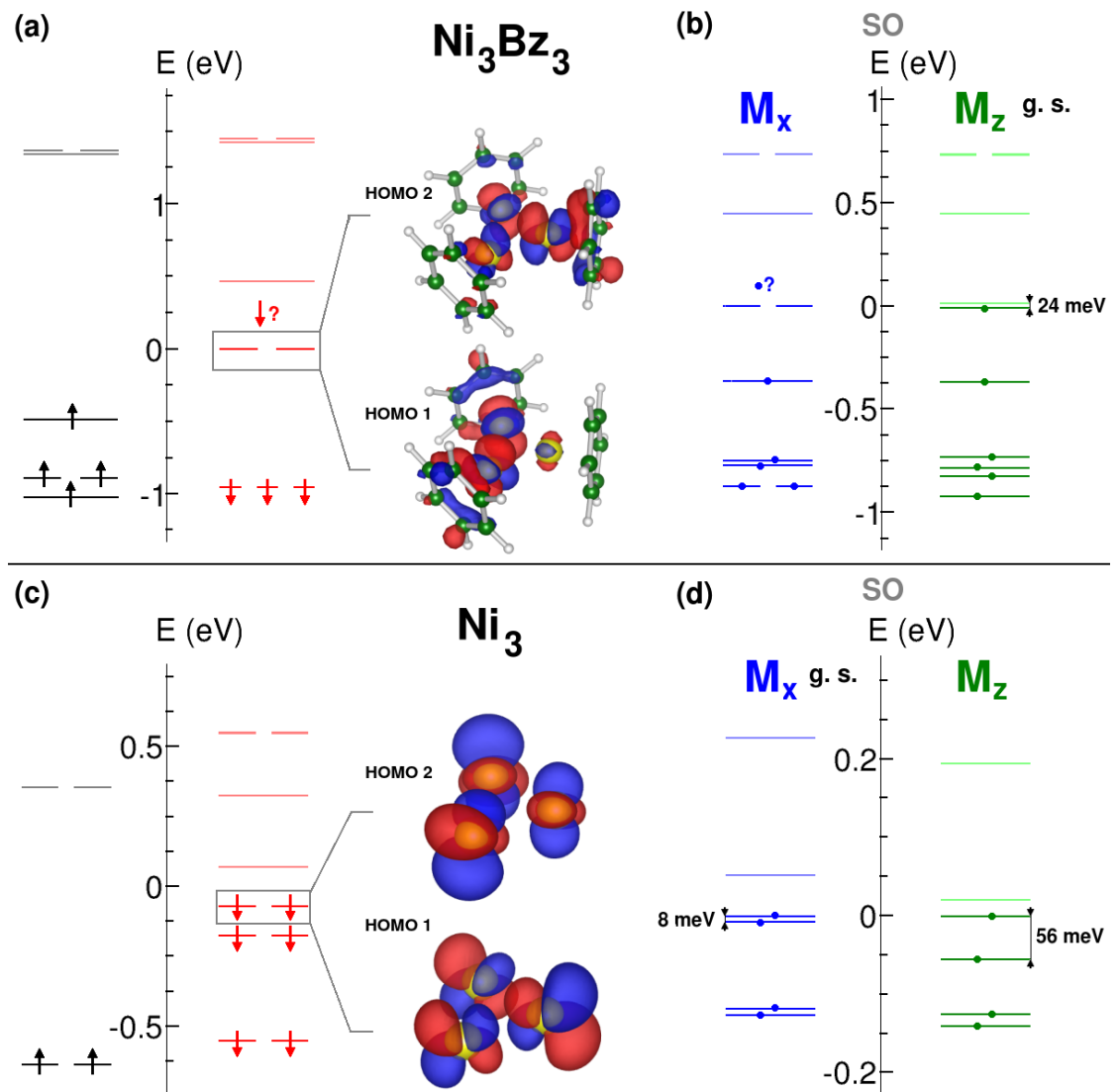


Figure 3.23: Levels close to the Fermi energy for a set of calculations. (a) non-spin-orbit Ni_3Bz_3 , (b) spin-orbit (SO) M_x and M_z configurations of Ni_3Bz_3 , (c) non-spin-orbit Ni_3 , and (d) spin-orbit (SO) M_x and M_z configurations of Ni_3 .

lobes of the wave functions mark d orbitals with strong z component. The non-spin-orbit calculations were carried out using the VASP and the SIESTA methods, both yielding similar levels.

Next we compare with spin-orbit calculations of Ni_3Bz_3 cluster carried out using the ELK code. For spin-orbit calculations there is no distinction between majority and minority spin. We found three different magnetic configurations for the Ni_3Bz_3 cluster, two in-plane and one out-of-plane. The degenerated in-plane configurations, M_x and M_y , present a similar distribution of the electronic levels. Figure 3.23(b) shows the levels for M_x and M_z configurations. For the in-plane configuration there are two degenerated levels at the Fermi energy, replicating the behavior found for the non-spin-orbit calculations. Nevertheless, for the out-of-plane configuration M_z there is a splitting of 24 meV for these levels. As a result, the highest energy bonded electron is perfectly located on the lowest energy level. The stabilization of the M_z configuration by 8 meV with respect to in-plane configurations is explained by the breaking of degeneration of levels at the Fermi energy and the consequent filling of a single level. The band splitting for the M_z configuration apply to all levels, such as those shown in the lower part of Fig. 3.23(b).

Ni_3

We repeat a similar study for the bare Ni_3 cluster. Figure 3.23 shows the levels for the non-spin-orbit (c) and the spin-orbit (d) cases. For non-spin-orbit calculations the HOMO is again a doubly degenerated minority spin level. However, now there are two electrons filling the two levels. The wave functions of these levels shown in Fig. 3.23(c) have d orbitals with a strong z component. These two levels are equivalent to those found for Ni_3Bz_3 cluster. For the spin-orbit calculations of Ni_3 cluster the levels shown in Fig. 3.23(d) follow a similar behavior as for Ni_3Bz_3 . The Ni_3 out-of-plane configuration M_z shows a levels splitting of 56 meV, while the in-plane configurations show a slight levels splitting of 8 meV. However, both levels were occupied for non-spin-orbit calculations and remain filled for spin-orbit calculations. The levels splitting does not change the levels filling and therefore it is not a source of stability as it happens for Ni_3Bz_3 .

Density of states

Next we try to look at the composition of the couple of degenerated levels that split when an out-of-plane magnetic field is applied. We plot the projected density of states (DOS) for Ni_3Bz_3 and Ni_3 in Fig. 3.24. The projected density of states is obtained from non-spin-orbit calculations. For both clusters the $3d$ levels hybridize in two couples according to symmetry: $3d_{xz}$ - $3d_{yz}$, and $3d_{xy}$ - $3d_{x^2-y^2}$. The first couple hybridize the levels with z component and the second the levels lying within the plane of nickel atoms. For Ni_3Bz_3 there is also carbon contribution at most energies.

For Ni_3Bz_3 there is a peak at the Fermi energy which is formed by $3d_{xz}$ - $3d_{yz}$ in equal part. This peak represent the two degenerated levels that split when an out-of-plane magnetic field is applied. The spin splitting for this peak is roughly 0.9 eV. The lowest unoccupied molecular orbitals (LUMO) is a single level formed by hybridization of $3d_{xy}$ -

3 Zero-dimensional systems

$3d_{x^2-y^2}$, and the spin splitting for this peak is around 1 eV. This picture agrees with Fig. 3.23(a). For Ni_3 the peak near the Fermi energy, now is shifted to lower energies, agreeing with the fully occupied degenerated levels shown in Fig. 3.23(c). This peak is composed by the hybridized couple $3d_{xz}-3d_{yz}$, like for Ni_3Bz_3 . A difference compared with Ni_3Bz_3 is that the $4s$ and $3d_{z^2}$ contribution appear near the Fermi energy, while for Ni_3Bz_3 they are at deeper energies.

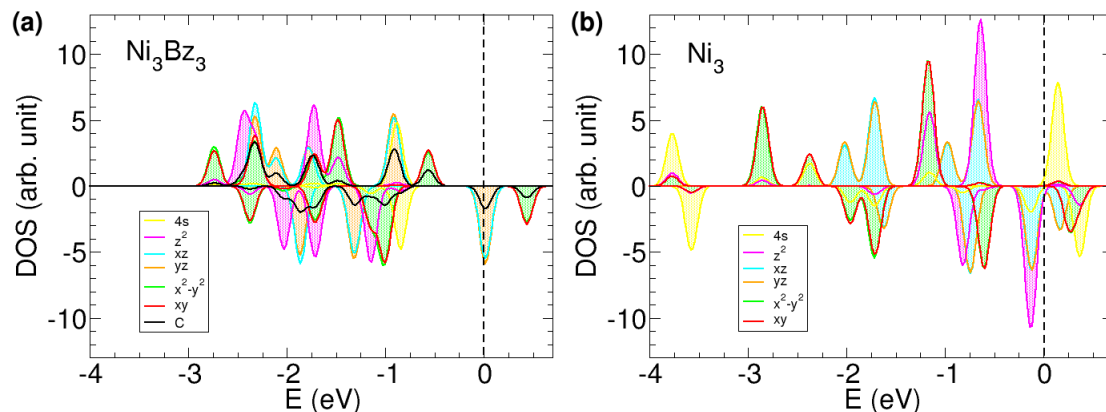


Figure 3.24: Projected density of states for (a) Ni_3Bz_3 and (b) Ni_3 .

Reason for the spin splitting

After commenting on the levels and the density of states of Ni_3Bz_3 and Ni_3 clusters, we focus on the reason for the splitting of the two degenerated levels at the Fermi energy. These two levels have the $3d_{xz}-3d_{yz}$ hybridization, with a strong z component. Thus, when an out-of-plane magnetic field is applied, as for M_z , these levels are affected. The reason for the splitting is the two non-equivalent levels, although degenerated. A level present major contributions from nickel atoms (2) and (3), which behave similarly, and the other level has larger contribution from the nickel atom (1). These differences are related with distances between nickel atoms, forming slightly distorted isosceles triangle. The two degenerated z -contributed levels respond differently to the out-of-plane magnetic field because they are not equivalent, and consequently there is spin splitting.

3.6 Conclusions

In this chapter we have studied molecules formed by transition metal atoms or clusters combined with benzene or polycyclic aromatic hydrocarbons. The two main interactions are the metal-metal interaction and metal-carbon interaction. For cobalt, manganese and nickel, the metal-metal interaction is the leading term. Direct outcomes of the strong metal-metal interaction are the preference for the rice-ball structure for the metal-benzene compounds, and the cobalt atoms bonded together when they are over circumcoronene. First, we comment on the results obtained for the adsorption of cobalt

atoms and clusters on the PAH circumcoronene. We checked that the ground state of bare circumcoronene has no local magnetic moments on the edges, which requires even larger size PAHs. When depositing cobalt atoms, they prefer to be over hollow sites rather than top or bridge sites. When a cobalt atom is over a hollow site, the six carbon-carbon bonds are weakened and six cobalt-carbon bonds are established. There is large hybridization of cobalt $3d$ orbitals with carbon p_z orbitals. Further, the edge hollows are largely favored over the center ones. The preference of cobalt atoms and clusters for the edges is explained because of the charge accumulation on this area of circumcoronene. The electron localization function of circumcoronene shows the existence of double bonds on the corners and charge accumulation on carbon atoms located on the border. The cobalt dimer prefer to be arranged perpendicularly to circumcoronene, with the lower cobalt atom placed over a hollow site in the edges. The Co_4 cluster adopts a tetrahedral geometry with three cobalt atoms forming a plane that lies parallel over circumcoronene. Preferably, the three cobalt atoms lie over three neighbor hollows close to the edge. However, there are several configurations with the cobalt tetrahedron lying over different locations of circumcoronene within a stability interval of 0.4 eV. This suggests that Co_4 could easily slide over the surface of circumcoronene, although further calculations would be required to study barriers. The cobalt atoms for Co_2 and Co_4 gain stability when they are bonded together rather than spread separately over the surface of circumcoronene. The cobalt-cobalt bond is the strongest interaction.

Although the circumcoronene is not magnetic, the adsorption of cobalt atoms yield a system with net magnetic moment. For cobalt atoms over hollow sites a total magnetic moment of $1 \mu_B$ per atom is obtained, and it is $3 \mu_B$ for cobalt atoms on top sites. Values of $4 \mu_B$ and $6 \mu_B$ are obtained for Co_2 and Co_4 over circumcoronene, respectively. The presence of cobalt atoms induce negative magnetic moments on circumcoronene. For the ground state of each case the values are $-0.25 \mu_B$ for the cobalt atom, almost zero for the cobalt dimer and $-0.4 \mu_B$ for the Co_4 cluster.

When cobalt atoms are deposited over circumcoronene, cobalt electrons transfer towards carbon atoms agreeing with the electronegativity of these elements. A value of 0.16 electrons is found for the ground state of Co atom, and the values is ten times smaller for the Co_4 case. However, when the cobalt dimer is perpendicular to circumcoronene, electrons are gained by cobalt atoms. There is no clear correlation between the charge transfer and the stability.

We study the hyperfine structure of circumcoronene and cobalt clusters, focusing on the contact charge of carbon atoms, which can be directly related to the isomer shift observable on the experiments. Our aim was to give guidelines to detect the cobalt presence over circumcoronene or any other PAH. We obtained two main peaks for bare circumcoronene, which swap and shift to smaller values when cobalt is deposited. The shift is larger for two cobalt atoms than for isolated cobalt atoms.

We then discuss the results for cobalt interacting with benzene, specifically the Co_3Bz_3 cluster. The cobalt atoms form an almost equilateral triangle in the center, covered by three benzene molecules. Previously the interaction between cobalt atoms in small clusters had been reported to be ferromagnetic. Here we find for the first time non-

3 Zero-dimensional systems

collinear states for the cobalt atoms as the ground state. There is a set of three non-collinear states almost degenerated, and two non-collinear states at 22 meV. Higher in energy at 170 meV we find an anti-ferromagnetic state, and even higher at more than 0.9 eV we find a ferromagnetic state. Note that the bare Co_3 has a ferromagnetic ground state. Covering with benzenes we find non-collinear magnetic states, with the local magnetic moments on each cobalt atom parallel or perpendicular to the benzene plane.

We modeled the Co_3Bz_3 system using a Hamiltonian with two different exchange constants, J and J' , to account for two different interactions between cobalt atoms and we include a term representing the local anisotropy. The fitting of the model according to the energy spectra yielded two possible pictures: $J > J'$ or $J < J'$. Note that the equilateral case does not provide solutions to fit the data. The results suggest that two cobalt atoms interact differently with the other, following the small differences in the cobalt-cobalt distances.

Substituting the cobalt atoms by manganese atom to obtain Mn_3Bz_3 produces scalene triangle in the center, with two manganese atoms at about 1.9 Å. We calculated other manganese benzene clusters, such as Mn_2Bz_2 , for which we also find an ultrashort manganese-manganese distance of 1.8 Å and total magnetism depletion. The presence of benzenes allow for this strange bonding where the distance is highly reduced compared with the bare Mn_2 and to any other manganese bonds. Associated with this ultrashort bond length we found the absence of magnetism. We analyzed a new manganese-manganese bonding scheme by varying the manganese-manganese distances, finding that it provides the system with high stability. Consequently, we are able to find ultrashort Mn-Mn bonds in larger systems, such as Mn_3Bz_3 and Mn_4Bz_4 . Further, we study the possible synthesis of Mn_2Bz_2 varying the distance and the spin. It seems that there are barriers that can be overcome by spin changes, a fact that is key for experimentalists.

Finally, we study the same cluster with nickel atoms, the Ni_3Bz_3 cluster. The structure is similar to Co_3Bz_3 ; however we are not able to stabilize non-collinear configurations. We find that all the collinear states within the nickel plane are degenerated, and the out of plane configuration is 8 meV lower in energy. The magnetic anisotropy of Ni_3Bz_3 is 8 meV and the easy axis of magnetization is out of plane. The detailed analysis of the cluster electronic structure showed that there is a couple of degenerated levels at the Fermi energy formed by $3d$ orbitals with z component. These levels share an electron, and when an out-of-plane magnetic field is applied they split and stabilize the system. In-plane magnetic fields keep the degeneration of these levels. When comparing with the bare Ni_3 cluster, we find that again the in-plane configurations are degenerated, however now they are 8 meV more stable than the out-of-plane configuration. Benzenes addition produces these degenerated levels, sharing an electron, which are responsible for the change of the easy axis respect to bare Ni_3 .

In summary, the attachment of benzene molecules to cluster of three transition metal atoms produce novel and unexpected effects such as the non-collinear magnetism for cobalt, the ultrashort Mn-Mn bonds for the manganese case, and the change of the easy axis of magnetization for the nickel clusters.

4 Graphene doping: cluster adsorption and substitutional atoms

4.1 Introduction

Graphene outstanding properties stimulated the research on possible applications for the new two-dimensional material. However, the use of graphene for applications in devices requires in most cases to tune its properties, either to open a band gap or to induce magnetic moment, etc. In this context, the study of doped graphene appears to be central. Although there are plenty of possibilities to dope graphene we study here transition metal atoms and clusters, including traditional ferromagnets as cobalt. In this chapter we follow two approaches to the problem of graphene doping: first we study cobalt clusters adsorption on graphene, and second consider on transition metal atoms as substitutional atoms in graphene single vacancies.

4.2 Adsorption of clusters over graphene

We study cobalt clusters interacting with graphene focusing on Co_{13} . Experiments evidence isomers for cobalt clusters [419]. It is important to comment on isomerization effects for transition metal clusters. When magnetic properties are measured for a beam of certain size transition metal clusters the outcome is the averaged value taken into account all the isomers present in the beam. Therefore, it is interesting to gain knowledge on isomers present for the clusters under study. Nevertheless, experimental techniques are not enough to clarify the predominant isomer; it is required to carry out theoretical calculations that help ordering isomers attending to stability and magnetism. To shed some light over cobalt clusters and their interaction with graphene we carry out theoretical calculations of Co_{13} clusters deposited on graphene. Figure 4.1 shows the five isomers proposed here for Co_{13} moving towards a graphene sheet, representing the experimental setup associated to our calculations.

4.2.1 Stability of free Co_{13} clusters

We check the stability order of the free Co_{13} clusters. Calculations on the growing patterns of cobalt clusters suggest a bi-planar structure as the most stable Co_{13} isomer [420]. Table 4.1 collects our results for the free isomers of Co_{13} cluster. Looking at the values of the binding energy, the two-dimensional isomer called *hcp 2d* appears as the ground state agreeing with the previous results. It is followed by the *pine* isomer, which appears as slightly more stable than the *icosahedron* isomer. Other two isomers labeled

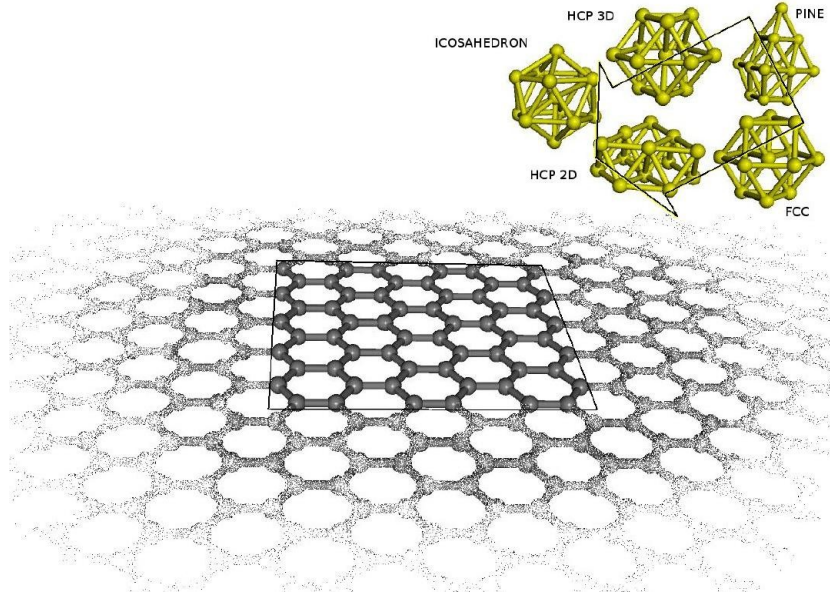


Figure 4.1: Image of the proposed experiment: isomers of Co_{13} move toward graphene.

as *fcc* and *hcp 3d* appear with lower binding energy. The binding energies are similar compared to previous results [421] and the bond lengths are slightly large [421, 422].

On the total spin magnetic moment, the largest value is found for the *icosahedron* around $31 \mu_B$, followed by *hcp 2d* and *fcc* with $27 \mu_B$, *hcp 3d* with $25 \mu_B$ and *pine* with $23 \mu_B$. The difference in the magnetic moment between *hcp 2d* and *icosahedron* can help to differentiate them in experiments and identify the ground state isomer. For the magnetic moment per atom the *icosahedron* shows $2.38 \mu_B$ similarly to previous results [423], while the *hcp 2d* has $2.07 \mu_B$. Experimental values reported for Co_{13} clusters are close to $2 \mu_B$ [424, 425], which supports the two-dimensional isomer as the ground state. The larger magnetic moment obtained for the *icosahedron* is related to the narrowing of the *d* bands because of a slightly larger average bond length caused by the cobalt-cobalt repulsion between central and surface atoms.

Finally, the average coordination number shows that *icosahedron* isomer presents more neighbors with a different local environment than other isomers. So we expect it as the most stable isomer. However, stability order for these clusters takes into account the ion and the electron repulsion [426]. The ion-ion repulsion term becomes dominant for the late *3d* transition metal elements over the term accounting for the electrons and ionic cores interaction, which favored *icosahedron*. The *hcp 2d* isomer allows the reduction of both ion and electron repulsion [426] and becomes the most stable isomer for Co_{13} -free cluster.

We comment on the role of the on-site electron interactions in the stability order of free Co_{13} isomers. For the values of 2 or 3 for U_{eff} , the *icosahedron* emerges as the most stable isomer over the two-dimensional isomer [367]. U_{eff} is defined as Coulomb minus

exchange parameters $U_{eff} = U - J$.

Table 4.1: Binding energies ($E_{b_{free}}$), total magnetic moment (μ_T), average magnetic moment per cobalt atom (μ_{av}), average bond length (d_{av}), and average coordination number ($coord_{av}$) for five different free Co_{13} isomers in decreasing order of stability.

isomer	$E_{b_{free}}$ (eV)	$\mu_T(\mu_B)$	$\mu_{av} (\mu_B)$	$d_{av}(\text{Å})$	$coord_{av}$
<i>hcp 2d</i>	3.508	26.954	2.073	2.44	5.54
<i>pine</i>	3.452	23.000	1.769	2.40	5.54
<i>icosahedron</i>	3.444	30.974	2.383	2.48	6.31
<i>fcc</i>	3.413	27.000	2.077	2.42	5.54
<i>hcp 3d</i>	3.406	25.000	1.923	2.42	5.54

4.2.2 Stability of Co_{13} isomers bonded to graphene

Figure 4.1 shows the Co_{13} clusters flying towards graphene, previously to their adsorption. In this section we analyze the stability of the isomers once they are deposited over graphene. The adsorption process can imply a noticeably structural distortion or rearrangement. Figure 4.2 shows all the studied relaxed geometries of the five isomers adsorbed on graphene. We have tried plenty of possible configurations for each isomer. The *icosahedron* was deposited on vertex, edge and triangular face. For *pine* and *hcp 2d* isomers there are different faces and we tested them. The most stable disposition for each isomer is shown enlarged in Fig. 4.3.

We check which isomer presents the most stable disposition when adsorbed on graphene. The *hcp 2d* was the ground state isomer for the free cluster. We found that the *icosahedron* isomer adsorbed on graphene yields a more stable configuration, reversing the stability order.

The *icosahedron* ground state consists of a relaxed icosahedron-like cluster that distorts because of the rearrangement of cobalt atoms close to graphene. The isomer is bonded by an edge of the icosahedron with two cobalt atoms bonding graphene directly. Other two cobalt atoms forming triangular faces with that edge move towards graphene and establish cobalt-carbon bonds, summing up to four cobalt atoms bonding carbon atoms. Previously a different arrangement of the icosahedron with only three cobalt atoms bonding carbon atoms was proposed as the ground state [421]. We have also obtained this structure appearing higher in energy (0.16 eV).

Now we comment on other isomers minima. For the *hcp 2d* isomer we have found four different minima, lying at 0.06, 0.22 and 0.25 eV respect to the most stable arrangement. When we set the zero energy for the most stable minimum of each isomer as done in the Fig.4.2, there are some trends that let us group the different isomers. For example, *pine* and *hcp 2d* structures present minima at 0.38-0.58 eV and at 0.36-0.59 eV respectively;

4 Graphene doping: cluster adsorption and substitutional atoms

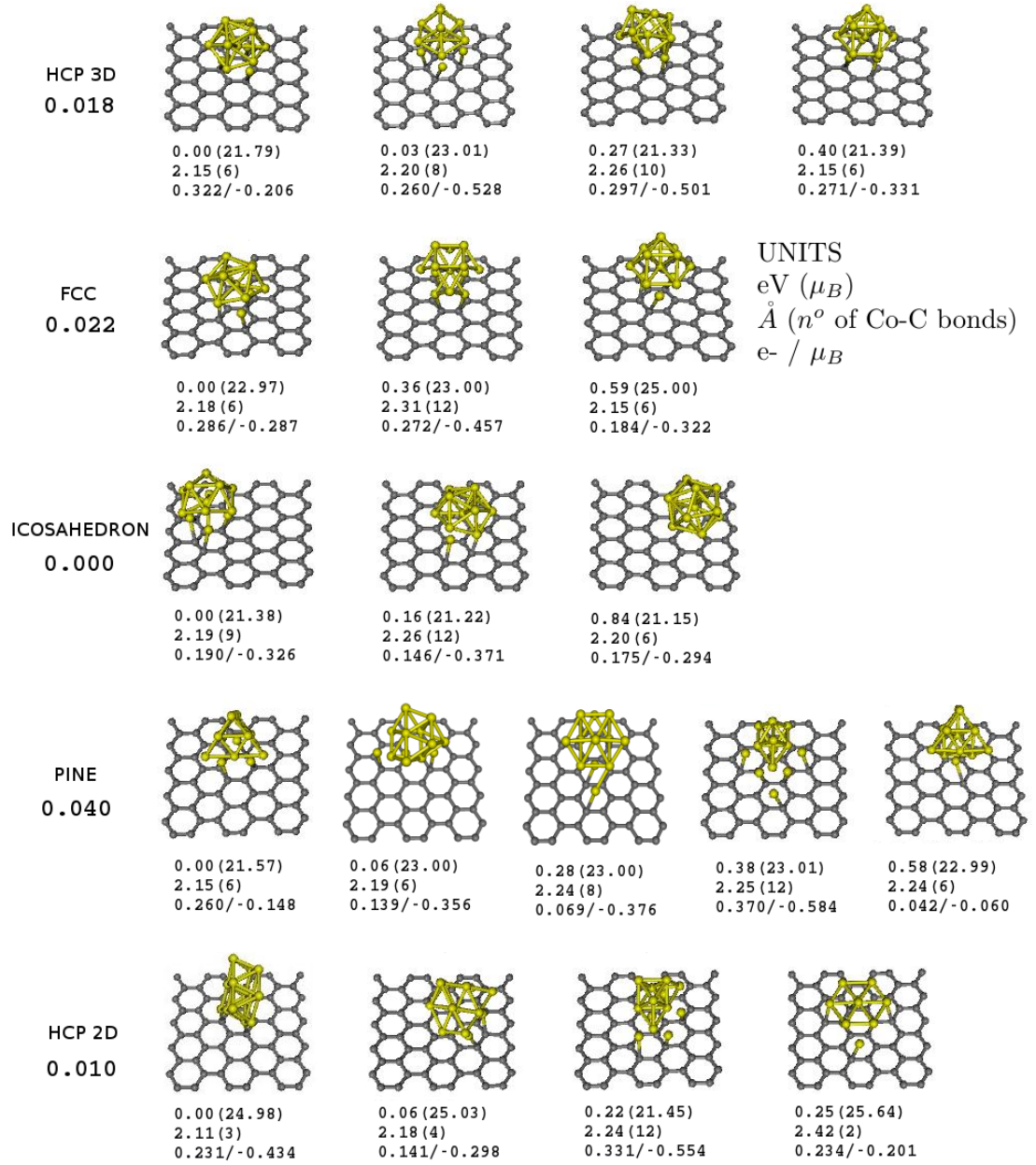


Figure 4.2: Relaxed geometries for each isomer of Co_{13} . For each of the geometries we show below in the first line the energy difference in eV respect to the lowest energy geometry of each isomer and the total spin polarization in Bohr magnetons; in the second line, the average Co-C bond length in \AA and the number of Co-C bonds; in the third line, the number of electrons gained by graphene and the induced magnetic moment on graphene in Bohr magnetons. Besides the isomer name, the relative energy in eV of the minimum energy geometry for each isomer respect to the icosahedron is shown.

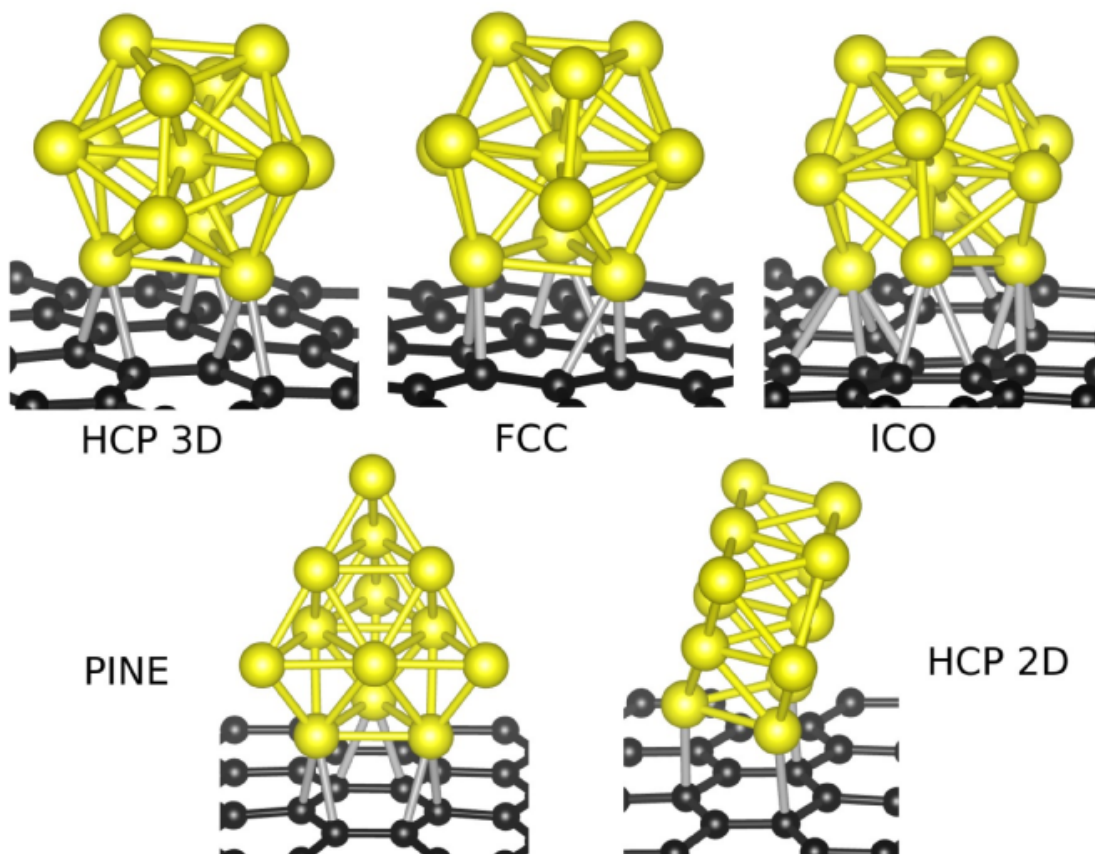


Figure 4.3: Interfacial structure of the most stable arrangement lying over graphene for each isomer.

4 Graphene doping: cluster adsorption and substitutional atoms

the *pine* structures have other two minima at 0.06 and 0.28 eV. The *hcp 3d* structures seems also to follow this pattern with minima at 0.03, 0.27 and 0.40 eV.

Finally we comment on the most stable arrangement for each isomer, which are shown enlarged in Fig. 4.3. Note that the most stable free isomers, *pine* and *hcp 2d*, which are also the most anisotropic, remain largely unchanged when bonding graphene. On the other hand, the *icosahedron*, *fcc* and *hcp 3d* suffers larger structural distortions and the last two transform into icosahedra.

Binding energy E_B

Previously we have compared the minima of each isomer. We now compare all the minima of the different isomers in Fig. 4.2. We define the binding energy as

$$E_b = (E_{\text{graphene}} + 13E_{\text{Co}} - E_{\text{Co}_{13}/\text{graphene}})/13 \quad (4.1)$$

where E_{graphene} is the energy of pristine graphene, E_{Co} is the total energy of a single Co atom, and $E_{\text{Co}_{13}/\text{graphene}}$ is the energy of the Co_{13} cluster on graphene. To understand the meaning imagine an initial state with graphene already formed and cobalt atoms isolated. The binding energy represents the energy gain per cobalt atom when they form a cluster adsorbed on graphene starting from the previously described initial state. The binding energy allow us to comment on two different issues: the comparison with the free Co_{13} isomers and the most stable arrangements of the adsorbed isomers on graphene.

Firstly we compare the values obtained for the adsorbed clusters with those of free isomers shown in Table 4.1. The most stable minimum for each isomer adsorbed on graphene has binding energies of 3.592, 3.562, 3.602, 3.580 and 3.584 eV for *hcp 2d*, *pine*, *icosahedron*, *fcc* and *hcp 3d*, respectively. The binding energies of the free isomers were no larger than 3.51 eV, lower than values for the most stable adsorbed clusters. Therefore, we find that Co_{13} clusters prefer to be adsorbed on graphene rather than to be in the free state.

Secondly, we focus on the adsorbed isomers on graphene. Figure 4.4(a) shows the binding energy of each adsorbed isomer. The *icosahedron* is now the most stable isomer, which means that it is stabilized by adsorption on graphene. The *hcp 2d* follows it as the second most stable structure. Then we find *fcc* and *hcp 3d* at similar energies which is expected at least for the most stable arrangement of each isomer because both reconstruct into icosahedral-like structures. Finally we have *pine* arrangements as the least stable structures. Figure 4.4(a) clearly shows the common trends in the energy differences between the several arrangements within each isomer; the *icosahedron* and the *hcp 2d* cases look related and the others follow similar patterns.

A beam of Co_{13} clusters contains all the different isomers although *hcp 2d* is expected to be majority. Once clusters are adsorbed on graphene, the *icosahedron* would be found as the most stable isomer. A thermal treatment of the adsorbed clusters could drive the least stable isomers (*hcp 3d*, *fcc* and *pine*) into *icosahedron* and *hcp 2d* isomers mostly.

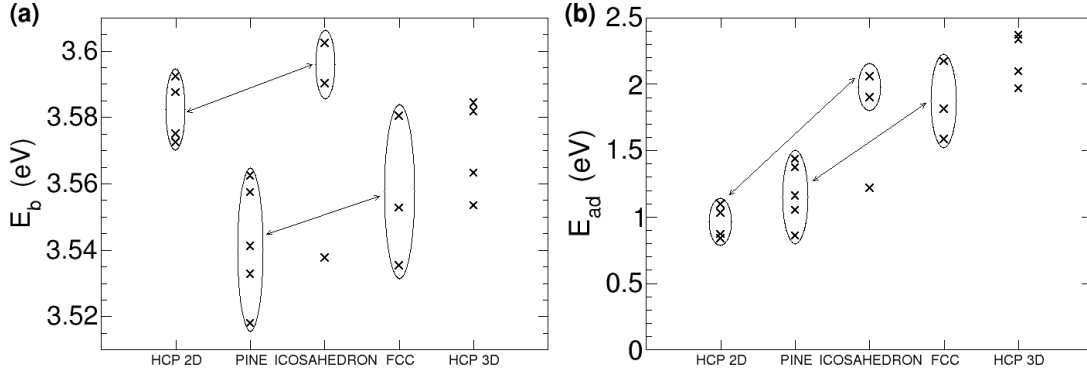


Figure 4.4: (a) Binding energies E_b and (b) adsorption energies E_{ad} of the different calculated geometries for each isomer of Co_{13} on graphene.

Adsorption energy E_{ad}

We also study the process of adsorption of isomers on graphene from a different perspective by computing the adsorption energy E_{ad} defined as

$$E_{ad} = E_{\text{graphene}} + E_{\text{Co}_{13}} - E_{\text{Co}_{13}/\text{graphene}} \quad (4.2)$$

where $E_{\text{Co}_{13}}$ is the energy of the isolated cobalt cluster, and E_{graphene} and $E_{\text{Co}_{13}/\text{graphene}}$ are the same as previously defined in equation (4.1). The adsorption energy shows the energy released when the cobalt cluster is adsorbed on graphene. It is the energy difference between an initial state where both the cluster and graphene are formed but they are infinitely separated so they do not interact, and a final state where the cluster is adsorbed on graphene. It is related to the cobalt-carbon bonds established during the adsorption process and includes effects because of structural rearrangements.

Figure 4.4(b) shows the values of the adsorption energies for the different arrangements of the five isomers of Co_{13} on graphene. The same trends on the energy differences between the different isomer arrangements are observed, grouping the *icosahedron* and the *hcp 2d* structures together, and the other three isomers separately.

The adsorption energy of the most stable arrangement of each isomer shows a monotonous increase from *hcp 2d* to *hcp 3d*. Note that it follows the opposite trend to the stability order of the free isomers; it is larger for the least stable free Co_{13} isomers and decreases when going to more stable free isomers. The explanation for this behavior is the resistance to deformation of highly stable isomers such as *pine* and *hcp 2d*, while other three isomer suffer large reconstruction especially *fcc* and *hcp 3d* which end as *icosahedra*.

Notice the slight shift of *icosahedron* from an uniform increase in the adsorption energy, which is related to the isomer distortion, with two cobalt atoms towards graphene, as we commented above. This increase of the adsorption energy for *icosahedron* explains the change between *hcp 2d* and *icosahedron* when the isomers are adsorbed on graphene.

The *hcp 2d* presents much lower adsorption energy than *icosahedron*. Although the beam of Co_{13} clusters would have majority of *hcp 2d*, *icosahedron* clusters would stick

more easily to graphene. Furthermore, the most stable isomer over graphene was *icosahedron*. As a result, icosahedron-like clusters are expected to be present at large when Co_{13} clusters attach to graphene.

Next we try to shed light over the trends in the adsorption energy of cobalt clusters on graphene. Some authors [421] proposed that larger adsorption energies are found when there are more cobalt-carbon bonds and the bond lengths are minimized yielding stronger bonds. Although it seems a reasonable argument, a further check seems necessary. We tested its validity using two different approaches: comparison between ground state of each adsorbed isomer and comparison between different arrangements of the same isomer.

First we comment on the ground state of each isomer. In our case we have found average bond lengths of 2.15, 2.18, 2.19, 2.15 and 2.11 Å going from larger to smaller adsorption energy, i.e in the order *hcp 3d*, *fcc*, *icosahedron*, *pine* and *hcp 2d*, respectively. The bonds number in the same isomer order is 6, 6, 9, 6 and 3. The proposed trends work nicely for the first three isomers. For example the *hcp 2d* has the shortest average bond length and the lowest adsorption energy among the five isomers, with only three bonds. It can be argued that the larger number of bonds, although weaker, compensates for the shortest and stronger bonds. The other problematic case are *pine* structures which have six bonds as *fcc* structures but with shorter average bond length; however, it has lower adsorption energy. We give a word of caution about using this simple argument that appears logical and reasonable but can fail and should not be used as foolproof.

Second, we consider different arrangements of the same isomer. The values of the average bond lengths and the number of bonds for all the minima obtained for the five isomers are included in Fig. 4.2. For most of the cases the average bond length increases when moving towards right in Fig. 4.2 which means towards less stable arrangements within the same isomer. As commented before, when the average bond length does not follow the trend the number of bonds can help to explain the stability order. An example is the second and third geometries of *fcc* isomer. The second geometry is more stable because of having many bonds, with their average bond length larger than for the third geometry. Note that the most stable geometries of *fcc* and *hcp 3d* isomers suffer large structural modification ending in icosahedron-like structures. So, these minima should not be compared with the rest of isomers geometries. The relation between number of bonds, average bond length and stability can be useful to explain some results, but must not be thought as a general rule because many examples does not fall in this explanation.

4.2.3 Charge transfer between Co_{13} cluster and graphene

We analyze the electronic properties of the Co_{13} clusters adsorbed on graphene by studying the charge transfer using the Mulliken scheme. We can comment safely on the charge differences between the different cases because the same basis sets are used. Figure 4.2 includes the charge transfer from cobalt cluster towards graphene for all the computed geometries. A positive value means that electrons are gained by graphene, which ends negatively charged. For all the cases studied here graphene ends negatively charged because there is net charge transfer from the cobalt cluster.

We study the charge transfer versus the stability of the arrangements of each isomer. We distinguish the five isomers attending to their structure. On the one hand the spherical isomers such as *hcp 3d*, *fcc* and *icosahedron* have a central atom. On the other hand we have the irregular structures such as *pine* and *hcp 2d*. For the spherical isomers the largest charge transfer is found the most stable geometry. However the stability order of the rest of geometries does not follow a monotonous decrease of charge transfer.

For the irregular structures the largest charge transfer is not even found for the most stable isomer. For the *pine* and *hcp 2d* there are some geometries where large charge transfer occurs because there are many atoms bonded to graphene. The irregular clusters shapes include large planar faces with many cobalt atoms that can bond many carbon atoms simultaneously.

Related to the discussion about number of bonds and stability, one could think that the higher number of cobalt atoms bonding to graphene, the higher amount of electrons transferred to graphene, and the higher the stability. Nevertheless, as we have already shown, neither the number of bonds, the average bond length or the charge transfer determines unequivocally the stability of the clusters on graphene.

Therefore there must be other important factors that explain the stability order between the geometries of each isomer and further inquiry is needed. Cobalt atoms over graphene prefer to form clusters rather than to be spread over the monolayer. This is a result of the strength of the cobalt-cobalt bonds, which are stronger than the cobalt-carbon bonds. When bonding graphene, the cobalt atoms closer to the surface have to share electrons with carbon and the cobalt-cobalt bonds are weakened somehow. Summing-up, there are two opposed trends, more cobalt-carbon bonds imply more stability, but also it also weakens the cobalt-cobalt bonds. In order to clarify the stability order of each isomer when adsorbed on graphene we have to consider more deeply the free Co_{13} isomers.

4.2.4 Bonding mechanism

We have analyzed different ideas or trends that have been proposed to explain the bonding between cobalt clusters and graphene: number of bonds, bond length or the charge transfer. These ideas work correctly for some cases, but they fail in other cases. For the spherical isomers, the most stable geometry has the largest charge transfer, but the stability for other isomer geometries does not follow a charge transfer criterion.

We consider ionic and chemical bonding. Firstly, we focus on the ionic character because the bonding of cobalt clusters on graphene has been claimed to be ionic-like. To shed more light about the bonding, we compute the potential induced by each cluster on graphene to consider not only the charge transferred but also the distance. The graphene potential induced by each isomer can be related to the bonding ionic character.

To estimate the potential created by each isomer on graphene we have localized the place where the cobalt cluster contributes with zero dipoles, the center of charges, as shown in Fig. 4.5(b). Therefore, we can expand the potential as Q/r as there is no dipoles and we neglect the higher terms. The charge transfers are within the interval 0.2-0.3 for the ground states of the isomers. However the center of charges varies largely 1-5 Å,

4 Graphene doping: cluster adsorption and substitutional atoms

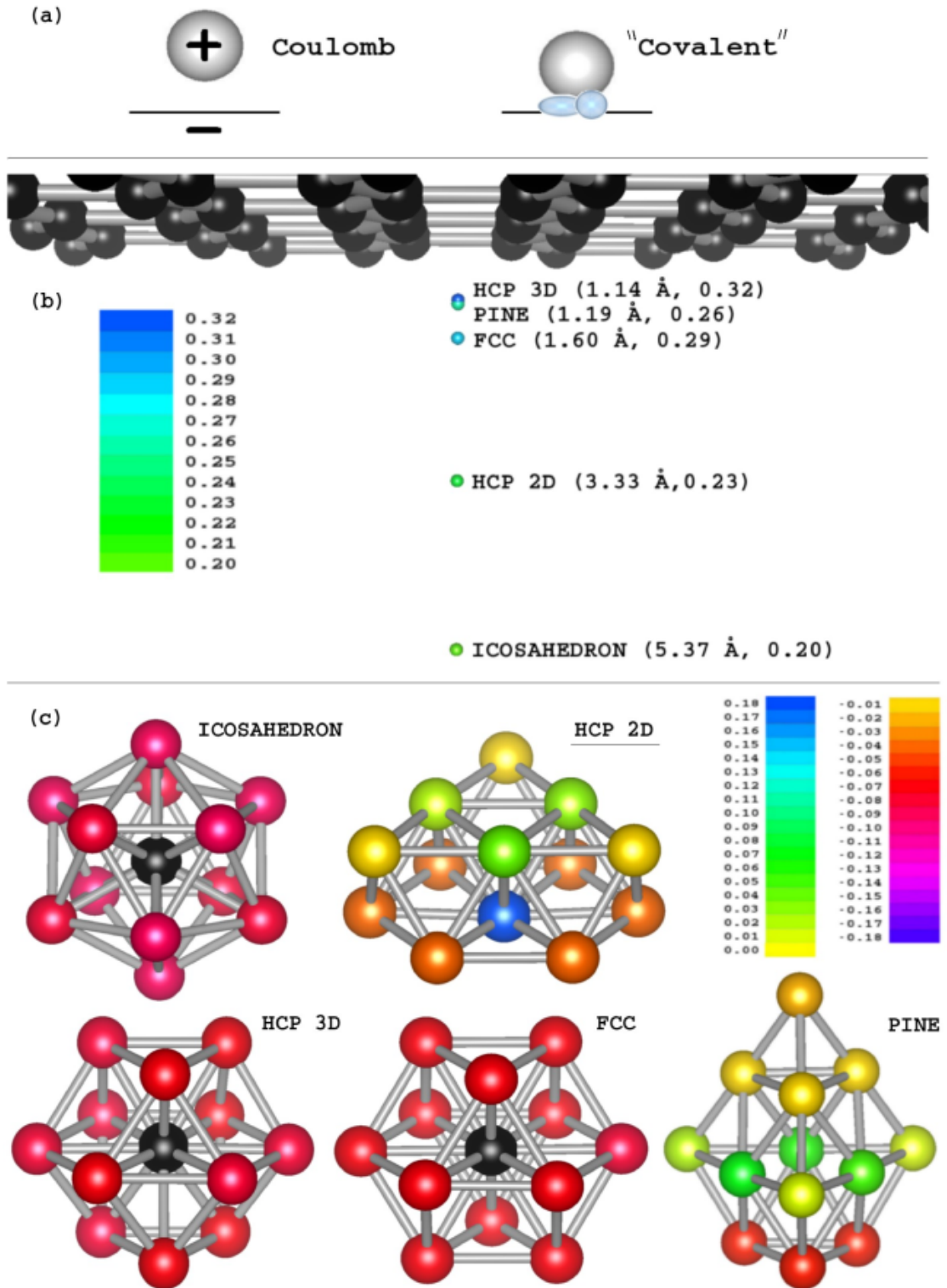


Figure 4.5: (a) Coulomb and chemical "covalent" binding mechanisms. (b) Cluster charges (in units of $|e|$) as functions of the free isomers with respect to graphene (c) Local charges (in units of $|e|$) on atoms in cluster isomers. The central atom (in black color) loses charge to compensate the surface ones. The local charges on the central atom of *icosahedron*, *hcp 3d* and *fcc* isomers are 1.01, 0.87 and 0.86 $|e|$, respectively.

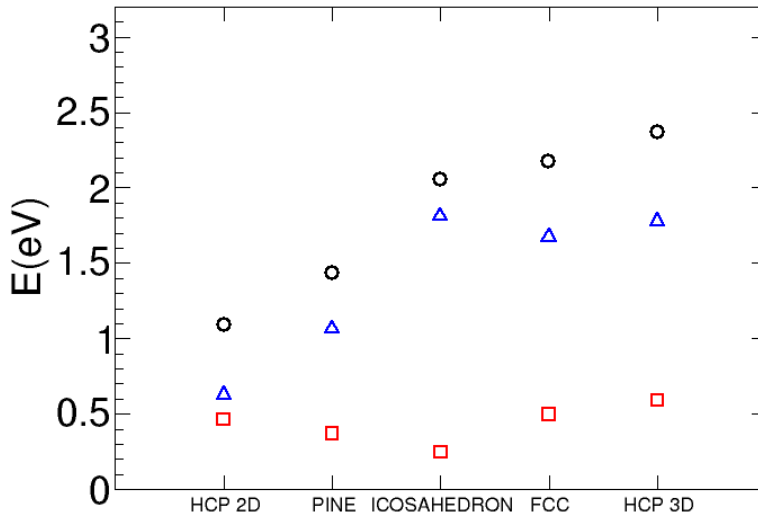


Figure 4.6: Decomposition of the adsorption energies (black circles) for the minima arrangement of each Co_{13} isomer, showing also the estimated Coulomb (red squares) and covalent (blue triangles) contributions.

yielding different potentials on graphene. For the most stable *icosahedron* structure, we find the smallest potential induced on graphene of the five isomers. So we can affirm that the Coulomb interaction is not key for the bonding.

We estimate the part of the adsorption energy that could be ascribed to the Coulomb interaction. The Coulomb energy for the most stable arrangement of the five isomers is calculated as the sum of the interactions between all cobalt and carbon atoms. Each Coulomb interaction is computed as $q_1 * q_2 / r$, being q_1 and q_2 the charges associated to each atom and r the distance between these atoms. Figure 4.6 shows the results of the estimation of the Coulomb energy for the five different isomers. For comparison we included the adsorption energy and the "chemical" energy, which is the result of subtracting the Coulomb energy from the adsorption energy. The Coulomb term is not the main contribution to the adsorption energy, especially for the *icosahedron*, *fcc* and *hcp 3d* cases.

We also estimated the Coulomb energies for the free isomers following the same procedure. We obtained values of 3-4 eV for the spherical-like clusters such as the *icosahedron*, *fcc* and *hcp 3d* isomers and only 0.1 eV for *hcp 2d* and *pine* isomers. This difference is explained because the spherical clusters have an inner atom that is highly positively charged, and the external atoms are negatively charged. When the isomers are over graphene, the Coulomb energy because of interaction between cobalt atoms is reduced in 2 eV for *icosahedron*, about 0.7 eV for *fcc* and *hcp 3d*. The Coulomb energy is destabilizing the bonding.

Nevertheless, the estimation we carried out have some drawbacks. First, we use the Mulliken population analysis to estimate the charges on each atom. The Mulliken

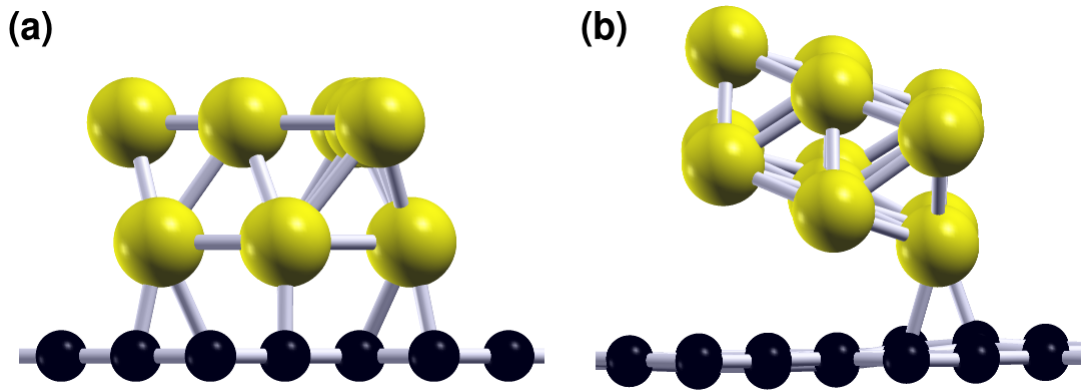


Figure 4.7: (a) Input and (b) relaxed geometries of the second most stable geometry of *hcp 2d* over graphene.

method ascribe to each atom their orbitals charge, which could be an errors source. Second, we approximate atoms by punctual charges, losing all the information of distribution of charge around the atom. Thus, although the results are qualitatively correct, some variations in the data should be expected for more accurate estimations.

Then, we look at the chemical bonding, that is the leading term. It seems that the cobalt-carbon bonds should studied in detail. We found net charge transfer to graphene for all the cases. Therefore it seems reasonable to study cobalt atoms in the free isomers. Carbon atoms in graphene are all equivalent. Nevertheless, cobalt atoms on the free isomers show different character depending on their position because their local environment changes noticeably.

Figure 4.5(c) shows the local charges on each atom for the free isomers. We find the two groups already commented, spherical and irregular isomers. For the three spherical cobalt isomers with a central atom all the surface atoms are mostly equivalent. Electrons are depleted from the central atom and the cluster is negatively charged on its surface, as denoted by the red-colored atoms. The difference between the three isomers is the total surface charge, which increases in the order of *fcc*, *hcp 3d* and *icosahedron*. Electrons are transferred in the cluster adsorption on graphene. It seems that cobalt clusters would prefer to lie over a face that is negatively charged. For the spherical isomers all the surface appears likely to bond graphene.

Nevertheless, a more interesting behavior is found for those isomers without central atom, such as the *hcp 2d* and *pine* structures, which present positively and negatively charged cobalt atoms on surfaces. The ground state of these isomers adsorbed on graphene, shown in Fig. 4.3, shows that the isomers prefer to bond graphene by cobalt atoms that were negatively charged in the free state, even for few atoms. Note that *hcp 2d* could lie over graphene with seven cobalt atoms, establishing a large number of bonds. However, it prefers to lie over only three cobalt atoms. The reason is that one of the seven atoms (shown in blue in Fig. 4.5(c)) was positively charged and the

adsorption process imply a large charge reorganization within the cobalt cluster, which is penalized. Another clarifying example is the *pine* structures that do not lie on a face with six atoms. Most of the cobalt atoms in that face are positively charged in the free *pine* isomer. Therefore they are not prone to lose more electrons in the adsorption process, which penalize this arrangement.

Even for the *hcp 2d* we found that from an initial state lying over a planar face, the cluster relax to a final state where it is tilted separating most cobalt atoms from graphene as shown in Fig. 4.7. The geometry in Fig. 4.7 was found to be the second most stable arrangement of the *hcp 2d* isomer over graphene.

We conclude that isomers prefer to lie over a face with negatively charged cobalt atoms in the free state. This explain why the bonds number is not maximized, and it shows that charge distribution on the free cluster surface plays an important role.

4.2.5 Magnetic moment

We study how the adsorption on graphene affects the spin magnetic moment of the clusters. For the free Co_{13} isomers the values of the magnetic moment are shown in Table 4.1. Figure 4.2 contains the magnetic moments for all the computed geometries of the cobalt clusters adsorbed on graphene. For the more irregular clusters, *hcp 2d* and *pine*, the reduction of the magnetic moment when adsorbed in graphene is about 2 and $1.5 \mu_B$ for the most stable geometries. The rest of geometries for the *pine* isomer have the same magnetic moment as the free state isomer. For the spherical isomers the reduction of the magnetic moment is larger. Although we can try to explain the magnetic moment decrease based on the electrons that passed to graphene, charge transfers are too small to account for the large magnetic moment decrease.

The explanation must come from charge reorganization within the cluster during the adsorption process because of the geometry distortion, changing the local environment of the cobalt atoms, the bond lengths, and the coordination number. Thus, larger changes are expected for those isomers that suffers major structural rearrangements. Indeed, *fcc*, *hcp 3d* and *icosahedron* display large reduction of magnetic moment associated with large structural modification. For the ground state, the *icosahedron* structure suffers noticeable modification with two cobalt atoms moving towards graphene and changing the coordination number and bond lengths. The magnetic moment decreases from approximately $31 \mu_B$ to less than $22 \mu_B$.

However, the *pine* and the *hcp 2d* isomers maintain their structure with minor changes, and the magnetic moment is not drastically reduced. Note that this trend is similar for the adsorption energy. Larger adsorption energies and larger magnetic moment reductions are found for largely distorted isomers.

Then, we study the induced magnetic moment on graphene as a result of the cobalt-carbon chemical bonding [357]. All the computed geometries have negative induced magnetic moments on graphene when the cobalt cluster is deposited. The values vary between -0.06 and $-0.58 \mu_B$ depending mainly on the number of cobalt atoms bonded to graphene: the larger the number of bonds the larger the induced negative magnetic moment. Nevertheless, as we have already seen, these simple ideas fail and other factors

such as the isomer geometry and the bonding site being hollow, top or bridge are playing a role.

Notice also that values of $-0.5 \mu_B$, which are found for some geometries, are quite high and could be of interest to develop spintronic devices. In these arrangements the cluster maximizes the number of bonds with graphene. Nevertheless, these arrangements are not the ground state of each isomer over graphene. The most stable *icosahedron* geometry induces a negative magnetic moment of $0.33 \mu_B$ in graphene, of interest for spin devices.

4.2.6 DFT+U study: on-site interaction

When dealing with strongly correlated systems it is advisable to strength the on-site electronic interaction directly. Cobalt clusters on graphene can be classified into this category because of the $3d$ electrons. To settle precisely the importance of this effect on our system we have calculated using the DFT+U method the three most stable configurations of the cluster bonding graphene, *icosahedron*, *hcp 2d* and *hcp 3d*.

There are no drastic changes and the *icosahedron* remains as the ground state configuration. However, *hcp 3d* becomes more stable than *hcp 2d*, and they are found 0.15 and 0.82 eV higher in energy from the *icosahedron*. The effect of the on-site interactions on the geometries is negligible as the structures are largely preserved during DFT+U relaxations.

The magnetic moment converges to $26 \mu_B$ for the three studied isomers, an effect that is expected including the on-site interaction. Without the on-site interaction the values were smaller and different between them.

4.2.7 Bringing results into contact with experiments

In experiments we deal with charged clusters instead of neutral, and graphene is usually doped by the influence of the substrate. To give wider weight to our results we study in this section the doping effects both on the free clusters and on the cluster adsorbed on graphene.

Free charged Co_{13} clusters

Experimental setups produce beams of charged clusters [355, 427–430]. Here we study charged free Co_{13} clusters to check whether the previously reported stability order within isomers is kept. We have calculated the free isomers both negatively and positively charged allowing full relaxation of the structures to check the possible influence of the charge. The *hcp 2d* isomer appears again as the most stable isomer and a few changes affect the stability order: an exchange between the *hcp 3d* and *fcc* isomers for the positively charged clusters and between the *pine* and *icosahedron* isomers for the negatively charged clusters.

Our calculations of the charged clusters shed more light over the charge transfer process when bonding graphene. Using the results of the total energies of the neutral and charged clusters it is straightforward to compute the ionization energy and electron affinity of each isomer, and the two quantities allow to obtain the work function defined as

one half of the sum of them. We obtained for the work function values of 4.33, 4.17, 4.32, 4.35 and 4.21 eV for the *hcp 2d*, *pine*, *icosahedron*, *fcc* and *hcp 3d* isomers, respectively.

In our system, the clusters work function measures the tendency to transfer electrons to graphene. We obtained similar values for all the isomers, which agrees with the fact there are no large variations on the charge transfer.

This result supports the ideas we proposed concerning the bonding, reducing the importance of the charge transfer. The stability of the isomers over graphene is determined by the cobalt-carbon bonds established during the adsorption. If cobalt-cobalt bonds were the most important terms, the *hcp 2d* would stay as the most stable structure also over graphene, which would mean that the bonding is weak and causes low modifications. Nevertheless, we have already seen that there are changes in stability between different isomers because of the strength and importance of the cobalt-carbon bonds. Another implication is that placing *hcp 2d* over different faces is not equivalent with energy differences of 0.25 eV, which clearly shows that the bonds with graphene are key to the stability order. As commented, the local cobalt charges in the free isomer are relevant to explain the preference for one or other arrangement over graphene, more than the number of bonds.

Summing-up, we have learned two main ideas. First, when the Co_{13} cluster lies over graphene the cobalt-carbon bonds are crucial to understand the stability order between isomers. Second, these bonds are favored when all the cobalt atoms close to graphene were negatively charged in free Co_{13} because the charge transfer to graphene happens without large charge reorganization within the isomer itself.

Doped graphene

Our previous calculations consider graphene idealized as a freestanding sheet with no interactions with possible substrate and neutral carbon atoms. In experiments, graphene however lies over a substrate and it is normally doped, shifting the Fermi level upwards or downwards. To assess this possible situation and check the effect on our previous results, we have carried out calculations of the Co_{13} cluster deposited on graphene doped with a positive and negative charge. The SIESTA method offered two different ways to carry out the graphene doping, globally or locally. The global approach removes an electron from the whole graphene supercell. The local approach consists in the substitution of a carbon atom by a boron or nitrogen atom to remove or add an extra electron, respectively. This second picture recalls doping in semiconductors. Considering that we are interested in the cobalt clusters interacting with pristine graphene, we place the impurity atom as far as possible from the cluster to avoid interactions.

Specifically, we have carried out calculations of the ground state geometry of three most stable isomers on graphene, such as the *icosahedron*, *hcp 2d* and *pine* isomers, to test whether the stability order is well kept when graphene is doped. Note that the other two isomers, *fcc* and *hcp 3d*, apart from being less stable, present icosahedron-like geometries in the relaxed state.

Figure 4.8 shows that the relative order of stability is preserved for all the cases computed here, which generalizes our results. We present the energy differences between

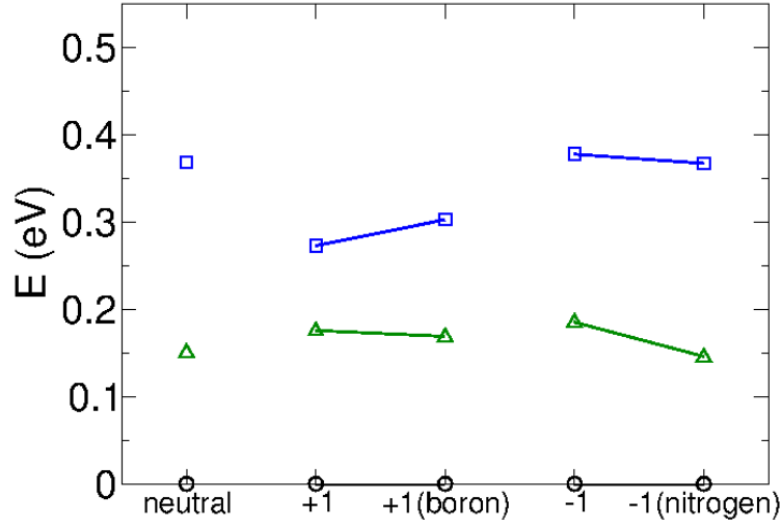


Figure 4.8: Differences in energy between the *icosahedron* (circles), *hcp 2d* (triangles) and *pine* (squares) isomers on graphene for different charge states by changing uniformly the Fermi level or by doping with boron or nitrogen atoms.

the three isomers for the neutral and charged states, including both approaches to charge the system. Once we know that charging the system does not swap isomers in the stability order, we comment briefly on the changes of the energy differences. For the positively charged systems, the energy differences between *icosahedron* and *hcp 2d* is enlarged while the differences between *icosahedron* and *pine*, and *hcp 2d* and *pine* become smaller. For the negatively charged system the energy differences slightly grow for the global approach, while they remain the same for the local approach.

4.3 Substitutional impurities in graphene

Above we have addressed the functionalization of graphene with transition metal clusters deposited over the surface, specifically Co_{13} clusters. Next we study the importance of defects on graphene. Defects can be intrinsic such as vacancies, divacancies and dislocations, or extrinsic such as adatoms and substitutional impurities. We focus on extrinsic defects, studying substitutional impurities in graphene. Much research has been carried out on extrinsic defects on graphene, such as transition metal adatoms and $3d$ substitutional impurities. Although $4d$ and $5d$ transition metals have been studied as adatoms on graphene [221, 431], systematic work of them as substitutional impurities is still missing. We here study the $4d$ and $5d$ transition metals as substitutional impurities in a single vacancy on graphene, as shown in Fig. 4.9.

4.3 Substitutional impurities in graphene

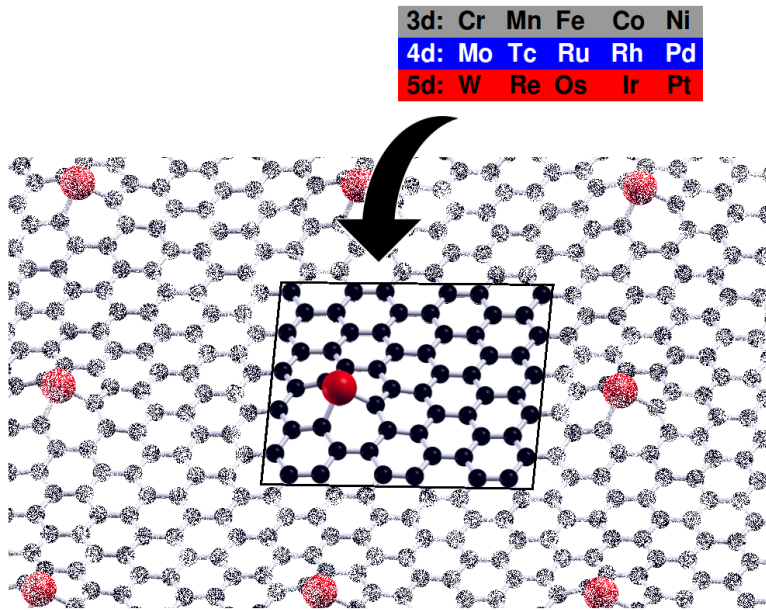


Figure 4.9: Studied 3*d*, 4*d*, and 5*d* substitutional impurities in graphene. The rectangle highlights the rectangular unit cell.

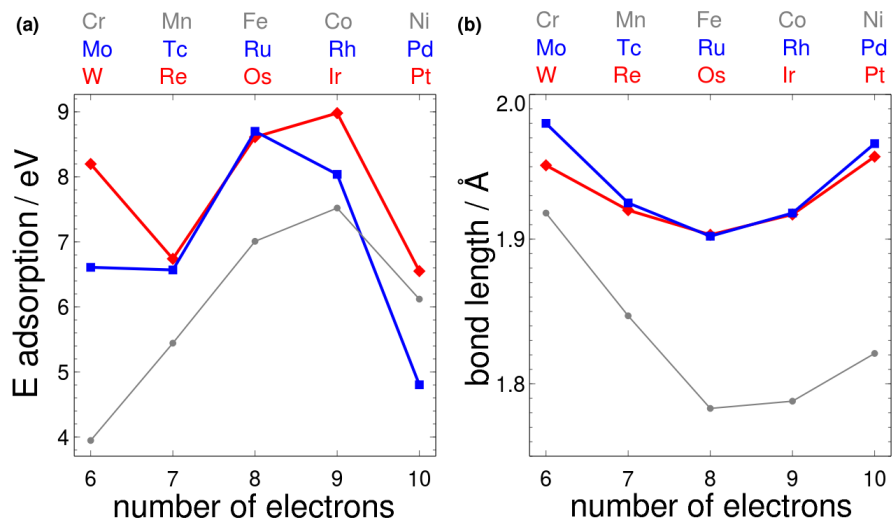


Figure 4.10: (a) Adsorption energies and (b) average bond lengths for the computed 3*d* (grey circles), 4*d* (blue squares) and 5*d* (red rhombuses) impurities in graphene. Number of electrons refers to the impurity electrons.

4.3.1 Adsorption energies and bond lengths

We study the stability of the $3d$, $4d$ and $5d$ substitutional impurities on graphene. Figure 4.10(a) shows the values of the adsorption energy for the substitutional impurities, computed as $E_{ad} = E_{vacancy} + E_{imp} - E_{total}$. $E_{vacancy}$ denotes the energy of the fully relaxed vacancy, E_{imp} is the energy of the isolated transition metal atom and E_{total} is the energy of the impurity on graphene. The values obtained for the adsorption energy varies largely in the interval 4-9 eV. The smaller values are obtained for the $3d$ transition metals except for nickel group where palladium becomes less stable. The results for $3d$ transition metals using a square supercell agree with those reported previously in a hexagonal supercell [229].

For the $3d$ transition metals the adsorption energy increases until cobalt group. Cobalt is the most stable impurity agreeing with previous results [229]. A similar pattern is found for $5d$ transition metals, the maximum now is iridium. However the maximum for the $4d$ shifts to the iron group and it is found for ruthenium. Note that the monotonous increase of adsorption energy found in $3d$ is lost for $4d$ and $5d$ in manganese group: technetium and rhenium are less stable than expected when following the $3d$ trend. The reason for the reduced stability of technetium and rhenium is the drastic depletion of magnetic moment with respect to manganese to be explained later. It seems that the $4d$ and $5d$ differs from the $3d$ when the d shells are half filled. It is also noticeable that for the iron group stability changes between $4d$ and $5d$, becoming ruthenium more stable than osmium. Summing-up, the most stable substitutional impurities on graphene are cobalt in $3d$, ruthenium in $4d$, and iridium in $5d$.

We also comment on the distances between the impurity atom and the first carbon neighbor. Substitutional impurities are in a single vacancy, and have three first carbon neighbors. We fully relax the geometry after placing the transition metal atom. We find that the three bond lengths to the carbon first neighbors are equal between them for all impurities, with differences less than 0.004 Å. This means that the symmetry of the vacancy is well preserved after impurity adsorption. Furthermore, this let us comment safely on the average bond length of the three bond lengths, because they are equal. Figure 4.10(b) shows the average bond length for $3d$, $4d$ and $5d$ transition metal impurities in graphene. The same behavior is found for the $3d$, $4d$ and $5d$ impurities; the bond length decreases from the chromium group until the iron group and then it increases for the cobalt and nickel group. This behavior is explained straightforward by looking at the size of the impurities. Within the same d shell, the size decreases for the first elements because of the increasing nuclear charge and then the effect of screening balance it allowing for larger distances.

Although the trend is similar for $3d$, $4d$ and $5d$ impurities, the values are noticeably different between the $3d$ series and the $4d$ and $5d$ series. Again the explanation comes from the size of the impurities; $3d$ impurities are smaller than $4d$ and $5d$ and shorter average bond lengths were expected. The $4d$ impurities are considerably larger because of the addition of a shell, mainly the 4p electrons, which screen the effective nuclear charge felt by the $4d$ electrons.

One could expect a similar difference between $4d$ and $5d$ transition metals. However,

the results show similar average bond lengths for $4d$ and $5d$. The explanation is equally related to the size of the impurities because $4d$ and $5d$ transition metals are similar in size. The cause for the similar size is the so-called lanthanide contraction [432–434]. For $5d$ elements the $4f$ levels have been filled before the addition of $5d$ electrons. The $4f$ electrons are far from the nucleus and in consequence they yield poor shielding; however, the corresponding protons strongly increases the effective nuclear charge. As a result, the $5d$ atoms shrink and have similar size as the $4d$ atoms. The difference in the average bond lengths between $4d$ and $5d$ is small and for some cases such as tungsten, rhenium, and platinum, the order is actually reversed, showing the $5d$ impurities shorter bond lengths.

4.3.2 Magnetism

After the energetic and geometric considerations we focus on the magnetism of graphene with the $4d$ and $5d$ transition metal substitutional impurities to compare with the $3d$ impurities. The total cell magnetic moment for each case is shown in Fig. 4.11(a). For the $4d$ and $5d$ impurities in graphene the total cell magnetic moment is the same, $2 \mu_B$ for molybdenum and tungsten, $1 \mu_B$ for technetium and rhenium, and then alternating values of 0, 1, 0 μ_B for ruthenium and osmium, rhodium and iridium, and palladium and platinum, respectively. The fact that the total cell magnetic moment and the number of electrons are correlated provides evidence of common properties within the same group.

If we compare with $3d$ results we find a noticeable difference on the manganese group. The total cell magnetic moment decreases from 3 μ_B for manganese to 1 μ_B for technetium and rhenium. As we commented previously, this sudden decrease is related with the abrupt change in the trend of the adsorption energy for the manganese group. The reduction of the magnetic moment for technetium and rhenium widen the alternating series 0-1 μ_B .

We can group the impurities of the $4d$ and $5d$ transition metals in graphene attending to the alignment of the local magnetic moments on the impurity and on the first carbon neighbors. For half-filled and less than half-filled elements, which correspond to chromium and manganese groups, the impurity induces negative local magnetic moments on first carbon neighbors. The cobalt group impurities in graphene present local magnetic moments of the majority spin on both the impurity and the first carbon neighbors. Figure 4.11(b) shows the spin densities for molybdenum and rhodium as representative examples of the two different kinds or behaviors, agreeing with those reported for $3d$ impurities [229]. Notice that the magnetism induced in graphene follows the sublattice AB pattern, with positive magnetic moment on one sublattice and negative on the other. The local magnetic moments of the three carbon neighbors set one sublattice positive or negative, and the results are opposed for molybdenum and rhodium: negative and positive induced magnetic moment, respectively. These results agree with the standard model in p-d coupling systems such as magnetic semiconductors [435].

Next we analyze the local magnetic moments on the impurity and on the neighboring carbon atoms as shown in Fig. 4.11 (c) and (d) respectively. For the induced magnetic moment on the three carbon atoms we comment safely on the average value as the three

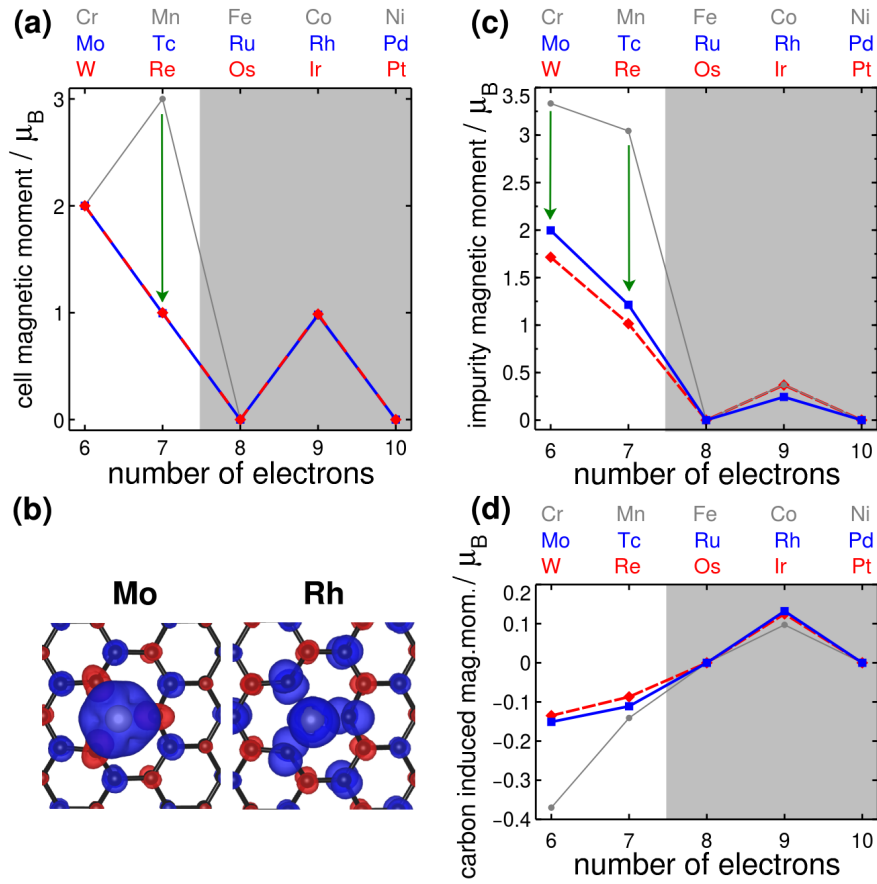


Figure 4.11: Magnetic moments of graphene doped with $4d$ and $5d$ impurities, shown by blue squares and red rhombuses respectively. Number of electrons refers to the electrons of the impurity. $3d$ impurities are indicated in grey circles for comparison. (a) Total magnetic moments in the cell depicted using filled symbols joined with lines. (b) Spin densities for molybdenum and rhodium impurities, taken as examples of two magnetic regions. Positive and negative spin polarization are denoted in blue and red colors, respectively. (c) Local magnetic moments of impurity atoms. (d) Induced graphene magnetic moments, taken as the averaged values for the three carbon neighboring atoms. Note that for $4d$ and $5d$ impurities the magnetic moments are lower, as signaled by the down arrows in (a) and (c).

of them are equivalent. Figure 4.11(c) shows a drastic reduction of the impurity magnetic moment for $4d$ and $5d$ compared with $3d$ within the chromium and manganese groups. For chromium and manganese impurities the values are 3.33 and $2.93 \mu_B$, while for molybdenum and technetium are 2 and $1.21 \mu_B$ and for tungsten and rhenium are 1.72 and $1.02 \mu_B$. Reducing the local magnetic moment of the impurity for the manganese group is correlated with the total cell magnetic moment depletion of $1 \mu_B$. For $4d$ and $5d$ chromium group elements, molybdenum and tungsten, the impurity presents a similar value to the total cell magnetic moment. However, the value for chromium is noticeably larger than the total cell magnetic moment, which imply a larger induced magnetic moment in graphene of $-0.38 \mu_B$.

Figure 4.11 (d) shows that the induced graphene magnetic moments decrease following the $3d$, $4d$ and $5d$ trend. The values of the induced magnetic moments are the already commented -0.38 for chromium and $-0.11 \mu_B$ for manganese, -0.15 and $-0.11 \mu_B$ for molybdenum and technetium, and -0.13 and $-0.09 \mu_B$ for tungsten and rhenium.

Finally we comment on the cobalt group, which presents magnetism with the same alignment on the impurity and on the carbon first neighbors. The local magnetic moment of the impurity is largely reduced, being 0.37 , 0.25 and $0.37 \mu_B$ for cobalt, rhodium and iridium, respectively. The induced magnetic moment on each carbon neighbor is 0.1 , 0.13 and $0.13 \mu_B$, respectively. Note that the total cell magnetic moment is $1 \mu_B$ for the three cases, implying a large delocalization of the magnetic moment.

4.3.3 Manganese group magnetism

We next consider the decrease of the total cell magnetic moment from 3 to $1 \mu_B$ when moving from manganese to technetium. Rhenium follows technetium behavior as expected attending to the similar patterns of $4d$ and $5d$ transition metals. We have studied the levels close to the Fermi energy of the impurities over graphene, as shown in Fig. 4.12. Note that the C_{3v} symmetry of the vacancy was preserved when the impurity was added. Therefore, levels can be classified into A or E irreducible representation of this symmetry, respectively. The orbitals involved in the A -symmetry levels are d_{z^2} , s and p_z , the rest form E -symmetry levels.

When moving from chromium to manganese group, a proton and an electron are added. Here we look at the scheme of levels of graphene with chromium group impurities to guess the possible location of next added electron. There is similarly an unoccupied A -symmetry up level. However, we find substantial differences of chromium with respect to molybdenum and tungsten. For chromium there is a large spin splitting of 6.15 eV between a couple of E -symmetry levels. For molybdenum and tungsten the spin splitting is reduced to 1.06 and 0.80 eV, respectively.

An added electron goes to a different level for the $3d$ than for the $4d$ and $5d$. For manganese, the electron fills the up A -symmetry level yielding a total cell magnetic moment of $3 \mu_B$. For technetium and rhenium it goes to the unoccupied E -symmetry down level, reducing the magnetic moment to $1 \mu_B$. The levels filling is explained by the balance of the spin splitting and the energy cost to promote an electron to the upper level. When the spin splitting is large, as for manganese, it is easier to promote the

4 Graphene doping: cluster adsorption and substitutional atoms

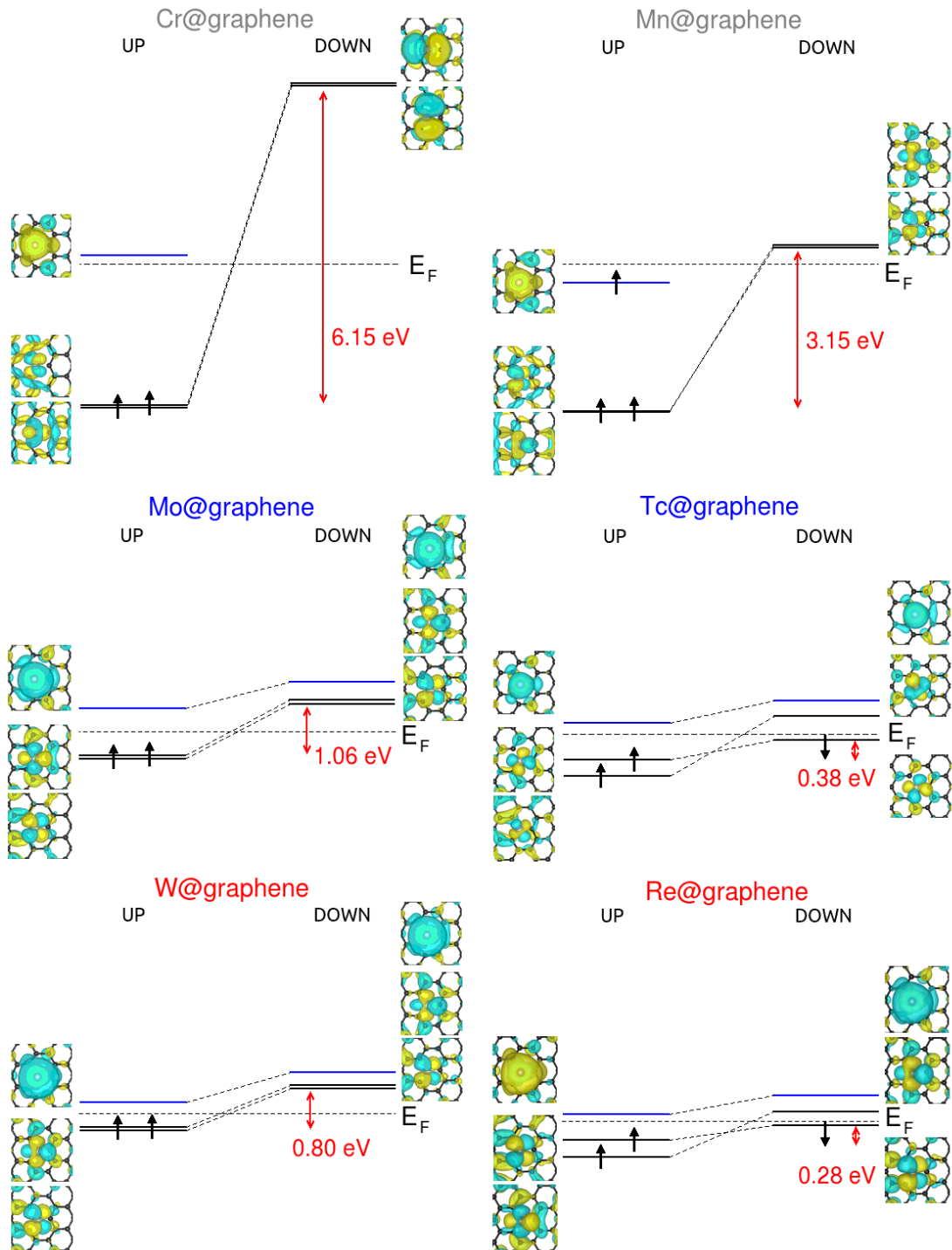


Figure 4.12: Levels close to the Fermi energy at the gamma point for graphene with an impurity of (left) Cr, Mo, and W, and (right) Mn, Tc, and Re. The A (E) symmetry levels are indicated in blue (black). Majority (minority) spin electrons are represented by up (down) black arrows. Wave functions are shown to the side of each level. The spin splitting values are marked on the energy scale by vertical red lines with double-headed arrows.

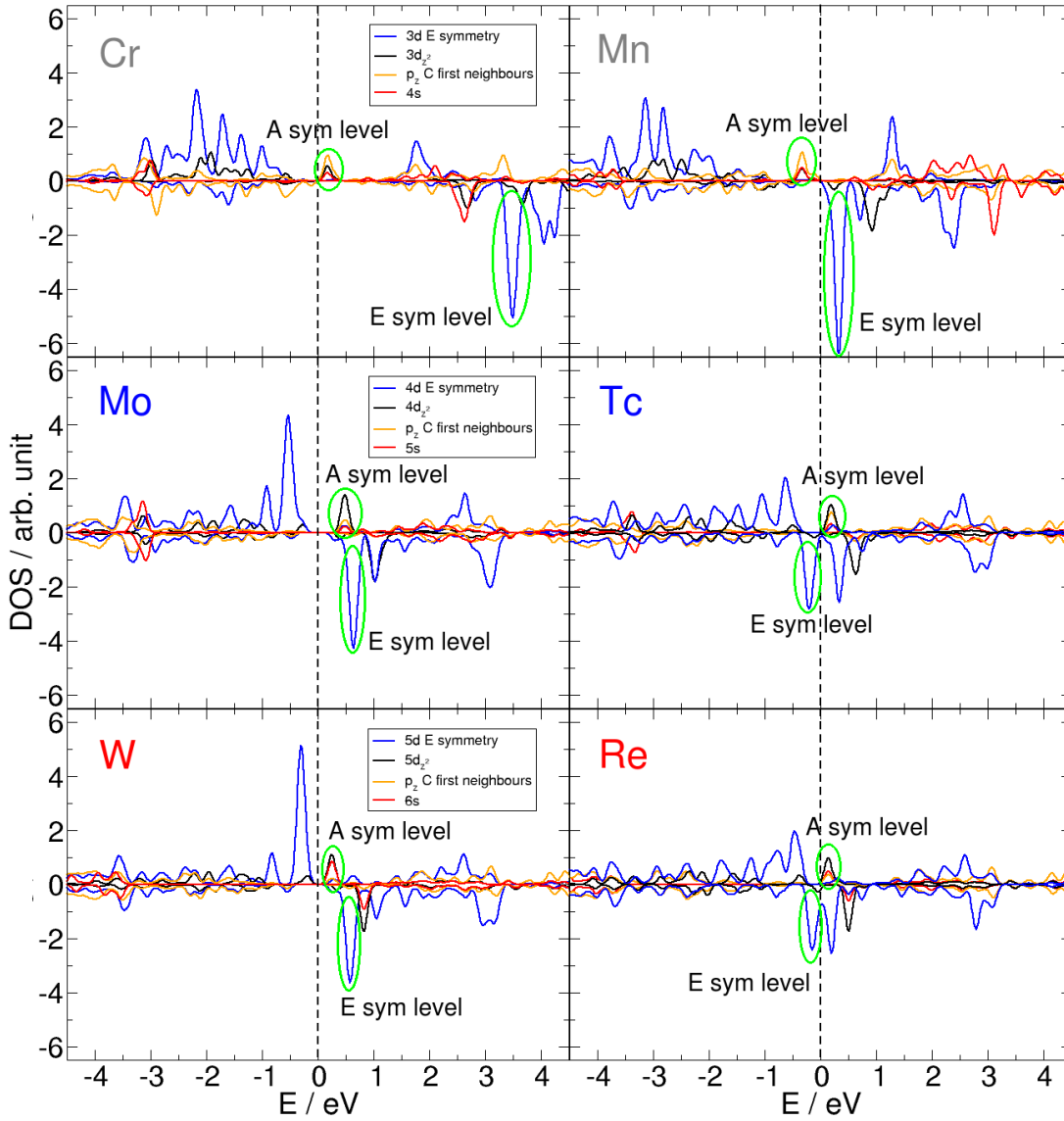


Figure 4.13: Projected density of states for graphene including impurities of the chromium and manganese groups, labeled in each graph. Green ellipses denote the A and E -symmetry levels, which are key to understand the decrease of the total magnetic moment between the technetium and manganese cases.

electron to the A -symmetry up level. When the spin splitting is lower as for technetium and rhenium, the electron fills the E -symmetry down level. In conclusion, the differences in the spin splitting of $3d$ with respect to the $4d$ and $5d$ explain the observed differences in the magnetic moments.

We next study in more detail the source of these differences in the spin splitting. We plot the density of states (DOS) projected on the different orbitals of each atom, as shown in Fig.4.13. The projected DOS let us comment on the hybridization of the impurities with neighboring carbon atoms. We focus on the A -symmetry level close to the Fermi energy which appears key to the magnetic solution. For $3d$ impurities, such as chromium and manganese, this level receives the larger contribution from carbon p_z orbitals. However, for $4d$ and $5d$ impurities in these groups, the largest contribution comes from d_{z^2} orbitals. The causes of the larger impurity contribution for $4d$ and $5d$ elements are their larger size and the larger shielding of the d electrons by internal electrons with respect to $3d$ elements. Thus there is larger interaction with graphene and more hybridization, which causes the partial lost of the impurity atomic character and the reduction of the spin splitting.

We have then further tested our results in the frontier case of technetium. We have carried out calculations fixing the total magnetic moment to $3 \mu_B$ and relaxing the geometry in order to compare with our result of $1 \mu_B$ obtained allowing free magnetization. Apart from being higher in energy, we found a slight enlargement of impurity-carbon distances (0.03 \AA) which reduced the hybridization being p_z the largest contribution. This agrees with our ideas above. Furthermore, we have followed a different approach and we varied the carbon-impurity distance gradually computing the variation of the total magnetic moment. The ground state distance is 1.92 \AA , and we found that for 1.95 \AA the magnetic moment rises to $3 \mu_B$.

Because our system could be considered strongly correlated, we include the Coulomb term for the case of technetium using values of 1, 2, and 3 for the parameter $U_{eff} = U - J$. The total magnetic moment remained $1 \mu_B$. We also included the U term for the iron group impurities, obtaining that iron gains magnetization, but no effect is observed for ruthenium and osmium. The role of U on $4d$ and $5d$ impurities seems softened with respect to $3d$ impurities as the spin splitting is smaller.

Density of states: late groups

Figure 4.14 shows the projected density of states for graphene with an impurity of the elements of iron, cobalt and nickel groups. As commented for chromium and manganese groups, the density of states is similar for the cases when graphene has $4d$ and $5d$ impurities. The pairs of ruthenium-osmium, rhodium-iridium and palladium-platinum show a similar projected density of states. There are differences with respect to iron, cobalt and nickel cases.

The states close to the Fermi energy show similar behavior for the three periods. For the non-magnetic cases of iron group, the lowest unoccupied molecular orbital (LUMO) is formed by two degenerated levels, two A -symmetry levels with spin up and down, which are marked up with green ellipses for the iron case in Fig.4.14. When moving

to cobalt group, the spin majority A -symmetry level, marked up with a green ellipse, is occupied due the addition of an electron and leads to a total cell magnetic moment of $1 \mu_B$. Adding another electron for the nickel group cases fills the spin minority A -symmetry level, removing the magnetic moment.

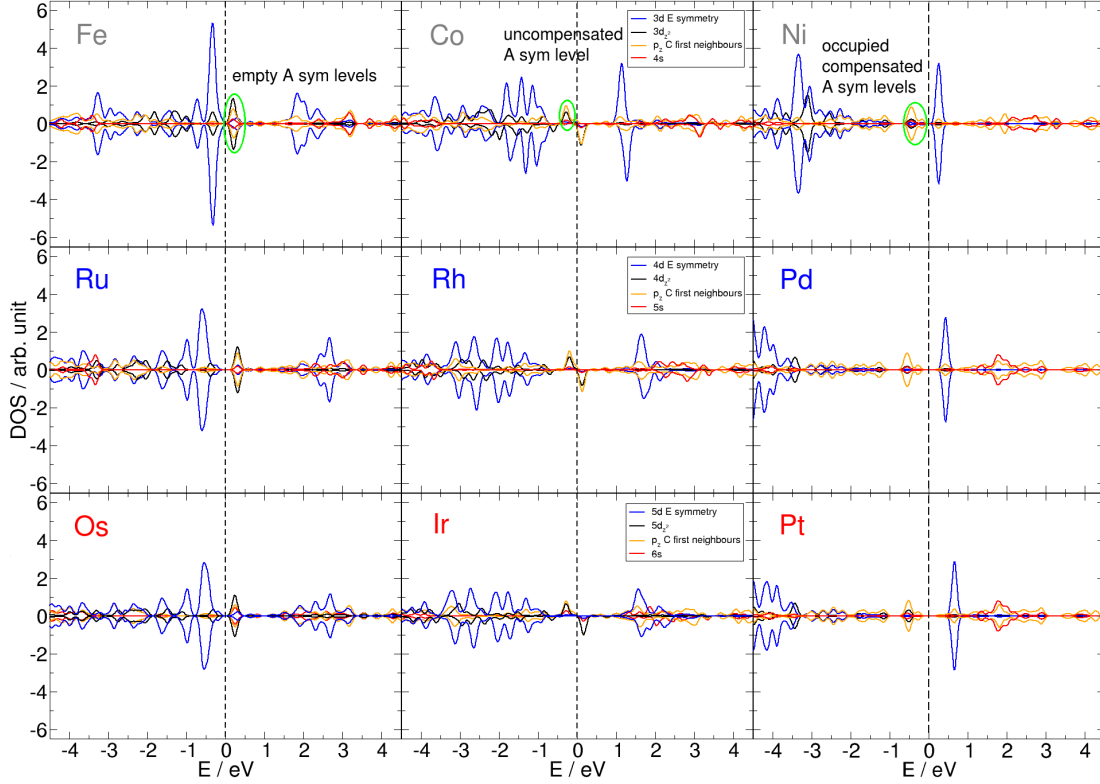


Figure 4.14: Projected density of states for graphene including impurities of the iron, cobalt and nickel groups, labeled in each graph. Green ellipses denote A -symmetry levels, which are key to understand the evolution of the total magnetic moment within the three groups.

4.4 Conclusions

In this chapter we have studied the doping of pristine graphene in two different ways. First we analyzed the adsorption of cobalt clusters on graphene, and second we investigated $4d$ and $5d$ substitutional impurities on graphene.

We chose to study Co_{13} clusters, which have different isomers. Firstly, we checked the stability order of the free isomers, obtaining that a two-dimensional isomer is preferred over the icosahedron structure. When deposited on graphene the icosahedron becomes the most stable isomer followed by the two-dimensional structure attending to the binding energy. The icosahedron over graphene is different to other previously reported as

the ground state. The cobalt cluster lies over graphene by an edge, and two other cobalt atoms forming triangular faces with this edge move towards carbon atoms. Therefore, there are four cobalt atoms bonding carbon atoms. The binding energy for cobalt atoms is larger when they are over graphene rather than in the free state for all the isomers, meaning that the cobalt clusters will stick to graphene.

The adsorption energy follows an opposed trend to the free isomers stability. The reason is that highly stable free isomers are reluctant to deformation and preserve their structure after adsorption. We study the relationship between number of bonds and distances with adsorption energy. We consider the stability order between different arrangements of the same isomer and between different isomers. We conclude that this empiric observation is useful to explain some cases but fails in many occasions as to be considered a general rule.

Thus we study other features as the explanation for the bonding and stability. Focusing on the global charge transfer, we found that there is not correlation between the bonding and the Coulomb interaction. Nevertheless, studying in detail the charge distribution within the free cobalt isomers and the stability of different arrangements over graphene, we find that cobalt clusters prefer to lie over graphene by cobalt atoms that have excess of electrons in the free state.

On magnetism, there is large magnetic moment decrease for the spherical clusters and smaller for the irregular clusters. For all the cases there is negative induced magnetic moments on graphene. For example, a value of $-0.33 \mu_B$ is found for the ground state icosahedron geometry.

Finally we repeated some of our calculations to extend to experimental setups. First, including the on-site interaction maintains the geometry of the structures and the icosahedron as the ground state geometry. Second, we compute free charged clusters as they are produced in the experiments obtaining that the two-dimensional isomer remains as the ground state free isomer. Third, we doped graphene by adding or removing an electron by two different methods and we computed the interaction with cobalt clusters. We found that the relative order of stability of the most stable isomers on graphene is preserved.

We have also studied $4d$ and $5d$ substitutional impurities in graphene. We found larger adsorption energies and larger bond lengths to carbon neighbors because of the larger size of the $4d$ and $5d$ impurities. From magnetism, the $4d$ and $5d$ impurities behave equally between them and similarly to the $3d3d$ impurities. We obtained that the bond lengths are almost equal for the $4d$ and $5d$ impurities. The explanation is that the $4d$ and $5d$ atoms have similar size because of the lanthanide contraction. Previously to filling $5d$ shell, $4f$ electrons are added. These electrons are far from the nucleus so the shielding is low. However, the atomic number is increased, which implies that $5d$ electrons are strongly attracted and the size is similar to $4d$ impurities. All the results are similar for the $4d$ and $5d$ impurities.

For the early groups, chromium and manganese groups, there are magnetic moments with large contribution on the impurity atom and induced magnetic moments of opposed sign are found on the three carbon neighbors. For the late groups, iron, cobalt and nickel,

the magnetic moment is 0 and $1 \mu_B$, alternatively. It has the same sign on the impurity and the three neighbor carbon atoms.

However, there is a noticeable difference for the manganese group. The total magnetic moment varies from $3 \mu_B$ for manganese to $1 \mu_B$ for technetium and rhenium. The reduction of the spin splitting for technetium and rhenium cases compared to manganese case changes the filling order of the levels near the Fermi energy. A minority spin level is favored over the majority spin level, and the total magnetic moment decreases to $1 \mu_B$. The cause for reducing the spin splitting is the larger size of the impurity atom, that hybridize with carbon orbitals. Thus, the impurity lost the atomic character and the spin splitting is reduced.

We checked the role of the on-site interaction on our results, obtaining no noticeable variation. It is interesting to comment that although for iron the on-site term induces magnetism, for the $4d$ and $5d$ impurities of its group, ruthenium and osmium, the on-site term does not vary the zero magnetic moment.

5 New two-dimensional materials design

5.1 Introduction

The isolation of graphene in 2004 begins a race for two-dimensional materials. Using theoretical calculations and experimental techniques, graphene revealed striking and promising properties, such as high electron mobility and ballistic transport among others. Other two-dimensional materials have been proposed. For example, phosphorene appears as a promising material for electronic devices because of high electron mobility and the existence of a band gap. The design of isoelectronic compounds to graphene and phosphorene is a way to search for new two-dimensional materials with different properties. We study two different isoelectronic compounds to phosphorene, such as silicon monosulfide (SiS) and carbon monosulfide (CS). For silicon monosulfide we propose a new phase that improves stability with respect to other thin phases. Parallel to our work, other group found other more stable SiS phases, but they are thicker than ours. We comment and compare all different SiS layers. For carbon monosulfide we present for the first time monolayers, thin films, and chains.

5.2 Silicon monosulfide monolayers

Silicon monosulfide nanostructures have been notably studied during the last years from the computational point of view. Different nanostructures have been predicted, but none has yet been synthesized experimentally. The α and β monolayers were proposed in analogy to phosphorene and buckled graphene, respectively [318]. Then, thicker structures that can be considered as thin films were reported [319]. Those structures were named *Pma2* and *Pmma* attending to their symmetry group. The *Pmma* structure was found to be unstable. Another structure called *silicene sulfide* was also reported [319]. The thicker structures are more stable than the reported α and β structures.

Simultaneously to these works on SiS thin films, we studied other silicon monosulfide nanostructures. We have found other SiS structures combining silicon and sulfur in nanoscale sizes, such as a monolayer labeled γ . The γ monolayer is more stable than α and β phases by more than 80 meV/atom.

Next we focus on the γ SiS monolayer looking at its stability and electronic properties. We bring into contact with other SiS nanostructures, to unveil the key parameters for stability.

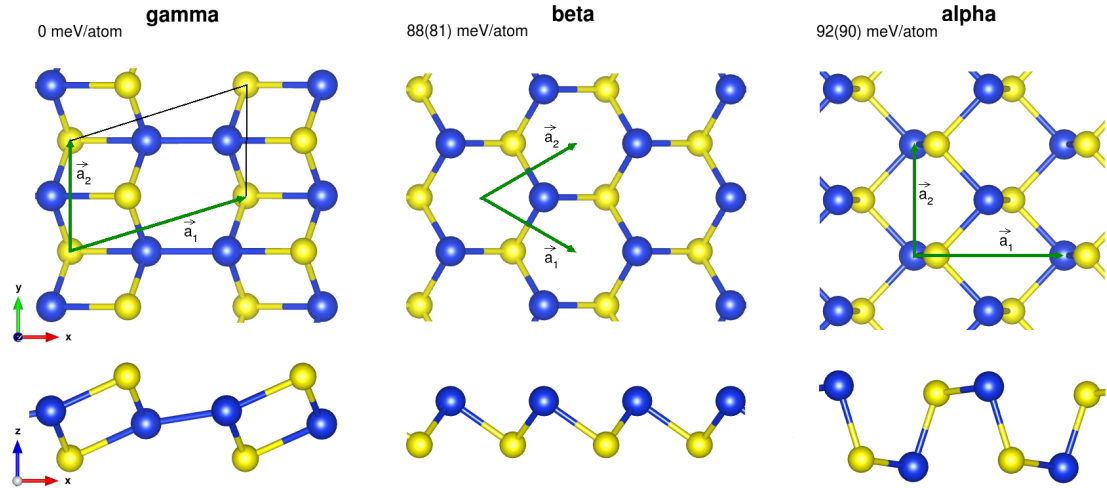


Figure 5.1: Geometries of three silicon monosulfide monolayers in order of increasing energy. Energies correspond to test results obtained using the SIESTA (VASP) method. The unit cell employed for the electronic analysis is shown in each case. Silicon (sulfur) atoms are denoted by blue (yellow) spheres; this color code is used throughout the article. The γ layer is the most stable and anisotropic of the three forms.

5.2.1 SiS monolayers: a new phase

We have found a new phase of silicon monosulfide that we called γ following the notation of the two previously reported SiS monolayers α and β . Figure 5.1 includes the three different SiS monolayers. The γ phase improves the stability by more than 88 meV per atom compared to the β and α phases. The difference in energy between α and β phases is 4 meV, a value smaller than the 12 meV previously reported [318], which can be ascribed to slight differences in the bond lengths. Our results are cross-checked using two codes, SIESTA and VASP, obtaining similar energy differences. Also, the stability of the γ monolayer is guaranteed by molecular dynamic simulations and phonon dispersion calculation, to be commented below.

The main different between the γ phase and the previously reported β and α phases is the shape of the cell. For the β and α phases hexagonal and rectangular cells were allowed, and each atom was restricted to establish three bonds. For the γ phase we used a rhombohedral cell with two silicon and two sulfur atoms, and silicon establishes a fourth bond with another silicon atom. We will see later that larger cells provide a large variety of silicon monosulfide structures.

We now comment on the γ phase structure. The γ phase combines rippled hexagons and squares in the y direction, which forces silicon to be four-fold coordinated including three sulfur bonds in the squares and a silicon-silicon bond. The silicon-silicon bonds rib the hexagon line in a stair-like fashion. The γ structure is highly anisotropic, much more than the reported α phase. On the contrary, the β phase is isotropic. The stability

enhancement of the γ phase can be ascribed to the extra silicon-silicon bond with respect to the β and α phases, in agreement with the fourfold coordination preferred local environment for silicon [319].

Stability: phonons and molecular dynamics

We carried out molecular dynamics simulations of the γ structure to investigate the monolayer stability at room temperature. We used the Nose thermostat at 300 K, with a Nose mass of 10.0 Ry f^2 and a time step of 1 fs [436–438]. The relaxation time to reach the target temperature was 2500.0 fs. We built a 3×3 supercell of 36 atoms to carry out the simulation. Figure 5.2(a) shows slight total energy fluctuations for four different simulation steps. The fluctuations are consequence of the oscillations of the atoms around their equilibrium positions. Figure 5.2(b) includes four snapshots of the γ monolayer during the molecular dynamics simulation. These snapshots correspond to steps marked up in Fig. 5.2(a). The molecular dynamics simulation shows that the γ phase is stable at room temperature. We double checked the stability of the γ monolayer by calculating the phonon dispersion as shown in Fig. 5.2(c). We find that there are no negative frequencies or softenings. Thus, the nanostructure stability is ensured.

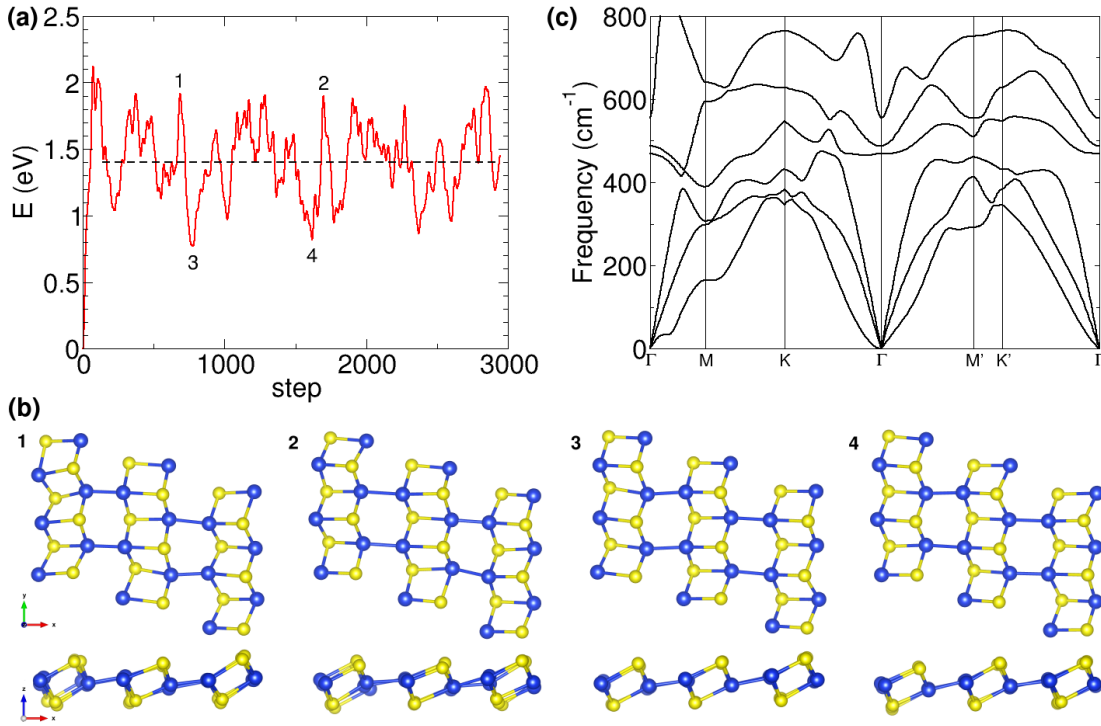


Figure 5.2: (a) Energy versus time step for the γ silicon monosulfide monolayer using a Nose thermostat at 300 K; (b) Snapshots at the four steps (1-4) marked up in (a); (c) Phonon dispersion of the γ silicon monosulfide monolayer.

Density of states of SiS monolayers

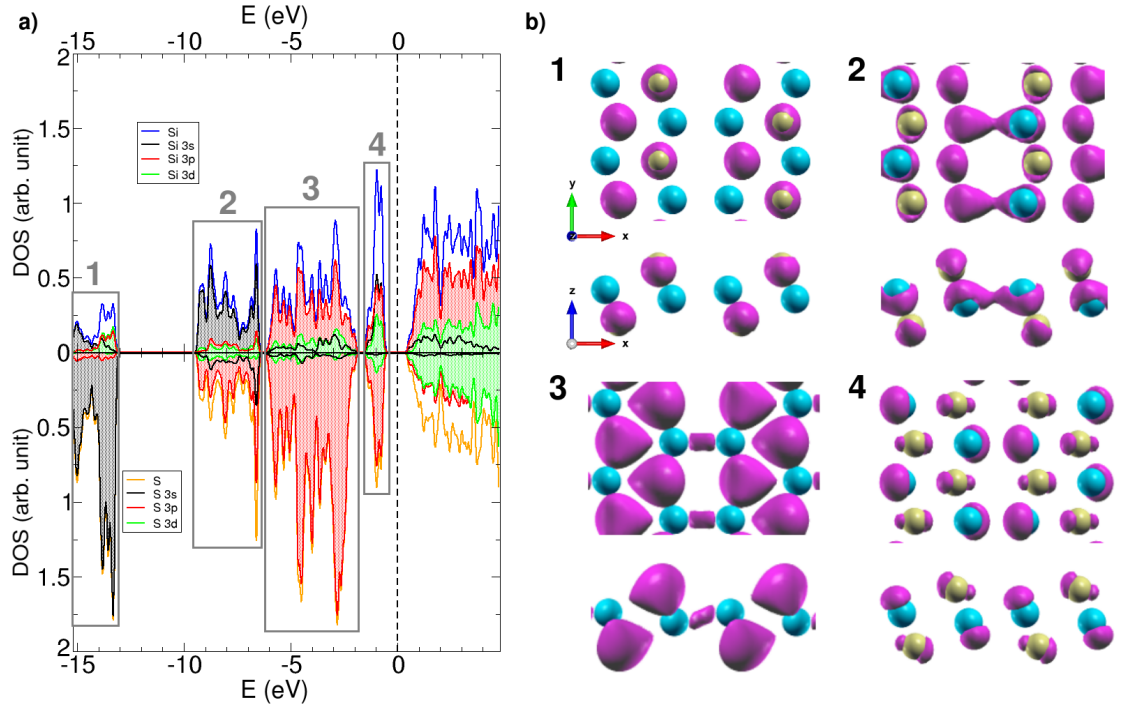


Figure 5.3: Electronic structure of the γ monolayer. (a) Projected density of states separated in silicon (upper panel) and sulfur (bottom panel). The four zones 1-4 highlighted within the rectangles are separated by small gaps. (b) Spatial local density of states in energy zones 1-4. Zones 2-3 have a component in the Si-Si bond. Zone 4 is p on sulfur and a dangling bond on Si, with a large *spd* hybridization.

We study the bonding and the local environment on each atom for the three SiS monolayers. The α and β monolayers present a silicon atom bonded to three sulfur atoms, with isotropic distances of 2.37 Å for β , and 2.37 and 2.39 Å for α . The angles between the bonds are 90° for the β structure and 93° (one) and 97° (two) for the α structure. The similar local environments for the atoms in these two phases explain the similar stability they show, as reported for phosphorene phases [439].

The γ phase has a silicon atom with four bonds in a different local environment. Apart from three sulfur bonds of 2.31 Å, there is an extra bond to a silicon atom of 2.50 Å. The angles between these bonds are close to right angles in all directions. There are two S-Si-S angles of 92° and one of 94°, and there are two Si-Si-S angles of 99° and one of 164°. Those angles makes a structure that requires a different hybridization from *sp* and includes the *d* orbitals to yield *spd* hybridization. The involvement of silicon *d* orbitals is a novelty with respect to the β and α phases.

We check the presence of the *spd* hybridization by studying the projected and the local

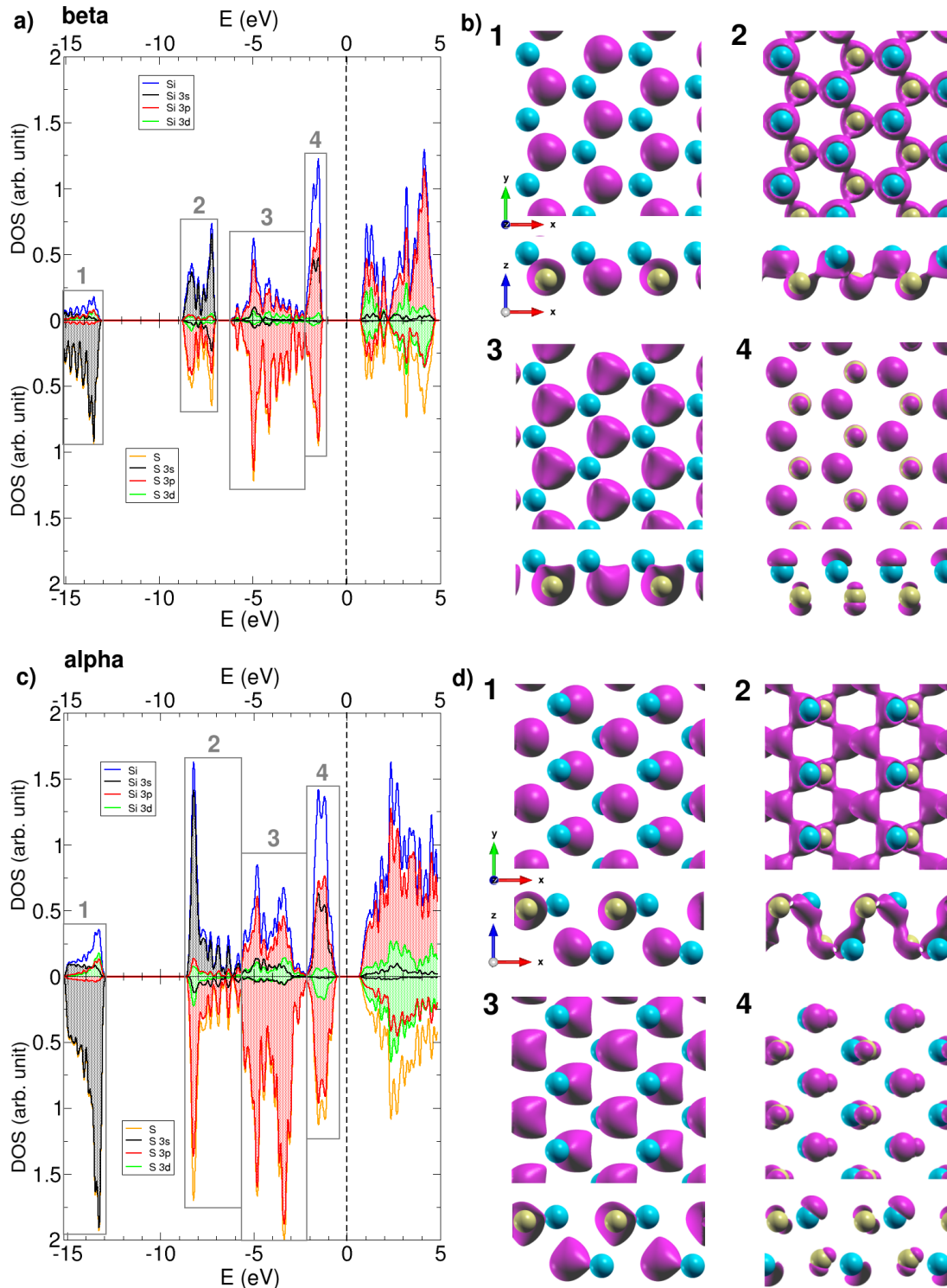


Figure 5.4: Projected (a) and local (b) density of states of the β monolayer. Projected (c) and local (d) density of states of the α monolayer, following Fig. 5.3 caption.

density of states (DOS) for the γ phase, as shown in Fig. 5.3 (a) and (b), respectively. The projected DOS show several issues to be commented. In general there are more sulfur states than silicon states as expected because of the larger number of valence electrons for sulfur. However, silicon contributes more in regions 2 and 4. There are four different regions within the density of states separated by small gaps, which we enclose by grey rectangles in Fig. 5.3 (a). The region number 1 is formed by s states from sulfur with very low contribution from silicon. The region number 2 is contributed by silicon s states and s and p states from sulfur. The region number 3 is formed by p states from silicon and sulfur. Finally, the region number 4 shows p states from sulfur and spd contribution from silicon. The d states amounts to half the s and p states, which indicates the spd hybridization. Besides, in the region 3 there is some contribution from s and d states from silicon.

The found conclusions are holding by analyzing the local density of states as shown in Fig. 5.3 (b). For the region 1 there is s -type lobes on sulfur atoms. For the region 2 there sp contribution on sulfur atoms, and s contribution on silicon atoms. There are σ silicon-silicon bonds denoted by the s -type lobes. Note that the silicon-silicon bonds lie deep in energy. In the region 3 there are p -type orbitals on the sulfur atoms, and there is some p -type contribution to the π silicon-silicon bond. Notice that this imply the presence of a double bond like between the silicon atoms, breaking the double bond rule. Finally in the region 4 there are p orbitals over sulfur atoms and spd lobes over silicon atoms. The lobes over silicon atoms seems dangling bonds. Although the regions 3 and 4 have p -type contribution, the local DOS show that the lobes are largely orthogonal between them.

For comparison, we also present the same analysis including the projected and local DOS for the β and the α phases in Fig 5.4. As for the γ monolayer, four different regions can be distinguished, and similar conclusions are obtained. However, there are some differences in the projected DOS in Fig. 5.4(a) and (c). Silicon and sulfur contribute almost equally in the region 2, and silicon is more important in the γ phase. The d contribution for the silicon atoms in the region 4 is negligible, while for γ was the half of the s and p contributions. This change is ascribed to the different hybridization of silicon in these phases: sp for the α and β structures, and spd for the γ monolayer.

The local DOS of β and α phases is shown in Fig. 5.4(b) and (d). In agreement with the equal contribution of silicon and sulfur showed by the projected DOS, we find that in the region 2 there is an isotropic and uniform structure for silicon and sulfur atoms. The regions 1 and 3 are similar to those of γ phase, although for the β and α structures there is no π silicon-silicon bond. In the region 4 there are p -type orbitals over sulfur atoms and dangling bonds over silicon atoms, as for the γ phase. The difference is the composition of the silicon dangling bond, spd for the γ phase and sp for the β and α phases.

Band structures

Figure 5.5 includes the band structures for the γ , β and α SiS monolayers, and the corresponding paths on the reciprocal space. For the β and α monolayers the band

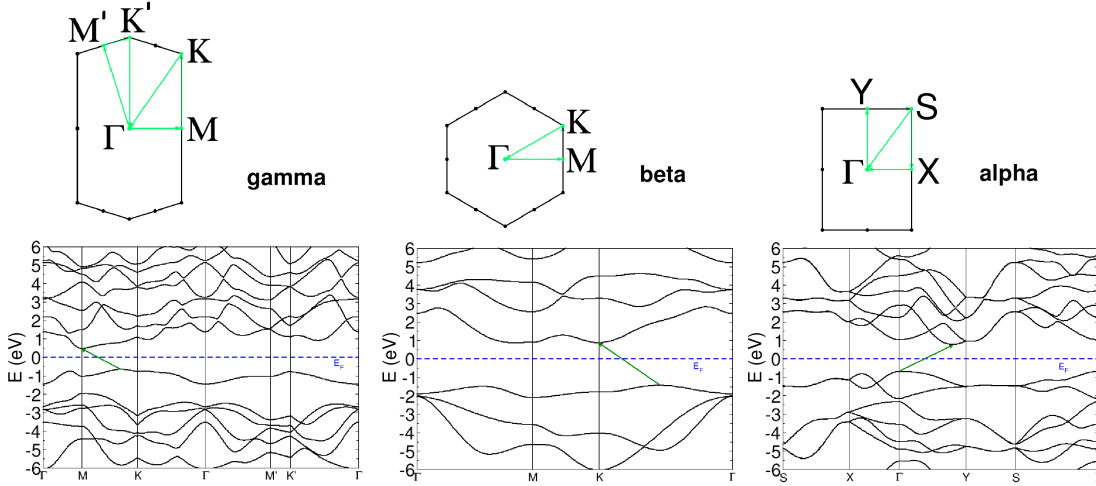


Figure 5.5: Band structures of three silicon monosulfide monolayers together with the path followed in the reciprocal space for each case.

structures reproduce faithfully the results reported previously [318]. We obtain band gaps of 2.3 and 1.5 eV for β and α SiS monolayers. For the three SiS monolayers the band structures show indirect band gap. The γ phase has an indirect band gap of 1.13 eV. Note that there is no correlation between the band gap size the stability order. The three structures are semiconductors. The band gaps are probably larger because of the well-known underestimation of band gaps when using LDA and GGA functionals within the density functional theory calculations [328, 329]. A particular feature of the γ phase is the presence of an isolated localized band near the Fermi energy. This band also has a pseudo gap with respect to deeper energy states. The analysis of the projected and local DOS showed that this band has larger contribution from silicon than from sulfur, with p_z lobes on sulfur atoms and spd dangling bonds over silicon atoms. The hexagonal Brillouin zone is distorted because of the rhombohedral shape of the γ unit cell. So there is anisotropy in the localized band, with the shortest valence-conductance distance found for the M-K path. This direction partially represents the silicon dimers, which are stability but also anisotropy sources.

5.2.2 Summary of structures: stability

We comment on the variety of nanostructures for silicon monosulfide. In the section beginning, we explain the rise of proposed minima for SiS layers. Now we try to provide a global vision on these structures and their stability. Figure 5.6 shows the side view of the most representative SiS nanostructures, because it allows to distinguish between monolayers (γ , β and α) and thin films ($Pma2$ and *silicene sulfide*).

SiS thin films are largely more stable than the monolayers by more than 200 meV/atom. We could think that the thicker the structure the larger the stability. Furthermore, thicker structures allow a larger number of atoms per surface unit, which could enhance

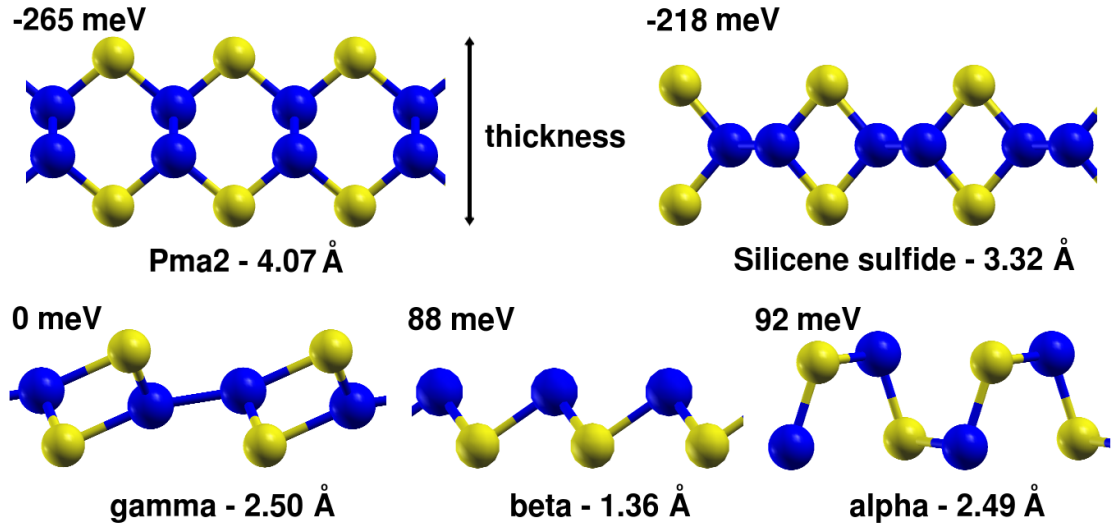


Figure 5.6: Side views of five different phases already reported for silicon monosulfide including their thicknesses in angstrom units and the relative stability in meV attending to our calculations.

the stability. However, there are cases where larger densities does not imply more stability [440]. Looking at the three monolayers we find that the β and α phases are almost degenerated, being the β phase thinner than the α phase. So there is not a clear relation between stability and thickness. Specifically, the β and α structures have a similar energy per atom because each atom has a similar environment [439] on both structures. Each silicon (sulfur) atom is bonded to three sulfur (silicon) atoms, with similar bond lengths and angles.

We want to understand the stability order of SiS nanostructures, related to the number of bonds and the hybridization. The *Pma2* phase stability is justified by the four and two bonds established by silicon and sulfur, respectively [319]. The number of bonds of silicon and sulfur is based on the octet rule.

For the α and β phases each atom has three bonds. For the γ phase we found in our calculations, the silicon atom has three bonds to sulfur atoms plus one bond to another silicon atom. Sulfur atoms remain with three bonds to silicon atoms. Concerning the number of bonds, the extra stability of the γ phase with respect to β and α phases comes from the silicon-silicon extra bond. For the SiS thin films, the silicon atoms have four bonds and the sulfur only two. Then, the extra stability of the SiS thin films comes from a lower number of bonds by sulfur atoms.

We go back to discuss the relation between thickness and stability. We showed that there is no direct relationship between thickness and stability. Now we find that the bonds number of each atom is crucial to stability. The landscape of SiS nanostructures is shown in Fig. 5.6. Thicker structures allow sulfur to have two bonds. Indeed, there is an indirect relationship between thickness and stability. The thicker structures, like the

thin films, allow for different hybridizations and more stable structures are predicted.

After reviewing the different nanostructures for SiS and their stability, it remains a challenge to design a SiS monolayer with four and two bonds for silicon and sulfur, respectively. The arrangement of sulfur atoms to establish only two bonds appears as the main obstacle.

The predicted SiS nanostructures have not been yet synthesized. Therefore, it is not clear which structure would be favored during the experiments. Here we propose a possible synthesis route using chemical vapor deposition (CVD) as the appropriated experimental technique. Using adequate precursors of silicon and sulfur, still to be determined, there would be a reaction of those at high temperatures in a furnace. This reaction would lead to the deposition of a SiS monolayer over a substrate. Control of the SiS nanostructure to be obtained among those proposed theoretically could be achieved by controlling rates, substrate treatment or election of precursor materials. We expect that experimental work on the synthesis of this promising material will be carried out in the future.

Metastable SiS structures

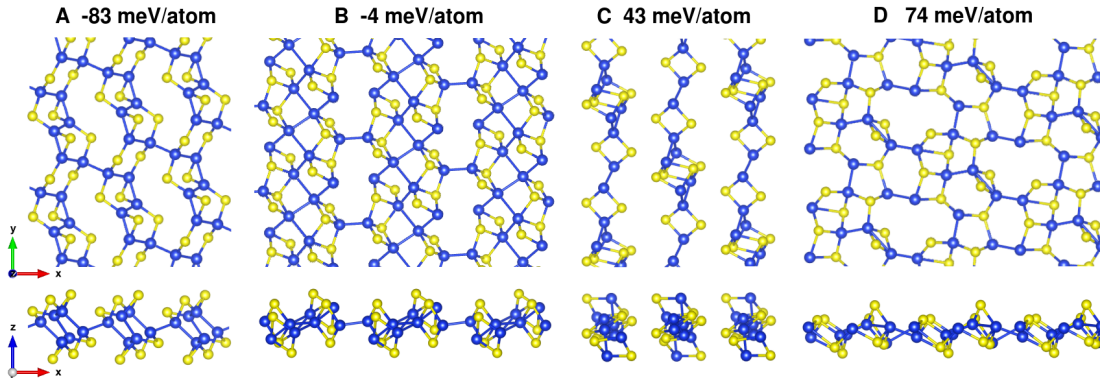


Figure 5.7: Examples of metastable monosulfide chain-like structures with large cells. Chains are linked by Si dimers except for the C structure. The energies reference is the γ monolayer from Fig. 5.1. Note that Si atoms form larger chains, percolating through the SiS layer.

Apart from the γ SiS monolayer, we have found few SiS metastable nanostructures that are also more stable than the β and α monolayers. Figure 5.7 include four different SiS nanostructures we called A, B, C and D in order of stability. The first nanostructure, A, is even more stable by 83 meV/atom than the γ monolayer, and the second, B, is almost degenerated to it. We got these structures allowing larger unit cells and different shapes such as square, rectangular or hexagonal. Full relaxation of the atom coordinates and the cell vectors yielded these structures.

The large stability of the A nanostructure can be explained because silicon has four bonds and sulfur has two bonds, following the previous discussion. Side views show that

these structures have more atoms per surface unit, compared to SiS monolayers. The A and B nanostructures follow a similar pattern to that of the γ monolayer: silicon monosulfide chains connected by strong silicon-silicon covalent bonds of 2.4 Å. A difference to γ monolayer is the existence of silicon chains of four atoms bonded in a row, which suggest Si-Si percolation through SiS layers. The silicon-silicon bonds within the SiS chain let sulfur to have only two bonds, which rises stability. The C nanostructure shows SiS chains linked by dispersion forces. Within the chain, sulfur has only two bonds, while silicon has three or four depending on the position. Finally, the D nanostructure display more complicated SiS chains that are linked by silicon-silicon bonds, as for A and B. As we have seen there are plenty of different silicon monosulfide nanostructures, which are explained by the possible different hybridizations of silicon and sulfur atoms and the number of bonds they form. Although silicon forming four bonds and sulfur two seems the preferred picture, there are plenty of other alternatives to be investigated.

5.3 Carbon monosulfide nanostructures

Designing new two-dimensional materials is an active field nowadays. Specifically, a wide variety of isoelectronic compounds to phosphorene are being proposed and studied thoroughly nowadays. None of the already proposed compounds is based on carbon. In this section, we study carbon monosulfide nanostructures.

5.3.1 Monolayers

We computed a large variety of different monolayer structures of carbon monosulfide. We follow the transmutation approach, substituting phosphorus atoms by carbon and sulfur in a phosphorene-like structure. Besides, we computed other cells and structures.

Geometries

Figure 5.8 shows the geometries of the four most stable carbon monosulfide monolayers. The ground state monolayer is the α structure similar to phosphorene. This structure has been proposed for phosphorene isoelectronic monolayers with other compounds, in the group V and in the groups IV-VI also called group IV monochalcogenides [313–316]. The group V compounds are nitrogene, phosphorene, arsenene [306–308] and antimonene [308], and their binary compounds [309].

The stability order has been also checked by VASP calculations. The same results are found although with slightly larger energy differences, as shown in Fig. 5.8. Next in energy we find the δ structure, which shows a specific structure with a square-like lattice visible in a top view. The unit cell is a square, while it was a rectangle for the α structure. The side view reveals the same height for all the carbon atoms and two different heights for sulfur atoms. The κ monolayer is next in energy and has a rectangular unit cell. It seems a distorted δ structure with some carbon atoms displaced horizontally with respect to the others. It seems halfway between the α and δ structures. Carbon and sulfur atoms have two different heights. Last we have the β phase with a hexagonal

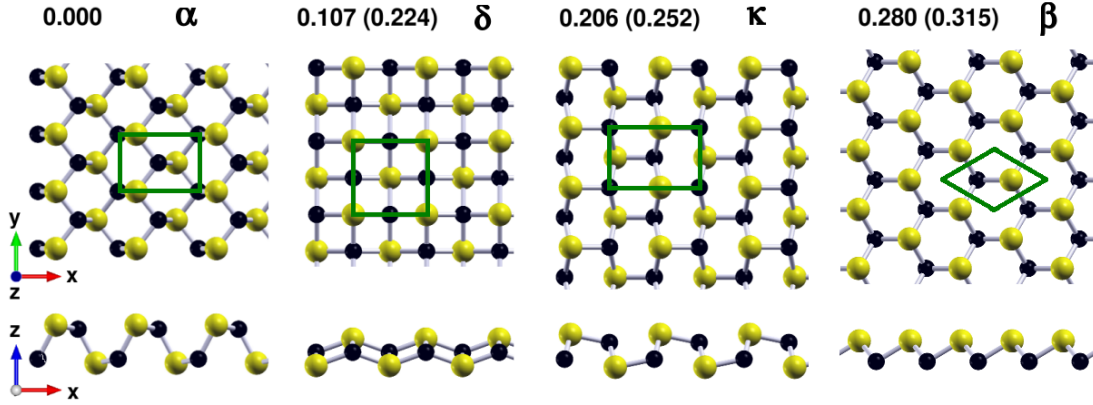


Figure 5.8: Geometries of four carbon monosulfide monolayers in order of increasing energy. Energies in parenthesis correspond to test results obtained using the VASP method. The unit cell employed for the electronic analysis is shown in each case. Carbon (sulfur) atoms are denoted by black (yellow) spheres; this color code is used throughout. The α layer is the most stable.

lattice similar to graphene from a top view. The side view reveals a buckled structure with two different heights as for silicene [287].

Electronic properties

Figure 5.9 shows the band structures of the four different monolayers of carbon monosulfide described previously. The band structure for the α , κ and β structures show that they are semiconductors with indirect band gaps of 0.97, 0.77 and 1.64 eV, respectively. For the α and κ layers the minimum of the conduction bands is located at the Γ point. The δ structure is metallic, with valence states at the Fermi energy at the M point and conduction states at the Fermi energy in the $M\Gamma$ path. The band structures of the α and κ phases are similar. The α and κ bands display a couple of occupied bands close to the Fermi energy, which are isolated from deeper states by 2 and 0.5 eV, respectively. The δ band structure is different from α and β because the two bands close to the Fermi energy are now metallized and go down in energy following a parabolic shape. While for the α and β cases these two bands were localized in 2 eV, for the δ structure they broad up to 6 eV. In the conduction bands there are two bands close to the Fermi energy that mimic the behavior of the two occupied bands. In the δ case these unoccupied bands are also metallized, leading to conduction states at the Fermi energy. For the β monolayer, the two valence bands close to the Fermi energy are degenerated over the whole path in the Brillouin zone. We also study the charge transfer under the Mulliken scheme. Although carbon and sulfur have similar values of electronegativity in the Pauling scale, 2.55 and 2.58 respectively, there is large charge transfer from carbon to sulfur atoms for the four structures. We obtained values of 0.81, 0.92, 0.65 and 0.66 electrons for the α , δ , κ , and β phases, respectively. Note that almost an electron goes from carbon to

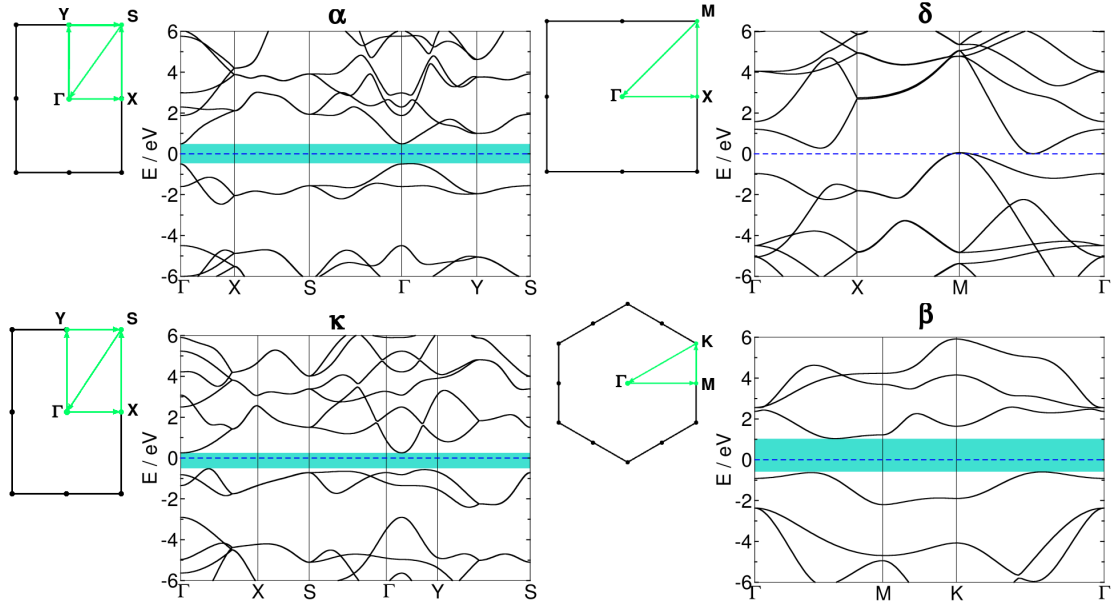


Figure 5.9: Band structures of four carbon monosulfide monolayers. Insets show the path followed in the reciprocal space for each case.

sulfur for the two most stable monolayers. A possible explanation can be the larger size of sulfur atoms with respect to carbon atoms.

Stability: phonon dispersion and molecular dynamics

Figure 5.10 includes the phonon dispersion for the four carbon monosulfide monolayers. The phonon dispersion of the α and δ monolayers shown in Fig. 5.10(a) and (b) display no negative frequencies, ensuring their stability. The κ and β cases have negative frequencies in Fig. 5.10(c) and (d), respectively. The κ phase seems an intermediate state between the α and δ phases. We check the α and δ phases stability at room temperature by carrying out molecular dynamics simulations, as shown in Fig. 5.10(e) and (f). The energy shows temperature fluctuations with small displacements of the atoms with respect to their equilibrium positions. Our results show that the α and δ phases are stable up to room temperature.

α monolayer

We now focus on the α ground state carbon monosulfide monolayer. Each carbon atom is bonded to three sulfur atoms and vice versa, with two bond lengths of 1.82 Å and one of 1.90 Å. The angles between the bonds established by carbon atoms are two of 113° and one of 103°. In the case of sulfur there are two angles of 101° and one of 103°. The bonds points towards a sp^3 hybridization for carbon.

To study hybridization and gain knowledge about the band structure, we plot the

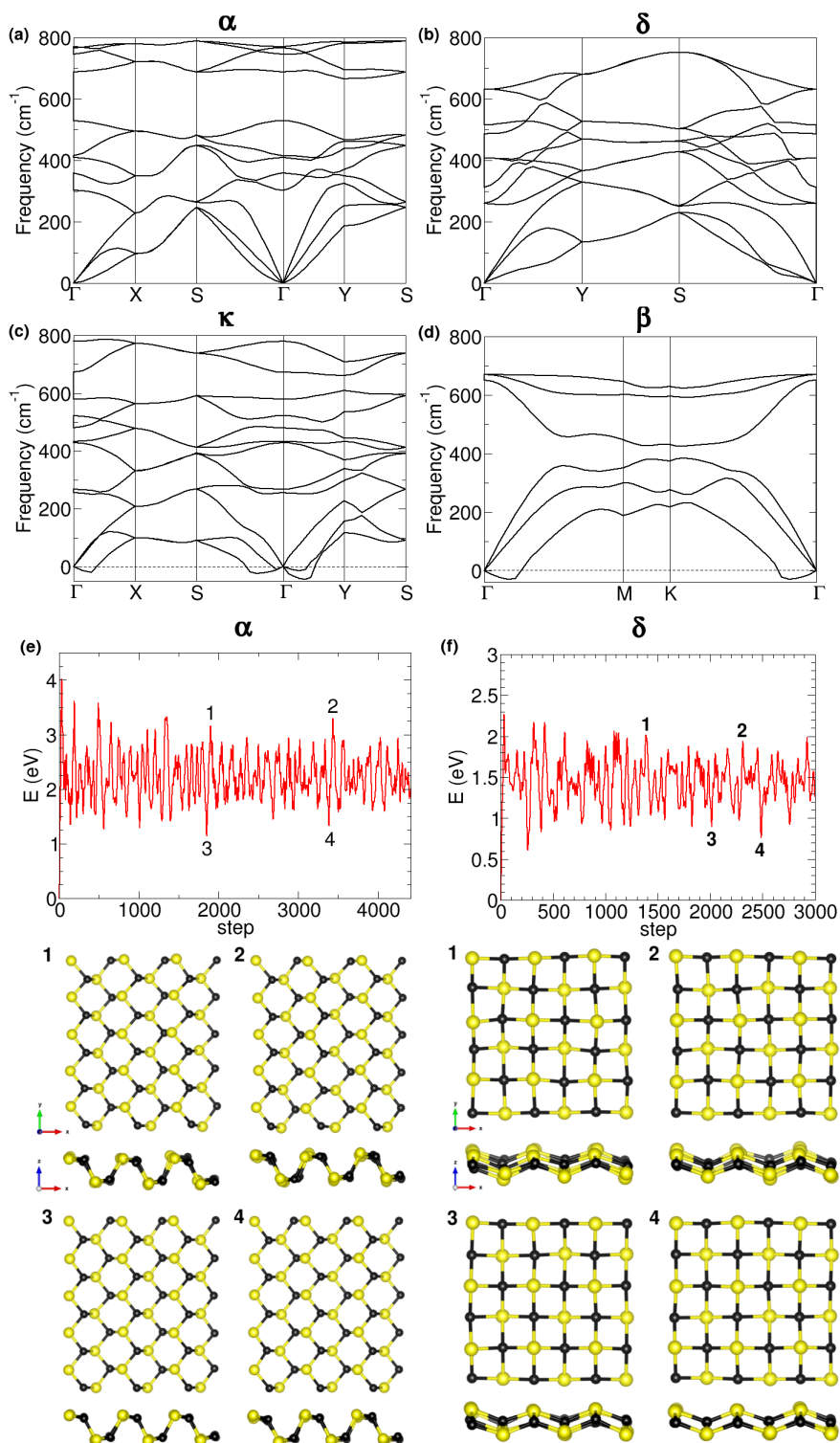


Figure 5.10: (a-d) Phonon dispersion of the α , δ , κ and β carbon monosulfide monolayers. (e-f) Energy versus time step for the α and δ carbon monosulfide monolayers using a Nose thermostat at 300 K. Snapshots at four steps (1-4) are given below.

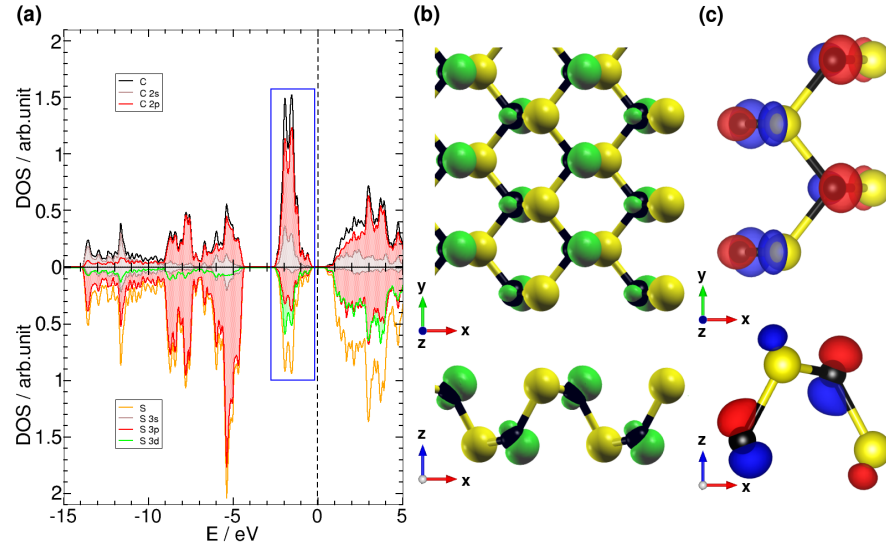


Figure 5.11: Electronic properties of the α ground state structure. (a) Density of states projected on carbon (upper panel) and sulfur (bottom panel). (b) Spatial localized density of states for the energy peak marked up with a blue rectangle in (a). (c) Highest occupied orbital of the valence band at the Γ point.

density of states projected on the carbon and sulfur orbitals in Fig. 5.11(a). Sulfur contributes more than carbon to the density of states at most energies because of the larger number of valence electrons. However, there is an isolated peak close to the Fermi energy, enclosed by a blue rectangle in Fig. 5.11(a), where the carbon contribution is larger. This peak matches to the isolated bands near the Fermi energy commented on the band structures. The projected density of states shows that carbon provides the main contribution with s and p states. The presence of carbon s states near the Fermi energy agrees with the sp^3 hybridization. There is also sulfur contribution to these states, and surprisingly there is a strong d contribution combined with p orbitals. The sulfur d contribution is highly concentrated at the bands close to the Fermi energy. Consequently, some spd hybridization is expected for sulfur, with sulfur d orbitals being important near the Fermi energy.

Figure 5.11(b) shows the localized density of states for the energy range given by a blue rectangle in Fig. 5.11(a). Carbon is the main contributor in this energy range, and there are lobes only over carbon atoms. The green lobes shape over carbon atoms suggests a large p -type contribution mixed with some s orbitals. The carbon lobes seem to be dangling bonds in agreement with the sp^3 hybridization. To complete the analysis we plot the highest occupied molecular orbital (HOMO) at the Γ point as shown in Fig. 5.11(c). There is a p -type lobe over carbon atoms with negligible s contribution, agreeing with the higher occupied states shown in Fig. 5.11(a). The carbon p orbitals constitute the largest contribution in this energy range, and are responsible for the band

broadening when the lattice is distorted to a square.

The α geometry is similar to that of phosphorene, and has been reported for other isoelectronic compounds, such as silicon monosulfide [441]. Different from phosphorene, the binary isoelectronic compounds leave one of the elements in the outer part of the structure, as shown in the side view for the α phase in Fig. 5.8. Comparing the SiS and CS α phases, some parallelisms are obtained. The two SiS and CS leave the larger atom as the outer atom, which is sulfur for CS and silicon for SiS. The outer and inner positions show two different hybridization roles. The inner atom, carbon for CS and sulfur for SiS, shows a p -type contribution to the frontier orbitals at the Γ point. The outer atom, sulfur for CS and silicon for SiS, displays a dangling bond. For sulfur in CS, the dangling bond has pd hybridization as shown in Fig. 5.11(a) and in the case of silicon in SiS it was spd hybridization [441]. There are two differentiated roles in the phosphorene-like structure. Sulfur can play the two roles depending on the counterpart element, as shown for SiS and CS.

δ monolayer

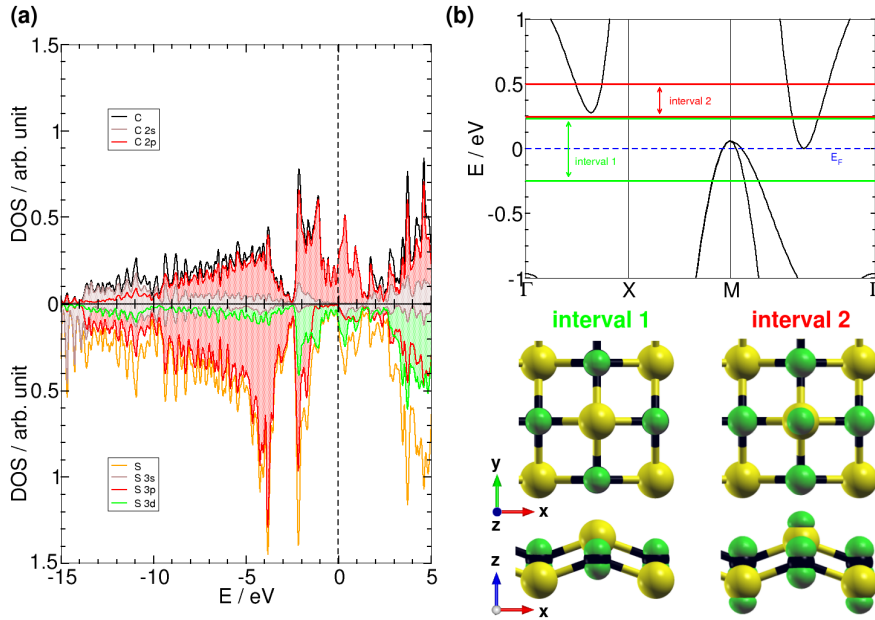


Figure 5.12: Electronic properties of the δ monolayer. (a) Density of states projected on carbon (upper panel) and sulfur (bottom panel). (b) Spatial localized density of states for the two energy intervals shown in the band structure.

The δ phase is the second most stable carbon monosulfide monolayer. It is particular because it is metallic. It seems that the α and δ phases can be connected by a distortion of the structure using strain to control the semiconductor-metal transition. The δ phase is isotropic and it has a rippled square-like pattern for carbon and sulfur atoms. The

carbon-sulfur bonds have a distance of 1.93 \AA . Although carbon atoms are in the same plane, sulfur atoms are found at two different heights, producing different angles between the bonds. The consecutive carbon bonds form four angles of 96° , with an angle of 141° for opposed bonds. From sulfur atoms, the four bonds to carbon atoms form four angles of 84° . The angles are close to right angles, which suggests that d orbitals are involved producing spd hybridization for sulfur. Then we plot the projected density of states in Fig. 5.12(a). There is large d contribution near the Fermi energy for sulfur, combined with p orbitals at deeper energies. In general, sulfur contributes with more states than carbon, because sulfur has two extra valence electron. However, carbon p states prevail over the sulfur d states near the Fermi energy. Therefore, it seems that carbon is responsible for the conduction states. Near the Fermi energy, we plot the localized density of states (LDOS) in Fig. 5.12(c) for the energy intervals marked by green and red lines in Fig. 5.12(b). The LDOS within interval 1 shows p -type orbitals over carbon atoms, forming a square lattice of p orbitals responsible for conduction. The conduction is along the path ΓM in the reciprocal space, equivalent to the (110) direction in real space. Interval 2 is higher in valence states and includes a band in the ΓX path, which has a gap of 0.22 eV with respect to conduction band at Γ point. The LDOS within interval 2 shows p orbitals on carbon, but also dangling bonds on sulfur atoms over the outer part of the monolayer.

From α to δ monolayer under strain

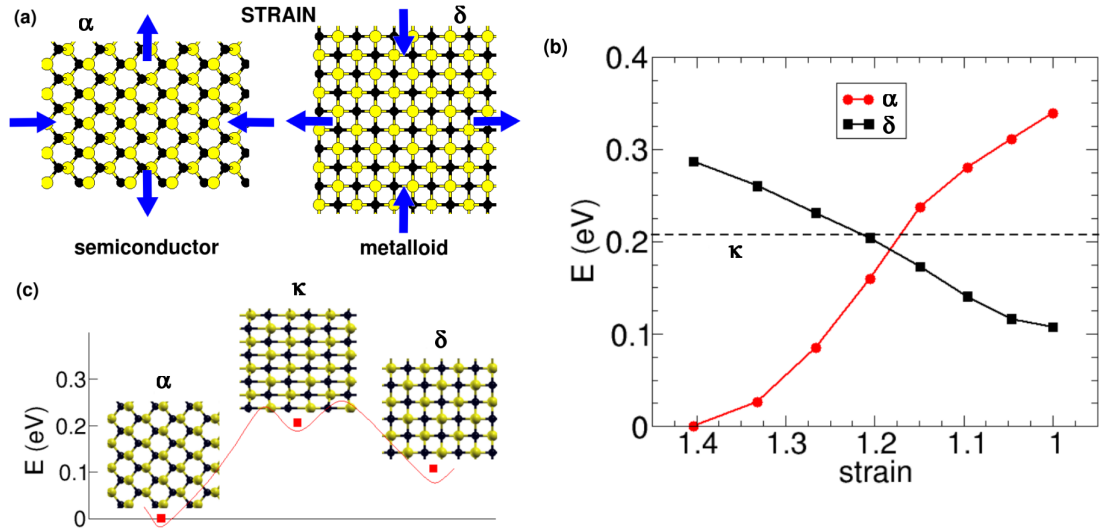


Figure 5.13: Stretching the α and δ monolayer as shown in (a) yields an increasing energy as shown in (b), suggesting the existence of a barrier between these phases. (c) Relative position in energy of the three most stable monolayers.

We suggested previously the connection between the α and δ phases by applying strain,

as shown in Fig. 5.13(a). The main idea is to apply strain to the monolayers in order to induce a transition between these structures. We adjust step-by-step the rectangular α unit cell to transform it into the δ unit cell, and vice versa. During the calculations the unit cell is fixed at each step and the atoms are fully relaxed. The strain parameter controlling the transformation is the ratio between length and width, which is 1 for the δ phase and 1.4 for the α phase. We expected that, when relaxing the atoms positions, the δ phase would transform into the α phase because of its higher stability. We found that the δ phase is well-preserved, although distorted. Similar results are obtained when starting from the α phase. Figure 5.13 shows the relative energy of the α and δ distorted phases for different steps. The energy increases monotonously in both directions when the original structures suffer strain. There is a barrier of about 0.2 eV per atom between the α and β phases. The energy of the κ structure is shown for comparison, close to the crossing between the two curves. This is agreeing with our idea that the κ phase is an intermediate state between the α and δ phases, as schematically shown in Fig. 5.13(c). The δ phase is retained even after large distortions of the cell, which reinforces its stability. The stability of the δ phase has also been proved by molecular dynamics simulation at room temperature and phonon dispersion calculations.

5.3.2 Chains

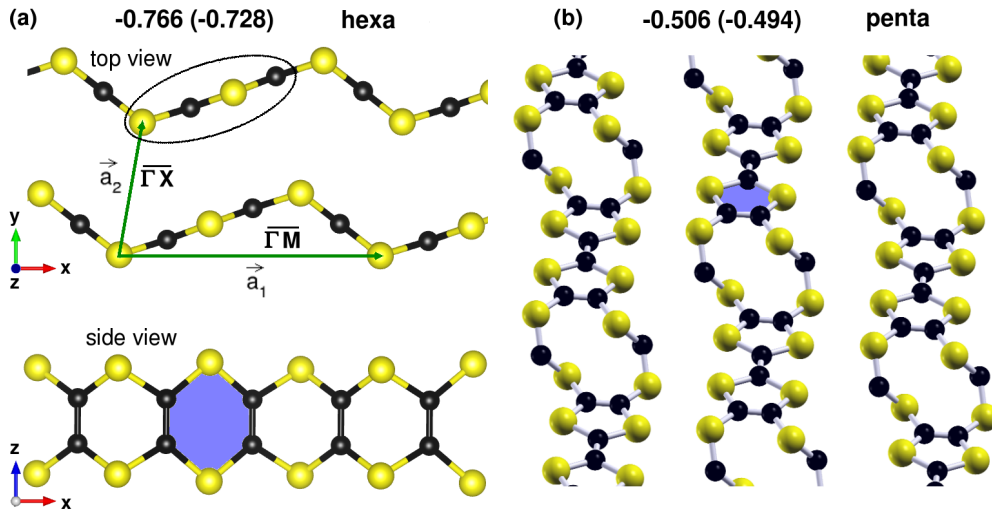


Figure 5.14: Chain structures for carbon-monosulfide. The chains are labeled (a) *hexa* and (b) *penta* motifs, because one has hexagons and the other pentagons, respectively. Carbon (sulfur) atoms are represented by black (yellow) spheres. The unit cell for the *hexa* chains is marked by green vectors. The energies per atom obtained using SIESTA (VASP) method are given referred to the ground state monolayer α .

When computing different structures of carbon monosulfide monolayers, we also ob-

tain chains structures. Substituting silicon atoms by carbon atoms in the γ SiS structure and fully relaxation lead to chains. These chains are forming a layer and the distances between atoms of contiguous chains are larger than 3 Å. Surprisingly, the chains structures are most stable than the ground state monolayer by more than half eV per atom. Figure 5.14 includes two different chains structures, which we refer to as *hexa* and *penta* accordingly to the presence of hexagonal and pentagonal motifs in the chains, as highlighted in blue in the figure.

Chains with hexagonal motif

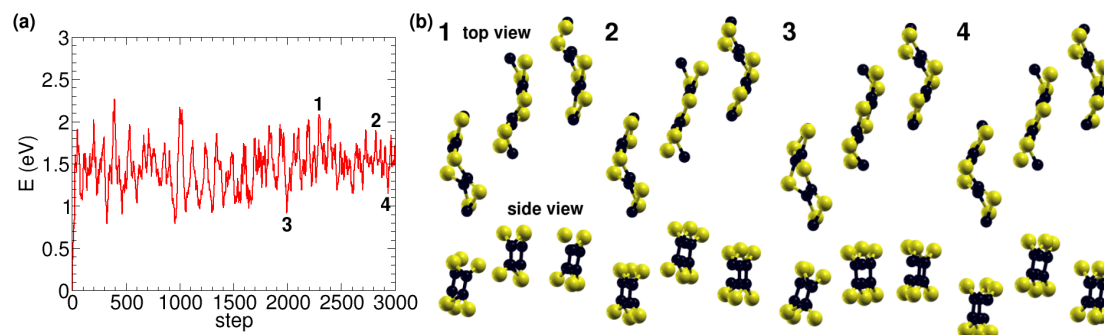


Figure 5.15: (a) Energy versus time step for the *hexa* chains using a Nose thermostat at 300 K. (b) Snapshots at the four steps (1-4) marked up in the graph are shown below.

Figure 5.14(a) shows the top and side views of the *hexa* chains. The *hexa* structure largely improves stability to the α monolayer in 0.766 eV per atom. The distance between atoms of close chains is larger than 3.7 Å, which means that they are mediated by dispersion forces. Therefore, the interaction between neighbor chains is expected to be considerably smaller than the strong covalent bonds within a single chain. Although we are interested in the bonding within a chain, we carried out calculations using a van der Waals functional in the VASP method to estimate the dispersion forces. The direct inclusion of van der Waals increases the stability of the chains with respect to α monolayer by about 70 meV per atom. Figure 5.14 shows the cell vectors of a unit cell formed by twelve atoms, six carbon and six sulfur atoms. Note that a straight chain keeping the same structural pattern would require only two carbon and two sulfur atoms in the unit cell. However, the presence of kinks in the structure impose a larger unit cell. Kinks arise spontaneously, and there is a gain about 70 meV per atom with respect to the straight chain. The chain alternates long and short stretches of two units and one unit of the motif S-C-S seen from above. The kinks presence shows two different roles for the carbon and sulfur atoms depending on whether they are in a short or a long straight stretch, or in a kink.

We checked the chains stability by molecular dynamics simulations at 300 K as shown in Fig. 5.15. There are strong covalent bonds between carbon and sulfur atoms. Each

carbon atom has three bonds, two with sulfur atoms of 1.82 Å and one with carbon of 1.38 Å. The angles between the three bonds around carbon are close to 120° , although there are slight variations depending on the carbon atom in the *hexa* chain. The angles suggests sp^2 hybridization for carbon atoms. The short carbon-carbon bond is characteristic of a double bond, with σ and π bonds. The σ bond is formed by sp^2 hybridization lobes of carbon. The π bond, formed by two p -type orbitals of carbon, is spatially seen in the HOMO wave function at the Γ point of the *hexa* structure shown in Fig. 5.16(a). About sulfur, each atom has two bonds with carbon atoms, and there are small differences in the angle between these bonds depending on the position of the sulfur atom on the *hexa* chain. The chain alternates two consecutive twisted sulfur atoms and one in a straight stretch. The angle is 103° and 99° for the twisted and straight sulfur atoms, respectively. The HOMO wave function at Γ point in Fig. 5.16(a) shows a p_z orbital over the sulfur atoms. Because of the kinks, the twisted sulfur tilts the p_z orbital about 25° compared to the straight sulfur, as marked in Fig. 5.16(a).

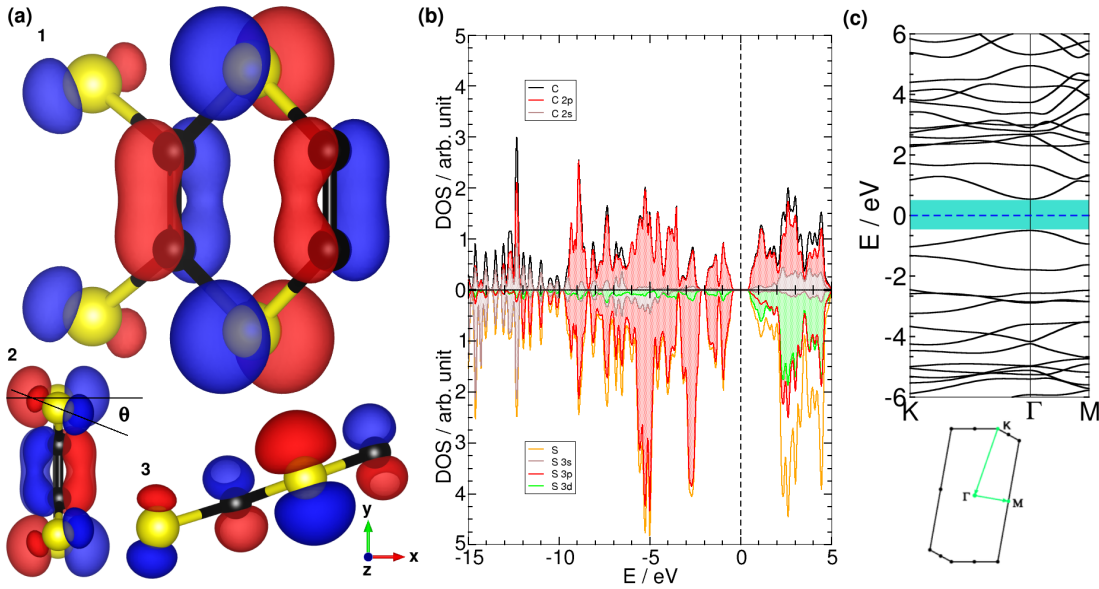


Figure 5.16: Electronic properties of *hexa*: (a) highest occupied molecular orbital at Γ point, (b) density of states projected on carbon (up) and sulfur (down), and (c) band structure.

To study the electronic structure of the chains we plot the projected density of states of the *hexa* chain in Fig. 5.16(b). Carbon and sulfur shows s and p contribution at deep energies, and mainly p contribution close to the Fermi energy. Note that sulfur atoms in chains lack significant d contribution, in contrast with the α and δ monolayers. The electronic population using the Mulliken scheme reveals a charge transfer of 0.6 electrons from carbon to sulfur atoms, following the same trend as the monolayers. Fig. 5.16(c) also includes the band structure of the *hexa* chain in two directions, parallel and perpendicular to the chain. The most important feature is the existence of a direct band

gap of 1.03 eV at the Γ point.

Chains with pentagonal motif

Figure 5.14(b) presents the *penta* chains, which are 0.506 meV per atom more stable than the α monolayer, and 0.260 meV per atom less stable than the *hexa* chains. There are three important differences between the *hexa* and *penta* chains, which explain the energy difference between them. First, a carbon-carbon double bond is rotated 90° , producing two pentagons linked by the carbon-carbon double bond instead of the two contiguous hexagons. This recalls the rotation of the Stone-Wales defect [442], and motivates the name of the structure. Second, there are terraces with an abrupt step after two consecutive pentagons. And the third difference is that the chains are interacting between them through edges. This decreases the van der Waals contribution because the interacting atoms number is smaller. The distance between the closest atoms from different neighbors is no shorter than 3.5 Å.

On geometric parameters, the double bond is well preserved with a distance of 1.39 Å in most of the cases, and 1.45 Å close to a step. The carbon-sulfur bond length is 1.8 Å along the chain. The angles between the three bonds from a carbon atom in a terrace are 120° . Carbon atoms in the steps have two bonds; however the angle between them is 120° and the sp^2 hybridization is preserved. For sulfur atoms, the angle between the two bonds with vertex in sulfur in a terrace is 95° . For the sulfur atoms close to a step, the angles are 99° and 115° . Using Mulliken population analysis we find a charge transfer of 0.5 electrons from carbon to sulfur, agreeing with the result for *hexa* chains.

In summary, *penta* chains show similar hybridizations and bonding patterns as *hexa* chains. It seems that the motif consisting on two strongly bonded carbon atoms separated by two-coordinated sulfur atoms is the key pattern for high stability in carbon monosulfide compounds.

5.3.3 Thin films

Finally we study carbon monosulfide thin films following the results found for silicon monosulfide. Carbon-group elements such as silicon prefer to have sp^3 rather than sp^2 hybridization, as shown by the buckled structure of silicene. This is in agreement with the double bond rule, because silicon double bond would require sp^2 hybridization to leave free a p -type orbital for the π bond. So, SiS thin film structures such *Pma2* are more stable than SiS monolayers. We check if this applies for carbon monosulfide. Figure 5.17 shows the geometry of *Pma2* and *Pmma* thin films, following the nomenclature used for silicon monosulfide. The cohesive energy of both structures shows an energy gain of almost 0.5 eV with respect to the α monolayer. The explanation for the energy gain is the extra bond for silicon and the lost of a sulfur bond compared to the α monolayer. In the α monolayer, carbon shows sp^3 hybridization with a dangling bond, which is saturated for thin film structures. Sulfur prefers to have two bonds to fulfill the octet rule.

The *Pma2* structure is slightly more stable than the *Pmma* structure because of a

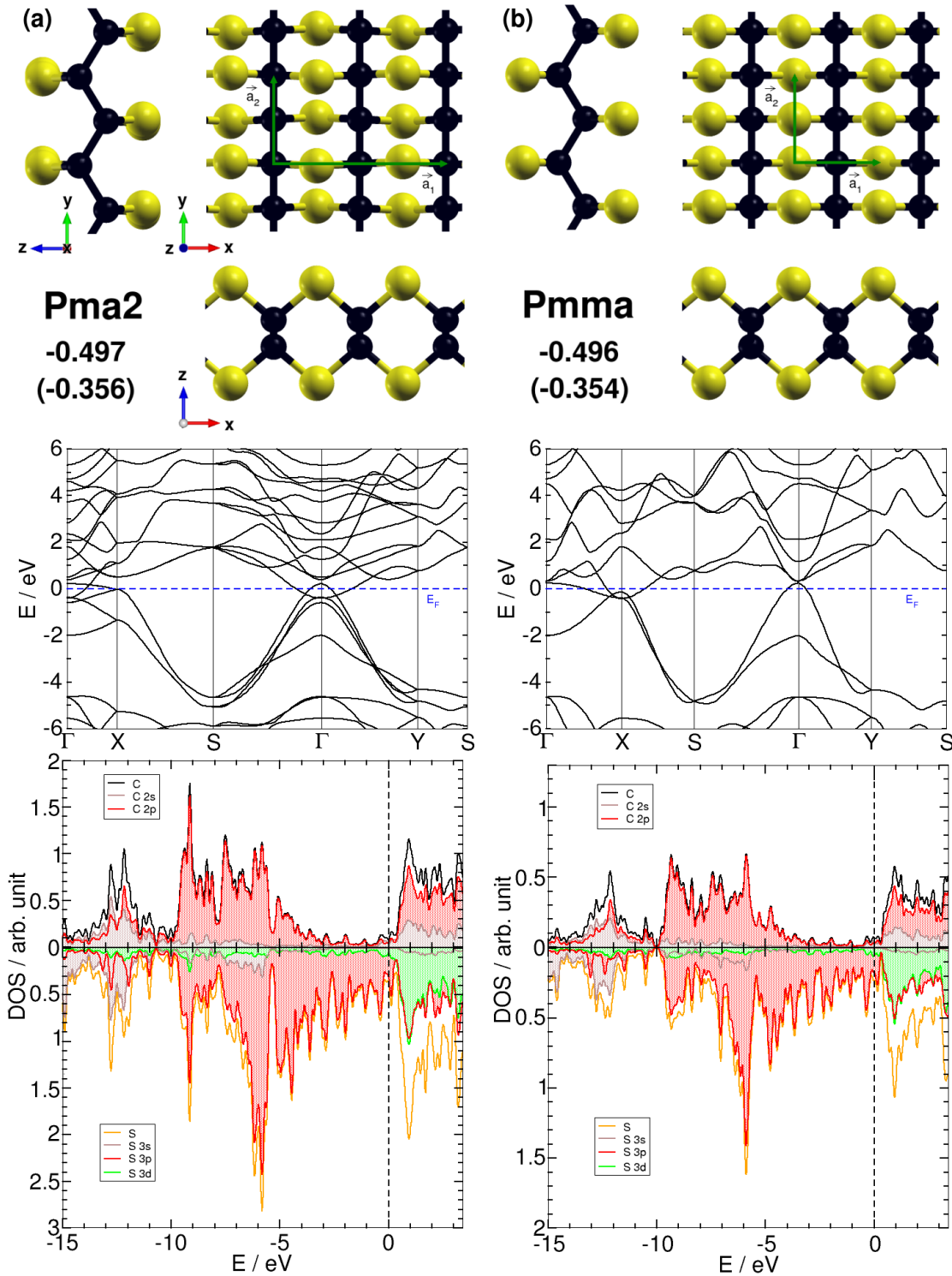


Figure 5.17: Geometries for two carbon monosulfide thin films in the (a) *Pma2* and (b) *Pmma* structures. The unit cells employed for the electronic analysis are shown in green. Energies per atom (in parenthesis) using the SIESTA (VASP) method relative to the α monolayer in Fig.5.8 are given. Band structures and projected density of states are shown in the lower part.

larger unit cell as shown in Fig. 5.17, which allows for a slight distortion of sulfur positions stabilizing the system. However, the geometries are highly similar so we just comments the $Pma2$ structure, being the $Pmma$ one almost identical. Each sulfur atom has two bonds to carbon atoms of lengths 1.86 Å, with angles of 99° between them. Each carbon atom bonds two sulfur atoms and two carbon atoms at 1.71 Å. The four angles between the carbon bonds are close to 109.5°, which is the characteristic angle of the sp^3 hybridization as for methane.

Now we focus on the analysis of the electronic properties of the carbon monosulfide thin films. Figure 5.17 shows the band structures of the $Pma2$ and $Pmma$ thin films. The band structures are metallic for both cases. There are conduction states at the Fermi energy at the Γ point, and the direction ΓX is responsible for conduction. The band structure is similar for both the $Pma2$ and $Pmma$ thin films as expected because of their similar geometry. However, the distortion of sulfur atoms split the higher conduction bands for the $Pma2$ case, which are degenerated along the Brillouin zone for the $Pmma$ structure. Those conduction bands are broadly delocalized around more than 4 eV. Figure 5.17 also presents the projected density of states of Pma and $Pmma$ carbon monosulfide structures. There is little differences between them. For carbon there are three different regions in the $Pma2$ case. We distinguish the interval $[-15,-10]$ with large sp hybridization, the interval $[-10,-4]$ with p -type contribution, and the interval $[-4,0]$ with low carbon contribution compared to sulfur. For sulfur, there is also sp hybridization at deep energies $[-15,-11]$, and for the rest of energies there is large p -type contribution, including the states near the Fermi energy. Therefore, sulfur is responsible for the conduction bands delocalized over 4 eV. The conduction states at the Fermi energy are mainly sulfur p states.

There is no band gap for the $Pma2$ and $Pmma$ thin film structures, which question their stability. Molecular dynamic simulations at 300 K show that carbon monosulfide thin films are indeed unstable at room temperature. The structure is broken into separate parts after certain number of steps leading to carbon monosulfide chain-like geometries.

5.3.4 Comments on stability

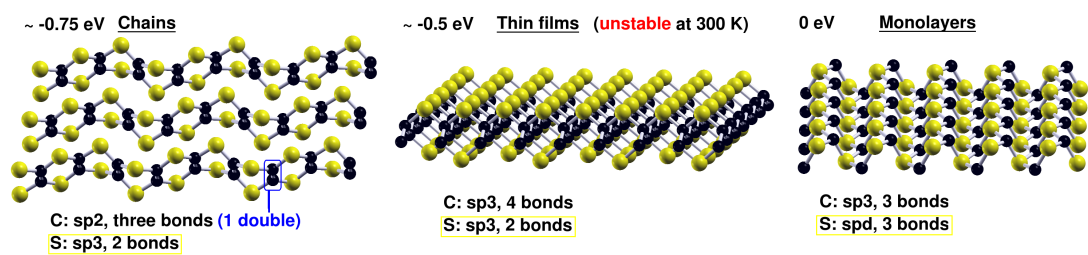


Figure 5.18: Summary of the different studied carbon monosulfide nanostructures.

We explain the stability order between the three different types of carbon monosulfide nanostructures studied. In order of decreasing stability we have found chains, thin films

and monolayers. The relative stability between these nanostructures is explained by two factors: the bonds number from carbon and sulfur atoms, and the hybridizations. The ground state α monolayer displays sp^3 hybridized carbon atoms with three bonds to sulfur atoms, leaving a dangling bond. A similar situation is found for sulfur. The thin films have sp^3 hybridized carbon atoms saturating the fourth bond. Besides, sulfur atoms in thin films keep two bonds, which is the main source of stability as shown for silicon monosulfide nanostructures [318, 319, 441]. So, the increased stability of the thin films with respect to the α monolayer is explained by the saturation of the dangling bond and the lost of a sulfur bond. Finally, we focus on the extra stability of the *hexa* chain with respect to the thin films. Sulfur atoms play a similar role in both structures, showing two bonds. Nevertheless, there are noticeable differences for carbon. For the *hexa* chain, the carbon atoms have three bonds instead of four as for thin films, and present sp^2 hybridization with a carbon-carbon double bond. Figure 5.18 summarizes the number of bonds, hybridizations and stability of the different carbon monosulfide nanostructures. An important conclusion is that in carbon monosulfide nanostructures carbon atoms favor sp^2 hybridization over sp^3 hybridization.

5.4 Conclusions

In this chapter we have studied new two-dimensional materials which could be useful for electronic devices and help setting up the members of the growing two-dimensional realm. Graphene impulsed the field of bidimensional materials with the required experimental techniques. Alternatives to graphene such as phosphorene also appears highly promising. Here we follow the isoelectronics approach to design two-dimensional materials. Specifically we have studied two phosphorene isoelectronic compounds, silicon monosulfide and carbon monosulfide.

We have presented a novel silicon monosulfide monolayer labeled γ following the notation for the previously reported α and β phases. The γ phase improves stability with respect to those by about 90 meV per atom. It has a rhombohedral cell with two silicon and two sulfur atoms, forming a structure with rippled hexagons and squares. The γ phase is stable at room temperature as shown by phonon dispersion calculations and molecular dynamics simulations. The source of extra stability with respect to the α and β phases is the extra silicon-silicon bond of the γ phase, establishing silicon four bonds instead of three. The electronic structure reveals that the silicon-silicon bond looks like a double bond, with σ and π bonds. The projected density of states show large d contribution for silicon, suggesting spd hybridization for silicon. The band structure shows that the γ phase is semiconductor with an indirect band gap of 1.13 eV

We comment on some other silicon monosulfide nanostructures which improve stability with respect to the α and β phases. Thin films are even more stable than γ phase; however, the structure is thicker and more complicated than monolayers. Indeed, other silicon monosulfide thin films have been recently reported to improve the α and β stability. We have analyzed the stability order of all these structures to gain general trends. We have found that, although there is no direct correlation between stability and thick-

ness, thicker structures are more stable in general because they allow for more favorable local environments for silicon and sulfur. The preferred coordination is fourfold and twofold for silicon and sulfur, respectively.

Following a similar approach, we have presented carbon monosulfide nanostructures including monolayers, thin films and chains. The most stable carbon monosulfide α monolayer is a semiconductor phase which exhibits phosphorene-like structure. Second in stability we found the δ phase, a metal with a square lattice, and third in stability the κ structure which seems to be halfway between the first and the second more stable phases. We have studied a possible transition between the α and δ phases by applying strain, which indeed would imply control of semiconductor-metal transition by strain. Nevertheless, the two α and δ phases seems stable and preserve their structure under deformation.

When computing the γ silicon monosulfide phase replacing silicon by carbon atoms, the structure split into chains. These chains largely improves stability with respect to the monolayers by more than 700 meV per atom. Carbon and sulfur atoms are disposed forming hexagons, although we have also found less stable chains with pentagonal motifs.

In order to complete the analysis, we have also considered carbon monosulfide thin films. The thin film structures have also more cohesive energy than monolayers by 500 meV per atom and show metallic character. Nevertheless, molecular dynamics simulations reveals that they are unstable at room temperature.

With the aim of finding some general trends and similarly as for silicon monosulfide, we have analyzed the different nanostructures attending to factors such as the coordination and hybridizations found from their electronic structure analysis. Carbon and sulfur atoms in the α phase have three bonds. Similarly as for silicon monosulfide, sulfur prefers to have two bonds, which explain the higher stability of thin films and chains with respect to the monolayers. Sulfur has spd hybridization for monolayers and carbon has sp^3 hybridization for the α monolayer with a dangling bond, which is saturated for thin films. However, carbon prefers to have sp^2 hybridization with a carbon-carbon double bond rather than sp^3 with four bonds, as meant by the larger stability shown by the chains.

6 Summary and outline

In this thesis we have studied low dimensional materials by first principles calculations. Isolation of graphene supposed a big boost for the research in two-dimensional materials. The absence of band gap and magnetism in graphene are drawbacks for some applications, which has stimulated the doping with transition metals to tune its properties. We have studied in this thesis the carbon transition metal interaction resulting from the doping but also for other carbon nanostructures. Furthermore, we have designed some new two-dimensional structures which widen the offer further from graphene, and suppose a different approach from doping to overcome graphene drawbacks.

In the third chapter we have studied transition metals interacting with carbon nanostructures such as the polycyclic aromatic hydrocarbons (PAHs). We focused on the interaction of cobalt atoms and clusters with circumcoronene. Also, we studied manganese, cobalt and nickel interacting with the smallest hydrocarbon system, benzene. Next we summarize some of the most important conclusions from this chapter:

- Cobalt atoms and clusters gain energy when bonding circumcoronene. Specifically, they prefer to bond hollow sites in the edges of circumcoronene, because of the extra charge in the borders as shown by the electron localization function. Cobalt dimers adopt a perpendicular arrangement, and Co_4 form tetrahedra with three cobalt atoms over consecutive neighbor hollows.
- When bonding with carbon, cobalt reduce its magnetic moment to 1, 2 and $6 \mu_B$ for the atom, dimer and Co_4 , respectively, because of the large rehybridization of $3d$ and p_z orbitals. Bare circumcoronene has no local magnetic moments in the edges in the isolated state, agreeing with theoretical predictions requiring larger size. Negative induced magnetic moment is found on carbon atoms close to cobalt atoms.
- The study of the contact charge term of the hyperfine interaction provide some guidelines for the experimental detection of adsorbed cobalt on hydrocarbons, through the experimental measurement of the isomer shift.
- The cobalt-cobalt interaction is stronger than the cobalt-carbon interaction, which explains the preference for grouping cobalt atoms over circumcoronene rather than spread them separately. The metal-metal interaction is the strongest for the compounds of benzene with manganese, cobalt and nickel. This settles the preference of Mn_3Bz_3 , Co_3Bz_3 , and Ni_3Bz_3 compounds for a bowl-like geometry instead of a multiple-decker one.

6 Summary and outline

- The Co_3Bz_3 cluster display an antiferromagnetic ground state for the cobalt triangle inside the benzenes, which is opposed to the ferromagnetic ground state of the bare Co_3 . Indeed, when non-collinear solutions are allowed the energy is lowered even more. The behavior of non-collinear solutions is explained by a model hamiltonian including two terms: local anisotropy and two different exchange interactions.
- The Mn_3Bz_3 cluster shows superdimerization with an ultrashort manganese-manganese distance of 1.8 Å and magnetism depletion. The phenomenon is perfectly observed for the smaller Mn_2Bz_2 cluster, and the large associated energy saving enable its presence for large clusters such as Mn_4Bz_4 . Our calculations show that the total magnetism quenching produces a barrier preventing experimental synthesis of these manganese benzene compounds.
- The Ni_3Bz_3 and Ni_3 clusters show collinear magnetic behavior, with a magnetic anisotropy of 8 meV. Nevertheless, the addition of benzenes swaps the easy axis of magnetization from in-plane for Ni_3 to out-of-plane for Ni_3Bz_3 . Out-of-plane magnetic field split two degenerated levels sharing one electron for Ni_3Bz_3 , stabilizing this configuration over those in-plane, which are all degenerated.

Then, in the fourth chapter we study transition metals interacting with carbon atoms of graphene. We cover graphene doping with Co_{13} clusters adsorption, and the study of substitutional impurities of $3d$, $4d$ and $5d$ transition metals. The most important ideas are collected next:

- Free Co_{13} clusters, neutral and charged, prefer a two-dimensional structure; however the icosahedral geometry is the most stable deposited over graphene. We report a new more stable arrangement of the icosahedron with four cobalt atoms bonding carbon atoms. These results are checked including on-site interaction, and doping graphene with one extra or less electron.
- When deposited on graphene the binding energy of cobalt atoms increase, which means Co_{13} will stick to graphene. Larger adsorption energy is obtained for the less stable free isomers, those with spherical shape, which are prone to suffer larger structural rearrangements and cuts on the isomer magnetic moment. Negative magnetic moment is induced on graphene, for instance $-0.33 \mu_B$ for the icosahedron ground state.
- The bonding of Co_{13} clusters to graphene is not ionic because the charge transfer towards graphene fails to explain the stability order between different arrangements of the same isomer. Similarly, the supposed relationship between stability and the number of carbon-cobalt bonds and their length fails in too many cases. However, we found that Co_{13} isomers prefer to bond graphene by cobalt atoms negatively charged in the free state.

- Substitutional impurities of $4d$ and $5d$ metal in single vacancies of graphene have larger binding energies and bond lengths than $3d$ impurities. $4d$ and $5d$ impurities have similar size and behavior as impurities because of the lanthanide contraction. The $4f$ shell filling between $4d$ and $5d$ shells leads to an increase of the effective nuclear charge which shrinks the $5d$ metals.
- Early groups (Mo, Tc) show large magnetic moments in the impurities with opposed contribution in the close carbon atoms. Late groups (Ru, Rh, Pd) alternate 0, 1, 0 μ_B values. For the cobalt group, the magnetic moments localized in the impurity and in the carbon neighbors have the same sign.
- The larger size of $4d$ and $5d$ impurities compared to $3d$ impurities produces larger hybridization with carbon p_z orbitals, decreasing the spin splitting. Thus, the levels filling order is reverse for technetium, causing a large reduction of magnetic moment from 3 μ_B for manganese to 1 μ_B for technetium case.

Finally, in the fifth chapter we follow a different approach and we design novel two-dimensional materials which broaden opportunities for novel devices and enrich the growing 2D realm. Here we list the main remarks out of this study:

- New silicon monosulfide monolayer γ improves stability by 90 meV per atom compared to previously reported α and β monolayers. It is stable at room temperature as shown by molecular dynamics and phonon dispersions. The γ phase have an extra silicon-silicon bond which recalls a double bond and explain the stability gain.
- The γ monolayer is a semiconductor with a band gap of 1.13 eV. Silicon presents large d states contribution near the Fermi energy, involving d hybridization explained by the almost right angles between the silicon bonds.
- Carbon monosulfide monolayers are studied, finding a phosphorene-like structure α as the ground state. The α monolayer is semiconductor with a band gap of about 1 eV. Second in stability we find the metallic δ phase. Strain could induce transition between α and δ phases providing control of conductivity.
- Carbon monosulfide thin films show larger cohesive energy than monolayers and are metallic phases; however they are not stable at room temperature.
- The most stable carbon monosulfide nanostructures are semiconductor chains with a direct band gap of 1 eV and mediated by dispersion forces, with a gain of more than 0.7 eV per atom compared to the α monolayer. The stability order between monolayers, thin films and chains is explained by the local environments of carbon and sulfur. Sulfur prefers to have two bonds, and carbon favors sp^2 hybridization with two single bonds and a double bond.

6.1 **Outline**

Nanoscience and nanotechnology are among the most important fields for basic and applied research nowadays, with a great support from the private industry and public governments because of the possible disruptive and profitable applications, already implemented sometimes. First principles computational calculations appear as one of the main tools to develop this fundamental research, explaining experimental observations, suggesting possible experiments, helping in the design of novel materials dealing with the huge number of possibilities, etc.

Graphene is still under thorough study to ease the always complicated path from basic research to applications. This includes doping with clusters and substitutional impurities, among many other defects. There are also more and more two-dimensional counterparts, like those we present in this thesis, which could be used for devices in the future. The bi-dimensional realm is one of the hottest topic nowadays, and it seems the research pace will be maintained or increased during the next years.

Furthermore, the interaction of carbon atoms and metals is not only interesting on two-dimensional systems but also on zero-dimensional, such as the benzene-metals compounds reported here. Magnetic properties change drastically in these small molecules, including non-collinear cobalt, non-magnetic manganese and promising nickel-benzene magnetic units. More research is needed on these small clusters, useful for magnetic devices, expanding the field of organometallics.

7 List of publications

1. T. Alonso-Lanza, A. Ayuela and F. Aguilera-Granja (2015). *Chemical Bonding of Transition-Metal Co₁₃ Clusters with Graphene*. ChemPhysChem, 16(17), 3700-3710.
2. T. Alonso-Lanza, A. Ayuela and F. Aguilera-Granja (2016). *Substitutional 4d and 5d impurities in graphene*. Physical Chemistry Chemical Physics, 18(31), 21913-21920.
3. T. Alonso-Lanza, A. Ayuela and F. Aguilera-Granja (2016). *An array of layers in silicon sulfides: Chainlike and monolayer*. Physical Review B, 94(24), 245441.
4. J. W. González, T. Alonso-Lanza, F. Delgado, F. Aguilera-Granja and A. Ayuela (2017). *Non-Collinearity in Small Magnetic Cobalt-Benzene Molecules*. (Submitted) <https://arxiv.org/abs/1611.07846>
5. T. Alonso-Lanza, F. Aguilera-Granja, J. W. González and A. Ayuela (2017). *Carbon Monosulfide Nanostructures: Chains Arrays, Monolayers, and Thin Films*. (Submitted) <https://arxiv.org/abs/1703.02756>
6. T. Alonso-Lanza, J. W. González, F. Aguilera-Granja and A. Ayuela (2017). *Ultrashort Mn-Mn Bonds in Organometallic Clusters*. (Submitted) <https://arxiv.org/abs/1703.04903>
7. T. Alonso-Lanza, A. Mañanes and A. Ayuela (2017). *Bonding of Cobalt Atoms, Dimers and Co₄ Clusters to Circumcoronene*. (Submitted) <https://arxiv.org/abs/1704.07718>
8. T. Alonso-Lanza, J. W. González, F. Aguilera-Granja and A. Ayuela (2017). *Large Magnetic Anisotropy Energy in Nickel-Benzene Clusters*. (In preparation)

8 Bibliography

- [1] R. P. Feynman. There's plenty of room at the bottom. *Eng Sci*, 23(5):22–36, 1960.
- [2] G. Binnig and H. Rohrer. Scanning tunneling microscopy. *Surf. Sci. science*, 126(1-3):236–244, 1983.
- [3] J. A. Strosio and D. M. Eigler. Atomic and molecular manipulation with the scanning tunneling microscope. *Science*, 254(5036):1319, 1991.
- [4] H. W. Kroto, J. R. Heath, S. C. O'Brien, R. F. Curl, and R. E. Smalley. C 60: buckminsterfullerene. *Nature*, 318(6042):162–163, 1985.
- [5] O. C. Farokhzad and R. Langer. Impact of nanotechnology on drug delivery. *ACS Nano*, 3(1):16–20, 2009.
- [6] J. Geng, K. Kim, J. Zhang, A. Escalada, R. Tunuguntla, L. R. Comolli, F. I. Allen, A. V. Shnyrova, K. R. Cho, D. Munoz, Y. Morris Wang, C. P. Grigoropoulos, C. M. Ajo-Franklin, V. A. Frolov, and A. Noy. Stochastic transport through carbon nanotubes in lipid bilayers and live cell membranes. *Nature*, 514(7524):612–615, 2014.
- [7] X. Wang, L. Yang, Z. G. Chen, and D. M. Shin. Application of nanotechnology in cancer therapy and imaging. *CA: Cancer J. Clin.*, 58(2):97–110, 2008.
- [8] K. S. Kim, Y. Zhao, H. Jang, S. Y. Lee, J. M. Kim, K. S. Kim, J. Ahn, P. Kim, J. Choi, and B. H. Hong. Large-scale pattern growth of graphene films for stretchable transparent electrodes. *Nature*, 457(7230):706–710, 2009.
- [9] S. Hong and S. Myung. Nanotube electronics: A flexible approach to mobility. *Nat. Nanotechnol.*, 2(4):207, 2007.
- [10] T. Zhang, S. Mubeen, N. V. Myung, and M. A. Deshusses. Recent progress in carbon nanotube-based gas sensors. *Nanotechnology*, 19(33):332001, 2008.
- [11] C. Manzano, W. H. Soe, H. S. Wong, F. Ample, A. Gourdon, N. Chandrasekhar, and C. Joachim. Step-by-step rotation of a molecule-gear mounted on an atomic-scale axis. *Nat. Mater.*, 8(7):576–579, 2009.
- [12] C. Elschenbroich. *Organometallics*. John Wiley & Sons, 2016.
- [13] A. Hirsch, Z. Chen, and H. Jiao. Spherical aromaticity in I_h symmetrical fullerenes: the $2(n+1)^2$ rule. *Angew. Chem. Int. Ed.*, 39(21):3915–3917, 2000.

8 Bibliography

- [14] A. Karton, B. Chan, K. Raghavachari, and L. Radom. Evaluation of the heats of formation of corannulene and C_{60} by means of high-level theoretical procedures. *J. Phys. Chem. A*, 117(8):1834–1842, 2013.
- [15] M. Yoon, S. Yang, E. Wang, and Z. Zhang. Charged fullerenes as high-capacity hydrogen storage media. *Nano Lett.*, 7(9):2578–2583, 2007.
- [16] R. Bakry, R. M. Vallant, M. Najam-ul Haq, M. Rainer, Z. Szabo, C. W. Huck, and G. K. Bonn. Medicinal applications of fullerenes. *Int. J. Nanomedicine*, 2(4):639, 2007.
- [17] A. W. Jensen, S. R. Wilson, and D. I. Schuster. Biological applications of fullerenes. *Bioorg. Med. Chem*, 4(6):767–779, 1996.
- [18] R. B. Ross, C. M. Cardona, D. M. Guldi, S. G. Sankaranarayanan, M. O. Reese, N. Kopidakis, J. Peet, B. Walker, G. C. Bazan, E. Van Keuren, B. C. Holloway, and M. Drees. Endohedral fullerenes for organic photovoltaic devices. *Nat. Mater.*, 8(3):208–212, 2009.
- [19] L. Dunsch, M. Krause, J. Noack, and P. Georgi. Endohedral nitride cluster fullerenes: Formation and spectroscopic analysis of $L_{3-x}M_xN@C_{2n}$ ($0 \leq x \leq 3$; $N=39,40$). *J. Phys. Chem. Solids*, 65(2):309–315, 2004.
- [20] R. Tellgmann, N. Krawez, S. H. Lin, I. V. Hertel, and E. E. B. Campbell. Endohedral fullerene production. *Nature*, 382(6590):407, 1996.
- [21] M. Saunders, H. A. Jiménez-Vázquez, R. J. Cross, and R. J. Poreda. Stable compounds of helium and neon: He C_{60} and Ne C_{60} . *Science*, 259(5100):1428–1431, 1993.
- [22] A. A. Popov, S. Yang, and L. Dunsch. Endohedral fullerenes. *Chem. Rev.*, 113(8):5989–6113, 2013.
- [23] J. Averdung and J. Mattay. Exohedral functionalization of [60] fullerene by [3+2] cycloadditions: Syntheses and chemical properties of triazolino-[60] fullerenes and 1, 2-(3, 4-dihydro-2H-pyrrolo)-[60] fullerenes. *Tetrahedron*, 52(15):5407–5420, 1996.
- [24] G. Lu, K. Deng, H. Wu, J. Yang, and X. Wang. Geometric and electronic structures of metal-substitutional fullerene $C_{59}Sm$ and metal-exohedral fullerenes $C_{60}Sm$. *J. Chem. Phys.*, 124(5):054305, 2006.
- [25] M. Yamada, T. Nakahodo, T. Wakahara, T. Tsuchiya, Y. Maeda, T. Akasaka, M. Kako, K. Yoza, E. Horn, N. Mizorogi, K. Kobayashi, and S. Nagase. Positional control of encapsulated atoms inside a fullerene cage by exohedral addition. *J. Am. Chem. Soc.*, 127(42):14570–14571, 2005.

- [26] S. J. Rosenthal, J. C. Chang, O. Kovtun, J. R. McBride, and I. D. Tomlinson. Biocompatible quantum dots for biological applications. *Chem. Biol.*, 18(1):10–24, 2011.
- [27] J. Deng, Q. Lu, H. Li, Y. Zhang, and S. Yao. Large scale preparation of graphene quantum dots from graphite oxide in pure water via one-step electrochemical tailoring. *RSC Adv.*, 5(38):29704–29707, 2015.
- [28] P. Reiss, M. Protiere, and L. Li. Core/shell semiconductor nanocrystals. *Small*, 5(2):154–168, 2009.
- [29] S. A. Empedocles, D. J. Norris, and M. G. Bawendi. Photoluminescence spectroscopy of single CdSe nanocrystallite quantum dots. *Phys. Rev. Lett.*, 77(18):3873, 1996.
- [30] J. Chen and C. Zhu. Functionalized cadmium sulfide quantum dots as fluorescence probe for silver ion determination. *Anal. Chim. Acta*, 546(2):147–153, 2005.
- [31] J. J. Peterson and T. D. Krauss. Fluorescence spectroscopy of single lead sulfide quantum dots. *Nano Lett.*, 6(3):510–514, 2006.
- [32] R. J. Ellingson, M. C. Beard, J. C. Johnson, P. Yu, O. I. Micic, A. J. Nozik, A. Shabaev, and A. L. Efros. Highly efficient multiple exciton generation in colloidal PbSe and PbS quantum dots. *Nano Lett.*, 5(5):865–871, 2005.
- [33] U. Banin, Y. Cao, D. Katz, and O. Millo. Identification of atomic-like electronic states in indium arsenide nanocrystal quantum dots. *Nature*, 400(6744):542–544, 1999.
- [34] J. L. Blackburn, D. C. Selmarten, R. J. Ellingson, M. Jones, O. Micic, and A. J. Nozik. Electron and hole transfer from indium phosphide quantum dots. *J. Phys. Chem. B*, 109(7):2625–2631, 2005.
- [35] L. A. Ponomarenko, F. Schedin, M. I. Katsnelson, R. Yang, E. W. Hill, K. S. Novoselov, and A. K. Geim. Chaotic dirac billiard in graphene quantum dots. *Science*, 320(5874):356–358, 2008.
- [36] H. Li, X. He, Z. Kang, H. Huang, Y. Liu, J. Liu, S. Lian, C. H. A. Tsang, X. Yang, and S. Lee. Water-soluble fluorescent carbon quantum dots and photocatalyst design. *Angew. Chem.*, 122(26):4532–4536, 2010.
- [37] S. Kim, S. W. Hwang, M. Kim, D. Y. Shin, D. H. Shin, C. O. Kim, S. B. Yang, J. H. Park, E. Hwang, S. Choi, G. Ko, S. Sim, C. Sone, H. J. Choi, S. Bae, and B. H. Hong. Anomalous behaviors of visible luminescence from graphene quantum dots: interplay between size and shape. *ACS Nano*, 6(9):8203–8208, 2012.
- [38] X. Yan, B. Li, X. Cui, Q. Wei, K. Tajima, and L. Li. Independent tuning of the band gap and redox potential of graphene quantum dots. *J. Phys. Chem. Lett.*, 2(10):1119–1124, 2011.

- [39] S. Zhu, J. Zhang, C. Qiao, S. Tang, Y. Li, W. Yuan, B. Li, L. Tian, F. Liu, R. Hu, H. Gao, H. Wei, H. Zhang, H. Sun, and B. Yang. Strongly green-photoluminescent graphene quantum dots for bioimaging applications. *Chem. Commun.*, 47(24):6858–6860, 2011.
- [40] J. Wu, Ž. Tomović, V. Enkelmann, and K. Müllen. From branched hydrocarbon propellers to C₃-symmetric graphite disks. *J. Org. Chem.*, 69(16):5179–5186, 2004.
- [41] C. D. Simpson, J. D. Brand, A. J. Berresheim, L. Przybilla, H. J. Räder, and K. Müllen. Synthesis of a giant 222 carbon graphite sheet. *Chem. Eur. J.*, 8(6):1424–1429, 2002.
- [42] D. Pan, J. Zhang, Z. Li, and M. Wu. Hydrothermal route for cutting graphene sheets into blue-luminescent graphene quantum dots. *Adv. Mater.*, 22(6):734–738, 2010.
- [43] M. Bacon, S. J. Bradley, and T. Nann. Graphene quantum dots. *Part. Part. Syst. Char.*, 31(4):415–428, 2014.
- [44] X. Li, M. Rui, J. Song, Z. Shen, and H. Zeng. Carbon and graphene quantum dots for optoelectronic and energy devices: a review. *Adv. Funct. Mater.*, 25(31):4929–4947, 2015.
- [45] N. Wohner, P. Lam, and K. Sattler. Energetic stability of graphene nanoflakes and nanocones. *Carbon*, 67:721–735, 2014.
- [46] H. Richter and J. B. Howard. Formation of polycyclic aromatic hydrocarbons and their growth to soot: A review of chemical reaction pathways. *Prog. Energy Combust.*, 26(4):565–608, 2000.
- [47] D. K. Bohme. PAH [polycyclic aromatic hydrocarbons] and fullerene ions and ion/molecule reactions in interstellar and circumstellar chemistry. *Chem. Rev.*, 92(7):1487–1508, 1992.
- [48] C. W. Bauschlicher and E. L. O. Bakes. Infrared spectra of polycyclic aromatic hydrocarbons (PAHs). *Chem. Phys.*, 262(2):285–291, 2000.
- [49] H. A. Galué and J. Oomens. On the electronic structure of isolated monodehydrogenated polyaromatic hydrocarbon ions and their astrophysical relevance. *Astrophys. J.*, 746(1):83, 2012.
- [50] D. M. Hudgins, C. W. Bauschlicher Jr, and L. J. Allamandola. Variations in the peak position of the 6.2 μm interstellar emission feature: A tracer of n in the interstellar polycyclic aromatic hydrocarbon population. *Astrophys. J.*, 632(1):316, 2005.
- [51] J. Zhou, W. Wang, and K. Fan. Novel compounds with cobalt, copper, and nickel dimers sandwiched between benzene molecules: A DFT study. *Chem. Phys. Lett.*, 424(4):247–251, 2006.

- [52] A. N. Rudenko, F. J. Keil, M. I. Katsnelson, and A. I. Lichtenstein. Adsorption of cobalt on graphene: Electron correlation effects from a quantum chemical perspective. *Phys. Rev. B*, 86(7):075422, 2012.
- [53] G. Compagnini, G. Forte, F. Giannazzo, V. Raineri, A. La Magna, and I. Deretzis. Ion beam induced defects in graphene: Raman spectroscopy and DFT calculations. *J. Mol. Struct.*, 993(1):506–509, 2011.
- [54] S. Ikäläinen, P. Lantto, P. Manninen, and J. Vaara. NMR tensors in planar hydrocarbons of increasing size. *Phys. Chem. Chem. Phys.*, 11(48):11404–11414, 2009.
- [55] P. V. C. Medeiros, G. K. Gueorguiev, and S. Stafström. Bonding, charge rearrangement and interface dipoles of benzene, graphene, and PAH molecules on Au (111) and Cu (111). *Carbon*, 81:620–628, 2015.
- [56] M. H. Ghatee and F. Moosavi. Physisorption of hydrophobic and hydrophilic 1-alkyl-3-methylimidazolium ionic liquids on the graphenes. *J. Phys. Chem. C*, 115(13):5626–5636, 2011.
- [57] E. M. Huff and P. Pulay. A potential surface for the interaction between water and coronene as a model for a hydrophobic surface. *Mol. Phys.*, 107(8-12):1197–1207, 2009.
- [58] I. Gutman, Ž. Tomović, K. Müllen, and J. P. Rabe. On the distribution of π -electrons in large polycyclic aromatic hydrocarbons. *Chem. Phys. Lett.*, 397(4):412–416, 2004.
- [59] R. H. Crabtree. *The organometallic chemistry of the transition metals*. John Wiley & Sons, 2009.
- [60] I. Omae. *Applications of organometallic compounds*. Wiley, 1998.
- [61] J. Kollonitsch. Industrial use of organometallics in organic synthesis. *Ann. New York Acad. Sci.*, 125(1):161–171, 1965.
- [62] M. P. Coogan, P. J. Dyson, and M. Bochmann. Introduction to the organometallics in biology and medicine issue. *Organometallics*, 31(16):5671–5672, 2012.
- [63] J. F. Harrod and R. M. Laine. *Applications of Organometallic Chemistry in the Preparation and Processing of advanced materials*, volume 297. Springer Science & Business Media, 2012.
- [64] J. J. BelBruno. Half-sandwich metal atom complexes with benzene: a model for adsorption onto graphite. *Surf. Sci.*, 577(2):167–174, 2005.
- [65] X. Zhang and J. Wang. Structural, electronic, and magnetic properties of $\text{Co}_n(\text{benzene})_m$ complexes. *J. Phys. Chem. A*, 112(2):296–304, 2008.

8 Bibliography

- [66] N. R. Foster, G. A. Grieves, J. W. Buchanan, N. D. Flynn, and M. A. Duncan. Growth and photodissociation of $\text{Cr}_x\text{-(coronene)}_y$ complexes. *J. Phys. Chem. A*, 104(47):11055–11062, 2000.
- [67] R. Xiao, D. Fritsch, M. D. Kuzmin, K. Koepernik, H. Eschrig, M. Richter, K. Vitze, and G. Seifert. Co dimers on hexagonal carbon rings proposed as subnanometer magnetic storage bits. *Phys. Rev. Lett.*, 103(18):187201, 2009.
- [68] X. Li, S. Eustis, K. H. Bowen, A. K. Kandalam, and P. Jena. Photoelectron spectroscopic and theoretical studies of $\text{Fe}_m\text{-(coronene)}_n$ ($m=1, 2, n=1, 2$) complexes. *J. Chem. Phys.*, 129(7):074313, 2008.
- [69] J. W. Buchanan, J. E. Reddic, G. A. Grieves, and M. A. Duncan. Metal and multimetal complexes with polyaromatic hydrocarbons: Formation and photodissociation of $\text{Fe}_x\text{-(coronene)}_y$ cations. *J. Phys. Chem. A*, 102(32):6390–6394, 1998.
- [70] C. W. Bauschlicher Jr. Fe^+ - and Mg^+ - polycyclic aromatic hydrocarbon complexes. *Mol. Phys.*, 107(8-12):809–818, 2009.
- [71] A. Simon and C. Joblin. The computed infrared spectra of a variety of $[\text{FePAH}]^+$ complexes: Mid- and far-infrared features. *Astrophys. J.*, 712(1):69, 2010.
- [72] A. K. Kandalam, B. Kiran, P. Jena, X. Li, A. Grubisic, and K. H. Bowen. Ground state structures and photoelectron spectroscopy of $[\text{Co}_m\text{(coronene)}]^-$ complexes. *J. Chem. Phys.*, 126(8):084306, 2007.
- [73] T. J. Kealy and P. L. Pauson. A new type of organo-iron compound. *Nature*, 168:1039–1040, 1951.
- [74] S. A. Miller, J. A. Tebboth, and J. F. Tremaine. 114. dicyclopentadienyliron. *J. Chem. Soc.*, pages 632–635, 1952.
- [75] J. D. Dunitz, L. E. Orgel, and A. Rich. The crystal structure of ferrocene. *Acta Crystallogr.*, 9(4):373–375, 1956.
- [76] H. Werner. At least 60 years of ferrocene: the discovery and rediscovery of the sandwich complexes. *Angew. Chem. Int. Ed.*, 51(25):6052–6058, 2012.
- [77] W. Pfab and E. O. Fischer. Zur kristallstruktur der di-cyclopentadienylverbindungen des zweiwertigen eisens, kobalts und nickels. *Z. Anorg. Allg. Chem.*, 274(6):316–322, 1953.
- [78] F. A. Cotton, R. O. Whipple, and G. Wilkinson. Bis-cyclopentadienyl compounds of rhodium (III) and iridium (III). *J. Am. Chem. Soc.*, 75(14):3586–3587, 1953.
- [79] G. Wilkinson and F. A. Cotton. Cyclopentadienyl compounds of manganese and magnesium. Technical report, Harvard Univ., 1954.

- [80] F. N. N. Pansini and F. A. L. de Souza. Trends in the spin states and mean static dipole polarizability of the group VIIIA metallocenes. *J. Phys. Chem. A*, 120(17):2771–2778, 2016.
- [81] Y. Zeng, H. Feng, R. B. King, and H. F. Schaefer III. Metallocene versus metallabenzene isomers of nickel, palladium, and platinum. *Organometallics*, 33(24):7193–7198, 2014.
- [82] J. Yu, J. Chang, R. Wei, X. Liu, and X. Li. Quantum transport of the single metallocene molecule. *Physica E*, 2016.
- [83] R. Liu, S. Ke, W. Yang, and H. U. Baranger. Cobaltocene as a spin filter. *J. Chem. Phys.*, 127(14):141104, 2007.
- [84] R. Liu, S. Ke, H. U. Baranger, and W. Yang. Organometallic spintronics: Dicobaltocene switch. *Nano Lett.*, 5(10):1959–1962, 2005.
- [85] C. Timm and F. Elste. Spin amplification, reading, and writing in transport through anisotropic magnetic molecules. *Phys. Rev. B*, 73(23):235304, 2006.
- [86] C. Ornelas. Application of ferrocene and its derivatives in cancer research. *New J. Chem.*, 35(10):1973–1985, 2011.
- [87] S. Gomez-Ruiz, D. Maksimović-Ivanić, S. Mijatović, and G. N. Kaluderović. On the discovery, biological effects, and use of cisplatin and metallocenes in anticancer chemotherapy. *Bioinorg. Chem. Appl.*, 2012, 2012.
- [88] X. Li, L. M. Guard, J. Jiang, K. Sakimoto, J. Huang, J. Wu, J. Li, L. Yu, R. Pokhrel, G. W. Brudvig, S. Ismail-Beigi, N. Hazari, and A. D. Taylor. Controlled doping of carbon nanotubes with metallocenes for application in hybrid carbon nanotube/Si solar cells. *Nano Lett.*, 14(6):3388–3394, 2014.
- [89] A. Ishii and T. Miyasaka. A metallocene molecular complex as visible-light absorber for high-voltage organic–inorganic hybrid photovoltaic cells. *ChemPhysChem*, 15(6):1028–1032, 2014.
- [90] K. Park, S. Oh, D. Jung, H. Chae, H. Kim, and J. Boo. Hafnium metallocene compounds used as cathode interfacial layers for enhanced electron transfer in organic solar cells. *Nanoscale Res. Lett.*, 7(1):1, 2012.
- [91] K. M. Wedderburn, S. Bililign, M. Levy, and R. J. Gdanitz. Geometries and stabilities of 3d-transition metal-cation benzene complexes, M^+Bz_n ($M = \text{Sc–Cu}$, $n = 1, 2$). *Chem. Phys.*, 326(2):600–604, 2006.
- [92] R. Pandey, B. K. Rao, P. Jena, and M. A. Blanco. Electronic structure and properties of transition metal-benzene complexes. *J. Am. Chem. Soc.*, 123(16):3799–3808, 2001.

- [93] R. Pandey, B. K. Rao, P. Jena, and J. M. Newsam. Unique magnetic signature of transition metal atoms supported on benzene. *Chem. Phys. Lett.*, 321(1):142–150, 2000.
- [94] R. Muhida, W. Agerico Diño, M. Mahmudur Rahman, H. Kasai, and H. Nakanishi. Spin polarization of a multiple-decked sandwich clusters: $M(C_6H_6)_2$ ($M = Mn, Fe, Co$). *J. Phys. Soc. Jpn.*, 73(8):2292–2295, 2004.
- [95] K. Miyajima, S. Yabushita, M. B. Knickelbein, and A. Nakajima. Stern-Gerlach experiments of one-dimensional metal-benzene sandwich clusters: $M_n(C_6H_6)_m$ ($M = Al, Sc, Ti, \text{ and } V$). *J. Am. Chem. Soc.*, 129(27):8473–8480, 2007.
- [96] M. A. Duncan. Structures, energetics and spectroscopy of gas phase transition metal ion–benzene complexes. *Int. J. Mass spectrom.*, 272(2):99–118, 2008.
- [97] G. A. Nemnes and A. Nicolaev. Transport in ferrocene single molecules for terahertz applications. *Phys. Chem. Chem. Phys.*, 16(34):18478–18482, 2014.
- [98] I. Resa, E. Carmona, E. Gutierrez-Puebla, and A. Monge. Decamethyldizincocene, a stable compound of Zn (I) with a Zn-Zn bond. *Science*, 305(5687):1136–1138, 2004.
- [99] G. Gao, X. Xu, and H. S. Kang. A theoretical study on fullerene-dizincocene hybrids. *J. Comput. Chem.*, 30(6):978–982, 2009.
- [100] P. K. Chattaraj, D. R. Roy, and S. Duley. Bonding and aromaticity in an all-metal sandwich-like compound. *Chem. Phys. Lett.*, 460(1):382–385, 2008.
- [101] Y. Kan. Covalent or not? energy decomposition analysis of metal–metal bonding in alkaline-earth dimetallocene complexes. *J. Mol. Struct. THEOCHEM*, 894(1):88–92, 2009.
- [102] Q. S. Li and Y. Xu. A DFT study on dinuclear metallocenes RM_2R [$R = (BCO)_5, (BNN)_5$; $M = Be, Mg, Ca, Zn, Cd$]. *J. Phys. Chem. A*, 110(42):11898–11902, 2006.
- [103] A. Velazquez, I. Fernández, G. Frenking, and G. Merino. Multimetallocenes. A theoretical study. *Organometallics*, 26(19):4731–4736, 2007.
- [104] H. Zhu, Y. Chen, S. Li, X. Yang, and Y. Liu. Novel sandwich-type dimetallocenes: Toward promising candidate media for high-capacity hydrogen storage. *Int. J. Hydrogen Energy*, 36(18):11810–11814, 2011.
- [105] Y. Meng, Y. Han, H. Zhu, Z. Yang, K. Shen, B. Suo, Y. Lei, G. Zhai, and Z. Wen. Two dimetallocenes with vanadium and chromium: Electronic structures and their promising application in hydrogen storage. *Int. J. Hydrogen Energy*, 40(36):12047–12056, 2015.

- [106] N. He, H. Xie, and Y. Ding. One-electron metal-metal bond stabilized in dinuclear metallocenes: Theoretical prediction of DBe-LiCp (D= C₅H₅ or C₅Me₅). *J. Phys. Chem. A*, 112(48):12463–12468, 2008.
- [107] H. Hu, L. Zang, W. Zhang, and X. Li. A series of novel sandwich complexes: MQ(η_4 -E₄)₂ (M= Be or Mg; Q= C or Si; E= P, As, Sb or Bi) with donor-acceptor bonds. *Comp. Theor. Chem.*, 1058:41–49, 2015.
- [108] E. Carmona and A. Galindo. Direct bonds between metal atoms: Zn, Cd, and Hg compounds with metal-metal bonds. *Angew. Chem. Int. Ed.*, 47(35):6526–6536, 2008.
- [109] R. A. Layfield. Organometallic single-molecule magnets. *Organometallics*, 33(5):1084–1099, 2014.
- [110] T. Kurikawa, H. Takeda, M. Hirano, K. Judai, T. Arita, S. Nagao, A. Nakajima, and K. Kaya. Electronic properties of organometallic metal-benzene complexes [M_n(benzene)_m (M= Sc-Cu)]. *Organometallics*, 18(8):1430–1438, 1999.
- [111] J. Kua and K. M. Tomlin. Computational study of multiple-decker sandwich and rice-ball structures of neutral titanium-benzene clusters. *J. Phys. Chem. A*, 110(43):11988–11994, 2006.
- [112] L. Bogani and W. Wernsdorfer. Molecular spintronics using single-molecule magnets. *Nat. Mater.*, 7(3):179–186, 2008.
- [113] S. J. van der Molen, R. Naaman, E. Scheer, J. B. Neaton, A. Nitzan, D. Natelson, N. J. Tao, H. van der Zant, M. Mayor, M. Ruben, M. Reed, and M. Calame. Visions for a molecular future. *Nat. Nanotechnol.*, 8(6):386, 2013.
- [114] A. Ardavan, O. Rival, J. J. L. Morton, S. J. Blundell, A. M. Tyryshkin, G. A. Timco, and R. E. P. Winpenny. Will spin-relaxation times in molecular magnets permit quantum information processing? *Phys. Rev. Lett.*, 98:057201, Jan 2007.
- [115] S. Bertaina, S. Gambarelli, T. Mitra, B. Tsukerblat, A. Müller, and B. Barbara. Quantum oscillations in a molecular magnet. *Nature*, 453(7192):203–206, 2008.
- [116] M. N. Leuenberger and D. Loss. Quantum computing in molecular magnets. *Nature*, 410(6830):789–793, 2001.
- [117] A. Ardavan and S. J. Blundell. Storing quantum information in chemically engineered nanoscale magnets. *J. Mater. Chem.*, 19(12):1754–1760, 2009.
- [118] M. Mannini, F. Pineider, P. Sainctavit, C. Danieli, E. Otero, C. Sciancalepore, A. M. Talarico, M. A. Arrio, A. Cornia, D. Gatteschi, and R. Sessoli. Magnetic memory of a single-molecule quantum magnet wired to a gold surface. *Nat. Mater.*, 8(3):194–197, 2009.

- [119] A. Candini, S. Klyatskaya, M. Ruben, W. Wernsdorfer, and M. Affronte. Graphene spintronic devices with molecular nanomagnets. *Nano Lett.*, 11(7):2634–2639, 2011.
- [120] K. W. Galloway, A. M. Whyte, W. Wernsdorfer, J. Sanchez-Benitez, K. V. Kamenev, A. Parkin, R. D. Peacock, and M. Murrie. Cobalt (II) citrate cubane single-molecule magnet. *Inorg Chem*, (16):7438–7442, 2008.
- [121] J. G. Louderback, A. J. Cox, L. J. Lising, D. C. Douglass, and L. A. Bloomfield. Magnetic properties of nickel clusters. *Z. Phys. D*, 26(1):301–303, 1993.
- [122] I. M. L. Billas, A. Chatelain, and W. A. de Heer. Magnetism from the atom to the bulk in iron, cobalt, and nickel clusters. *Science*, 265(5179):1682–1684, 1994.
- [123] F. Aguilera-Granja, J. M. Montejano-Carrizalez, and R. A. Guirado-López. Magnetic properties of small 3d and 4d transition metal clusters: The role of a non-compact growth. *Phys. Rev. B*, 73(11):115422, 2006.
- [124] A. J. Cox, J. G. Louderback, and L. A. Bloomfield. Experimental observation of magnetism in rhodium clusters. *Phys. Rev. Lett.*, 71(6):923, 1993.
- [125] F. Liu, S. N. Khanna, and P. Jena. Magnetism in small vanadium clusters. *Phys. Rev. B*, 43(10):8179, 1991.
- [126] J. A. Alonso. Electronic and atomic structure, and magnetism of transition-metal clusters. *Chem. Rev.*, 100(2):637–678, 2000.
- [127] G. M. Pastor, J. Dorantes-Dávila, S. Pick, and H. Dreyssé. Magnetic anisotropy of 3d transition-metal clusters. *Phys. Rev. Lett.*, 75(2):326, 1995.
- [128] G. M. Pastor, J. Dorantes-Dávila, and K. H. Bennemann. Size and structural dependence of the magnetic properties of small 3d-transition-metal clusters. *Phys. Rev. B*, 40(11):7642, 1989.
- [129] R. A. Guirado-López, J. Dorantes-Dávila, and G. M. Pastor. Orbital magnetism in transition-metal clusters: From Hund's rules to bulk quenching. *Phys. Rev. Lett.*, 90(22):226402, 2003.
- [130] J. Guevara, F. Parisi, A. M. Llois, and M. Weissmann. Electronic properties of transition-metal clusters: Consideration of the spillover in a bulk parametrization. *Phys. Rev. B*, 55(19):13283, 1997.
- [131] F. Aguilera-Granja, A. García-Fuente, and A. Vega. Comparative ab initio study of the structural, electronic, and magnetic trends of isoelectronic late 3d and 4d transition metal clusters. *Phys. Rev. B*, 78(13):134425, 2008.
- [132] N. O. Jones, S. N. Khanna, T. Baruah, and M. R. Pederson. Classical Stern-Gerlach profiles of Mn_5 and Mn_6 clusters. *Phys. Rev. B*, 70(4):045416, 2004.

- [133] S. E. Apsel, J. W. Emmert, J. Deng, and L. A. Bloomfield. Surface-enhanced magnetism in nickel clusters. *Phys. Rev. Lett.*, 76(9):1441, 1996.
- [134] I. M. L. Billas, J. A. Becker, A. Châtelain, and W. A. de Heer. Magnetic moments of iron clusters with 25 to 700 atoms and their dependence on temperature. *Phys. Rev. Lett.*, 71(24):4067, 1993.
- [135] R. Peierls. Quelques propriétés typiques des corps solides. In *Annales de l'institut Henri Poincaré*, volume 5, pages 177–222, 1935.
- [136] L. D. Landau. Zur theorie der phasenumwandlungen ii. *Phys. Z. Sowjetunion*, 11:26–35, 1937.
- [137] K. S. Novoselov, A. Mishchenko, A. Carvalho, and A. H. Castro Neto. 2D materials and van der waals heterostructures. *Science*, 353(6298):aac9439, 2016.
- [138] A. K. Geim and I. V. Grigorieva. Van der waals heterostructures. *Nature*, 499(7459):419–425, 2013.
- [139] K. S. Novoselov, A. K. Geim, S. V. Morozov, D. Jiang, Y. Zhang, S. V. Dubonos, I. V. Grigorieva, and A. A. Firsov. Electric field effect in atomically thin carbon films. *Science*, 306(5696):666–669, 2004.
- [140] A. H. Castro Neto, F. Guinea, N. M. R. Peres, K. S. Novoselov, and A. K. Geim. The electronic properties of graphene. *Rev. Mod. Phys.*, 81(1):109, 2009.
- [141] K. S. Novoselov, Fal'ko V. I., L. Colombo, P. R. Gellert, M. G. Schwab, and K. Kim. A roadmap for graphene. *Nature*, 490(7419):192–200, 2012.
- [142] C. Soldano, A. Mahmood, and E. Dujardin. Production, properties and potential of graphene. *Carbon*, 48(8):2127–2150, 2010.
- [143] V. Singh, D. Joung, L. Zhai, S. Das, S. I Khondaker, and S. Seal. Graphene based materials: past, present and future. *Prog. Mat. Sci.*, 56(8):1178–1271, 2011.
- [144] W. Hua-Qiang, L. Chang-Yang, L. Hong-Ming, and Q. He. Graphene applications in electronic and optoelectronic devices and circuits. *Chin. Phys. B*, 22(9):098106, 2013.
- [145] X. Huang, Z. Yin, S. Wu, X. Qi, Q. He, Q. Zhang, Q. Yan, F. Boey, and H. Zhang. Graphene-based materials: synthesis, characterization, properties, and applications. *Small*, 7(14):1876–1902, 2011.
- [146] A. K. Geim. Graphene: status and prospects. *Science*, 324(5934):1530–1534, 2009.
- [147] J. A. Lawlor and M. S. Ferreira. Sublattice asymmetry of impurity doping in graphene: A review. *Beilstein J. Nanotechnol.*, 5(1):1210–1217, 2014.
- [148] H. Liu, Y. Liu, and D. Zhu. Chemical doping of graphene. *J. Mater. Chem.*, 21(10):3335–3345, 2011.

- [149] H. Yang, J. Heo, S. Park, H. J. Song, D. H. Seo, K. Byun, P. Kim, I. Yoo, H. Chung, and K. Kim. Graphene barristor, a triode device with a gate-controlled Schottky barrier. *Science*, 336(6085):1140–1143, 2012.
- [150] F. Schwierz. Graphene transistors. *Nat. Nanotechnol.*, 5(7):487–496, 2010.
- [151] E. W. Hill, A. K. Geim, K. Novoselov, F. Schedin, and P. Blake. Graphene spin valve devices. *IEEE Trans. Magn.*, 42(10):2694–2696, 2006.
- [152] S. Cho, Y. Chen, and M. S. Fuhrer. Gate-tunable graphene spin valve. *Appl. Phys. Lett.*, 91(12):123105, 2007.
- [153] S. Roche, B. Beschoten, J. C. Charlier, M. Chshiev, S. P. Dash, B. Dlubak, J. Fabian, A. Fert, F. Guinea, I. Grigorieva, C. Schenberger, P. Seneor, C. Stampfer, S. O. Valenzuela, X. Waintal, and B. van Wees. Graphene spintronics: the european flagship perspective. *2D Mater.*, 2(3):030202, 2015.
- [154] N. Tombros, C. Jozsa, M. Popinciuc, H. T. Jonkman, and B. J. Van Wees. Electronic spin transport and spin precession in single graphene layers at room temperature. *Nature*, 448(7153):571–574, 2007.
- [155] K. Tsukagoshi, B. W. Alphenaar, and H. Ago. Coherent transport of electron spin in a ferromagnetically contacted carbon nanotube. *Nature*, 401(6753):572–574, 1999.
- [156] J. Maassen, W. Ji, and H. Guo. Graphene spintronics: the role of ferromagnetic electrodes. *Nano Lett.*, 11(1):151–155, 2010.
- [157] P. Lazić, G. M. Sipahi, R. K. Kawakami, and I. Žutić. Graphene spintronics: Spin injection and proximity effects from first principles. *Phys. Rev. B*, 90(8):085429, 2014.
- [158] A. R. Rocha, T. B. Martins, A. Fazzio, and A. J. R. Da Silva. Disorder-based graphene spintronics. *Nanotechnology*, 21(34):345202, 2010.
- [159] J. Fernández-Rossier and J. J. Palacios. Magnetism in graphene nanoislands. *Phys. Rev. Lett.*, 99(17):177204, 2007.
- [160] Y. Son, M. L. Cohen, and S. G. Louie. Half-metallic graphene nanoribbons. *Nature*, 444(7117):347–349, 2006.
- [161] O. V. Yazyev and L. Helm. Defect-induced magnetism in graphene. *Phys. Rev. B*, 75(12):125408, 2007.
- [162] P. O. Lehtinen, A. S. Foster, A. Ayuela, A. Krasheninnikov, K. Nordlund, and R. M. Nieminen. Magnetic properties and diffusion of adatoms on a graphene sheet. *Phys. Rev. Lett.*, 91(1):017202, 2003.

- [163] I. C. Gerber, A. V. Krasheninnikov, A. S. Foster, and R. M. Nieminen. A first-principles study on magnetic coupling between carbon adatoms on graphene. *New J. Phys.*, 12(11):113021, 2010.
- [164] L. Chen, L. Guo, Z. Li, H. Zhang, J. Lin, J. Huang, S. Jin, and X. Chen. Towards intrinsic magnetism of graphene sheets with irregular zigzag edges. *Sci, Rep.*, 3:2599, 2013.
- [165] J. M. D. Coey, M. Venkatesan, C. B. Fitzgerald, A. P. Douvalis, and I. S. Sanders. Ferromagnetism of a graphite nodule from the canyon diablo meteorite. *Nature*, 420(6912):156–159, 2002.
- [166] T. L. Makarova, B. Sundqvist, R. Höhne, P. Esquinazi, Y. Kopelevich, P. Scharff, V. A. Davydov, L. S. Kashevarova, and A. V. Rakhmanina. Magnetic carbon. *Nature*, 413(6857):716–718, 2001.
- [167] N. Park, M. Yoon, S. Berber, J. Ihm, E. Osawa, and D. Tománek. Magnetism in all-carbon nanostructures with negative gaussian curvature. *Phys. Rev. Lett.*, 91(23):237204, 2003.
- [168] M. Yi and Z. Shen. A review on mechanical exfoliation for the scalable production of graphene. *J. Mater. Chem. A*, 3(22):11700–11715, 2015.
- [169] Y. Hernandez, V. Nicolosi, M. Lotya, F. M. Blighe, Z. Sun, S. De, I. T. McGovern, B. Holland, M. Byrne, Y. K. Gun'Ko, J. J. Boland, P. Niraj, G. Duesberg, S. Krishnamurthy, R. Goodhue, J. Hutchison, V. Scardaci, A. C. Ferrari, and J. N. Coleman. High-yield production of graphene by liquid-phase exfoliation of graphite. *Nat. Nanotechnol.*, 3(9):563–568, 2008.
- [170] X. Li, C. W. Magnuson, A. Venugopal, R. M. Tromp, J. B. Hannon, E. M. Vogel, L. Colombo, and R. S. Ruoff. Large-area graphene single crystals grown by low-pressure chemical vapor deposition of methane on copper. *J. Am. Chem. Soc.*, 133(9):2816–2819, 2011.
- [171] X. Li, C. W. Magnuson, A. Venugopal, J. An, J. W. Suk, B. Han, M. Borysiak, W. Cai, A. Velamakanni, Y. Zhu, L. Fu, E. M. Vogel, E. Voelkl, L. Colombo, and R. S. Ruoff. Graphene films with large domain size by a two-step chemical vapor deposition process. *Nano Lett.*, 10(11):4328–4334, 2010.
- [172] S. J. Chae, F. Güneş, K. K. Kim, E. S. Kim, G. H. Han, S. M. Kim, H. Shin, S. Yoon, J. Choi, M. H. Park, C. W. Yang, D. Probat, and Y. H. Lee. Synthesis of large-area graphene layers on poly-nickel substrate by chemical vapor deposition: wrinkle formation. *Adv. Mater.*, 21(22):2328–2333, 2009.
- [173] A. Reina, X. Jia, J. Ho, D. Nezich, H. Son, V. Bulovic, M. S. Dresselhaus, and J. Kong. Large area, few-layer graphene films on arbitrary substrates by chemical vapor deposition. *Nano Lett.*, 9(1):30–35, 2008.

- [174] Y. Zhang, L. Zhang, and C. Zhou. Review of chemical vapor deposition of graphene and related applications. *Acc. Chem. Res.*, 46(10):2329–2339, 2013.
- [175] C. Berger, Z. Song, T. Li, X. Li, A. Y Ogbazghi, R. Feng, Z. Dai, A. N. Marchenkov, E. H. Conrad, P. N. First, and W. A. de Heer. Ultrathin epitaxial graphite: 2D electron gas properties and a route toward graphene-based nanoelectronics. *J. Phys. Chem. B*, 108(52):19912–19916, 2004.
- [176] C. Berger, Z. Song, X. Li, X. Wu, N. Brown, C. Naud, D. Mayou, T. Li, J. Hass, A. N. Marchenkov, E. H. Conrad, P. N. First, and W. A. de Heer. Electronic confinement and coherence in patterned epitaxial graphene. *Science*, 312(5777):1191–1196, 2006.
- [177] W. A. De Heer, C. Berger, M. Ruan, M. Sprinkle, X. Li, Y. Hu, B. Zhang, J. Hankinson, and E. Conrad. Large area and structured epitaxial graphene produced by confinement controlled sublimation of silicon carbide. *Proc. Natl. Acad. Sci. U.S.A.*, 108(41):16900–16905, 2011.
- [178] O. C. Compton and S. T. Nguyen. Graphene oxide, highly reduced graphene oxide, and graphene: versatile building blocks for carbon-based materials. *Small*, 6(6):711–723, 2010.
- [179] W. S. Hummers Jr and R. E. Offeman. Preparation of graphitic oxide. *J. Am. Chem. Soc.*, 80(6):1339–1339, 1958.
- [180] D. R. Dreyer, S. Park, C. W. Bielawski, and R. S. Ruoff. The chemistry of graphene oxide. *Chem. Soc. Rev.*, 39(1):228–240, 2010.
- [181] P. R. Wallace. The band theory of graphite. *Phys. Rev.*, 71(9):622, 1947.
- [182] J. C. Tan and A. K. Cheetham. Mechanical properties of hybrid inorganic–organic framework materials: establishing fundamental structure–property relationships. *Chem. Soc. Rev.*, 40(2):1059–1080, 2011.
- [183] V. Gavryushin. Graphene brillouin zone and electronic energy dispersion. *Wolfram Demonstrations Project*.
- [184] L. Van Hove. The occurrence of singularities in the elastic frequency distribution of a crystal. *Phys. Rev.*, 89(6):1189, 1953.
- [185] V. W. Brar, R. Decker, H.-M. Solowan, Y. Wang, L. Maserati, K. T. Chan, H. Lee, C. O. Girit, A. Zettl, S. G. Louie, M. L. Cohen, and M. F. Crommie. Gate-controlled ionization and screening of cobalt adatoms on a graphene surface. *Nature Phys.*, 7(1):43–47, 2011.
- [186] Y. Sanchez-Paisal, D. Sanchez-Portal, and A. Ayuela. Ab initio calculations of zirconium adsorption and diffusion on graphene. *Phys. Rev. B*, 80(4):045428, 2009.

- [187] X. Dai, Y. Tang, J. Zhao, and Y. Dai. Absorption of Pt clusters and the induced magnetic properties of graphene. *J. Phys.: Condens. Matter*, 22(31):316005, 2010.
- [188] M. M. Ugeda, I. Brihuega, F. Guinea, and J. M. Gómez-Rodríguez. Missing atom as a source of carbon magnetism. *Phys. Rev. Lett.*, 104(9):096804, 2010.
- [189] V. M. Pereira, F. Guinea, J. M. B. Lopes Dos Santos, N. M. R. Peres, and A. H. Castro Neto. Disorder induced localized states in graphene. *Phys. Rev. Lett.*, 96(3):036801, 2006.
- [190] E. J. G. Santos, S. Riikonen, D. Sánchez-Portal, and A. Ayuela. Magnetism of single vacancies in rippled graphene. *J. Phys. Chem. C*, 116(13):7602–7606, 2012.
- [191] Y. Wang, Y. Huang, Y. Song, X. Zhang, Y. Ma, J. Liang, and Y. Chen. Room-temperature ferromagnetism of graphene. *Nano Lett.*, 9(1):220–224, 2008.
- [192] J. J. Palacios and F. Ynduráin. Critical analysis of vacancy-induced magnetism in monolayer and bilayer graphene. *Phys. Rev. B*, 85(24):245443, 2012.
- [193] H. Kumazaki and D. S. Hirashima. Local magnetic moment formation on edges of graphene. *J. Phys. Soc. Jpn.*, 77(4), 2008.
- [194] W. Sheng, Z. Y. Ning, Z. Q. Yang, and H. Guo. Magnetism and perfect spin filtering effect in graphene nanoflakes. *Nanotechnology*, 21(38):385201, 2010.
- [195] L. R. Radovic and B. Bockrath. On the chemical nature of graphene edges: origin of stability and potential for magnetism in carbon materials. *J. Am. Chem. Soc.*, 127(16):5917–5927, 2005.
- [196] S. Bhowmick and V. B. Shenoy. Edge state magnetism of single layer graphene nanostructures. *J. Chem. Phys.*, 128(24):244717, 2008.
- [197] A. Zobelli, V. Ivanovskaya, P. Wagner, I. Suarez-Martinez, A. Yaya, and C. P. Ewels. A comparative study of density functional and density functional tight binding calculations of defects in graphene. *Phys. Status Solidi B*, 249(2):276–282, 2012.
- [198] A. W. Robertson and J. H. Warner. Atomic resolution imaging of graphene by transmission electron microscopy. *Nanoscale*, 5(10):4079–4093, 2013.
- [199] P. Y. Huang, C. S. Ruiz-Vargas, A. M. van der Zande, W. S. Whitney, M. P. Levendorf, J. W. Kevek, S. Garg, J. S. Alden, C. J. Hustedt, Y. Zhu, J. Park, P. L. McEuen, and D. A. Muller. Grains and grain boundaries in single-layer graphene atomic patchwork quilts. *Nature*, 469(7330):389–392, 2011.
- [200] C. Gong, A. W. Robertson, K. He, G. Lee, E. Yoon, C. S. Allen, A. I. Kirkland, and J. H. Warner. Thermally induced dynamics of dislocations in graphene at atomic resolution. *ACS Nano*, 9(10):10066–10075, 2015.

8 Bibliography

- [201] L. Zhang, Q. Xu, J. Niu, and Z. Xia. Role of lattice defects in catalytic activities of graphene clusters for fuel cells. *Phys. Chem. Chem. Phys.*, 17(26):16733–16743, 2015.
- [202] A. Carpio, L. L. Bonilla, F. de Juan, and M. A. H. Vozmediano. Dislocations in graphene. *New J. Phys.*, 10(5):053021, 2008.
- [203] O. Lehtinen, S. Kurasch, A. V. Krasheninnikov, and U. Kaiser. Atomic scale study of the life cycle of a dislocation in graphene from birth to annihilation. *Nat. Commun.*, 4, 2013.
- [204] O. V. Yazyev and Y. P. Chen. Polycrystalline graphene and other two-dimensional materials. *Nat. Nanotechnol.*, 9(10):755–767, 2014.
- [205] I. A. Ovid’ko and A. G. Sheinerman. Cracks at disclinated grain boundaries in graphene. *J. Phys. D: Appl. Phys.*, 46(34):345305, 2013.
- [206] O. V. Yazyev and S. G. Louie. Topological defects in graphene: Dislocations and grain boundaries. *Phys. Rev. B*, 81(19):195420, 2010.
- [207] D. Van Tuan, F. Ortmann, D. Soriano, S. O. Valenzuela, and S. Roche. Pseudospin-driven spin relaxation mechanism in graphene. *Nature Phys.*, 10(11):857–863, 2014.
- [208] L. Tsetseris, B. Wang, and S. T. Pantelides. Substitutional doping of graphene: The role of carbon divacancies. *Phys. Rev. B*, 89(3):035411, 2014.
- [209] P. O. Lehtinen, A. S. Foster, A. Ayuela, A. Krasheninnikov, K. Nordlund, and R. M. Nieminen. Magnetic properties and diffusion of adatoms on a graphene sheet. *Phys. Rev. Lett.*, 91(1):017202, 2003.
- [210] E. Faizabadi and E. Mostaani. Density of states of magnetic substitutional impurity-doped graphene in the paramagnetic and ferromagnetic phases. *J. Magn. Magn. Mater.*, 342:54–60, 2013.
- [211] D. W. Boukhvalov. First-principles modeling of the interactions of iron impurities with graphene and graphite. *Phys. Status Solidi B*, 248(6):1347–1351, 2011.
- [212] R. C. Longo, J. Carrete, and L. J. Gallego. Ab initio study of 3d, 4d, and 5d transition metal adatoms and dimers adsorbed on hydrogen-passivated zigzag graphene nanoribbons. *Phys. Rev. B*, 83(23):235415, 2011.
- [213] S. R. Power, V. M. de Menezes, S. B. Fagan, and M. S. Ferreira. Magnetization profile for impurities in graphene nanoribbons. *Phys. Rev. B*, 84(19):195431, 2011.
- [214] J. Hu, J. Alicea, R. Wu, and M. Franz. Giant topological insulator gap in graphene with 5d adatoms. *Phys. Rev. Lett.*, 109(26):266801, 2012.
- [215] D. Ma, Z. Li, and Z. Yang. Strong spin-orbit splitting in graphene with adsorbed Au atoms. *Carbon*, 50(1):297–305, 2012.

- [216] D. W. Boukhvalov and M. I. Katsnelson. Chemical functionalization of graphene with defects. *Nano Lett.*, 8(12):4373–4379, 2008.
- [217] P. O. Lehtinen, A. S. Foster, Y. Ma, A. V. Krasheninnikov, and R. M. Nieminen. Irradiation-induced magnetism in graphite: a density functional study. *Phys. Rev. Lett.*, 93(18):187202, 2004.
- [218] G. Forte, A. Grassi, G. M. Lombardo, A. La Magna, G. G. N. Angilella, R. Pucci, and R. Vilaridi. Modeling vacancies and hydrogen impurities in graphene: A molecular point of view. *Phys. Lett. A*, 372(40):6168–6174, 2008.
- [219] J. Sierański, K. and Szatkowski. The energies of the substitutional impurities in graphene. *Phys. Status Solidi B*, 250(8):1556–1562, 2013.
- [220] R. Singh and P. Kroll. Magnetism in graphene due to single-atom defects: dependence on the concentration and packing geometry of defects. *J. Phys. Condens. Matter*, 21(19):196002, 2009.
- [221] V. Zólyomi, A. Ruzsnyák, J. Kurti, and C. J. Lambert. First principles study of the binding of 4d and 5d transition metals to graphene. *J. Phys. Chem. C*, 114(43):18548–18552, 2010.
- [222] V. Zólyomi, A. Ruzsnyak, J. Koltai, J. Kürti, and C. J. Lambert. Functionalization of graphene with transition metals. *Phys. Status Solidi B*, 247(11-12):2920–2923, 2010.
- [223] J. A. Rodríguez-Manzo, O. Cretu, and F. Banhart. Trapping of metal atoms in vacancies of carbon nanotubes and graphene. *ACS Nano*, 4(6):3422–3428, 2010.
- [224] H. Wang, Q. Wang, Y. Cheng, K. Li, Y. Yao, Q. Zhang, C. Dong, P. Wang, U. Schwingenschlogl, W. Yang, and X. X. Zhang. Doping monolayer graphene with single atom substitutions. *Nano Lett.*, 12(1):141–144, 2011.
- [225] A. V. Krasheninnikov and K. Nordlund. Ion and electron irradiation-induced effects in nanostructured materials. *J. Appl. Phys.*, 107(7):071301, 2010.
- [226] A. Eckmann, A. Felten, I. Verzhbitskiy, R. Davey, and C. Casiraghi. Raman study on defective graphene: effect of the excitation energy, type, and amount of defects. *Phys. Rev. B*, 88(3):035426, 2013.
- [227] M. Ushiro, K. Uno, T. Fujikawa, Y. Sato, K. Tohji, F. Watari, W. Chun, Y. Koike, and K. Asakura. X-ray absorption fine structure (XAFS) analyses of Ni species trapped in graphene sheet of carbon nanofibers. *Phys. Rev. B*, 73(14):144103, 2006.
- [228] A. V. Krasheninnikov, P. O. Lehtinen, A. S. Foster, P. Pyykkö, and R. M. Nieminen. Embedding transition-metal atoms in graphene: structure, bonding, and magnetism. *Phys. Rev. Lett.*, 102(12):126807, 2009.

- [229] E. J. G. Santos, A. Ayuela, and D. Sánchez-Portal. First-principles study of substitutional metal impurities in graphene: structural, electronic and magnetic properties. *New J. Phys.*, 12(5):053012, 2010.
- [230] S. Sun, C. B. Murray, D. Weller, L. Folks, and A. Moser. Monodisperse FePt nanoparticles and ferromagnetic FePt nanocrystal superlattices. *Science*, 287(5460):1989–1992, 2000.
- [231] Y. Mao, J. Yuan, and J. Zhong. Density functional calculation of transition metal adatom adsorption on graphene. *J. Phys. Condens. Matter*, 20(11):115209, 2008.
- [232] C. Cao, M. Wu, J. Jiang, and H. Cheng. Transition metal adatom and dimer adsorbed on graphene: Induced magnetization and electronic structures. *Phys. Rev. B*, 81(20):205424, 2010.
- [233] T. O. Wehling, A. I. Lichtenstein, and M. I. Katsnelson. Transition-metal adatoms on graphene: Influence of local coulomb interactions on chemical bonding and magnetic moments. *Phys. Rev. B*, 84(23):235110, 2011.
- [234] I. Cabria, M. J. Lopez, and J. A. Alonso. Theoretical study of the transition from planar to three-dimensional structures of palladium clusters supported on graphene. *Phys. Rev. B*, 81(3):035403, 2010.
- [235] O. Ü. Aktürk and M. Tomak. Au_nPt_n clusters adsorbed on graphene studied by first-principles calculations. *Phys. Rev. B*, 80(8):085417, 2009.
- [236] K. Okazaki-Maeda, Y. Morikawa, S. Tanaka, and M. Kohyama. Structures of Pt clusters on graphene by first-principles calculations. *Surf. Sci.*, 604(2):144–154, 2010.
- [237] I. Fampiou and A. Ramasubramaniam. Binding of Pt nanoclusters to point defects in graphene: adsorption, morphology, and electronic structure. *J. Phys. Chem. C.*, 116(11):6543–6555, 2012.
- [238] G. Kim and S. Jhi. Carbon monoxide-tolerant platinum nanoparticle catalysts on defect-engineered graphene. *ACS Nano*, 5(2):805–810, 2011.
- [239] D. Lim, A. S. Negreira, and J. Wilcox. DFT studies on the interaction of defective graphene-supported Fe and Al nanoparticles. *J. Phys. Chem. C.*, 115(18):8961–8970, 2011.
- [240] X. Liu, K. X. Yao, C. Meng, and Y. Han. Graphene substrate-mediated catalytic performance enhancement of Ru nanoparticles: a first-principles study. *Dalton Trans.*, 41(4):1289–1296, 2012.
- [241] A. J. Logsdail and J. Akola. Interaction of Au_{16} nanocluster with defects in supporting graphite: A density-functional study. *J. Phys. Chem. C*, 115(31):15240–15250, 2011.

- [242] S. Sahoo, M. E. Gruner, S. N. Khanna, and P. Entel. First-principles studies on graphene-supported transition metal clusters. *J. Chem. Phys.*, 141(7):074707, 2014.
- [243] Q. Qi, H. Liu, W. Feng, H. Tian, H. Xu, and X. Huang. Theoretical investigation on the interaction of subnano platinum clusters with graphene using DFT methods. *Comput. Mater. Sci.*, 96:268–276, 2015.
- [244] S. Sahoo, M. F. Islam, and S. N. Khanna. Using graphene to control magnetic anisotropy and interaction between supported clusters. *New J. Phys.*, 17(5):053052, 2015.
- [245] C. M. Ramos-Castillo, J. U. Reveles, R. R. Zope, and R. de Coss. Palladium clusters supported on graphene monovacancies for hydrogen storage. *J. Phys. Chem. C*, 119(15):8402–8409, 2015.
- [246] X. Liu, C. Wang, H. Lin, M. Hupalo, P. A. Thiel, K. Ho, and M. C. Tringides. Structures and magnetic properties of Fe clusters on graphene. *Phys. Rev. B*, 90(15):155444, 2014.
- [247] H. D. Ozaydin, H. Sahin, R. T. Senger, and F. M. Peeters. Formation and diffusion characteristics of Pt clusters on graphene, 1H-MoS₂ and 1T-TaS₂. *Annalen der Physik*, 526(9-10):423–429, 2014.
- [248] D. Xu, J. Zhao, and X. Wang. A density functional theory study of the adsorption of bimetallic Fe_nPt_m clusters on defective graphene: structural, electronic, and magnetic properties. *J. Nanopart. Res.*, 15(4):1–14, 2013.
- [249] W. Ji, C. Zhang, F. Li, P. Li, P. Wang, M. Ren, and M. Yuan. First-principles study of small Pd–Au alloy clusters on graphene. *RSC Adv.*, 4(99):55781–55789, 2014.
- [250] M. J. Lopez, I. Cabria, and J. A. Alonso. Palladium clusters anchored on graphene vacancies and their effect on the reversible adsorption of hydrogen. *J. Phys. Chem. C*, 118(10):5081–5090, 2014.
- [251] R. Zan, U. Bangert, Q. Ramasse, and K. S. Novoselov. Metal- graphene interaction studied via atomic resolution scanning transmission electron microscopy. *Nano Lett.*, 11(3):1087–1092, 2011.
- [252] J. E. Santos, N. M. R. Peres, J. M. B. L. dos Santos, and A. H. Castro Neto. Electronic doping of graphene by deposited transition metal atoms. *Phys. Rev. B*, 84(8):085430, 2011.
- [253] T. Eelbo, M. Waśniowska, P. Thakur, M. Gyamfi, B. Sachs, T. O. Wehling, S. Forti, U. Starke, C. Tieg, A. I. Lichtenstein, and R. Wiesendanger. Adatoms and clusters of 3d transition metals on graphene: Electronic and magnetic configurations. *Phys. Rev. Lett.*, 110(13):136804, 2013.

- [254] K. Pi, K. M. McCreary, W. Bao, W. Han, Y. F. Chiang, Y. Li, S.-W. Tsai, C. N. Lau, and R. K. Kawakami. Electronic doping and scattering by transition metals on graphene. *Phys. Rev. B*, 80(7):075406, 2009.
- [255] C. Vo-Van, Z. Kassir-Bodon, H. Yang, J. Coraux, J. Vogel, S. Pizzini, P. Bayle-Guillemaud, M. Chshiev, L. Ranno, V. Guisset, P. David, V. Salvador, and O. Fruchart. Ultrathin epitaxial cobalt films on graphene for spintronic investigations and applications. *New J. Phys.*, 12(10):103040, 2010.
- [256] Y. Gan, L. Sun, and F. Banhart. One-and two-dimensional diffusion of metal atoms in graphene. *Small*, 4(5):587–591, 2008.
- [257] T. O. Wehling, A. V. Balatsky, M. I. Katsnelson, A. I. Lichtenstein, and A. Rosch. Orbitaly controlled Kondo effect of Co adatoms on graphene. *Phys. Rev. B*, 81(11):115427, 2010.
- [258] Y. Virgus, W. Purwanto, H. Krakauer, and S. Zhang. Ab initio many-body study of cobalt adatoms adsorbed on graphene. *Phys. Rev. B*, 86(24):241406, 2012.
- [259] L. H. de Lima, R. Landers, and A. de Siervo. Patterning quasi-periodic Co 2D-clusters underneath graphene on SiC (0001). *Chem. Mater.*, 26(14):4172–4177, 2014.
- [260] K. I. Bolotin, K. J. Sikes, Z. Jiang, M. Klima, G. Fudenberg, J. Hone, P. Kim, and H. L. Stormer. Ultrahigh electron mobility in suspended graphene. *Solid State Commun.*, 146(9):351–355, 2008.
- [261] Y. Zhang, Y. Tan, H. L. Stormer, and P. Kim. Experimental observation of the quantum hall effect and Berry’s phase in graphene. *Nature*, 438(7065):201–204, 2005.
- [262] Y. Gogotsi. Not just graphene: The wonderful world of carbon and related nanomaterials. *MRS Bulletin*, 40(12):1110–1121, 2015.
- [263] A. Hashimoto, K. Suenaga, A. Gloter, K. Urita, and S. Iijima. Direct evidence for atomic defects in graphene layers. *Nature*, 430(7002):870–873, 2004.
- [264] Z. Liu, K. Suenaga, P. J. F. Harris, and S. Iijima. Open and closed edges of graphene layers. *Phys. Rev. Lett.*, 102(1):015501, 2009.
- [265] C. Jin, H. Lan, L. Peng, K. Suenaga, and S. Iijima. Deriving carbon atomic chains from graphene. *Phys. Rev. Lett.*, 102(20):205501, 2009.
- [266] H. Liu, A. T. Neal, Z. Zhu, Z. Luo, X. Xu, D. Tománek, and P. D. Ye. Phosphorene: an unexplored 2D semiconductor with a high hole mobility. *ACS Nano*, 8(4):4033–4041, 2014.

- [267] J. Sun, H. Lee, M. Pasta, H. Yuan, G. Zheng, Y. Sun, Y. Li, and Y. Cui. A phosphorene–graphene hybrid material as a high-capacity anode for sodium-ion batteries. *Nat. Nanotechnol.*, 10(11):980–985, 2015.
- [268] Z. Zhu and D. Tománek. Semiconducting layered blue phosphorus: a computational study. *Phys. Rev. Lett.*, 112(17):176802, 2014.
- [269] R. Hultgren, N. S. Gingrich, and B. E. Warren. The atomic distribution in red and black phosphorus and the crystal structure of black phosphorus. *J. Chem. Phys.*, 3(6):351–355, 1935.
- [270] A. Simon, H. Borrmann, and J. Horakh. On the polymorphism of white phosphorus. *Chem. Ber.*, 130(9):1235–1240, 1997.
- [271] H. Thurn and H. Kerbs. Crystal structure of violet phosphorus. *Angew. Chem. Int. Ed.*, 5(12):1047–1048, 1966.
- [272] A. Castellanos-Gómez, L. Vicarelli, E. Prada, J. O. Island, K. L. Narasimha-Acharya, S. I. Blanter, D. J. Groenendijk, M. Buscema, G. A. Steele, J. V. Alvarez, H. W. Zandbergen, J. J. Palacios, and H. S. J. van der Zant. Isolation and characterization of few-layer black phosphorus. *2D Mater.*, 1(2):025001, 2014.
- [273] Q. Wei and X. Peng. Superior mechanical flexibility of phosphorene and few-layer black phosphorus. *Appl. Phys. Lett.*, 104(25):251915, 2014.
- [274] J. Dai and X. C. Zeng. Structure and stability of two dimensional phosphorene with =O or =NH functionalization. *RSC Adv.*, 4(89):48017–48021, 2014.
- [275] F. Xia, H. Wang, and Y. Jia. Rediscovering black phosphorus as an anisotropic layered material for optoelectronics and electronics. *Nat. Commun.*, 5, 2014.
- [276] L. Li, Y. Yu, G. J. Ye, Q. Ge, X. Ou, H. Wu, D. Feng, X. Hui Chen, and Y. Zhang. Black phosphorus field-effect transistors. *Nat. Nanotechnol.*, 9(5):372–377, 2014.
- [277] A. Castellanos-Gómez. Black phosphorus: narrow gap, wide applications. *J. Phys. Chem. Lett.*, 6(21):4280–4291, 2015.
- [278] J. Dai and X. C. Zeng. Bilayer phosphorene: effect of stacking order on bandgap and its potential applications in thin-film solar cells. *J. Phys. Chem. Lett.*, 5(7):1289–1293, 2014.
- [279] J. D. Wood, S. A. Wells, D. Jariwala, K. Chen, E. Cho, V. K. Sangwan, X. Liu, L. J. Lauhon, T. J. Marks, and M. C. Hersam. Effective passivation of exfoliated black phosphorus transistors against ambient degradation. *Nano Lett.*, 14(12):6964–6970, 2014.
- [280] J. O. Island, G. A. Steele, H. S. J. van der Zant, and A. Castellanos-Gómez. Environmental instability of few-layer black phosphorus. *2D Mater.*, 2(1):011002, 2015.

- [281] A. Ziletti, A. Carvalho, D. K. Campbell, D. F. Coker, and A. H. Castro Neto. Oxygen defects in phosphorene. *Phys. Rev. Lett.*, 114(4):046801, 2015.
- [282] V. V. Kulish, O. I. Malyi, C. Persson, and P. Wu. Adsorption of metal adatoms on single-layer phosphorene. *Phys. Chem. Chem. Phys.*, 17(2):992–1000, 2015.
- [283] L. Kou, T. Frauenheim, and C. Chen. Phosphorene as a superior gas sensor: Selective adsorption and distinct I–V response. *J. Phys. Chem. Lett.*, 5(15):2675–2681, 2014.
- [284] X. Peng, A. Copple, and Q. Wei. Edge effects on the electronic properties of phosphorene nanoribbons. *J. Appl. Phys.*, 116(14):144301, 2014.
- [285] A. Carvalho, A. S. Rodin, and A. H. Castro Neto. Phosphorene nanoribbons. *EPL*, 108(4):47005, 2014.
- [286] H. Guo, N. Lu, J. Dai, X. Wu, and X. C. Zeng. Phosphorene nanoribbons, phosphorus nanotubes, and van der waals multilayers. *J. Phys. Chem. C*, 118(25):14051–14059, 2014.
- [287] P. Vogt, P. De Padova, C. Quaresima, J. Avila, E. Frantzeskakis, M. C. Asensio, A. Resta, B. Ealet, and G. Le Lay. Silicene: compelling experimental evidence for graphenelike two-dimensional silicon. *Phys. Rev. Lett.*, 108(15):155501, 2012.
- [288] B. Lalmi, H. Oughaddou, H. Enriquez, A. Kara, S. Vizzini, B. Ealet, and B. Aufray. Epitaxial growth of a silicene sheet. *Appl. Phys. Lett.*, 97(22):223109, 2010.
- [289] B. Aufray, A. Kara, S. Vizzini, H. Oughaddou, C. Leandri, B. Ealet, and G. Le Lay. Graphene-like silicon nanoribbons on Ag (110): A possible formation of silicene. *Appl. Phys. Lett.*, 96(18):183102, 2010.
- [290] S. Balendhran, S. Walia, H. Nili, S. Sriram, and M. Bhaskaran. Elemental analogues of graphene: silicene, germanene, stanene, and phosphorene. *Small*, 11(6):640–652, 2015.
- [291] D. Jose and A. Datta. Structures and chemical properties of silicene: unlike graphene. *Acc. Chem. Res.*, 47(2):593–602, 2013.
- [292] A. Nijamudheen, R. Bhattacharjee, S. Choudhury, and A. Datta. Electronic and chemical properties of germanene: the crucial role of buckling. *J. Phys. Chem. C*, 119(7):3802–3809, 2015.
- [293] Z. Ni, H. Zhong, X. Jiang, R. Quhe, G. Luo, Y. Wang, M. Ye, J. Yang, J. Shi, and J. Lu. Tunable band gap and doping type in silicene by surface adsorption: towards tunneling transistors. *Nanoscale*, 6(13):7609–7618, 2014.
- [294] Y. Du, J. Zhuang, H. Liu, X. Xu, S. Eilers, K. Wu, P. Cheng, J. Zhao, X. Pi, K. W. See, G. Peleckis, X. Wang, and S. X. Dou. Tuning the band gap in silicene by oxidation. *ACS Nano*, 8(10):10019–10025, 2014.

- [295] L. E. Gusel’Nikov and N. S. Nametkin. Formation and properties of unstable intermediates containing multiple p_{π} - p_{π} . bonded group 4B metals. *Chem. Rev.*, 79(6):529–577, 1979.
- [296] P. Jutzi. New element-carbon (p-p) π bonds. *Angew. Chem. Int. Ed.*, 14(4):232–245, 1975.
- [297] R. S. Mulliken. Overlap integrals and chemical binding. *J. Am. Chem. Soc.*, 72(10):4493–4503, 1950.
- [298] E. Bekaroglu, M. Topsakal, S. Cahangirov, and S. Ciraci. First-principles study of defects and adatoms in silicon carbide honeycomb structures. *Phys. Rev. B*, 81(7):075433, 2010.
- [299] J. O. Sofo, A. S. Chaudhari, and G. D. Barber. Graphane: A two-dimensional hydrocarbon. *Phys. Rev. B*, 75(15):153401, 2007.
- [300] J. C. Garcia, D. B. de Lima, L. V. C. Assali, and J. F. Justo. Group IV graphene- and graphane-like nanosheets. *J. Phys. Chem. C*, 115(27):13242–13246, 2011.
- [301] N. G. Chopra, R. J. Luyken, K. Cherrey, V. H. Crespi, M. L. Cohen, S. G. Louie, and A. Zettl. Boron nitride nanotubes. *Science*, 269(5226):966–967, 1995.
- [302] A. Zunger, A. Katzir, and A. Halperin. Optical properties of hexagonal boron nitride. *Phys. Rev. B*, 13(12):5560, 1976.
- [303] L. Song, L. Ci, H. Lu, P. B. Sorokin, C. Jin, J. Ni, A. G. Kvashnin, D. G. Kvashnin, J. Lou, B. I. Yakobson, and P. M. Ajayan. Large scale growth and characterization of atomic hexagonal boron nitride layers. *Nano Lett.*, 10(8):3209–3215, 2010.
- [304] X. Blase, A. Rubio, S. G. Louie, and M. L. Cohen. Quasiparticle band structure of bulk hexagonal boron nitride and related systems. *Phys. Rev. B*, 51(11):6868, 1995.
- [305] K. Watanabe, T. Taniguchi, and H. Kanda. Direct-bandgap properties and evidence for ultraviolet lasing of hexagonal boron nitride single crystal. *Nat. Mater.*, 3(6):404–409, 2004.
- [306] C. Kamal and M. Ezawa. Arsenene: Two-dimensional buckled and puckered honeycomb arsenic systems. *Phys. Rev. B*, 91(8):085423, 2015.
- [307] S. Mardanya, V. K. Thakur, S. Bhowmick, and A. Agarwal. Four allotropes of semiconducting layered arsenic that switch into a topological insulator via an electric field: Computational study. *Phys. Rev. B*, 94(3):035423, 2016.
- [308] S. Zhang, Z. Yan, Y. Li, Z. Chen, and H. Zeng. Atomically thin arsenene and antimonene: semimetal–semiconductor and indirect–direct band-gap transitions. *Angew. Chem. Int. Ed.*, 54(10):3112–3115, 2015.

- [309] W. Yu, C. Niu, Z. Zhu, X. Wang, and W. Zhang. Atomically thin binary V-V compound semiconductor: a first-principles study. *J. Mater. Chem. C*, 4:6581–6587, 2016.
- [310] Q. Wang, W. Yu, X. Fu, C. Qiao, C. Xia, and Y. Jia. Electronic and magnetic properties of SnSe monolayers doped by Ga, In, As, and Sb: a first-principles study. *Phys. Chem. Chem. Phys.*, 18:8158–8164, 2016.
- [311] L. C. Gomes, A. Carvalho, and A. H. Castro Neto. Vacancies and oxidation of two-dimensional group-IV monochalcogenides. *Phys. Rev. B*, 94:054103, Aug 2016.
- [312] I. S. S. de Oliveira and R. Longuihos. Effects of oxygen contamination on monolayer GeSe: A computational study. *Phys. Rev. B*, 94(3):035440, 2016.
- [313] L. C. Gomes and A. Carvalho. Phosphorene analogues: isoelectronic two-dimensional group-IV monochalcogenides with orthorhombic structure. *Phys. Rev. B*, 92(8):085406, 2015.
- [314] L. C. Gomes, A. Carvalho, and A. H. Castro Neto. Enhanced piezoelectricity and modified dielectric screening of two-dimensional group-IV monochalcogenides. *Phys. Rev. B*, 92(21):214103, 2015.
- [315] B. R. Tuttle, S. M. Alhassan, and S. T. Pantelides. Large excitonic effects in group-IV sulfide monolayers. *Phys. Rev. B*, 92(23):235405, 2015.
- [316] M. Mehboudi, A. M. Dorio, W. Zhu, A. van der Zande, H. O. H. Churchill, A. A. Pacheco-Sanjuan, E. O. Harriss, P. Kumar, and S. Barraza-Lopez. Two-dimensional disorder in black phosphorus and monochalcogenide monolayers. *Nano Letters*, 16(3):1704–1712, 2016.
- [317] A. K. Singh and R. G. Hennig. Computational prediction of two-dimensional group-IV mono-chalcogenides. *Appl. Phys. Lett.*, 105(4):042103, 2014.
- [318] Z. Zhu, J. Guan, D. Liu, and D. Tománek. Designing isoelectronic counterparts to layered group V semiconductors. *ACS Nano*, 9(8):8284–8290, 2015.
- [319] J. Yang, Y. Zhang, W. Yin, X. G. Gong, B. I. Yakobson, and S. Wei. Two-dimensional SiS layers with promising electronic and optoelectronic properties: Theoretical prediction. *Nano Lett.*, 16(2):1110–1117, 2016.
- [320] Z. Ma, B. Wang, L. Ou, Y. Zhang, X. Zhang, and Z. Zhou. Structure and properties of phosphorene-like IV-VI 2D materials. *Nanotechnology*, 27(41):415203, 2016.
- [321] Y. Chen, Q. Sun, and P. Jena. SiTe monolayers: Si-based analogues of phosphorene. *J. Mater. Chem. C*, 2016.
- [322] F. Li, X. Liu, Y. Wang, and Y. Li. Germanium monosulfide monolayer: a novel two-dimensional semiconductor with a high carrier mobility. *J. Mater. Chem. C*, 4(11):2155–2159, 2016.

- [323] R. M. Martin. *Electronic structure: basic theory and practical methods*. Cambridge university press, 2004.
- [324] P. Pulay. Convergence acceleration of iterative sequences. the case of SCF iteration. *Chem. Phys. Lett.*, 73(2):393–398, 1980.
- [325] P. Pulay. Improved SCF convergence acceleration. *J. Comput. Chem.*, 3(4):556–560, 1982.
- [326] A. Van de Walle and G. Ceder. Correcting overbinding in local-density-approximation calculations. *Phys. Rev. B*, 59(23):14992, 1999.
- [327] M. Ernzerhof, J. P. Perdew, and K. Burke. Coupling-constant dependence of atomization energies. *Int. J. Quantum Chem.*, 64(3):285–295, 1997.
- [328] D. Bagayoko. Understanding density functional theory (DFT) and completing it in practice. *AIP Advances*, 4(12):127104, 2014.
- [329] J. P. Perdew. Density functional theory and the band gap problem. *Int. J. Quantum Chem.*, 28(S19):497–523, 1985.
- [330] J. M. Soler, E. Artacho, J. D. Gale, A. García, J. Junquera, P. Ordejón, and D. Sánchez-Portal. The SIESTA method for ab initio order-n materials simulation. *J. Phys. Condens. Matter*, 14(11):2745, 2002.
- [331] E. Artacho, E. Anglada, O. Diéguez, J. D. Gale, A. García, J. Junquera, R. M. Martin, P. Ordejón, J. M. Pruneda, D. Sánchez-Portal, and J. M. Soler. The SIESTA method; developments and applicability. *J. Phys. Condens. Matter*, 20(6):064208, 2008.
- [332] J. P. Perdew, K. Burke, and M. Ernzerhof. Generalized gradient approximation made simple. *Phy. Rev. Lett.*, 77(18):3865, 1996.
- [333] D. Geatches. *Clay minerals and their gallery guests: an ab initio investigation into their interactions*. PhD thesis, Durham University, 2011.
- [334] N. Troullier and J. L. Martins. Efficient pseudopotentials for plane-wave calculations. *Phys. Rev. B*, 43(3):1993, 1991.
- [335] G. Kresse and J. Furthmüller. Efficiency of ab-initio total energy calculations for metals and semiconductors using a plane-wave basis set. *Comput. Mater. Sci.*, 6(1):15–50, 1996.
- [336] G. Kresse and J. Hafner. Ab initio molecular-dynamics simulation of the liquid-metal–amorphous-semiconductor transition in germanium. *Phys. Rev. B*, 49(20):14251, 1994.
- [337] G. Kresse and J. Hafner. Ab initio molecular dynamics for liquid metals. *Phys. Rev. B*, 47(1):558, 1993.

8 Bibliography

- [338] G. Kresse and J. Furthmüller. Efficient iterative schemes for ab initio total-energy calculations using a plane-wave basis set. *Phys. Rev. B*, 54(16):11169, 1996.
- [339] G. Kresse and D. Joubert. From ultrasoft pseudopotentials to the projector augmented-wave method. *Phys. Rev. B*, 59(3):1758, 1999.
- [340] P. E. Blöchl. Projector augmented-wave method. *Phys. Rev. B*, 50(24):17953, 1994.
- [341] D. J. Singh and L. Nordstrom. *Planewaves, Pseudopotentials, and the LAPW method*. Springer Science & Business Media, 2006.
- [342] E. Sjöstedt, L. Nordström, and D. J. Singh. An alternative way of linearizing the augmented plane-wave method. *Solid State Commun.*, 114(1):15–20, 2000.
- [343] U. von Barth and L. Hedin. A local exchange-correlation potential for the spin polarized case. i. *J. Phys. C: Solid State Phys.*, 5(13):1629, 1972.
- [344] M. R. Philpott and Y. Kawazoe. Bonding and magnetism in nanosized graphene molecules: Singlet states of zigzag edged hexangulenes $C_{6m^2}H_{6m}$ ($m= 2, 3, 10$). *J. Chem. Phys.*, 131(21):214706, 2009.
- [345] L. Wang, X. Gao, X. Yan, J. Zhou, Z. Gao, S. Nagase, S. Sanvito, Y. Maeda, T. Akasaka, W. N. Mei, and J. Lu. Half-metallic sandwich molecular wires with negative differential resistance and sign-reversible high spin-filter efficiency. *J. Phys. Chem. C*, 114(50):21893–21899, 2010.
- [346] J. P. Perdew and M. Levy. Physical content of the exact Kohn-Sham orbital energies: band gaps and derivative discontinuities. *Phys. Rev. Lett.*, 51(20):1884, 1983.
- [347] C. A. Coulson. Energy bands in graphite. *Nature*, 159:265–266, 1947.
- [348] V. L. J. Joly, K. Takahara, K. Takai, K. Sugihara, T. Enoki, M. Koshino, and H. Tanaka. Effect of electron localization on the edge-state spins in a disordered network of nanographene sheets. *Phys. Rev. B*, 81(11):115408, 2010.
- [349] G. R. Jenness, O. Karalti, and K. D. Jordan. Benchmark calculations of water–acene interaction energies: Extrapolation to the water–graphene limit and assessment of dispersion–corrected DFT methods. *Phys. Chem. Chem. Phys.*, 12(24):6375–6381, 2010.
- [350] P. Schyman and W. L. Jorgensen. Exploring adsorption of water and ions on carbon surfaces using a polarizable force field. *J. Phys. Chem. Lett.*, 4(3):468–474, 2013.
- [351] F. Nunzi, F. Mercuri, and A. Sgamellotti. The interaction of $Cr(CO)_3$ on the $(n, 0)$ nanotube side-walls: a density functional study through a cluster model approach. *Mol. Phys.*, 101(13):2047–2054, 2003.

- [352] J. I. Martínez, I. Cabria, M. J. López, and J. A. Alonso. Adsorption of lithium on finite graphitic clusters. *J. Phys. Chem. C*, 113(3):939–941, 2008.
- [353] H. Johll, H. C. Kang, and E. S. Tok. Density functional theory study of Fe, Co, and Ni adatoms and dimers adsorbed on graphene. *Phys. Rev. B*, 79(24):245416, 2009.
- [354] S. Datta, M. Kabir, S. Ganguly, B. Sanyal, T. Saha-Dasgupta, and A. Mookerjee. Structure, bonding, and magnetism of cobalt clusters from first-principles calculations. *Phys. Rev. B*, 76(1):014429, 2007.
- [355] H. Yoshida, A. Terasaki, K. Kobayashi, M. Tsukada, and T. Kondow. Spin-polarized electronic structure of cobalt cluster anions studied by photoelectron spectroscopy. *J. Chem. Phys.*, 102(15):5960–5965, 1995.
- [356] J. L. Rodríguez-López, F. Aguilera-Granja, K. Michaelian, and A. Vega. Structure and magnetism of cobalt clusters. *Phys. Rev. B*, 67(17):174413, 2003.
- [357] H. Johll, J. Wu, S. W. Ong, H. C. Kang, and E. S. Tok. Graphene-adsorbed Fe, Co, and Ni trimers and tetramers: Structure, stability, and magnetic moment. *Phys. Rev. B*, 83(20):205408, 2011.
- [358] A. N. Andriotis and M. Menon. Tight-binding molecular-dynamics study of ferromagnetic clusters. *Phys. Rev. B*, 57(16):10069, 1998.
- [359] D. M. Duffy and J. A. Blackman. Magnetism of 3d transition-metal adatoms and dimers on graphite. *Phys. Rev. B*, 58(11):7443, 1998.
- [360] Y. Virgus, W. Purwanto, H. Krakauer, and S. Zhang. Ab initio many-body study of cobalt adatoms adsorbed on graphene. *Phys. Rev. B*, 86(24):241406, 2012.
- [361] T. Alonso-Lanza, A. Ayuela, and F. Aguilera-Granja. Chemical bonding of transition-metal co13 clusters with graphene. *ChemPhysChem*, 16(17):3700–3710, 2015.
- [362] G. K. Shenoy and F. E. Wagner. *Mössbauer Isomer Shifts*. North-Holland Publishing Company, 1978.
- [363] S. Blügel, H. Akai, R. Zeller, and P. H. Dederichs. Hyperfine fields of 3d and 4d impurities in nickel. *Phys. Rev. B*, 35(7):3271, 1987.
- [364] D. Gatteschi, R. Sessoli, and J. Villain. *Molecular nanomagnets*. Oxford University Press, New York, 2006.
- [365] G. Toulouse. Theory of the frustration effect in spin glasses: I. *Commun. Phys.*, pages 99–103, 1987.
- [366] M. Pickel, A. B. Schmidt, F. Giesen, J. Braun, J. Minár, H. Ebert, M. Donath, and M. Weinelt. Spin-orbit hybridization points in the face-centered-cubic cobalt band structure. *Phys. Rev. Lett.*, 101:066402, Aug 2008.

- [367] M. J. Piotrowski, P. Piquini, L. Candido, and J. L. F. Da Silva. The role of electron localization in the atomic structure of transition-metal 13-atom clusters: the example of Co_{13} , Rh_{13} , and Hf_{13} . *Phys. Chem. Chem. Phys.*, 13(38):17242–17248, 2011.
- [368] T. N. Nguyen, W. Wernsdorfer, M. Shiddiq, K. A. Abboud, S. Hill, and G. Christou. Supramolecular aggregates of single-molecule magnets: exchange-biased quantum tunneling of magnetization in a rectangular $[\text{Mn}_3]_4$ tetramer. *Chem. Sci.*, 2016.
- [369] S. Yamamoto, H. Tatewaki, H. Moriyama, and H. Nakano. A study of the ground state of manganese dimer using quasidegenerate perturbation theory. *J. Chem. Phys.*, 124(12):124302, 2006.
- [370] E. O. Brimm, M. A. Lynch Jr, and W. J. Sesny. Preparation and properties of manganese carbonyl. *J. Am. Chem. Soc.*, 76(14):3831–3835, 1954.
- [371] L. F. Dahl, E. Ishishi, and R. E. Rundle. Polynuclear metal carbonyls. I. Structures of $\text{Mn}_2(\text{CO})_{10}$ and $\text{Re}_2(\text{CO})_{10}$. *J. Chem. Phys.*, 26(6):1750–1751, 1957.
- [372] X. Chong, Y. Jiang, R. Zhou, and J. Feng. First principles study the stability, mechanical and electronic properties of manganese carbides. *Comput. Mater. Sci.*, 87:19–25, 2014.
- [373] P. Karen, H. Fjellvag, A. Kjekshus, and A. F. Andresen. On the phase relations and structural and magnetic properties of the stable manganese carbides Mn_{23}C_6 , Mn_5C_2 and Mn_7C_3 . *Acta Chem. Scand.*, 45(6):549–557, 1991.
- [374] S. K. Nayak, B. K. Rao, and P. Jena. Equilibrium geometries, electronic structure and magnetic properties of small manganese clusters. *J. Phys. Condens. Matter*, 10(48):10863, 1998.
- [375] T. Alonso-Lanza, A. Ayuela, and F. Aguilera-Granja. Substitutional 4d and 5d impurities in graphene. *Phys. Chem. Chem. Phys.*, 18:21913–21920, 2016.
- [376] I. D. Hughes, M. Däne, A. Ernst, W. Hergert, M. Lüders, J. Poulter, J. B. Staunton, A. Svane, Z. Szotek, and W. M. Temmerman. Lanthanide contraction and magnetism in the heavy rare earth elements. *Nature*, 446(7136):650–653, 2007.
- [377] R. J. Morris and G. S. Girolami. High-valent organomanganese chemistry. 1. synthesis and characterization of manganese (III) and -(IV) alkyls. *Organometallics*, 10(3):792–799, 1991.
- [378] H. Sevinçli, M. Topsakal, E. Durgun, and S. Ciraci. Electronic and magnetic properties of 3d transition-metal atom adsorbed graphene and graphene nanoribbons. *Phys. Rev. B*, 77(19):195434, 2008.

- [379] B. P. Stoicheff. High resolution raman spectroscopy of gases: II. Rotational spectra of C_6H_6 and C_6D_6 , and internuclear distances in the benzene molecule. *Can. J. Phys.*, 32(5):339–346, 1954.
- [380] M. Qing-Min, X. Zun, L. Ying, and L. You-Cheng. Configurations, electronic structure and magnetic ordering of small manganese clusters. *Chin. Phys. Lett.*, 24(7):1908, 2007.
- [381] P. Bobadova-Parvanova, K. A. Jackson, S. Srinivas, and M. Horoi. Structure, bonding, and magnetism in manganese clusters. *J. Chem. Phys.*, 122(1):14310–14310, 2005.
- [382] R. C. Longo, E. G. Noya, and L. J. Gallego. Fully unconstrained density-functional study of the structures and magnetic moments of small Mn_n clusters ($n=2-7$). *Phys. Rev. B*, 72(17):174409, 2005.
- [383] M. Kabir, A. Mookerjee, and D. G. Kanhere. Structure, electronic properties, and magnetic transition in manganese clusters. *Phys. Rev. B*, 73(22):224439_1–224439_11, 2006.
- [384] D. Tzeli, U. Miranda, I. G. Kaplan, and A. Mavridis. First principles study of the electronic structure and bonding of Mn_2 . *J. Chem. Phys.*, 129(15):154310, 2008.
- [385] A. Wolf and H. H. Schmidtke. Nonempirical calculations on diatomic transition metals. II. RHF investigation of lowest closed-shell states of homonuclear 3d transition-metal dimers. *Int. J. Quantum Chem.*, 18(5):1187–1205, 1980.
- [386] S. Paul and A. Misra. On magnetic nature of Mn clusters. *J. Mol. Struct. THEOCHEM*, 907(1):35–40, 2009.
- [387] J. Mejía-López, A. H. Romero, M. E. Garcia, and J. L. Morán-López. Understanding the elusive magnetic behavior of manganese clusters. *Phys. Rev. B*, 78(13):134405, 2008.
- [388] M. D. Morse. Clusters of transition-metal atoms. *Chem. Rev.*, 86(6):1049–1109, 1986.
- [389] F. López-Urías and A. Díaz-Ortiz. Magnetism in Mn clusters: Role of correlation effects. *Phys. Rev. B*, 68(18):180406, 2003.
- [390] S. Yamanaka, T. Ukai, K. Nakata, R. Takeda, M. Shoji, T. Kawakami, T. Takada, and K. Yamaguchi. Density functional study of manganese dimer. *Int. J. Quantum Chem.*, 107(15):3178–3190, 2007.
- [391] M. Cheeseman, R. J. Van Zee, H. L. Flanagan, and W. Weltner Jr. Transition-metal diatomics: Mn_2 , Mn^+_2 , $CrMn$. *J. Chem. Phys.*, 92(3):1553–1559, 1990.
- [392] C. A. Baumann, R. J. Van Zee, S. V. Bhat, and W. Weltner Jr. ESR of Mn_2 and Mn_5 molecules in rare-gas matrices. *J. Chem. Phys.*, 78(1):190–199, 1983.

8 Bibliography

- [393] J. C. Rivoal, J. S. Emampour, K. J. Zeringue, and M. Vala. Ground-state exchange energy of the Mn_2 antiferromagnetic molecule. *Chem. Phys. Lett.*, 92(3):313–316, 1982.
- [394] R. J. Van Zee, C. A. Baumann, and W. Weltner Jr. The antiferromagnetic Mn_2 molecule. 1981.
- [395] K. D. Bier, T. L. Haslett, A. D. Kirkwood, and M. Moskovits. The resonance raman and visible absorbance spectra of matrix isolated Mn_2 and Mn_3 . *J. Chem. Phys.*, 89(1):6–12, 1988.
- [396] T. Yasuike, A. Nakajima, S. Yabushita, and K. Kaya. Why do vanadium atoms form multiple-decker sandwich clusters with benzene molecules efficiently? *J. Phys. Chem. A*, 101(29):5360–5367, 1997.
- [397] M. B. Knickelbein. Nickel clusters: The influence of adsorbates on magnetic moments. *J. Chem. Phys.*, 116(22):9703–9711, 2002.
- [398] D. Fritsch, K. Koepf, M. Richter, and H. Eschrig. Transition metal dimers as potential molecular magnets: a challenge to computational chemistry. *J. Comput. Chem.*, 29(13):2210–2219, 2008.
- [399] M. C. Micheli, R. Pis Diez, and A. H. Jubert. A density functional study of small nickel clusters. *Int. J. Quantum Chem.*, 70(4-5):693–701, 1998.
- [400] F. A. Reuse and S. N. Khanna. Geometry, electronic structure, and magnetism of small Ni_n ($n=2-6, 8, 13$) clusters. *Chem. Phys. Lett.*, 234(1):77–81, 1995.
- [401] B. K. Rao and P. Jena. Caging of Ni clusters by benzene molecules and its effect on the magnetism of Ni clusters. *J. Chem. Phys.*, 116(4):1343–1349, 2002.
- [402] B. N. Papas and H. F. Schaefer III. Homonuclear transition-metal trimers. *J. Chem. Phys.*, 123(7):074321, 2005.
- [403] M. Castro, C. Jamorski, and D. R. Salahub. Structure, bonding, and magnetism of small Fe_n , Co_n , and Ni_n clusters, $n \leq 5$. *Chem. Phys. Lett.*, 271(1):133–142, 1997.
- [404] A. Bérces. The structures and vibrational frequencies of small clusters of transition metal and main group elements. A gradient corrected density functional study. *Spectrochim. Acta Mol. Biomol. Spectrosc.*, 53(8):1257–1272, 1997.
- [405] G. A. Cisneros, M. Castro, and D. R. Salahub. DFT study of the structural and electronic properties of small Ni_n ($n=2-4$) clusters. *Int. J. Quantum Chem.*, 75(4-5):847–861, 1999.
- [406] Z. Xie, Q. Ma, Y. Liu, and Y. Li. First-principles study of the stability and Jahn–Teller distortion of nickel clusters. *Phys. Lett. A*, 342(5):459–467, 2005.

- [407] G. L. Arvizu and P. Calaminici. Assessment of density functional theory optimized basis sets for gradient corrected functionals to transition metal systems: The case of small Ni_n ($n \leq 5$) clusters. *J. Chem. Phys.*, 126(19):194102, 2007.
- [408] M. C. Michelini, R. Pis Diez, and A. H. Jubert. Density functional study of the ionization potentials and electron affinities of small Ni_n clusters with $n = 2-6$ and 8. *Comput. Mater. Sci.*, 31(3):292–298, 2004.
- [409] W. Sucksmith and J. E. Thompson. The magnetic anisotropy of cobalt. In *Proc. R. Soc. A*, volume 225, pages 362–375. The Royal Society, 1954.
- [410] P. Escudier. Magnetization anisotropy-important parameter for study of magnetocrystalline anisotropy. In *Ann. Phys.*, volume 9, pages 125–173. Editions physique zi de courtaboeuf ave 7 av du hoggar, bp 112, 91944 Les Ulis Cedex, France, 1975.
- [411] G. H. O. Daalderop, P. J. Kelly, and M. F. H. Schuurmans. First-principles calculation of the magnetocrystalline anisotropy energy of iron, cobalt, and nickel. *Phys. Rev. B*, 41(17):11919, 1990.
- [412] J. Meyer, M. Tombers, C. van Wüllen, G. Niedner-Schatteburg, S. Peredkov, W. Eberhardt, M. Neeb, S. Palutke, M. Martins, and W. Wurth. The spin and orbital contributions to the total magnetic moments of free Fe, Co, and Ni clusters. *J. Chem. Phys.*, 143(10):104302, 2015.
- [413] J. Vogel and M. Sacchi. Polarization and angular dependence of the $L_{2,3}$ absorption edges in Ni (110). *Phys. Rev. B*, 49(5):3230, 1994.
- [414] C. T. Chen, N. V. Smith, and F. Sette. Exchange, spin-orbit, and correlation effects in the soft-x-ray magnetic-circular-dichroism spectrum of nickel. *Phys. Rev. B*, 43(8):6785, 1991.
- [415] A. Langenberg, K. Hirsch, A. Ławicki, V. Zamudio-Bayer, M. Niemeyer, P. Chmiela, B. Langbehn, A. Terasaki, B. v. Issendorff, and J. T. Lau. Spin and orbital magnetic moments of size-selected iron, cobalt, and nickel clusters. *Phys. Rev. B*, 90(18):184420, 2014.
- [416] P. Bruno. Tight-binding approach to the orbital magnetic moment and magnetocrystalline anisotropy of transition-metal monolayers. *Phys. Rev. B*, 39(1):865, 1989.
- [417] L. M. Liz-Marzán and P. V. Kamat. *Nanoscale Materials*. Springer, 2003.
- [418] H. Hopster and H. P. Oepen. *Magnetic Microscopy of Nanostructures*. NanoScience and Technology. Springer Berlin Heidelberg, 2006.
- [419] J. P. Bucher, D. C. Douglass, and L. A. Bloomfield. Magnetic properties of free cobalt clusters. *Phys. Rev. Lett.*, 66(23):3052, 1991.

- [420] F. Aguilera-Granja, A. Vega, and L. C. Balbás. A new family of star-like icosahedral structures for small cobalt clusters. *Chem. Phys.*, 415:106–111, 2013.
- [421] L. Liu, Y. Su, J. Gao, and J. Zhao. Electronic and magnetic properties for Co_{13} clusters deposited on graphene: A first-principles exploration. *Physica E*, 46:6–11, 2012.
- [422] J. L. Rodríguez-López, F. Aguilera-Granja, K. Michaelian, and A. Vega. Structure and magnetism of cobalt clusters. *Phys. Rev. B*, 67(17):174413, 2003.
- [423] S. Datta, M. Kabir, S. Ganguly, B. Sanyal, T. Saha-Dasgupta, and A. Mookerjee. Structure, bonding, and magnetism of cobalt clusters from first-principles calculations. *Phys. Rev. B*, 76(1):014429, 2007.
- [424] X. Xu, S. Yin, R. Moro, and W. A. de Heer. Magnetic moments and adiabatic magnetization of free cobalt clusters. *Phys. Rev. Lett.*, 95(23):237209, 2005.
- [425] S. Peredkov, A. Savci, S. Peters, M. Neeb, W. Eberhardt, H. Kampschulte, J. Meyer, M. Tombers, B. Hofferberth, F. Menges, and G. Niedner-Schatteburg. X-ray absorption spectroscopy of mass-selected transition metal clusters using a cyclotron ion trap: An experimental setup for measuring XMCD spectra of free clusters. *Electron. Spectrosc. Relat. Phenom.*, 184(3):113–118, 2011.
- [426] C. M. Chang and M. Y. Chou. Alternative low-symmetry structure for 13-atom metal clusters. *Phys. Rev. Lett.*, 93(13):133401, 2004.
- [427] P. J. Brucat, C. L. Pettiette, S. Yang, L. S. Zheng, M. J. Craycraft, and R. E. Smalley. Charge dependence of chemisorption patterns for transition metal clusters. *J. Chem. Phys.*, 85(8):4747–4748, 1986.
- [428] S. N. Schauer, P. Williams, and R. N. Compton. Production of small doubly charged negative carbon cluster ions by sputtering. *Phys. Rev. Lett.*, 65(5):625, 1990.
- [429] P. Milani and W. A. de Heer. Improved pulsed laser vaporization source for production of intense beams of neutral and ionized clusters. *Rev. Sci. Instrum.*, 61(7):1835–1838, 1990.
- [430] P. Scheier and T. D. Märk. Triply charged argon clusters: production and stability (appearance energy and appearance size). *Chem. Phys. Lett.*, 136(5):423–426, 1987.
- [431] B. F. Habenicht, D. Teng, L. Semidey-Flecha, D. S. Sholl, and Y. Xu. Adsorption and diffusion of 4d and 5d transition metal adatoms on graphene/Ru (0001) and the implications for cluster nucleation. *Top. Catal.*, 57(1-4):69–79, 2014.
- [432] K. N. R. Taylor and M. I. Darby. *Physics of rare earth solids*. 1972.

- [433] M. Seitz, A. G. Oliver, and K. N. Raymond. The lanthanide contraction revisited. *J. Am. Chem. Soc.*, 129(36):11153–11160, 2007.
- [434] C. Clavaguéra, J. P. Dognon, and P. Pyykkö. Calculated lanthanide contractions for molecular trihalides and fully hydrated ions: The contributions from relativity and 4f-shell hybridization. *Chem. Phys. Lett.*, 429(1):8–12, 2006.
- [435] H. Raebiger, A. Ayuela, and R. M. Nieminen. Intrinsic hole localization mechanism in magnetic semiconductors. *J. Phys. Condens. Matter*, 16(41):L457, 2004.
- [436] A. M. Souza, A. R. Rocha, A. Fazzio, and A. J. R. da Silva. Ab-initio calculations for a realistic sensor: A study of CO sensors based on nitrogen-rich carbon nanotubes. *AIP Adv.*, 2(3):032115, 2012.
- [437] Z. Zanolli and J. C. Charlier. Defective carbon nanotubes for single-molecule sensing. *Phys. Rev. B*, 80(15):155447, 2009.
- [438] E. Hobi Jr, R. B. Pontes, A. Fazzio, and A. J. R. da Silva. Formation of atomic carbon chains from graphene nanoribbons. *Phys. Rev. B*, 81(20):201406, 2010.
- [439] J. Guan, Z. Zhu, and D. Tománek. Phase coexistence and metal-insulator transition in few-layer phosphorene: a computational study. *Phys. Rev. Lett.*, 113(4):046804, 2014.
- [440] S. Cahangirov, V. O. Özçelik, L. Xian, J. Avila, S. Cho, M. C. Asensio, S. Ciraci, and A. Rubio. Atomic structure of the 3×3 phase of silicene on Ag (111). *Phys. Rev. B*, 90(3):035448, 2014.
- [441] T. Alonso-Lanza, A. Ayuela, and F. Aguilera-Granja. An array of layers in silicon sulfides: Chainlike and monolayer. *Phys. Rev. B*, 94(24):245441, 2016.
- [442] J. Ma, D. Alfe, A. Michaelides, and E. Wang. Stone-wales defects in graphene and other planar sp^2 -bonded materials. *Phys. Rev. B*, 80(3):033407, 2009.

